



**HAL**  
open science

# Flow drive in tokamak plasmas: competition and synergies between turbulence and neoclassical effects

Robin Varennes

► **To cite this version:**

Robin Varennes. Flow drive in tokamak plasmas: competition and synergies between turbulence and neoclassical effects. Physics [physics]. Aix-Marseille Université, France, 2022. English. NNT: . tel-03820772v2

**HAL Id: tel-03820772**

**<https://hal.science/tel-03820772v2>**

Submitted on 16 Jan 2023 (v2), last revised 23 Feb 2023 (v3)

**HAL** is a multi-disciplinary open access archive for the deposit and dissemination of scientific research documents, whether they are published or not. The documents may come from teaching and research institutions in France or abroad, or from public or private research centers.

L'archive ouverte pluridisciplinaire **HAL**, est destinée au dépôt et à la diffusion de documents scientifiques de niveau recherche, publiés ou non, émanant des établissements d'enseignement et de recherche français ou étrangers, des laboratoires publics ou privés.

# THÈSE DE DOCTORAT

Soutenue à Aix-Marseille Université  
le 13 Décembre 2022 par

**Robin VARENNES**

Génération d'écoulements dans les plasmas de tokamak :  
compétition et synergies entre turbulence et effets  
néoclassiques

Flow drive in tokamak plasmas : competition and synergies between  
turbulence and neoclassical effects

## Discipline

Physique et Science de la Matière

## Spécialité

Energie, Rayonnement et Plasma

## École doctorale

ED 352 Physique et Science de la Matière

## Laboratoire/Partenaires de recherche

- CEA-Cadarache - Institut de Recherche sur la Fusion par confinement Magnétique, Saint-Paul-lez-Durance, France
- Ecole Polytechnique - Laboratoire de Physique des Plasmas, Palaiseau, France
- Aix-Marseille Université, Marseille, France

## Composition du jury

• Stephan Brunner • EPFL/Swiss Plasma Center	Rapporteur
• Tobias Goerler • IPP Garching	Rapporteur
• Daniela Grasso • CNR/Politecnico di Torino	Examinatrice
• Peter Beyer • Aix-Marseille Université	Président du jury
• Etienne Gravier • Université de Lorraine	Examineur
• Yanick Sarazin • CEA/IRFM	Examineur
• Peter De Vries • Iter Organization	Invité
• Xavier Garbet • CEA/IRFM	Directeur de thèse
• Laure Vermare • CNRS/LPP	Directrice de thèse

# Affidavit

Je soussigné, Robin Varennes, déclare par la présente que le travail présenté dans ce manuscrit est mon propre travail, réalisé sous la direction scientifique de Laure Vermare et Xavier Garbet, dans le respect des principes d'honnêteté, d'intégrité et de responsabilité inhérents à la mission de recherche. Les travaux de recherche et la rédaction de ce manuscrit ont été réalisés dans le respect à la fois de la charte nationale de déontologie des métiers de la recherche et de la charte d'Aix-Marseille Université relative à la lutte contre le plagiat.

Ce travail n'a pas été précédemment soumis en France ou à l'étranger dans une version identique ou similaire à un organisme examinateur.

Fait à Cadarache le 26/09/2022



Cette œuvre est mise à disposition selon les termes de la [Licence Creative Commons Attribution - Pas d'Utilisation Commerciale - Pas de Modification 4.0 International](https://creativecommons.org/licenses/by-nc-nd/4.0/).

# Liste de publications et participation aux conférences

## Liste des publications réalisées dans le cadre du projet de thèse :

1. **R. Varennes**, X. Garbet, L. Vermare, Y. Sarazin, G. Dif-Pradalier, V. Grandgirard, P. Ghendrih, P. Donnel, M. Peret, K. Obrejan, and E. Bourne, *Synergy of turbulent momentum drive and magnetic braking*, Physical Review Letters 128, [10.1103/PhysRevLett.128.255002](https://doi.org/10.1103/PhysRevLett.128.255002) (2022).
2. **R. Varennes**, X. Garbet, L. Vermare, Y. Sarazin, G. Dif-Pradalier, V. Grandgirard, P. Ghendrih, P. Donnel, M. Peret, K. Obrejan, and E. Bourne, *Impact of magnetic ripple on neoclassical equilibrium in gyrokinetic simulations*, Submitted to Plasma Physics and Controlled Fusion (2022)
3. Y. Sarazin, G. Dif-Pradalier, X. Garbet, P. Ghendrih, A. Berger, C. Gillot, V. Grandgirard, K. Obrejan, **R. Varennes**, L. Vermare, and T. Cartier-Michaud, *Key impact of phase dynamics and diamagnetic drive on Reynolds stress in magnetic fusion plasmas*, Plasma Physics and Controlled Fusion 63, [10.1088/1361-6587/abf673](https://doi.org/10.1088/1361-6587/abf673) (2021).
4. L. Vermare, P. Hennequin, C. Honoré, M. Peret, G. Dif-Pradalier, X. Garbet, J. Gunn, C. Bourdelle, F. Clairet, J. Morales, R. Dumont, M. Goniche, P. Maget, **R. Varennes**, and the WEST Team, *Formation of the radial electric field profile in the WEST tokamak*, Nuclear Fusion 62, [10.1088/1741-4326/ac3c85](https://doi.org/10.1088/1741-4326/ac3c85) (2021).
5. C. Gillot, G. Dif-Pradalier, X. Garbet, O. Panico, Y. Sarazin, **R. Varennes**, and D. Zarzoso, *Investigation of tokamak turbulent avalanches using wave-kinetic formulation in toroidal geometry*, Journal of Plasma Physics 87, [10.1017/S0022377821000350](https://doi.org/10.1017/S0022377821000350) (2021).
6. X. Garbet, O. Panico, **R. Varennes**, C. Gillot, G. Dif-Pradalier, Y. Sarazin, V. Grandgirard, P. Ghendrih, and L. Vermare, *Wave trapping and  $E \times B$  staircases*, Physics of Plasmas 28, [10.1063/5.0042930](https://doi.org/10.1063/5.0042930) (2021).
7. Y. Sarazin, J. Hillairet, J.-L. Duchateau, K. Gaudimont, **R. Varennes**, X. Garbet, P. Ghendrih, R. Guirlet, B. Pégourié, and A. Torre, *Impact of scaling laws on tokamak reactor dimensioning*, Nuclear Fusion 60, [10.1088/1741-4326/ab48a5](https://doi.org/10.1088/1741-4326/ab48a5) (2019).

## Participation aux conférences et écoles d'été au cours de la période de thèse :

### Invited

- 12th Festival de Théorie 2022, *Interplay between magnetic braking and turbulent stress tensor regarding plasma flow*, 04/07/2022 - 28/07/2022, Aix-en-Provence, France

### Oral

- AAPPS-DPP (Association of Asia-Pacific Physical Societies, Division of Plasma Physics) 4th Asia Pacific Conference on Plasma Physics, *Impact of a rippled magnetic field on flows*, 26/10/2020 - 31/10/2020, Online
- KITP (Kavli Institute for Theoretical Physics) "Staircase" workshop, *Impact of a ripple magnetic field on flows in tokamaks*, 18/02/2021, Online
- 2021 EUROfusion TSVV1 (Theory, Simulation, Validation, Verification - Physics of the L-H Transition and Pedestals) Progress workshop, *Synergy between turbulent momentum drive and magnetic braking*, 21/10/2021 - 22/10/2021, Online
- 2022 EUROfusion TSVV1 (Theory, Simulation, Validation, Verification - Physics of the L-H Transition and Pedestals) Progress workshop, *Safety factor impact on the radial electric field in gyrokinetic simulations*, 27/09/2022 - 28/09/2022, Garching, Germany

### Poster

- 25th Virtual EU-US Transport Task Force (TTF) Meeting, *Non-axisymmetric magnetic field perturbations effect on flows*, 06/09/2021 - 10/09/2021, Online
- 19th European Fusion Theory Conference (EFTC), *Non-axisymmetric magnetic field perturbations effect on flows*, 11/10/2021 - 15/10/2021, Online
- 48th EPS Conference on Plasma Physics, *Plasma flow in tokamaks : unraveling the competition and synergy between turbulence and 3D magnetic perturbations*, 27/06/2022 - 01/07/2022, Online
- Joint Varenna - Lausanne International Workshop, *Intrinsic rotation drive in tokamaks : the competition between turbulence and magnetic braking*, 12/09/2022 - 16/09/2022, Varenna, Italy

# Résumé

Comprendre l'autogénération des écoulements dans les plasmas de tokamak est un sujet primordial. En effet, le contrôle des écoulements par injection de moment externe dans les futurs réacteurs sera difficilement réalisable, voire impossible. Les écoulements jouent pourtant un rôle majeur dans la stabilité et la performance d'un plasma de fusion. Dans cette thèse, l'autogénération de l'écoulement perpendiculaire aux lignes de champ, associée au champ électrique radial, est étudiée dans deux contextes expérimentalement pertinents. La manière dont s'établit ce champ est un enjeu majeur, car il est impliqué dans la formation et le maintien des barrières de transport qui apparaissent spontanément dans les décharges hautes puissance, réduisant fortement le transport turbulent.

Dans un premier temps, l'effet d'une perturbation 3D du champ magnétique comme celle causée par la modulation provenant du nombre fini de bobines toroïdales, aussi appelé "ripple", est étudié. Une telle perturbation affecte la vitesse toroïdale du plasma, elle-même générée de façon spontanée par la turbulence. Jusqu'à présent, la compétition et la synergie entre ces deux contributions n'avaient pas été étudiées numériquement et théoriquement. Pourtant, de nombreuses études expérimentales sur différents tokamaks ont montré que ces deux effets impactent drastiquement la vitesse toroïdale du plasma. À l'aide d'un modèle théorique et de simulations effectuées avec le code gyrocinétique GYSELA, la compétition a été observée et quantifiée. Une expression de l'amplitude critique du ripple pour laquelle la turbulence devient sous-dominante dans le contrôle de la rotation toroïdale a été définie puis validée avec ces simulations. Des études préliminaires montrent alors que ce seuil pourrait être franchi dans ITER. La synergie entre la turbulence et le ripple a également été évaluée. L'effet dominant est l'impact du ripple sur le tenseur de Reynolds au travers de la modification du cisaillement du champ électrique radial.

Dans un second temps, les expériences récentes sur le tokamak WEST montrant que le champ électrique radial est sensible au taux d'enroulement des lignes de champ magnétique, appelé "facteur de sécurité", sont investiguées numériquement via des simulations gyrocinétiques. Comme observé expérimentalement, ces simulations montrent que le champ électrique radial se creuse lorsque le facteur de sécurité et l'intensité turbulente diminuent. Les effets collisionnels apparaissent cependant négligeables pour l'établissement du champ électrique radial mettant en avant le rôle indéniable de la turbulence. L'effet majoritaire vient du transfert d'énergie turbulente variant avec le facteur de sécurité, qui favorise soit les écoulements à très basse fréquence appelés "zonal flows", soit ceux à plus haute fréquence appelés "GAMs".

Mots clés : Plasma, fusion, turbulence, néoclassique, simulations gyrocinétiques

# Abstract

Understanding the self-generation of flows in tokamak plasmas is of prime importance. Indeed, the control of flows by external momentum injection in future reactors will be challenging, if not impossible. However, flows play a major role in the stability and performance of a fusion plasma. In this thesis, the self-generation of the flow perpendicular to the field lines, associated with the radial electric field, is studied in two experimentally relevant contexts. The way this field is established is a major issue, as it is involved in the formation and sustainment of transport barriers that appear spontaneously in high power discharges, significantly reducing turbulent transport.

In a first step, the effect of a 3D perturbation of the magnetic field such as the one caused by the modulation arising from the finite number of toroidal coils, also called "ripple", is studied. Such a perturbation impacts the toroidal velocity of the plasma, itself generated spontaneously by the turbulence. Until now, the competition and synergy between these two contributions had not been studied numerically and theoretically. However, numerous experimental studies on different tokamaks have shown that these two effects drastically impact the toroidal velocity of the plasma. Using a theoretical model and simulations performed with the gyrokinetic code GYSELA, the competition has been observed and quantified. An expression of the critical ripple amplitude for which turbulence becomes subdominant in the control of the toroidal rotation has been defined and validated with these simulations. Preliminary studies show that this threshold could be reached in ITER. The synergy between turbulence and ripple has also been evaluated. The dominant effect is the impact of the ripple on the Reynolds tensor through the modification of the radial electric field radial shear.

In a second step, recent experiments on the WEST tokamak showing that the radial electric field is sensitive to the winding rate of the magnetic field lines, called "safety factor", are numerically investigated with gyrokinetic simulations. As observed experimentally, these simulations show that the radial electric field increases as the safety factor and the turbulent intensity decrease. However, collisional effects appear to be negligible for the establishment of the radial electric field, highlighting the undeniable role of turbulence. The main effect comes from the transfer of turbulent energy varying with the safety factor, which favors either very low frequency flows called "zonal flows", or higher frequency flows called "GAMs".

Keywords: Plasma, fusion, turbulence, neoclassic, gyrokinetic simulations

# Remerciements

Ces trois dernières années, bien que quelque peu perturbées par une petite pandémie mondiale, ont été pour moi très agréables et captivantes grâce à de nombreuses personnes que je tiens à remercier chaleureusement ici.

En première ligne, je tiens bien évidemment à particulièrement remercier mes directeurs de thèse : Xavier Garbet et Laure Vermare. Xavier (ou devrais-je plutôt dire Professeur Garbet maintenant), j'ai appris énormément grâce à toi, et même après ces trois années je reste sur le même point de vue : tu sembles être une source inépuisable de savoir, que tu prends toujours le temps de partager avec le sourire ! Tu es une inspiration pour moi et je me sens véritablement chanceux d'avoir pu travailler à tes côtés.

Laure, un immense merci pour l'aide que tu m'as apporté durant ces trois années, et également pour ta bienveillance et ta bonne humeur contagieuse. Merci d'avoir été là pour remettre la réalité au goût du jour quand les théoriciens s'égarèrent (moi y compris), sans quoi cette thèse n'aurait pas dépassé l'introduction ! Je suis heureux de pouvoir continuer à travailler avec toi pendant mon postdoc au CNRS.

J'aimerais aussi remercier chaleureusement Yanick Sarazin. Merci d'avoir pris autant de temps pour moi durant ma thèse, que ce soit en assistant aux réunions hebdomadaires, en relisant mes différentes productions ou en répondant à mes questions au fil de la thèse. Je te suis également très reconnaissant pour tes cours de Master qui m'ont vraiment donné envie de rejoindre le monde de la théorie et simulation ! Un grand merci également à Virginie Grandgirard pour ton aide inestimable sur tous les aspects numériques de ma thèse. Merci d'avoir toujours pris le temps de répondre à mes questions malgré ton emploi de temps qui semble toujours plein à craquer. Je voudrais également sincèrement remercier Guilhem Dif-Pradalier pour ton aide et tes nombreux conseils durant ces trois années. (Merci également d'être venu me chercher en voiture à Varenna à minuit, sans quoi je serais parti en randonnée d'une heure dans la nuit pour rentrer chez moi !). Je remercie également Philippe Ghendrih, Peter Donnel, Kévin Obrejan et Chantal Passeron. Merci pour votre disponibilité et pour toutes ces conversations enrichissantes ! Ce fut un véritable plaisir de passer ces trois années au sein de l'équipe GYSELA.

Je souhaiterais remercier mon jury, et notamment Stephan Brunner et Tobias Goerler pour leurs efforts en tant que rapporteur de cette thèse.

Je remercie également mes camarades thésards, postdocs et stagiaires. En particulier je remercie Mathieu Peret, mon plus fidèle adepte dans l'adoration de Fast & Furious, pour tous ces joyeux moments au travail mais surtout en dehors. Je remercie également Emily Bourne, pour l'entraide durant la thèse et aussi pour ces soirées chaleureuses. Tu m'as prouvé que la cuisine anglaise pouvait être délicieuse et ça, ce



n'est pas rien ! Une pensée particulière va aussi à mon co-bureau Raffael Düll et aux dommages irrémédiables qu'il a dû subir en ma présence. Merci à tous les camarades du 513: Nicolas Rivals, Olivier Panico, Yann Munsch, Sébastien Roux, Yoana Nakeva, Virginia Quadri, Mattia Dicorato, Hao Yang, Jai Kumar, Anatole Berger, Maylis Carrard et Baptiste Legoux. Malgré mes menaces à répétition, vous avez finalement réussi à convertir mon bureau en salle café de substitution (un grand merci à mon café soluble à qui je dois tout d'ailleurs), et je pense que vous serez tous d'accord pour dire qu'on y a bien rigolé. Un grand merci également aux collègues grimpeurs et musiciens qui se reconnaîtront.

Je voudrais maintenant remercier des personnes spéciales pour moi. Premièrement, je voudrais remercier ma famille : ma mère Annick Szabo, mon père Alain Varennes et mon frère Théodore Varennes. Merci de m'avoir emmené jusqu'ici et de m'avoir toujours soutenu dans mes choix. Un grand merci également à Rémi Duthu d'avoir été mon colocataire durant ces 5 dernières années ! Je dirais bien que j'admire le fait que tu sois encore sain d'esprit après tout ce temps passé ensemble mais on sait tous les deux que ce serait un mensonge. Bien sûr, un incommensurable merci à Éléonore Geulin. Parfois colocataire, parfois collègue thésarde, parfois co-bureau, mais surtout toujours une amie précieuse sur laquelle je peux toujours compter. Cette aventure n'aurait pas été la même sans toi.

Enfin, je remercie Camille Laguerre de m'avoir supporté durant l'écriture interminable de ce manuscrit, et d'être à mes côtés chaque jour.

# Contents

<b>Affidavit</b>	<b>2</b>
<b>Liste de publications et participation aux conférences</b>	<b>3</b>
<b>Résumé</b>	<b>5</b>
<b>Abstract</b>	<b>6</b>
<b>Remerciements</b>	<b>7</b>
<b>Contents</b>	<b>9</b>
<b>List of Figures</b>	<b>12</b>
<b>List of Tables</b>	<b>19</b>
<b>1. Introduction</b>	<b>20</b>
1.1. Fusion energy: context and purpose . . . . .	20
1.2. Nuclear reactions . . . . .	22
1.3. Hot and magnetized plasmas . . . . .	25
1.3.1. Lawson criterion . . . . .	26
1.3.2. Characteristic scales of a hot magnetized plasma . . . . .	28
1.4. Motion of charged particles in a magnetic field . . . . .	30
1.4.1. Cyclotron motion . . . . .	30
1.4.2. Newtonian, Lagrangian, and Hamiltonian formulations of the problem . . . . .	31
1.4.3. Integrable motion . . . . .	32
1.4.4. Confined particle trajectories . . . . .	33
1.4.5. Magnetic configuration of a tokamak . . . . .	35
1.4.6. Particle periodic motion and invariants in an axisymmetric tokamak	37
1.5. Why plasma flows matter . . . . .	39
1.5.1. Loss of symmetry and transport . . . . .	39
1.5.2. Flows and confinement . . . . .	40
1.5.3. Toroidal flow in presence of magnetic ripple and turbulence . .	42
1.5.4. Radial electric field dependency on the safety factor . . . . .	43
1.5.5. Thesis objectives and outline . . . . .	45

<b>2. Physics of flows in a 3D magnetic configuration</b>	<b>46</b>
2.1. Driving flows: a kinetic description . . . . .	47
2.1.1. The different descriptions of a plasma . . . . .	47
2.1.2. Channels of flow drive in tokamak plasmas . . . . .	48
2.2. Resonant surfaces in a rippled tokamak . . . . .	49
2.2.1. Phase space island generated by resonance . . . . .	50
2.2.2. $1/R$ magnetic decay and banana trapped particles . . . . .	52
2.2.3. Locally trapped particle in magnetic ripple wells . . . . .	53
2.2.4. Realistic magnetic configuration with two static perturbations . . . . .	55
2.2.5. Multiple fluctuating perturbations: turbulence . . . . .	58
2.3. Linking forces and fluxes with an entropy variational principle . . . . .	59
2.4. Neoclassical contribution in presence of ripple: the role of collisions . . . . .	61
2.5. Chaos and transport: the stochastic motion of particles . . . . .	66
2.5.1. Physical origin . . . . .	66
2.5.2. Resonance due to magnetic ripple . . . . .	67
2.5.3. Chirikov overlap criterions and diffusion coefficients . . . . .	71
2.6. An analytical model to predict flows in presence of magnetic ripple . . . . .	73
2.6.1. Explicit form of the reduced model . . . . .	73
2.6.2. Assessing the equilibrium flows with the model . . . . .	74
2.6.3. Assessing the dynamics of the flows with the model . . . . .	78
2.7. Turbulence: a short introduction . . . . .	79
2.8. Conclusion of chapter 2 . . . . .	83
<b>3. The GYSELA code</b>	<b>85</b>
3.1. Gyrokinetic model . . . . .	85
3.2. Code description . . . . .	86
3.3. Implementation of magnetic ripple . . . . .	89
3.3.1. GYSELA geometry . . . . .	89
3.3.2. Method of implementation . . . . .	89
3.3.3. Verification through toroidal angular momentum conservation . . . . .	92
3.3.4. Comparison of GYSELA global simulations with neoclassical predictions and NEO . . . . .	94
3.4. Conclusion of chapter 3 . . . . .	101
<b>4. Effect of magnetic ripple on toroidal rotation in presence of turbulence</b>	<b>102</b>
4.1. Introduction . . . . .	102
4.2. Reduced model for the competition between neoclassical effects and turbulence . . . . .	103
4.2.1. Turbulent coefficients using GYSELA simulations without ripple . . . . .	106
4.2.2. Assessing the competition thanks to simulations with ripple . . . . .	109
4.2.3. An heuristic expression for the critical ripple amplitude . . . . .	110
4.3. Interplay mechanisms between ripple and turbulence . . . . .	112
4.3.1. Ripple impact on the turbulent intensity . . . . .	114

4.3.2. Impact of ripple on the shear of radial electric field . . . . .	118
4.4. Conclusion of chapter 4 . . . . .	120
<b>5. Influence of the safety factor on the radial electric field</b>	<b>122</b>
5.1. Introduction . . . . .	122
5.2. Experimental observations . . . . .	123
5.2.1. Doppler back-scattering diagnostic . . . . .	123
5.2.2. Scan of velocity profiles with plasma current . . . . .	125
5.3. Effect of the safety factor in dedicated GYSELA simulations . . . . .	127
5.3.1. Isolating the safety factor effect . . . . .	127
5.3.2. GYSELA simulations parameters . . . . .	127
5.3.3. Observations of the safety factor impact in GYSELA simulations	128
5.3.4. Generalized vorticity conservation and force balance . . . . .	134
5.4. Mechanisms impacting flows carrying a $q$ dependence . . . . .	137
5.4.1. Neoclassical processes . . . . .	138
5.4.2. Zonal flows (ZFs) and Geodesic Acoustic Modes (GAMs) . . . . .	141
5.4.3. Reduced model of energy transfer between turbulence, zonal flows and GAMs . . . . .	144
5.4.4. Synergy between turbulence and neoclassical effects . . . . .	152
5.5. Conclusion of chapter 5 and discussion . . . . .	155
<b>Conclusion</b>	<b>160</b>
<b>Appendix</b>	<b>164</b>
A. Derivation of the guiding center equations of motion . . . . .	164
B. Radial jump of banana trapped particles due to ripple . . . . .	166
C. Derivation of Chirikov overlap parameters and diffusion coefficients related to stochastic transport . . . . .	169
D. Explicit expression of the transport matrix coefficients . . . . .	174
E. Development of a simple model for the neoclassical/turbulent competi- tion . . . . .	174
F. Stability of the equilibriums for the model of energy transfer . . . . .	177
<b>Bibliography</b>	<b>181</b>

# List of Figures

1.1. Measured global temperature evolution <b>(a)</b> as well as the frequency and intensity of exceptional heat waves compared to the pre-industrial era <b>(b)</b> . Extracted from the latest GIEC report [1]. . . . .	21
1.2. Cross-section of $^{235}_{92}\text{U}$ fission vs. the energy of the incident neutron (blue) and cross-section of fusion of two fusion reactions (red & purple) vs. the thermal energy of the reactants. . . . .	23
1.3. Binding energy per nucleus as a function of the number of nucleons in the nucleus. . . . .	24
1.4. Diversity of plasma in the universe. Source: Wikipedia . . . . .	26
1.5. $n\tau_E$ as a function of ion temperature $T$ for fusion experiments with different types of inertial and magnetized confinement devices. The right y-axis represents the ratio of fusion power to externally applied heating power. Extracted from [8]. . . . .	28
1.6. Illustration of the charge screening effect in plasmas. A Debye sphere of radius $\lambda_D$ defines the volume for which a charged particle is screened by particles of opposite charge. . . . .	29
1.7. Trajectory of a positively charged particle immersed in a uniform and stationary magnetic field. . . . .	31
1.8. Magnetic configuration of a tokamak. . . . .	36
1.9. Typical trajectories of passing (top) and banana-trapped (bottom) particle. On the right is the projection of these trajectories on the poloidal plane. Extracted from [15]. . . . .	38
1.10. Radial profile of the radial electric field (a) and plasma pressure (b) in ASDEX-Upgrade discharges in L-mode (black) and in H-mode (red). Extracted from [16]. . . . .	41
1.11. (a) Mach number at the plasma center $r/a \sim 0$ (blue) and plasma edge $r/a \sim 0.9$ (red) versus the ripple amplitude at the outer separatrix in JET discharges. Extracted from [27]. (b) Radial profiles of the toroidal velocity in Tore Supra discharges for different ripple amplitudes. Extracted from [25]. . . . .	43
1.12. Radial profile, near the edge of the plasma, of the transverse velocity measured in the WEST tokamak for different plasma current values in the Upper Single Null (left) and Lower Single Null (right) configurations. Extracted from [33]. . . . .	44

2.1. Iso-contour in the angle/action ( $\xi, I$ ) space of the new Hamiltonian $\mathcal{H}_I$ describing the resonance. Particles are passing (trapped) if the amplitude of the perturbation $h$ is higher (smaller) than $\mathcal{H}_I$ . . . . .	52
2.2. <b>(a)</b> Principle of the banana trapping. For the same perpendicular momentum, the blue trajectory is passing and the green trajectory is trapped due to a different parallel momentum. <b>(b)</b> Island generated by the banana trapping in the $(\theta, v_{\parallel})$ phase space. . . . .	53
2.3. Poloidal section of the ripple amplitude in the Tore Supra tokamak (Tore Supra and WEST contain 18 toroidal coils.) in closed flux surfaces. . . .	54
2.4. <b>(a)</b> Principle of trapping induced by ripple with $N_c = 8$ : for the same perpendicular momentum, the blue trajectory is passing and the green trajectory is trapped due to a different parallel momentum. <b>(b)</b> Island generated by the local trapping in the $(\varphi, v_{\parallel})$ phase space. . . . .	55
2.5. Typical shape of the kinetic energy as function of the angle $\varphi_0 + q\theta$ that parametrizes a particular field line for each $\varphi_0$ . Particle trajectory follows constant energy lines. . . . .	56
2.6. Trapped particle trajectories with both perturbations - $1/R$ magnetic field decay and magnetic ripple - obtained with the GCT code [44]. (Left) Banana trapped trajectories exhibit radial and poloidal shifts of bounce points due to magnetic ripple. (Right) Locally trapped particles drift vertically due to the magnetic drift induced by the $1/R$ magnetic decay perturbation. . . . .	58
2.7. Distribution function, taken at fixed radius and magnetic moment $\mu$ , of trapped particles without (left) and with (right) ripple, obtained with GYSELA with $N_c = 16$ . Ripple accounts for an additional trapping in the toroidal direction and also modifies the island of banana-trapped particles near bounce points. . . . .	62
2.8. Typical scaling of the radial neoclassical fluxes with the collisionality for each branch. . . . .	63
2.9. <b>(a)</b> Schematic view in toroidal section of bounce point for trapped particles either below the stochasticity limit (red) or above (blue). The green arrow shows the direction and amplitude of the radial shift $\Delta r$ exerted on the particle by ripple. <b>(b)</b> Successive radial positions of the bounce point for each case. . . . .	67
2.10. Iso-contour at constant $\mathcal{H}_{\omega, n_B}$ for 2 distinct $n_B$ (so for 2 different resonant surfaces). . . . .	69
2.11. Iso-contour at constant $\mathcal{H}_{\omega, n_B}$ (with the Bessel function dependence) for different $n_B$ and $\tau_{n_B}$ with $N_c = 18$ , $q = 3$ and $\theta_B(\mathbf{J}_R) = \pi/2$ . Units are arbitrarily chosen. . . . .	71
2.12. Condition of existence of ripple-induced magnetic wells in the Tore Supra tokamak <b>(a)</b> a radially gaussian ripple (see next Chapter for the reasons to consider such a shape) centered at mid-radius and poloidally symmetric with a $\delta = 3\%$ peak <b>(b)</b> and a $\delta = 0.5\%$ peak <b>(c)</b> . There are no magnetic wells in $Y > 1$ areas (blue) so no local trapping can occur. . .	75

2.13. Scan in ripple amplitude of thermal drives $k_{V_T}$ , $k_N$ and $k_{V_p}$ for a wide range of $v^*$ . Red plain lines represent the asymptotic values that appear in Tab.2.1. . . . .	77
2.14. Wavenumber spectrum of density fluctuations in the #45511 discharge of the Tore Supra tokamak. The region with a $k^{-3}$ scaling is the region of energy injection, and the region with a $k^{-3}/(1+k^2)^2$ scaling is the energy transfer region. Extracted from [75]. . . . .	80
2.15. Fluctuation of the electric potential $\tilde{\phi}$ seen through a colormap in the whole tokamak, simulated with the GYSELA code [76]. . . . .	81
2.16. Sketch of turbulence impact on the fluctuating part of the electric drift in a poloidal section (magnetic drift is neglected here). This drift adds to the parallel motion of the guiding center represented in red. . . . .	81
2.17. Illustration of the interchange instability. A positive (negative) convective cell tends to become even more positive (negative) when the magnetic field gradient and the pressure gradient are aligned, thus causing an instability on the electric field. . . . .	83
3.1. Spatiotemporal scales range described by the GYSELA code and the captured mechanisms. Inspired from Y. Sarazin presentation at Festival de théorie 2022. . . . .	88
3.2. Radial profile of the total toroidal momentum (dashed) and the sum of the expected contributions (plain) for different ripple amplitudes $\delta_0$ . . . . .	94
3.3. Magnetic braking force $\Gamma_{V_T}$ versus $A_{V_T}$ for different ripple amplitudes $\delta$ . Each point corresponds to a simulation with different initial toroidal velocity profiles and represents the $(A_{V_T}, \Gamma_{V_T})$ retrieved at $r/a = 0.5$ after the GAMs phase, here at $v^* = 0.1$ . . . . .	96
3.4. Initial radial profiles of the effective ripple amplitudes $\delta/\epsilon$ <b>(a)</b> , the collisionalities $v^*$ <b>(b)</b> and the normalized toroidal velocities $A_{V_T}$ <b>(c)</b> used for the scan. . . . .	96
3.5. From NEO simulations: Equilibrium particle flux $\Gamma_N$ <b>(a)</b> , equilibrium magnetic braking force $\Gamma_{V_T}$ <b>(b)</b> and equilibrium mean toroidal velocity $V_T$ <b>(c)</b> for different collisionalities $v^*$ at fixed $\delta/\epsilon = 0.03/0.16$ and $N_c q = 16 \times 1.4$ over a wide range of $A_T$ . . . . .	98
3.6. Zoom-up of Fig.3.5 in range of $A_T$ where $\Gamma_N = \Gamma_{V_T} = 0$ . The value of $V_T$ at $A_T$ for which $\Gamma_{V_T}$ cancels is directly linked to the neoclassical thermal drive $k_{V_T}$ . . . . .	99
3.7. Collisionality scan of $k_{V_T}$ obtained with the reduced model, GYSELA and NEO for $\delta = 0.5\%$ (left), $\delta = 1\%$ (middle) and $\delta = 3\%$ (right) at fixed $\epsilon = 0.16$ and $N_c q = 16 \times 1.4$ . . . . .	100
3.8. Collisionality scan of $v_\phi$ and $v_\phi^{\Gamma_N=0}$ obtained with the reduced model and GYSELA for $\delta = 0.5\%$ (left), $\delta = 1\%$ (middle) and $\delta = 3\%$ (right) at fixed $\epsilon = 0.16$ and $N_c q = 16 \times 1.4$ . . . . .	101

4.1. Sketch of the proposed simplified definition for the critical ripple amplitude describing the neoclassical/turbulence competition. The synergistic effects are not accounted for here, but are detailed further below. . .	106
4.2. Initial profiles in simulations. . . . .	107
4.3. Radial profiles of the toroidal velocity $V_T$ ( <b>a</b> ) and its shear $V_T'$ ( <b>b</b> ), as well as the stress tensor $\Pi$ ( <b>c</b> ), taken at turbulent saturation for simulations without ripple and with different initial toroidal velocity profiles $V_T(t=0) = V_{T0} \exp((-32(r/a - 0.5)^2))$ with $a$ the minor radius. Velocities are normalized to a reference ion thermal velocity $V_{T0}$ and lengths to a reference ion Larmor radius $\rho_0$ . . . . .	108
4.4. Evaluation of the turbulent viscosity $\chi$ by the least square method using profiles of Fig.4.3 obtained using GYSELA simulations without ripple for plasmas parameters summarized in Tab.4.1 (green). The incorrect points due to a lack of proper statistics at midradius are removed and this zone is reconstructed using splines, giving the final $\chi$ profile (orange). Distances are normalized to a reference Larmor radius $\rho_0$ . . . . .	108
4.5. Comparison of the theoretical prediction of $v_\phi$ in presence of ripple of different amplitude (green and blue lines) and the turbulent viscous contribution $\chi \lambda_\nu $ (orange) to assess Eq(4.7). The orange zone represents $\chi \lambda_\nu $ for $a/2 \leq  \lambda_\nu ^{-1/2} \leq a$ . Time is normalized to the cyclotron period $\omega_{c0}^{-1}$ . . . . .	109
4.6. Time traces of the toroidal velocity $V_T$ ( <b>a</b> ) and the radial electric field $E_r$ ( <b>b</b> ) in $0.45 < r/a < 0.55$ (shaded areas, mean: solid lines) for different ripple amplitudes. Markers are only here for better visibility. . . . .	110
4.7. ( <b>a</b> ) Radial profiles obtained in GYSELA of the turbulent viscosity $\chi$ normalized to the gyroBohm viscosity $\chi^{GB}$ (blue) and heat diffusivity $\chi^{HF}$ (orange). ( <b>b</b> ) Radial profiles obtained in GYSELA (red) of the neoclassical friction at $\delta_0 = 1\%$ for different $v^*$ (estimated at $r/a = 0.5$ ) and its asymptotic prediction (blue). . . . .	111
4.8. Ripple amplitude scan of $v_\phi^{GYS}/\chi$ (red points) and $v_\phi^{RP}/\chi^{GB}$ (blue line). . . . .	112
4.9. Radial profile of the coarse-grained total toroidal stress tensor $\langle \Pi \rangle_{CG}$ (dashed) and the coarse-grained diamagnetic part of the residual stress $\langle \Pi + \chi \partial_r V_T \rangle_{CG}$ (plain). . . . .	114
4.10. Spectra of $ \phi_{m,n} ^2$ in the $(m, n)$ space taken at $r/a = 0.65$ . . . . .	115
4.11. Spectra of $ \phi_{m,n} ^2$ in the $(m, n)$ space taken at $r/a = 0.65$ for the $\delta_0 = 3\%$ case. The resonance cone is defined by the lines $n = -m/q_{in}$ and $n = -m/q_{out}$ where $q_{out}/q_{in} = q(r \pm \delta r)$ with an arbitrary $\delta r = 0.1a$ . . . . .	116
4.12. Power spectrum $S$ at $r/a = 0.65$ of the turbulent modes for different ripple amplitudes $\delta_0$ (left) and the relative difference with the axisymmetric case (right). . . . .	117
4.13. Radial profile of the turbulent intensity (left) and its coarse-grained radial shear (right). . . . .	118



4.14. Solid lines: radial profile of coarse-grained (temporally and spatially for plain lines and only temporally for dashed lines) radial electric field <b>(a)</b> and its shear <b>(b)</b> , as well as residual stress (same as Fig.4.9 for full lines) <b>(c)</b> and the opposite of its divergence <b>(d)</b> for different ripple amplitudes.	119
4.15. Sketch summarizing Chapter 4.	121
5.1. Principle of back-scattering reflectometry. For probing wave in O-mode polarization, the iso-index-of-refraction surfaces are also the iso-density surfaces. The backscattered wave carries the plasma density fluctuations characteristics associated with the $k_f = -2k_i$ wavenumber.	124
5.2. Radial profiles, near the edge of the plasma, of the $V_{E \times B}$ velocity measured in the Tore Supra tokamak for different plasma current values. The plasma is in contact with the wall at the top (left) / bottom (right).	126
5.3. Radial profiles of the experimental safety factor in the Tore Supra tokamak for the discharges of Fig.5.2.	126
5.4. Radial profiles of the safety factor used in each simulation.	128
5.5. Radial profile of the temperature <b>(a)</b> and its radial gradient <b>(b)</b> for each safety factor profiles at $t = 140000\omega_{c0}^{-1}$ .	129
5.6. Radial profile of the radial electric field $E_r$ for each safety factor profile averaged between $100000 < t[\omega_{c0}^{-1}] < 145000$ .	130
5.7. Spatiotemporal map of the radial electric field $E_r$ for extremal safety factor profiles.	131
5.8. Radial profile of the turbulent intensity $\bar{I}$ time-averaged between $100000 < t[\omega_{c0}^{-1}] < 145000$ for each safety factor profile.	132
5.9. Fluctuations of the electric potential at $t=93600\omega_{c0}^{-1}$ at a toroidal angle $\varphi = \pi/8$ for each case.	133
5.10. $k_\theta$ -spectra of the electric potential spectral density for each safety factor profile at $r/a = 0.8$ and averaged between $100000 < t[\omega_{c0}^{-1}] < 140000$ . The maximal accessible $k_\theta$ decreases with $q$ since the resonant modes follow the $n = -m/q$ line so low $q$ means a steeper line that fastly reaches the limit of the $(m, n)$ box, fixed by the poloidal and toroidal resolution.	134
5.11. Radial profile of each term appearing in the generalized vorticity equation Eq(5.2) at $t = 130000\omega_{c0}^{-1}$ for each case.	135
5.12. Radial profile of each term appearing in the spatially integrated generalized vorticity equation at $t = 130000\omega_{c0}^{-1}$ for each case.	136
5.13. Radial profile of each term appearing in the force balance Eq(5.4) time averaged in the range $100000 < t[\omega_c^{-1}] < 145000$ . The black dashed curve represent the sum $\frac{\nabla_r P}{neB_T} - \frac{E_r}{B_T} + \frac{\varepsilon}{q} V_T$ .	137
5.14. Time evolution of the radial electric field for the $q_{0.5}$ and $q_{1.5}$ cases with only the $n = 0$ mode (top) and all toroidal modes (bottom).	139
5.15. Time evolution of the poloidal velocity for the $q_{0.5}$ and $q_{1.5}$ cases with only the $n = 0$ mode (top) and all toroidal modes (bottom).	139
5.16. Radial profile of ion collision frequency for each case.	140

5.17. Frequency-spectra of the radial electric field averaged in the range $0.75 < r/a < 0.85$ and taken at the beginning of the simulations (left) and in the turbulent phase (right) for the $q_{0.5}$ and $q_{1.5}$ cases. The vertical lines represent the theoretical GAMs frequency $\omega_{\text{GAM}}^{\text{theo}}$ . . . . .	143
5.18. Spatiotemporal evolution of the radial electric field (top) and the coarse-grained electric Reynolds stress divergence radial profile (bottom) for the $q_{0.5}$ case <b>(a)</b> and $q_{1.5}$ case <b>(b)</b> . . . . .	144
5.19. Sketch summarizing the 0D model for the energy exchanges between turbulence, zonal flows and GAMs. Note that the possible direct interplay between GAMs and zonal flows is not considered, which constitutes the main difference with the model of Miki & Diamond [137]. . . . .	145
5.20. GAMs damping rate obtained with the Gao theoretical prediction (lines) and obtained with several simulation codes (points). Extracted from [132].	148
5.21. Safety factor dependence of the normalized damping rates $\mathcal{I}_0$ (ZFs) and $\mathcal{I}_G$ (GAMs) and the normalized turbulent growth rate $\mathcal{I}_L$ in the collisionless case. The parameters of control are $A_0 = 0.1$ , $A_L = 1$ and $A_G = 1$ . . . . .	149
5.22. Zonal flows (left), GAMs (middle) and turbulent (right) energy in the situation described in Fig.5.21. . . . .	150
5.23. Safety factor dependence of the normalized damping rates $\mathcal{I}_0$ (ZFs) and $\mathcal{I}_G$ (GAMs) and the normalized turbulent growth rate $\mathcal{I}_L$ in the collisional case. The parameters of control are $A_0 = 0.1$ , $A_L = 1$ and $A_G = 1$ . . . . .	151
5.24. Zonal flows (left), GAMs (middle) and turbulent (right) energy in the situation described in Fig.5.23. . . . .	151
5.25. Radial profile of the diamagnetic stress tensor $\Pi^*$ and the electric Reynolds stress $\Pi_{r\theta}$ for each simulation at $t = 93600\omega_{c0}^{-1}$ . . . . .	153
5.26. Radial profile of $V_{\text{Peq}}^{\text{neo}}$ obtained with the "neoclassical" simulations (green), $-\frac{\nabla \cdot \Pi}{v_{\theta, \text{neo}}}$ obtained with the electric Reynolds stress from turbulent simulations and the heuristic neoclassical friction Eq(5.33) (blue) and the poloidal velocity from turbulent simulations (red) for the $q_{0.5}$ and $q_{1.5}$ cases. These profiles are also temporally averaged between $65000 < t[\omega_{c0}^{-1}] < 70000$ . . . . .	154
5.27. Radial profile of coarse-grained $-\nabla \cdot \Pi_r$ in range $100000 < t[\omega_c^{-1}] < 145000$ with a sliding radial average with a $50\rho_i$ window (a) for each simulation. Safety factor scan of $-\langle \nabla \cdot \Pi_r \rangle_{\text{CG}}$ taken in simulation in radial range $0.79 < r/a < 0.81$ ( $C$ is a constant) (b). . . . .	155
5.28. Sketch summarizing Chapter 5. . . . .	157
5.29. Amplitude of the fluctuations associated with frequencies in the range of GAMs in the #45333 discharge of Tore Supra as a function of the safety factor. . . . .	158

5.30. Safety factor dependence of the normalized damping rates $\mathcal{I}_0 = A_0 q$ (ZFs) and $\mathcal{I}_G = A_G q$ (GAMs) and the normalized growth rate $\mathcal{I}_L = A_L q^{1/3}$ in the collisional case. The parameters of control are $A_L = 1$ , $A_0 = 0.1$ and $A_G = 0.15$ . . . . .	159
5.31. Zonal flows (left), GAMs (middle) and turbulent (right) energy in the situation described in Fig.5.30. . . . .	159
32. Comparison between the Bessel function of the first kind (plain) and an approximation (dashed) for different order $n_B$ , for the argument range $N_c q [0, \pi]$ with $q = 3$ and $N_c = 18$ . . . . .	170
33. Radial profile of the r.h.s of the toroidal angular momentum conservation Eq..98. These quantities are temporally averaged between $100000 < t \omega_{c0} < 150000$ and radially slide-averaged with a $50\rho_i$ window. . . . .	175
34. Radial profile of the total toroidal Reynolds stress (dashed) and the electric drift component of the Reynolds stress (plain), both averaged in time between $100\ 000 < t < 150\ 000$ cyclotron periods, for different ripple amplitudes $\delta$ . . . . .	176
35. Form of $d\mathcal{P}/d\lambda$ . . . . .	179
36. (a) General form of $\mathcal{P}(\lambda)$ when all eigenvalues are reals. (b) General form of $\mathcal{P}(\lambda)$ when $\Delta' < 0$ or when $\Delta' > 0$ and two eigenvalues are complex. . . . .	180

# List of Tables

1.1. Angle, frequency and action for each of the three periodic motions of banana trapped particles in a tokamak. . . . .	39
2.1. Asymptotic values of $k_{VT}$ , $k_N$ and $k_{Vp}$ for different ranges of $\delta/\varepsilon$ , $\nu^*$ and $N_c q$ . . . . .	75
3.1. Simulation parameters. $L_N$ and $L_T$ are the density and temperature gradient's lengths, $\rho_i$ is the ion Larmor radius. . . . .	93
4.1. Simulation parameters. $L_N$ and $L_T$ are the density and temperature gradient length and $\rho_i$ the ion Larmor radius. . . . .	107
5.1. Parameters appearing in the system of equations. . . . .	145
5.2. Normalization parameters . . . . .	146

# 1. Introduction

## Table of contents

1.1. Fusion energy: context and purpose . . . . .	20
1.2. Nuclear reactions . . . . .	22
1.3. Hot and magnetized plasmas . . . . .	25
1.3.1. Lawson criterion . . . . .	26
1.3.2. Characteristic scales of a hot magnetized plasma . . . . .	28
1.4. Motion of charged particles in a magnetic field . . . . .	30
1.4.1. Cyclotron motion . . . . .	30
1.4.2. Newtonian, Lagrangian, and Hamiltonian formulations of the problem . . . . .	31
1.4.3. Integrable motion . . . . .	32
1.4.4. Confined particle trajectories . . . . .	33
1.4.5. Magnetic configuration of a tokamak . . . . .	35
1.4.6. Particle periodic motion and invariants in an axisymmetric tokamak	37
1.5. Why plasma flows matter . . . . .	39
1.5.1. Loss of symmetry and transport . . . . .	39
1.5.2. Flows and confinement . . . . .	40
1.5.3. Toroidal flow in presence of magnetic ripple and turbulence . .	42
1.5.4. Radial electric field dependency on the safety factor . . . . .	43
1.5.5. Thesis objectives and outline . . . . .	45

## 1.1. Fusion energy: context and purpose

The energy crisis is one of the most pressing challenges the world faces as of 2022, the year this thesis was written, and presumably for the upcoming century. Indeed, the energy demand is increasing rapidly as the supply of fossil fuels dwindles. In addition to the resulting sharp increase in the price of energy, its current production is one of the main sources of released greenhouse gases from human activity. The greenhouse effect is the process by which radiation from the Sun warms the planet's surface up to a temperature above what it would be without an atmosphere, due to greenhouse gases trapping the associated heat. Consequently, the Earth's atmosphere is warming at an unprecedented rate, causing several serious problems including rising sea levels, more extreme weather events, or the loss of biodiversity. Many reports (see for example the recent [IPCC reports](#) or french [RTE report](#)) provide evidence of this global warming and project multiple scenarios for the future. Most foresee

## 1. Introduction – 1.1. Fusion energy: context and purpose

catastrophic implications if no drastic changes are made to the way we produce and consume energy. Among numerous examples, let us look at the current projection regarding the global temperature which acts as a good proxy for the global warming intensity. Extracted from the latest GIEC report [1], Fig.1.1a shows the evolution in time of the observed global temperature variations between 1850 and 2020. A relatively constant behavior was reported until the fifties from which a sharp increase started. In addition, this figure shows the simulated temperature variation with and without human activity, showing clearly its responsibility for this increase. From the same report, Fig.1.1b shows the increase in frequency and intensity of the heat waves with a reference taken before 1900. An exceptional heat wave that occurred once every 50 years before the first industrial revolution now occurs more often and will occur even more often in the future, and with increasing intensity. In 2050, it indicates that heat waves would reach as high as 50°C in France. The recent deadly heat wave in Pakistan in Spring 2022 illustrates this global trend: an event of this scale was expected to occur once every 3000 years in the pre-industrial age, but is rendered 30 times more probable due to human activity. Following this figure, if the current trend on CO<sub>2</sub> emission does not change, it will be 8 times more probable in 2050 than it is today.

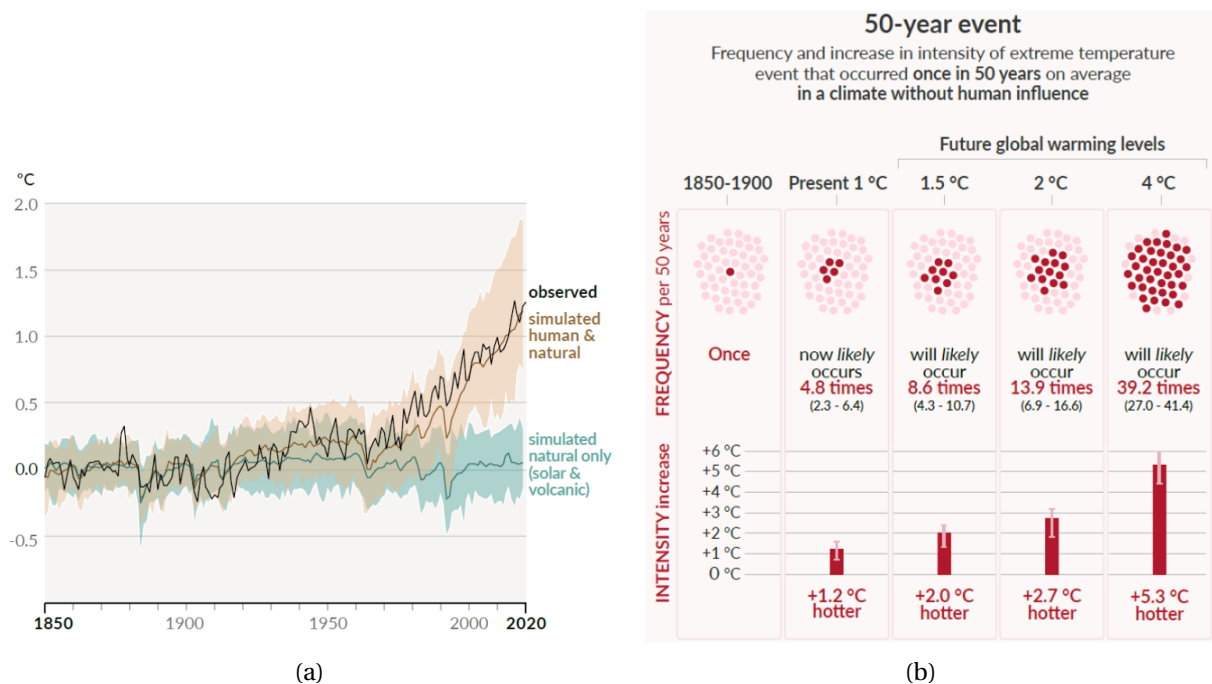


Figure 1.1. – Measured global temperature evolution (a) as well as the frequency and intensity of exceptional heat waves compared to the pre-industrial era (b). Extracted from the latest GIEC report [1].

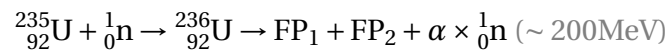
All of these elements make it clear that we need to find alternative long term sources of energy. Among the possible ones, nuclear energy presents a viable option to address both the energy crisis and global warming. Indeed nuclear power plants generate

large amounts of continuous energy without emitting greenhouse gases, making them a reliable and sustainable energy source.

This energy is harvested from nuclear reactions, described in the next section, that eject one or more particles with high kinetic energy. The most widely used method to convert kinetic energy of particles is through collisions with the nucleus of atoms that constitute a fluid. This causes the fluid to heat up as a result, which can then be used as the hot reservoir for a Carnot cycle and hence generate electricity.

## 1.2. Nuclear reactions

A nuclear reaction is the evolution of a nucleus that follows a triggering event. Two types of nuclear reactions release energy: fission and fusion. Nuclear fission is a process in which an atom splits into two or more lighter atoms generally as a result of neutron absorption. One can take the example of the fission of Uranium 235, which is the most common in current nuclear reactors. It reads



where FP stands for "Fission Product" which can be many different combinations of atoms lighter than  ${}_{92}^{235}\text{U}$  (the most probable ones are the Krypton 92 and Barium 141), and  $\alpha$  is average number of neutron emitted per fission (usually around 2-3). When the  ${}_{92}^{235}\text{U}$  absorbs a neutron, a new unstable nucleus of Uranium 236 is formed and quickly splits into other more stable nuclei. While the kinetic energy of the incident neutron can be as low as 0.025 eV, around 200 MeV are released in the process as kinetic energy carried mainly by the fission product. Furthermore, the ejected neutrons can trigger another fission reaction and entertain the reaction chain used in current reactors.

The other class of nuclear reaction that releases energy, and on which we will focus, is fusion. Nuclear fusion is a process in which two small atoms merge into a bigger one, as a result of nuclei collision. An example is the fusion of Deuterium  ${}^2_1\text{D}$  and Tritium  ${}^3_1\text{T}$  into a Helium  ${}^4_2\text{He}$  nucleus as well as an energetic neutron. It reads



Triggering a fusion reaction requires making two nuclei collide, although they are both positively charged and hence repel each other. Contrarily to fission, fusion is then only accessible by providing enough energy to the reactants such that the Coulomb barrier can be crossed. In practice, this input energy is obtained by heating the  ${}^2_1\text{D} / {}^3_1\text{T}$  mixture so that the thermal energy becomes comparable to the electrostatic potential energy<sup>1</sup>. In the remainder of the manuscript, the thermal energy  $E_{\text{th}}$  will be assimilated to the temperature  $T$  as they are related with the Boltzmann constant  $k_B$  through the relation  $E_{\text{th}} = k_B T_K (\text{Kelvin}) / e = T (\text{eV})$ , where  $e \simeq 1.6 \times 10^{-19} \text{C}$  is the absolute value of the electron charge.

---

1. Quantum tunnelling allows the fusion reaction to occur at thermal energy lower (but comparable) than the electric potential energy.

On Fig.1.2 the cross-section, representative of the interaction probability, of the fission of  $^{235}_{92}\text{U}$  and the fusion of different mixtures including  $^2_1\text{D} / ^3_1\text{T}$  as a function of the energy of the incident neutron for fission and of the thermal energy of reactants for fusion is displayed. It appears that, while fission probability is maximum with thermal neutrons at around  $\sim 0.01$  eV or lower, fusion is more likely to occur at thermal energy around  $\sim 10 - 100$  keV which converts to  $\sim 10^8 - 10^9$  °C. Heating and confining matter at these temperatures is a major challenge for fusion. It is discussed in more detail in the next section.

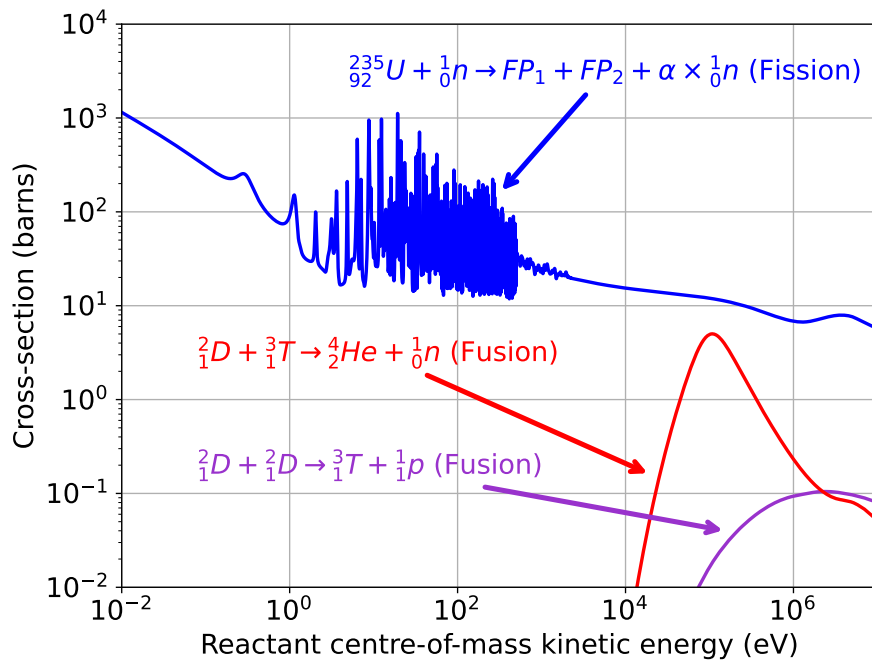


Figure 1.2. – Cross-section of  $^{235}_{92}\text{U}$  fission vs. the energy of the incident neutron (blue) and cross-section of fusion of two fusion reactions (red & purple) vs. the thermal energy of the reactants.

So where does this energy come from? Whether it's fission or fusion, the same underlying physics is at play. The nucleus of an atom is composed of nucleons that are held close by the strong interaction. It manifests in the binding potential energy between nucleons. Depending on the nucleus structure, which is determined by the number of neutrons/protons  $A$  that constitute it, the mean binding energy associated with each nucleon  $E/A$  is variable. A high mean binding energy relates to a tightly bound nucleus and consequently a more stable element. The binding energy per nucleon  $E/A$  of stable elements is shown in the Aston curve displayed Fig.1.3 (represented here with negative energy). It appears that  $E/A$  increases with  $A$  up to the iron  $^{56}_{26}\text{Fe}$ , which is the most stable nucleus, and then decreases for higher elements. This binding energy translates into the *deficit of mass*, which means that a bound nucleus is lighter than the sum of each nucleon that constitutes it. This is a consequence of the famous Einstein relation  $E = mc^2$  where  $m$  is the nucleus mass,  $c$  is the speed of light and  $E$



is the energy held by the matter. Following the Aston curve, it means that fusing elements lighter than  ${}^{56}_{26}\text{Fe}$  into a more stable nucleus also means the formation of a nucleus weighting less than the combined mass of the reactants. Analogously, the fission of elements heavier than  ${}^{56}_{26}\text{Fe}$  forms fission products that are more tightly bound, i.e. weighting less, than the original nucleus. This surplus of mass converts into energy, explaining the important kinetic energy carried by the products of the reaction.

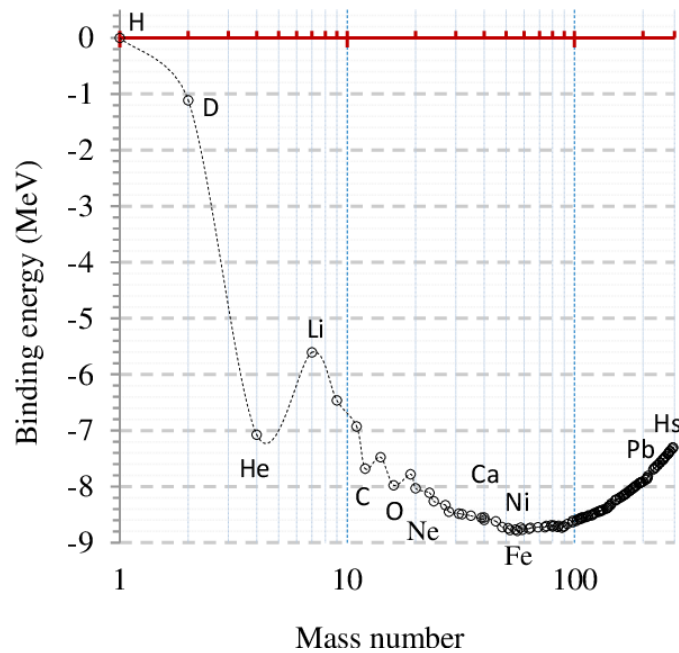


Figure 1.3. – Binding energy per nucleus as a function of the number of nucleons in the nucleus.

To grasp the magnitude of this released energy, one can compare it to the energy released by carbon  ${}^{12}_6\text{C}$  combustion used in charcoal power plant:

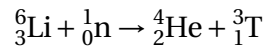


Compared to the fission of  ${}^{235}_{92}\text{U}$ , even when taking the atomic mass ratio 235/12 into account, the energy content per mass unit released in the fission reaction exceeds the carbon combustion by about a factor  $2.5 \times 10^6$ . For the fusion of  ${}^2_1\text{D}$  and  ${}^3_1\text{T}$ , this factor reaches about  $1 \times 10^7$ . It means that the oxidation of one ton of carbon releases the same energy as the fission of 0.4 gram of uranium 235 or the fusion of 0.1 gram of deuterium and tritium.

It partly explains why nuclear fission and fusion are attractive sources of energy. Of course, many constraints and challenges are linked with the harnessing of nuclear energy, and they are quite different in fission and fusion devices. Here no exhaustive list of the advantages and drawbacks of each technology will be made, but it is interesting to draw the current picture of nuclear energy implementation and the foreseen future.

## 1. Introduction – 1.3. Hot and magnetized plasmas

First, the current industrial nuclear reactors all make use of the fission of uranium or plutonium, although the reactor designs can be very different. They all share at least one issue: the shortening of the available fuel. Indeed, it is expected that the extraction and enrichment of  $^{235}_{92}\text{U}$  will cease to be profitable in about 100-200 years [2]. However, at least two technologies of reactors can alleviate this problem. The first one is the next generation of fission reactors that are designed to be *fast-breeder*, meaning that fuel will be produced (from a currently unusable uranium isotope) while the reactor is running. Also, some of these reactors plan to use alternatives to Uranium, like Thorium for which global supply is believed to be significant. The other technology is fusion reactors for which the planned fuel is a  $^2_1\text{D}/^3_1\text{T}$  mixture. Tritium is a radioactive element with a half-life of 12.3 years, such that it does not exist in nature. However, there are multiple ways to generate tritium. Currently, the main producer of tritium is Canada thanks to their CANDU-type nuclear reactors [3]. CANDU reactors make use of heavy water  $\text{D}_2\text{O}$  as the neutron moderator, such that neutron captures can lead to the formation of tritiated water  $\text{T}_2\text{O}$  while the reactor is running. Approximately 20 kg of tritium are produced each year globally, which is enough for the short future of planned prototypes and demonstrators. For the longer term though, it is expected that a single industrial fusion reactor would require about 100 to 200 kg of tritium per year. Much like fast-breeder reactors, it is planned to use the neutrons created in the fusion reactor and walls of Lithium 6,  $^6_3\text{Li}$ , and Lithium 7,  $^7_3\text{Li}$ , to trigger the reactions



and<sup>2</sup>



This way, it is expected that the resulting fuel would meet the current demand for energy for several thousand years.

While both of these nuclear technologies are very relevant to the energy crisis, the focus in this thesis concerns fusion reactors and more specifically magnetized confined plasmas in a tokamaks which are detailed in the next sections.

### 1.3. Hot and magnetized plasmas

As previously mentioned, the peak fusion cross sections for the most accessible fusion reaction is in the range of  $T \sim 10\text{keV}$ . The matter at this temperature comes with its share of interesting physics but also operational constraints. At such thermal energy, electrons and nuclei are partially or totally unbound, forming gas of charged particles. The matter in this state is called *plasma*.

---

2. This reaction was discovered inadvertently when the USA tested their most powerful nuclear H-bomb ever launched: Castle Bravo. The detonation explosive yield was about 2.5 times the predicted 6 megatonnes of TNT because of the tritium generated by the lithium present inside the bomb.

## 1. Introduction – 1.3. Hot and magnetized plasmas

Plasma is by far the most abundant state of matter in the universe that makes up more than 99.99% of its constituents. However, there are few manifestations of plasma under terrestrial conditions, where natural and observable plasmas sum up to flames, stars, and auroras. Accounting for plasmas observed or created using new technologies, the resulting diversity in plasma density and temperature covers a broad range of orders of magnitude, as shown in Fig.1.4.

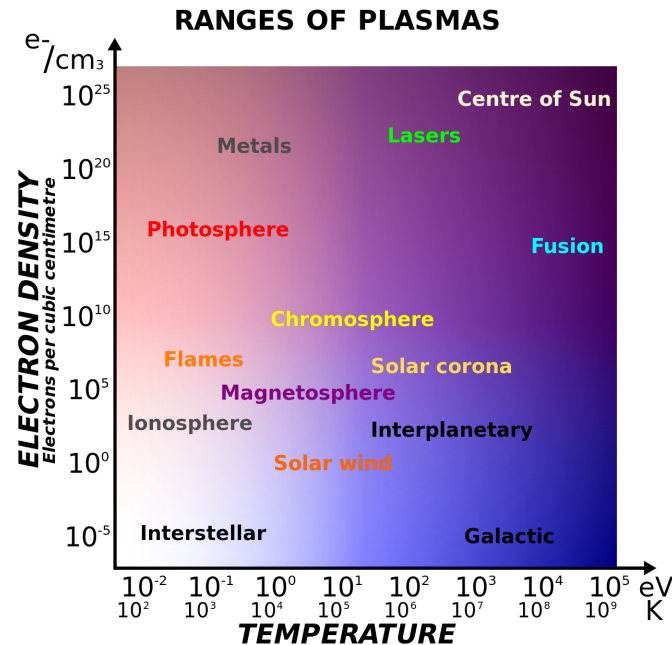


Figure 1.4. – Diversity of plasma in the universe. Source: Wikipedia

Compared with a neutral gas, plasma is sensitive to electromagnetic fields but also generates its own. The focus in this thesis is of course high temperature plasmas, commonly referred to as *hot plasmas*.

### 1.3.1. Lawson criterion

Despite the high energy needed to produce fusion reactions, it is relatively easy to achieve in a laboratory (examples are particle accelerators or in a more somber fashion, nuclear bombs). However, in a reactor, the production of energy by fusion needs to be superior to the energy lost to the environment. It is linked to a fundamental criterion for a reactor related to how much of the released energy is retrieved by the fuel, with the idea of self-sustainment of the reactions. In this context, a figure of merit characterizing fusion reactors, called *the Lawson criterion*, turns out to be quite handy to understand the current reactor designs. Three quantities appear in this 0D criterion:

- Not surprisingly, the plasma temperature  $T$ , which is a requirement for the fusion reactions to occur as already discussed in Sec.1.2;

## 1. Introduction – 1.3. Hot and magnetized plasmas

- The plasma density  $n$ , which can be understood as the measurement of the particles' proximity to each other. More particles in the same volume translates to a higher probability for two nuclei to collide and fusion reactions to occur.
- The energy confinement time  $\tau_E$ , which measures how fast the energy provided to the fuel escapes the device. Larger  $\tau_E$  corresponds to smaller required energy to reach the target temperature.

It turns out that maximizing the product of these quantities is beneficial for reaching reactor operational conditions. A common dimensionless parameter to characterize the power yield of a reactor is the energy gain factor  $Q$ . It is defined as the ratio between the power released by fusion reaction and the heating power provided to the plasma. The dream for fusion reactors is that  $\alpha$  particles transfer enough of their energy to the fuel such that no external heating is required. This self-sustainment limit is called the *ignition* and corresponds to  $Q \rightarrow \infty$ . Another interesting limit, referred to as the *break-even*, is  $Q = 1$ , i.e. when the fusion power compensates exactly the heating power. Back in 1957, J.D. Lawson proposed that break-even is reached past a threshold on the triple product  $nT\tau_E$  [4]. For the  ${}^2_1\text{D}/{}^3_1\text{T}$  fuel, it appears that the minimum of the  $n\tau_E$  product is reached at  $T \sim 26\text{keV}$ . From this point, two different ways of making a reactor emerge:

- By maximizing the density: this is done in practice by compressing and heating a target of fuel with energetic lasers. This method is called *inertial confinement fusion*. The most advanced projects are the National Ignition Facility (NIF) in the USA and the Laser Mégajoule in France [5].
- By maximizing the confinement time: this is done in practice by confining a hot plasma with magnetic fields. This is called *magnetic confinement fusion*. Numerous technologies based on magnetic confinement exist: tokamaks, stellarators, Z-pinch, Field Reversed Configuration, spheromaks, magnetic mirrors, Reverse Field Pinch ...

So how far are we from break-even?

Fig.1.5 shows the product  $n\tau_E$  as a function of the ion temperature for experiments done in both inertial and magnetized fusion devices. It appears that the only experiment that crossed this threshold has been performed at the NIF in 2021 [6]. However, NIF (as well as the Laser Megajoule) are not reactor-oriented projects. Next in line are tokamaks, which are coming closer and closer to the break-even. The record for a long reactor-oriented discharge has arguably been performed with the JET tokamak in 2021 [7], which released about  $60\text{MJ}$  of fusion power in about  $5\text{s}$ , yielding a gain factor of  $Q \sim 0.25$ . The first reactor prototypes (ITER, SPARC and STEP) are planned to function in the next decades and are expected to exceed break-even.



## 1. Introduction – 1.3. Hot and magnetized plasmas

which a particle turns over on a head-on collision. For two particles of charge  $e$ , it reads  $\lambda_L = \frac{e^2}{(4\pi\epsilon_0)T}$  where  $\epsilon_0$  is the vacuum permittivity.

- The **inter-particle distance** ( $\sim 10^{-7}$  m) is defined by  $\lambda_{i-p} = n^{-1/3}$  where  $n$  is the plasma density.
- The **Debye length**  $\lambda_D$  ( $\sim 10^{-4}$  m) is the distance above which the charge of a particle is screened by particles of opposite charges, as illustrated in Fig. 1.6. It is defined as  $\lambda_D = \sqrt{\frac{\epsilon_0 T}{e^2 n}}$ . At scales larger than  $\lambda_D$ , the plasma is considered *quasi-neutral* such that the relation  $en_e = Zen_i$ , with  $n_e/n_i$  the electron/ion density and  $Ze$  the ion charge, is valid.

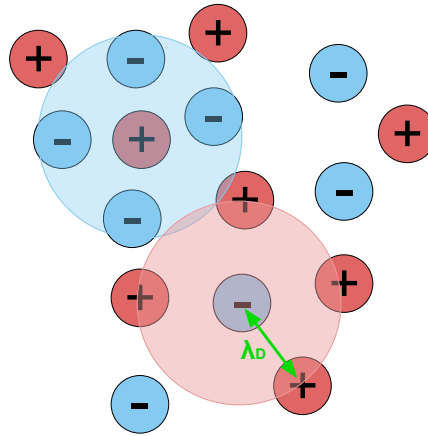


Figure 1.6. – Illustration of the charge screening effect in plasmas. A Debye sphere of radius  $\lambda_D$  defines the volume for which a charged particle is screened by particles of opposite charge.

- The **Larmor radius**  $\rho_c$  ( $\sim 10^{-3}$  m for ions,  $\sim 10^{-4}$  m for electrons) denote the radius of the circular trajectory of a charged particle in the plane orthogonal to the magnetic field direction, called the gyromotion (see Sec.1.4.1).
- The **thermodynamical gradient length** ( $\sim 1$  m), related to the spatial gradient of the equilibrium quantities, is comparable to the size of the reactor.

For temporal scales, from shorter to longer:

- The **inverse plasma frequency**  $\omega_p^{-1}$  ( $\sim 10^{-9}$  s), with  $\omega_p = \sqrt{\frac{ne^2}{\epsilon_0 m}}$ , is the characteristic time of plasma response to a charge displacement (without a magnetic field).
- The **cyclotron period** ( $\sim 10^{-7}$  s for ions,  $\sim 10^{-11}$  s for electrons) is associated with the gyromotion (see Sec.1.4.1).
- The **collision time** ( $\sim 10^{-3}$  s) is the mean time for the direction of the velocity vector of a particle trajectory to deviate of an angle of order  $\pi$  due to Coulomb collisions.

The next section is dedicated to explaining the charged particle trajectories immersed in a magnetic field in order to understand the magnetic configuration used in fusion devices.

## 1.4. Motion of charged particles in a magnetic field

To assess the complex problem of plasma confinement, one must be able to predict the motion of charged particle. A perfect situation for a reactor would be such that trajectories of all particles that constitute the plasma are restricted to a finite volume. Magnetic confinement devices are actually designed for this purpose. However, as is developed in the next sections, many instabilities make this goal extremely challenging. The aim of this section is to build a confined trajectory for a single charged particle in order to introduce essential key quantities and tools used throughout this document. First, the trajectory of a charged particle in a stationary and uniform magnetic field is derived to introduce the cyclotron motion. Then the tools to assess more complex problem with non-uniform and non-stationary electromagnetic fields are presented. Finally, a description of confined trajectories is given.

### 1.4.1. Cyclotron motion

In the Cartesian frame ( $\mathbf{e}_x, \mathbf{e}_y, \mathbf{e}_z$ ), the Newton equations of motion of a single particle of mass  $m$ , electric charge  $e$  and position coordinates  $(x, y, z)$ , immersed in a uniform and static magnetic field  $\mathbf{B} = B\mathbf{e}_z$  read

$$m \begin{pmatrix} \ddot{x} \\ \ddot{y} \\ \ddot{z} \end{pmatrix} = e \begin{pmatrix} \dot{y}B \\ -\dot{x}B \\ 0 \end{pmatrix} \quad (1.1)$$

meaning that the velocity in the direction parallel to the magnetic field is constant and that the magnetic field only modifies the motion in the plane normal to this direction. One can show<sup>3</sup> that the transverse motion is described by the following equations

$$x = (v_c/\Omega_c) \cos(\Omega_c t) \quad (1.2)$$

$$y = -(v_c/\Omega_c) \sin(\Omega_c t) \quad (1.3)$$

where one defines the *cyclotron frequency*  $\Omega_c = eB/m$  and the *cyclotron velocity*  $v_c$ . The transverse motion of the particle is circular: this is the *gyromotion*. The radius of this circle is called the *Larmor radius* and reads  $\rho_c = v_c/\Omega_c$ . The center of this circular motion is called the *guiding center*. It is often useful to decompose the particle motion as the guiding center of position  $\mathbf{X}$  and the gyromotion, as depicted in Fig.1.7.

---

3. It is straightforward by defining two new variables:  $\alpha = x - iy$  and  $\beta = x + iy$

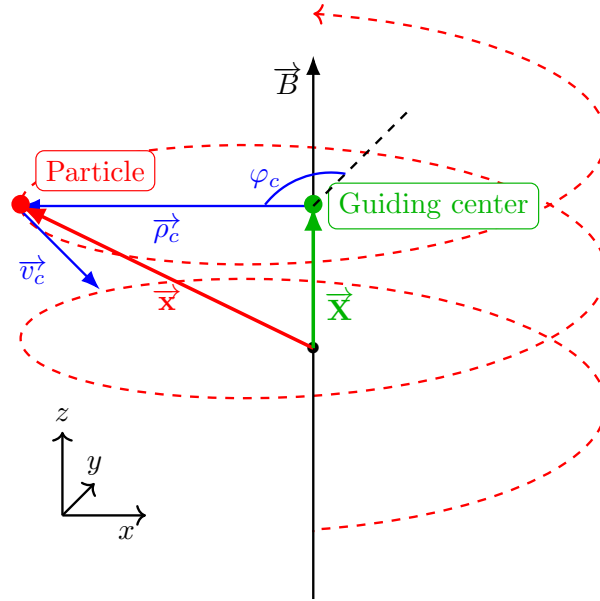


Figure 1.7. – Trajectory of a positively charged particle immersed in a uniform and stationary magnetic field.

### 1.4.2. Newtonian, Lagrangian, and Hamiltonian formulations of the problem

When accounting for a more general problem, i.e. a particle motion in an evolving and inhomogeneous electromagnetic field, the tractability of the associated derivation can become challenging (when at all possible). Multiple equivalent formulations of classical mechanics exist and one must choose the most appropriate to one particular problem. Here is a description of the formulations most commonly used in plasma physics:

- **Newtonian formulation:** this formulation makes use of the Newton equations of motion of a single particle of mass  $m$  and electric charge  $e$  immersed in an arbitrary electric field  $\mathbf{E}$  and magnetic field  $\mathbf{B}$  reads

$$m \frac{d\mathbf{v}}{dt} = e [\mathbf{E}(\mathbf{x}, t) + \mathbf{v} \times \mathbf{B}(\mathbf{x}, t)] \quad (1.4)$$

where  $\mathbf{x}$  is the particle position,  $t$  is the time and  $\mathbf{v} = \frac{d\mathbf{x}}{dt}$ . This formulation is intuitive but usually not the most practical for calculation.

- **Lagrangian formulation:** this formulation of the problem relies on the *least action principle* [9, 10] which leads to the definition of the particle *Lagrangian*  $\mathcal{L}$ . For a charged particle, this scalar quantity reads

$$\mathcal{L}(\mathbf{x}, \mathbf{v}, t) = \frac{1}{2} m v^2 - e[\phi(\mathbf{x}, t) - \mathbf{v} \cdot \mathbf{A}(\mathbf{x}, t)] \quad (1.5)$$



## 1. Introduction – 1.4. Motion of charged particles in a magnetic field

where  $\phi$  is the electric potential and  $\mathbf{A}$  is the magnetic vector potential. The particle Lagrangian is then the kinetic energy subtracted from the potential energy of the particle<sup>4</sup>.

With this description, the equations of motion read

$$\frac{dp_i(\mathbf{x}, \mathbf{v}, t)}{dt} - \frac{\partial \mathcal{L}}{\partial x_i} = 0 \quad (1.6)$$

where  $x_i$  is one coordinate of  $\mathbf{x}$  and  $p_i = \frac{\partial \mathcal{L}}{\partial \dot{x}_i}$  is the associated canonical momentum. With Eq(1.6), it is easy to notice that if  $\mathcal{L}$  does not depend on the coordinates  $x_i$ , the associated canonical momentum  $p_i$  are invariants of motion. This notion of invariance is essential in dynamical systems as it allows the formulation of conservation laws. Calculating the canonical momentum vector from Eq(1.5) gives  $\mathbf{p} = m\mathbf{v} + e\mathbf{A}(\mathbf{x}, t)$ . As compared to more common systems, the kinetic part of  $\mathbf{p}$  in magnetized plasmas is negligible compared to the electromagnetic part such that  $|\frac{e\mathbf{A}}{mv}| \gg 1$ .

- **Hamiltonian formulation:** this formulation makes use of another scalar field of interest that can describe dynamical systems: the Hamiltonian  $\mathcal{H}$ . For a charged particle immersed in an electromagnetic field, it reads

$$\mathcal{H}(\mathbf{x}, \mathbf{p}, t) = \frac{[\mathbf{p} - e\mathbf{A}(\mathbf{x}, t)]^2}{2m} + e\phi(\mathbf{x}, t) . \quad (1.7)$$

Note that the Hamiltonian depends on the momentum and not on the velocity as for the Lagrangian. The equations of motion then read

$$\frac{dx_i}{dt} = \frac{\partial \mathcal{H}}{\partial p_i} \quad (1.8)$$

$$\frac{dp_i}{dt} = -\frac{\partial \mathcal{H}}{\partial x_i} \quad (1.9)$$

and  $\mathbf{p}$  is said to be conjugate to  $\mathbf{x}$ . The Hamiltonian is convenient inter-alia for changing the considered set of coordinates while conserving the structure of Eq(1.8) and Eq(1.9).

In the following, both Lagrangian and Hamiltonian formulations are used. In particular, the Hamiltonian formulation can be used in a practical set of coordinates. This is the aim of the next section.

### 1.4.3. Integrable motion

Regardless of the adopted formulation, the complex nature of charged particle trajectories in an inhomogeneous and evolving electromagnetic field is analytically intractable in the general case. For the equations of motion to be integrable, three

---

4. There is actually an infinite number of Lagrangian for a given system, here is shown the conventional one.

## 1. Introduction – 1.4. Motion of charged particles in a magnetic field

invariants of motion are needed [11]. Furthermore, the constraint of confining particles further adds to the problem. Indeed, to have spatially bounded trajectories, the *hairy ball theorem* states that these trajectories should be inscribed in a torus<sup>5</sup>. In other words, the torus is the only shape that contains a singularity-free vector field, which is essential when the major confining element is the magnetic field which must respect the divergence-free condition. With this condition met, a convenient change of coordinates in the Hamiltonian formalism from the set  $(\mathbf{x}, \mathbf{p})$  to the *angle/action variables*  $(\boldsymbol{\alpha}, \mathbf{J})$  is possible. Equations of motion then read

$$\frac{d\alpha_i}{dt} = \frac{\partial \mathcal{H}}{\partial J_i} = \Omega_i \quad (1.10)$$

$$\frac{dJ_i}{dt} = -\frac{\partial \mathcal{H}}{\partial \alpha_i} = 0 \quad (1.11)$$

where  $\Omega_i$  are the Hamiltonian angular eigenfrequencies. With  $(\alpha_{i0}, J_{i0})$  the initial conditions, the trajectory then take the simple form

$$\alpha_i = \Omega_i t + \alpha_{i0} \quad (1.12)$$

$$J_i = J_{i0} . \quad (1.13)$$

A magnetic field then confines charged particles if three periodic directions characterize their motion. This also ensures the existence of *magnetic surfaces*, which are defined as finite surfaces of normal vector  $\mathbf{n}$  such that  $\mathbf{B} \cdot \mathbf{n} = 0$ . These surfaces are simply nested tori. Of course, the same difficulty remains regarding system integrability: one must find 3 invariants of motion.

### 1.4.4. Confined particle trajectories

Fortunately, plasmas in tokamaks are characterized by a strong confining magnetic field, in the sense that the Larmor radius is small compared to the magnetic field gradient length, i.e.  $|\nabla \ln B|^{-1} \gg \rho_c$ . This field also evolves slowly in time compared to the cyclotron period, such that  $|\partial_t \ln B| \ll \Omega_c$ . This ordering is referred as the *adiabatic theory*, and allows a perturbative treatment of Eq(1.4). Within this ordering, it is possible to show [12, 13] that an *adiabatic invariant*  $\mu$  exists. This invariant is nothing else than the particle magnetic moment

$$\mu = \frac{mv_c^2}{2B(\mathbf{X})} \quad (1.14)$$

which is proportional to the magnetization of a small magnet induced by the current

---

5. In a sphere, for example, there is no way to have a continuous vector field without any singularity. Taking the wind vector field on Earth, for instance, it means that there is at least one location where there is no wind at all.

1. Introduction – 1.4. Motion of charged particles in a magnetic field

which is generated by the gyromotion of the charged particle.

Under these hypotheses, it was demonstrated by Littlejohn [14] that a Lagrangian in the set of variables  $(\mathbf{X}, v_{\parallel}, \mu, \varphi_c)$ , where  $v_{\parallel}$  is the component of the particle velocity parallel to the magnetic field lines and the other coordinates are defined in Fig.1.7, is

$$\mathcal{L}(\mathbf{X}, v_{\parallel}, \mu, \varphi_c, t) = e\mathbf{A}^* \cdot \dot{\mathbf{X}} + \frac{m\mu}{e}\dot{\varphi}_c - \mathcal{H} \quad (1.15)$$

where the Hamiltonian is

$$\mathcal{H} = \frac{mv_{\parallel}^2}{2} + \mu B + e\phi \quad (1.16)$$

and

$$e\mathbf{A}^* = e\mathbf{A} + mv_{\parallel}\mathbf{b} \quad (1.17)$$

which can be seen as the canonical moment of a guiding center that follows magnetic field lines, with  $\mathbf{b} = \mathbf{B}/B$  the unit vector along the direction parallel to the magnetic field line.

Using the Euler-Lagrange equation Eq(1.6), the motion equations then read

$$\dot{\varphi}_c = \frac{eB}{m} = \Omega_c \quad (1.18)$$

$$\dot{\mu} = 0 \quad (1.19)$$

$$v_{\parallel} = \mathbf{b} \cdot \dot{\mathbf{X}} \quad (1.20)$$

$$B_{\parallel}^* \dot{\mathbf{X}} = v_{\parallel} \mathbf{B}^* + \frac{\mathbf{b}}{e} \times \nabla (\mu B + e\phi) \quad (1.21)$$

$$B_{\parallel}^* m \dot{v}_{\parallel} = -\mathbf{B}^* \cdot \nabla (\mu B + e\phi) \quad (1.22)$$

where

$$\mathbf{B}^* = \nabla \times \mathbf{A} + \frac{mv_{\parallel}}{e} \nabla \times \mathbf{b} \quad (1.23)$$

$$B_{\parallel}^* = \mathbf{b} \cdot \mathbf{B}^* . \quad (1.24)$$

The detailed derivation of these equations can be found in Appendix A.

Using the identity  $\nabla \times \mathbf{b} = (\mathbf{b} \cdot \nabla \times \mathbf{b})\mathbf{b} + \mathbf{b} \times \boldsymbol{\kappa}$  with  $\boldsymbol{\kappa} = (\mathbf{b} \cdot \nabla)\mathbf{b}$ , it is straightforward to show

$$\frac{\mathbf{B}^*}{B_{\parallel}^*} = \mathbf{b} + \frac{mv_{\parallel}}{eB_{\parallel}^*} \mathbf{b} \times \boldsymbol{\kappa} \quad (1.25)$$

such that the guiding center velocity can be recast in its most common expression

$$\dot{\mathbf{X}} = v_{\parallel}\mathbf{b} + \mathbf{v}_D + \mathbf{v}_E \quad (1.26)$$

where

$$\mathbf{v}_D = \frac{1}{eB_{\parallel}^*} \mathbf{b} \times (\mu \nabla B + mv_{\parallel}^2 \boldsymbol{\kappa}) \quad (1.27)$$

## 1. Introduction – 1.4. Motion of charged particles in a magnetic field

is the *magnetic drift velocity*, which depends on the particle charge, mass and magnetic moment, as well as

$$\mathbf{v}_E = \frac{\mathbf{B} \times \nabla \phi}{B_{\parallel}^* B} \quad (1.28)$$

is the *electric drift velocity*, which only depends on the electric and magnetic fields, and the parallel velocity of the particle through  $B_{\parallel}^*$ <sup>6</sup>.

These drifts are of fundamental importance and are basically the cause of departure from a perfect confinement of particles. Indeed, Eq(1.26) shows that the magnetic field and the electric field  $\mathbf{E} = -\nabla \phi$  inhomogeneities prevent the particle to strictly follow the magnetic field lines. A similar effect appears in the momentum evolution Eq(1.22). Indeed, neglecting the curvature  $\kappa$ , a parallel electric force  $f_{\parallel,E} = e\mathbf{b} \cdot \mathbf{E}$  and the *magnetic mirror force*  $f_{\parallel,D} = -\mu(\mathbf{b} \cdot \nabla)B$  modify the constant velocity of particle along the parallel direction. The mirror force describes the force exerted by the magnetic field gradient on small magnets of magnetic moment  $\mu$ . It can increase, decrease or even reverse the velocity of particles. In this last case, it means that a magnetic well along the parallel direction can trap particles that would reverse their velocity periodically. It has a significant impact on the plasma confinement properties, as is detailed further. With all this knowledge, the tokamak and its magnetic configuration can be introduced. We will see that one can recover three invariants of motion.

### 1.4.5. Magnetic configuration of a tokamak

To generate closed field lines winded around a torus, the technological solution chosen for tokamaks and stellarators is to use magnetic coils. It can be pictured this way: first starting from a linear solenoid composed of coils, one could join each end to form a loop. This would form a purely toroidal magnetic field. However there is a catch: looping back the solenoid unavoidably strengthens the magnetic field amplitude close to the center (where coils are closer) and weakens the one at the outer radius (where the coils are sparser). The resulting magnetic gradient causes a vertical magnetic drift  $\mathbf{v}_D$  which points in opposite directions for ions and electrons. The associated charge separation is responsible for a vertical electric field, retaining the charged particle from drifting vertically. This electric field in turn drives an electric drift  $\mathbf{v}_E$ , independent of particle characteristics, directed outward. A purely toroidal magnetic field would thus naturally drive particles out of the device. The solution adopted in tokamaks and stellarators to counteract this effect is to add a poloidal component to the magnetic field. Consequently, the upward and downward regions of the devices are connected by the helicity of the magnetic field lines. The charge separation is then perfectly compensated by the rapid motion of particles along the parallel direction. In stellarators, the helical magnetic field lines are directly induced by the

---

6. The approximation  $\mathbf{v}_E = \frac{\mathbf{B} \times \nabla \phi}{B^2}$  will be made in this manuscript, as in most cases the approximation  $B_{\parallel}^* \approx B$  holds.

1. Introduction – 1.4. Motion of charged particles in a magnetic field

magnetic coils that have a complex geometry. In tokamaks, the magnetic field results from the sum of a purely toroidal field, generated by coils that are aligned vertically and spatially distributed along the torus, and a weaker poloidal field generated by inducing a current  $I_P$  in the plasma along the parallel direction, which in turn induces the poloidal component of the magnetic field. The tokamak geometry and magnetic configuration are summed up in Fig.1.8. In this same figure is also introduced the toroidal set of coordinates  $(r, \theta, \varphi)$  in the specific case of a circular geometry. From now on, this simplified case is the one that will be considered throughout this manuscript.

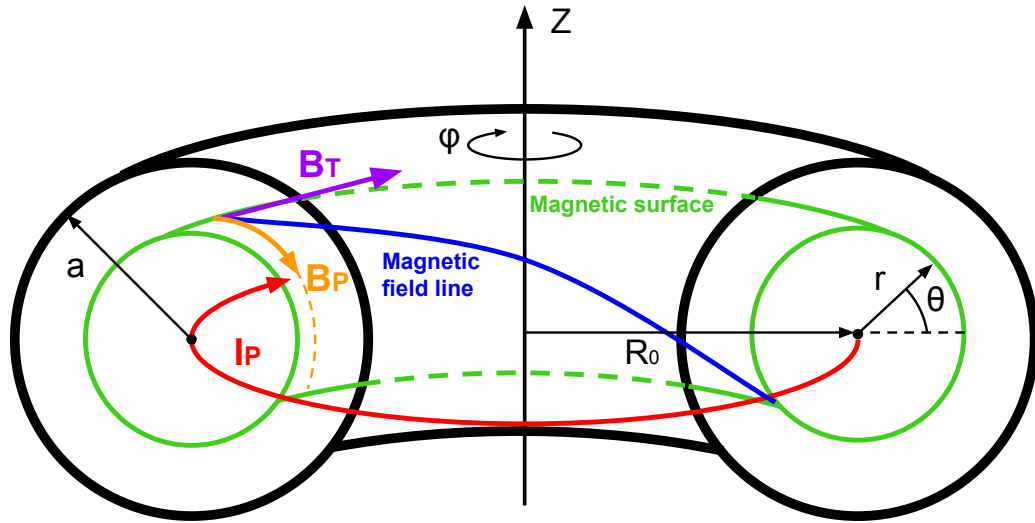


Figure 1.8. – Magnetic configuration of a tokamak.

The magnitude of the poloidal component is smaller than the toroidal one, and is often referred to through another quantity that appears naturally in most calculations: the *safety factor*  $q$ . It is defined as the number of toroidal revolutions of field lines for one poloidal revolution. It reads

$$q(\psi) = \frac{\mathbf{B} \cdot \nabla \varphi}{\mathbf{B} \cdot \nabla \theta^*} \quad (1.29)$$

where  $\theta^*$ , referred to as the intrinsic poloidal angle, is defined such that  $q$  only depends on  $\psi$  which is the poloidal magnetic flux normalized to  $(-2\pi)$  such that it is expressed

$$\psi = -\frac{1}{2\pi} \int_{\varphi=0}^{2\pi} \int_0^r \mathbf{B} \cdot \nabla \theta \frac{dr' d\varphi'}{|(\nabla \varphi \times \nabla r) \cdot \nabla \theta|}.$$

It should be stressed that the intrinsic poloidal angle  $\theta$  is not the geometric poloidal angle  $\theta^*$ . However, in the large aspect ratio limit that we will consider throughout this thesis, the difference between these two angles is small.

In tokamaks, the axisymmetry approximation is often made. It means that the equilibrium electric and magnetic fields are left invariant when rotating around the torus revolution axis. The fields are then independent of the toroidal angle  $\varphi$ . This

## 1. Introduction – 1.4. Motion of charged particles in a magnetic field

thesis will focus extensively on the disparity from this axisymmetric assumption. But first, it is important to define this reference situation where invariants can be constructed.

The axisymmetric magnetic field  $\mathbf{B}$  can be written

$$\mathbf{B} = I(\psi) \nabla \varphi + \nabla \varphi \times \nabla \psi \quad (1.30)$$

where  $I = \mu_0 I_P(\psi)/2\pi$  ( $\mu_0$  is the vacuum permeability).

### 1.4.6. Particle periodic motion and invariants in an axisymmetric tokamak

Fig.1.9 is helpful for understanding the following and also acts as a summary for this section. The usual angle/action coordinates in tokamaks are meant to describe particle motion in the axisymmetric case. In this limit, it is useful to make the difference between two classes of particle trajectories that can occur in such a configuration. To understand why there are two distinct classes of trajectories, one can look at the parallel velocity  $v_{\parallel}$  expression when the particle Hamiltonian  $\mathcal{H}$ , i.e. the particle energy, is conserved:

$$v_{\parallel} = \pm v \sqrt{1 - \lambda b} \quad (1.31)$$

where  $v$  is the particle velocity modulus,  $\lambda = \frac{\mu B_0}{\mathcal{H} - e\phi}$  is called the trapping parameter, with  $B_0$  the magnetic field amplitude taking at the magnetic axis, and  $b = B/B_0$ . As particles lie in the magnetic surface vicinity, the helicity of the magnetic field lines imposes on particles to explore a varying magnetic field amplitude along their transit. This is due to the fact that the magnetic field amplitude decays from the torus axis to the outward region. This magnetic field inhomogeneity due to the curvature is called the  $1/R$  magnetic decay. Then two situations emerge. If the maximum normalized magnetic field amplitude  $b_{\max}$  encountered by the particle is such that  $\lambda b_{\max} < 1$  then the sign of  $v_{\parallel}$  does not change during the particle transit. In other words, these particles have a sufficiently high parallel energy - compared to the perpendicular one - to cross any modulation of the magnetic field amplitude along the trajectory. These particles are referred to as *passing particles* and, in a first approximation, follow magnetic field lines. In the other case, i.e. when  $\lambda b_{\max}$  reaches unity, the particle encounters a magnetic field amplitude barrier during its trajectory, such that the parallel velocity vanishes, then reverses. These particles are referred to as *trapped particles*. These distinct periodic trajectories are shown in Fig.1.9. The action/angle sets of coordinates can now be introduced.

The first periodic motion, shared by both of these populations, is the gyromotion. The associated angle/action are the gyroangle  $\varphi_c$  and  $J_1 = \frac{m}{e} \mu$ . The frequency  $d\varphi_c/dt = \Omega_c$  is the cyclotron frequency. The two other periodic motions are however different for passing and trapped particles.

1. Introduction – 1.4. Motion of charged particles in a magnetic field

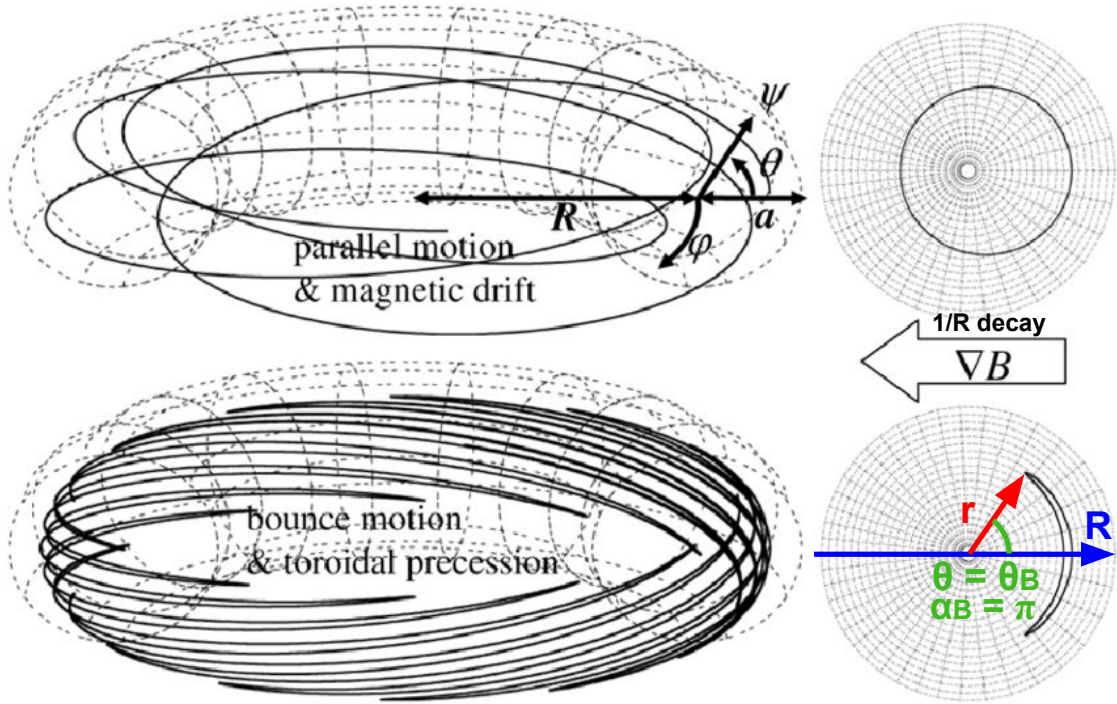


Figure 1.9. – Typical trajectories of passing (top) and banana-trapped (bottom) particle. On the right is the projection of these trajectories on the poloidal plane. Extracted from [15].

As mentioned previously, passing particles roughly follow the magnetic field lines. Their trajectory projected on the poloidal and toroidal plane then describe two periodic motions. The associated invariants are not detailed here as the focus is on trapped particles.

For trapped particles, the motion is more complex. In the poloidal plane, the projected trajectories have a banana shape. This movement is also periodic. The associated angle  $\alpha_B$  is defined such that the poloidal angle of the particle reads  $\theta = \theta_B \sin \alpha_B$  for the deeply trapped particles. This can be understood by looking at Fig.1.9. The angle  $\alpha_B$  then varies between  $-\pi$  and  $\pi$  whatever the span between  $-\theta_B$  and  $\theta_B$ . The frequency  $d\alpha_B/dt = \Omega_B$  is called the bounce frequency. The associated action is called the *longitudinal invariant* and reads  $J_2 = \mathcal{J}_\parallel = \oint \frac{dl}{2\pi} m v_\parallel$  where the integral is taken over the distance between two consecutive bounce points. In the toroidal plane, subtleties appear. The banana trapping is also present but superimposed to another slow regular motion called the *precession drift*. As the banana periodic motion is already described by the  $(\alpha_B/\mathcal{J}_\parallel)$  angle/action coordinates, there is no need to account for it again. The last periodic motion is then the precession motion. The associated angle is referred as  $\varphi_0$ . The frequency  $d\varphi_0/dt = \Omega_D$  is the precession frequency. The associated action is the canonical toroidal momentum  $J_3 = P_\varphi = -e\psi$ .

The angle, action and frequency of each periodic motion for banana trapped particles are summarized in Tab.1.1.

## 1. Introduction – 1.5. Why plasma flows matter

Motion	Angle	Frequency (+ rough expression in circular geometry)	Action
Gyromotion	$\varphi_c$	$\Omega_c = eB/m$	$J_1 = \frac{m}{e}\mu$
Banana	$\alpha_B = \arcsin(\theta/\theta_B)$	$\Omega_B \approx \sqrt{\varepsilon} \frac{v_\perp}{qR_0}$	$J_2 = \mathcal{J}_\parallel = \oint \frac{dl}{2\pi} m v_\parallel$
Precession	$\varphi_0 = \varphi - q\Omega_B t$	$\Omega_D \approx \frac{q\Omega_c \rho_i^2}{rR_0}$	$J_3 = P_\varphi = -e\psi$

Table 1.1. – Angle, frequency and action for each of the three periodic motions of banana trapped particles in a tokamak.

Outcome one

Outcome two

## 1.5. Why plasma flows matter

### 1.5.1. Loss of symmetry and transport

As detailed in the previous sections, confinement is ensured as long as three periodic motions exist. So why ignition hasn't been reached in any tokamak? The answer is clear: there are mechanisms at play causing breaking of symmetry and resulting in the loss of one or more invariant of motion. This loss of invariance usually leads to the onset of chaos, inevitably leading to transport. This will be detailed in the next Chapter. In short, three mechanisms can be linked to transport.

First, there is the effect of fluctuating perturbations. For instance, the kinetic energy is no longer an invariant of motion when the fields are time dependent. Multiple instabilities in magnetized plasmas can drive the electromagnetic fields. Especially, a family of these instabilities leads the plasma in a turbulent state in which electromagnetic fluctuations take place in a wide range of spatiotemporal scales. Turbulence is a chaotic process, i.e. a manifestation of the loss of symmetry, which appears in all tokamak experiments. It is usually the main cause of confinement degradation.

Secondly, breaking of symmetry can also come from static perturbations. Indeed, the three invariants of motion previously presented are valid in the axisymmetric limit. However, the true magnetic field in a tokamak is not axisymmetric because of error fields, external magnetic perturbations, or the toroidal modulation due to a finite number of coils referred to as *magnetic ripple*. The focus in this work is on the latter. When magnetic ripple is accounted for, the magnetic field has to be corrugated in the toroidal direction: its amplitude is weaker between two consecutive coils and stronger near the coils. This static perturbation is responsible for the loss of invariance of the canonical toroidal momentum  $P_\varphi$ .

Finally, the last transport channel is the effect of collisions. Collisions cause diffusion in the velocity space while conserving energy. Consequently, particles jump from one magnetic surface to another which translates into a net radial diffusion. This effect is enhanced by the presence of mirror trapping, constituting the *neoclassical transport*. This is discussed in details in Sec.2.4. Neoclassical physics is also a chaotic process,



but its interpretation is a bit different. During a collision, the particle energy and momentum are not conserved, resulting in a diffusive transport. However, between two successive collisions, the invariants are conserved and the particle motion is integrable.

Transport is unavoidable in fusion devices: there will always be mechanisms causing a disparity from an integrable system, i.e. a perfect confinement. However, perfect confinement is not needed to operate a fusion reactor. The goal is merely to reduce the transport in order to increase the confinement time sufficiently to reach ignition. This requires to understand transport, a tremendous task. Indeed, numerous transport channels exist and their very existence often causes the loss of integrability of the system. On the theoretical side, this imposes to either build reduced models, that can only include some physical ingredients, or to rely on simulation codes that currently can only scan a limited range of parameters. This is in fact exactly the approach taken in this thesis.

### 1.5.2. Flows and confinement

This thesis focuses on studying flows in tokamak plasmas. Study of "flows" should be understood as the study of the species average velocity  $\mathbf{V}$  and the flux  $\mathbf{\Gamma} = n\mathbf{V}$ . The velocity evolution for one species reads

$$mn \frac{d\mathbf{V}}{dt} = ne [\mathbf{E} + \mathbf{V} \times \mathbf{B}] - \nabla P + nm\nu \nabla^2 \mathbf{V} \quad (1.32)$$

with  $P$  the pressure,  $n$  the density,  $m$  and  $e$  the species mass and charge respectively and  $\nu$  the viscosity. The radial component of the velocity is small compared with poloidal and toroidal ones. Indeed, the associated radial flux is  $\Gamma_r = nV_r \approx -D\partial_r n$  with  $D$  a diffusion coefficient usually measured around  $\sim 10 \text{ m}^2.\text{s}^{-1}$  such that  $V_r \sim 10 \text{ m}.\text{s}^{-1}$ . In comparison, the measured poloidal and toroidal velocity lies around  $V_\theta, V_\varphi \sim 1 \text{ km}.\text{s}^{-1}$ . Capturing the mechanisms at play for transport, which is described by the radial flux  $= nV_r$ , and their respective weight is complex. Projecting Eq(1.32) on the radial direction yields the *force balance* which in a circular geometry reads

$$nm \frac{dV_r}{dt} = -\frac{dP}{dr} + neB_T \left( \frac{E_r}{B_T} + V_P - V_T \frac{\varepsilon}{q} \right) \quad (1.33)$$

with  $B_T$  the toroidal component of the magnetic field,  $V_P$  and  $V_T$  the poloidal and toroidal rotation velocities,  $\varepsilon = r/R$  with  $R = R_0 + r \cos(\theta)$  and  $R_0$  the major radius, and  $E_r$  the radial electric field. At fixed thermodynamical gradients, the transport is then ruled by the plasma velocity in the toroidal and poloidal direction as well as by the radial electric field. Predicting these quantities is the main objective of this thesis. Studying the transport with these quantities is handy to isolate some mechanisms as it will be developed in the manuscript. Furthermore, these quantities are also easier to obtain experimentally.

Another key aspect of confinement are *transport barriers*. They are regions exhibiting a strong shear of velocity, such that turbulent structures trying to cross this region

are cut into smaller structures. The consequence is a substantial reduction in turbulent transport. Transport barriers are regions of generally steep gradients of density and/or temperature. One of the most common transport barriers spontaneously appears at the edge in all tokamaks above a threshold in power transferred to the plasma. Once this barrier is set up, the plasma is said to be in an enhanced confinement mode. This is the case of the *High confinement mode* (H-mode) that was discovered in 1982 on ASDEX by F. Wagner. The transition to H-mode, 40 years later, is still not fully understood even though several tokamaks operate in this confinement mode daily. The role of flows is however expected to be important, as they are related to the radial electric field that drives the shear of the  $E \times B$  velocity that maintains the barrier. As an example, the radial profiles of the radial electric field and plasma pressure for a plasma in *Low confinement mode* (L-mode) and H-mode in the ASDEX-Upgrade tokamak are displayed in Fig. 1.10. This experimental result shows that a well of the radial electric field  $E_r$  forms at the plasma edge for the plasma in H-mode. In addition, this kind of discharge exhibits typical plasma pressure  $\sim 2$  times higher than the one in L-mode, with a steep gradient at the edge that correlates with the  $E_r$  well. This region of important gradients is often referred to as the *pedestal*. The price to pay for such a confining feature is the presence of Edge Localized Modes (ELMs), which are bursty relaxations of this steep pressure gradient that release an important heat quantity to the wall.

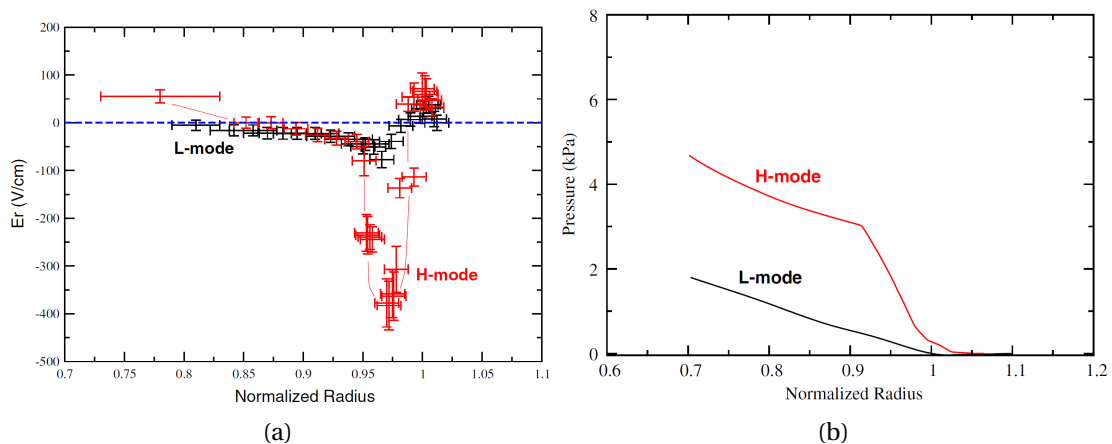


Figure 1.10. – Radial profile of the radial electric field (a) and plasma pressure (b) in ASDEX-Upgrade discharges in L-mode (black) and in H-mode (red). Extracted from [16].

Another type of self-generated flow is of particular interest in the fusion community: *zonal flows* (ZFs). ZFs are meso-scale flows in the direction perpendicular to the magnetic field lines that spontaneously appear in turbulent plasmas. They have been observed in experiment [17], and also in turbulent simulations [18, 19] in which they have been identified to greatly reduce the turbulent transport. A comprehensive review of ZFs is [20].

Flows are also involved in magnetic stability, which can be altered with magneto-hydrodynamic (MHD) instabilities. These instabilities, often driven by the plasma current, can lead to violent events that can damage the reactor if not controlled properly. In ITER, it is expected that a single *disruption*, i.e. a particular type of MHD instability, in the thermonuclear phase would mark the end of the machine. In this context, flows can act as a mean of control. For instance, it was shown [21] that the toroidal rotation can stabilize certain MHD modes.

### 1.5.3. Toroidal flow in presence of magnetic ripple and turbulence

In this thesis, first, the toroidal velocity dependency on the effect of 3D magnetic perturbations like magnetic ripple is studied. Particular attention is paid to the toroidal rotation in absence of any external momentum input, also referred to as *intrinsic rotation*. One of the reasons is that, for reactor-sized tokamaks like ITER, the control of the rotation will be very challenging, if at all possible [22]. The magnetic ripple is expected to play a role because, as explained in detail in Chapter 2, neoclassical effects in a 3D magnetic configuration strongly impact the toroidal velocity in a realistic, i.e. non-axisymmetric, magnetic configuration. Several experimental results [23–27] demonstrate that magnetic ripple impacts the plasma rotation from the edge up to the core. Examples from the JET and Tore Supra tokamaks are shown in Fig.1.11. Indeed, Fig.1.11a shows that the plasma rotation of the core and edge plasma in JET decreases with the ripple amplitude and Fig.1.11b shows the radial profile of the toroidal velocity that decreases when the ripple amplitude increases in Tore Supra. This neoclassical drive is competing with another drive source: turbulence. Indeed, turbulence can also drive plasma rotation due to complex wave-particle interactions. It is also shown in the previous figure, as even when the ripple amplitude is low, the plasma carries a finite toroidal velocity. An experimental study on Tore Supra [28] assessing this turbulent drive has also been carried out. Generally, the toroidal velocity is positive, meaning that the plasma rotates in the same direction as the plasma current (this is often called the "co-current direction"). However, when the ripple amplitude increases, the plasma velocity decreases and can change sign to spin in the other direction (often called the "counter-current direction").

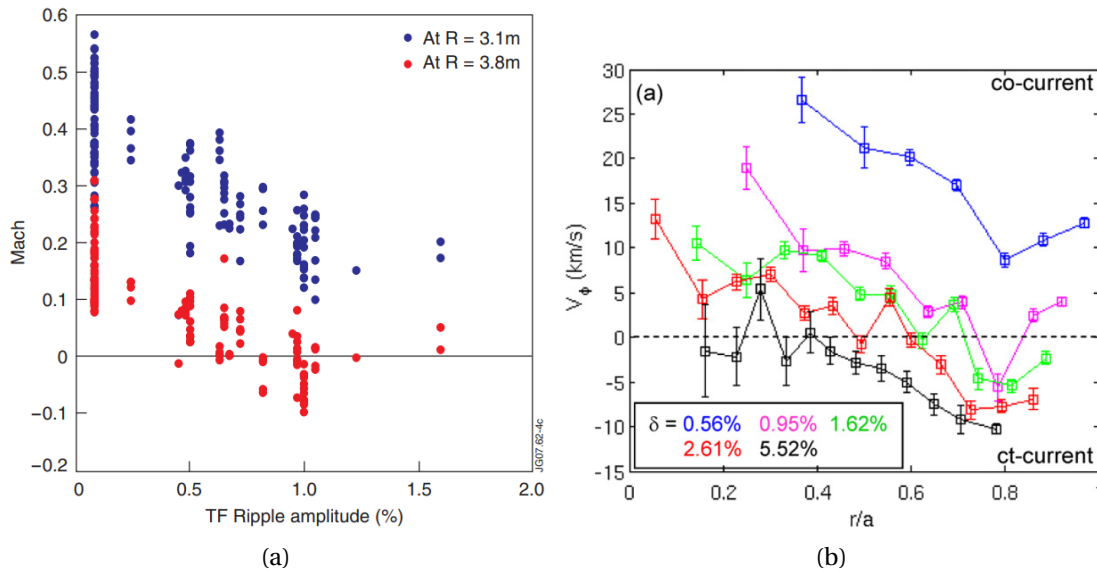


Figure 1.11. – (a) Mach number at the plasma center  $r/a \sim 0$  (blue) and plasma edge  $r/a \sim 0.9$  (red) versus the ripple amplitude at the outer separatrix in JET discharges. Extracted from [27]. (b) Radial profiles of the toroidal velocity in Tore Supra discharges for different ripple amplitudes. Extracted from [25].

The radial electric field is also affected. On Tore Supra [29], it has been observed that  $E_r$  follows its neoclassical prediction [30], i.e. it increases with the ripple amplitude. The knowledge of the resulting flows is important to assess the total transport. Especially, it has also been shown that magnetic ripple has an impact on H-mode plasmas. Indeed, it has been observed in JET that an increase of the edge ripple amplitude from  $\sim 0.01\%$  to  $\sim 1\%$  is responsible for a monotonic reduction up to  $\sim 20\%$  of the confinement time [31]. It was also observed in JET and JT-60U that ripple seems to ease the fast relaxations of the H-mode pedestal: the ELMs. It results that, with increasing ripple amplitude, the ELM amplitude decreases while their frequency increases [23, 24, 31] in such a way that the maximum ejected power is reduced. Finally, it was observed in JET [32] that the power threshold to access H-mode is unchanged between an edge ripple amplitude of  $0.08\%$  and  $1.1\%$ . Magnetic ripple is thus an important feature for reactor design and the way it impacts the plasma flows still lacks robust predictions.

In this thesis, we focus on the impact of ripple on the establishment of intrinsic toroidal rotation in a tokamak plasma. In particular, the competition and the synergy between the neoclassic and turbulent drive of the toroidal velocity are assessed for the first time, using a kinetic reduced model in 5D and simulations.

#### 1.5.4. Radial electric field dependency on the safety factor

Secondly, the impact of the safety factor on the edge radial electric field is assessed. The safety factor  $q$  is an important parameter as it is linked to the plasma current  $I_p$

near the edge. Experimental evidence, detailed below, shows that the radial electric field  $E_r$  is strongly impacted by the plasma current. Understanding the physics at play here is important as the radial electric field is involved in the formation and sustainment of transport barriers which are of great interest for fusion. The plasma current is also the main mean for heating plasma. In ITER,  $I_p$  will reach about 15MA, which can be compared to the maximum current of JET reaching  $\sim 5$ MA (current record holder) or the 2MA of ASDEX-Upgrade. However, predictions of the radial electric field under such a plasma current are currently lacking.

The focal point is on recent results [33] obtained with experiments performed in the WEST tokamak showing that the radial electric field  $E_r$  strongly increases in amplitude with the plasma current  $I_p$  at the plasma edge. Fig.1.12 shows the radial profile of the velocity transverse to the magnetic field lines measured by the Doppler Back-Scattering (DBS) diagnostic in dedicated WEST discharges.

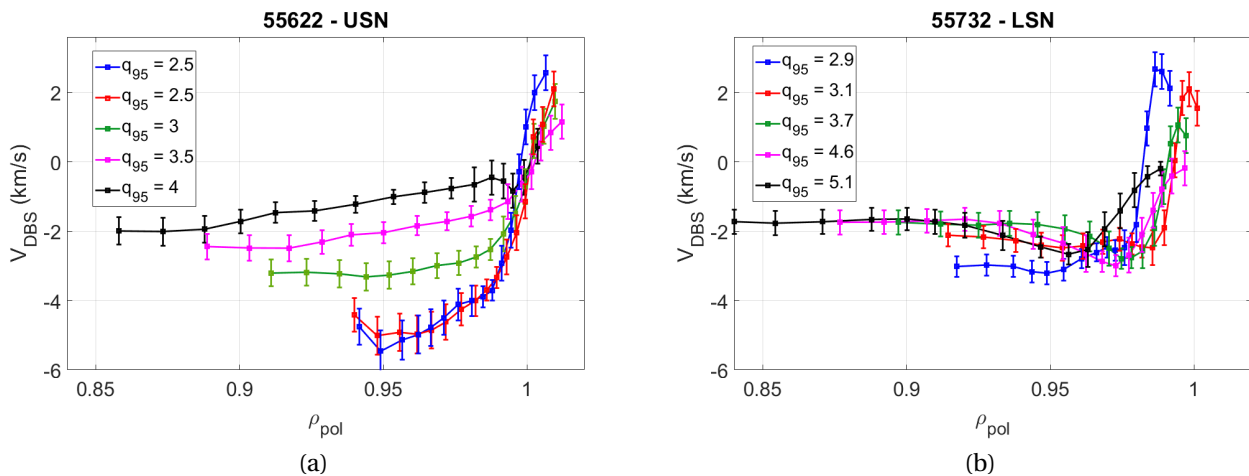


Figure 1.12. – Radial profile, near the edge of the plasma, of the transverse velocity measured in the WEST tokamak for different plasma current values in the Upper Single Null (left) and Lower Single Null (right) configurations. Extracted from [33].

This velocity is mainly due to the  $E \times B$  drift velocity  $V_{E \times B} \approx -E_r / B$ . As the magnetic field  $B$  only mildly decreases from the core to the edge, one can conclude that  $E_r$  is indeed strongly affected by the plasma current value. This deepening of edge  $E_r$  with the plasma current has also been witnessed in other tokamaks such as Tore Supra [34] and MAST [35]. As the plasma current is inversely proportional to the safety factor at the edge, a suggestion, further assessed in this thesis, is that  $q$  has a strong impact on  $E_r$ . Several mechanisms that carry a dependence on the safety factor are expected to play a role in the establishment of a radial electric field: neoclassical processes, zonal flows, Geodesic Acoustic Modes (GAMs), poloidal convective cells [36], turbulence and plasma-edge interactions.

Experimental evidence suggests that plasma current plays a role in the transition

toward enhanced confinement modes. Indeed, it has been observed in the ASDEX-Upgrade tokamak that  $I_p$  impacts the power threshold for the transition toward H-mode in the low-density branch [37]. However, in the high-density branch, the plasma current does not appear in the scaling law of this power threshold for a wide selection of tokamaks [38]. Understanding how the plasma current impacts the transition is therefore important to gain insight into the establishment of transport barriers.

In this thesis, the mechanisms that can impact the radial electric field and which depend on the safety factor are assessed using gyrokinetic simulations and further described with a 0D model.

### 1.5.5. Thesis objectives and outline

The present work aims to tackle the following questions:

- Can we build a reduced kinetic model in a 3D magnetic configuration to predict flows without turbulence? This is the subject of Chapter 2.
- Does this model agree with gyrokinetic simulations? This is the subject of Chapter 3.
- In presence of magnetic ripple, which is the main drive of the toroidal velocity between turbulence and neoclassical processes, and in which circumstances? This is the subject of Chapter 4.
- What are the mechanisms at play that make the plasma current impact the radial electric field in experiments and can it be explained with a safety factor dependence? This is the subject of Chapter 5.

# 2. Physics of flows in a 3D magnetic configuration

## Table of contents

2.1. Driving flows: a kinetic description . . . . .	47
2.1.1. The different descriptions of a plasma . . . . .	47
2.1.2. Channels of flow drive in tokamak plasmas . . . . .	48
2.2. Resonant surfaces in a rippled tokamak . . . . .	49
2.2.1. Phase space island generated by resonance . . . . .	50
2.2.2. $1/R$ magnetic decay and banana trapped particles . . . . .	52
2.2.3. Locally trapped particle in magnetic ripple wells . . . . .	53
2.2.4. Realistic magnetic configuration with two static perturbations . . . . .	55
2.2.5. Multiple fluctuating perturbations: turbulence . . . . .	58
2.3. Linking forces and fluxes with an entropy variational principle . . . . .	59
2.4. Neoclassical contribution in presence of ripple: the role of collisions . . . . .	61
2.5. Chaos and transport: the stochastic motion of particles . . . . .	66
2.5.1. Physical origin . . . . .	66
2.5.2. Resonance due to magnetic ripple . . . . .	67
2.5.3. Chirikov overlap criteria and diffusion coefficients . . . . .	71
2.6. An analytical model to predict flows in presence of magnetic ripple . . . . .	73
2.6.1. Explicit form of the reduced model . . . . .	73
2.6.2. Assessing the equilibrium flows with the model . . . . .	74
2.6.3. Assessing the dynamics of the flows with the model . . . . .	78
2.7. Turbulence: a short introduction . . . . .	79
2.8. Conclusion of chapter 2 . . . . .	83

The aim of this Chapter is to obtain a reduced model of transport that takes into account collisional physics and the chaos arising without turbulence. This model will be used to estimate the non-turbulent contribution to the total transport in simulations of Ion Temperature Gradient driven turbulence. This chapter is organized as follows.

- First, the different transport channels in tokamak plasmas are listed and described in Sec.2.1;
- Second, the concept of resonant surfaces, which are a way to treat the particle trajectories in a perturbed magnetic field, is presented in Sec.2.2. This formalism

## 2. Physics of flows in a 3D magnetic configuration – 2.1. Driving flows: a kinetic description

is convenient to introduce collisional and stochastic transport on the same footing;

- Then, a "variational principle", which is useful to write transport equations in a compact way, is outlined in Sec.2.3;
- The collisional contribution to transport is described and detailed in Sec.2.4;
- The stochastic contribution to transport is explained and derived in Sec.2.5;
- Finally, the turbulent channel of transport, not included in the model but of prime importance for the following chapters, is qualitatively addressed in Sec.2.7.

### 2.1. Driving flows: a kinetic description

In this section, a global picture of the mechanisms responsible for driving flows is drawn. In addition, the way to describe these processes, i.e. the chosen equations that rule their behavior, is detailed.

#### 2.1.1. The different descriptions of a plasma

There are multiple ways to describe a plasma, i.e. writing the equations that rule its behavior. Three possible ways allow a treatment of the plasma dynamics, particle and field-wise.

- **The particle description** is the most intuitive but also the least common description. It consists in treating the Newton equations of motion for each particle of mass  $m_p$ , charge  $e_p$  and velocity  $\mathbf{v}_p$ :  $m_p d_t \mathbf{v}_p = e_p (\mathbf{E} + \mathbf{v}_p \times \mathbf{B})$  and their relative interactions through the Maxwell equations. It is the description that carries the most detailed information: particle's position and velocity, and electromagnetic field. Regarding the plasma description needed for fusion, this is actually an overwhelming excess of information. On the one hand, because simulating a typical fusion plasma constituted of  $\sim 10^{22}$  particles would mean solving as many coupled equations. This is way out of reach of current High-Performance Computing (HPC) platforms. On the other hand, the knowledge of each particle characteristic is generally unusable on its own. More averaged data (i.e. density, mean velocity ...) are required.
- **The kinetic description** is a statistical approach that relies on the distribution function of a considered species (i.e. main ion, electrons, impurities...). Instead of considering a great number of particles, the distribution function  $F_s$  of the species  $s$  gives the probability of finding a particle at a certain position  $\mathbf{x}$  and velocity  $\mathbf{v}$ . The evolution of each distribution function is described through the *Fokker-Planck* equation coupled with the Maxwell equations. The Fokker-Planck equation treats the advection of  $F_s$  in time:

$$\frac{dF_s(\mathbf{x}, \mathbf{v}, t)}{dt} = \frac{\partial F_s}{\partial t} + \mathbf{v} \cdot \frac{\partial F_s}{\partial \mathbf{x}} + \frac{d\mathbf{v}}{dt} \cdot \frac{\partial F_s}{\partial \mathbf{v}} = \mathcal{C}(F_s) \quad (2.1)$$

in which  $\mathbf{v} = \frac{d\mathbf{x}}{dt}$  and  $\mathcal{C}$  is a collision operator. This formalism carries the informa-



## 2. Physics of flows in a 3D magnetic configuration – 2.1. Driving flows: a kinetic description

tion of interest for fusion-related studies. However, as discussed in Chapter 3, the numerical treatment of the kinetic approach is challenging.

- **The fluid description** is an integrated version of the kinetic approach that considers *moments* of the distribution function. A simplified expression of the moment of order  $k$  is  $M_k = \int d^3v F_s v^k$ . They are related to meaningful physical quantities:
  - ◊  $M_0 = n$  is the plasma density;
  - ◊  $\mathbf{M}_1 = n\mathbf{V}$  with  $\mathbf{V}$  is the averaged species velocity;
  - ◊  $M_2 = \frac{2}{m}P$  with  $P$  is the species pressure;
  - ◊ and so on ...

The huge advantage of this approach is that these quantities live in the physical 3D space, making both analytical and numerical treatment simpler. However, two critical issues are related to this approach. First, each evolution equation of moment  $M_k$  requires the knowledge of the next order moment  $M_{k+1}$  to be solved. It means that a closure equation must be considered. Second, the fluid approach fails to capture the mechanism causing a departure of the distribution function from a Maxwellian distribution as the distinction between trapped and passing populations (as described in Sec.1.4.6) are some examples. This is especially true for hot plasmas that are almost collisionless.

Kinetic simulation codes are heavier than fluid codes as one must calculate the distribution functions at each point in a 6D phase space grid. For this reason, both these approaches are generally used for usually different purposes. Fluid codes can be used to simulate long discharges, MHD activity, and realistic plasma-wall interactions. Kinetic codes are used to describe kinetic phenomena on short-time scales, like collision processes or micro-turbulence. The gyrokinetic model used in these codes is introduced in the next Chapter in Sec.3.2.

### 2.1.2. Channels of flow drive in tokamak plasmas

One can define 5 families of flow drive/damping channels:

- **Chaos physics** describes the global effect of stochastic particle motion or field that can arise in tokamaks. Here it is separated into two parts. First, there is the **ripple-induced chaos** coming from the co-existence of two static perturbations intrinsic to the tokamak magnetic configuration: the  $1/R$  magnetic decay and the magnetic ripple. Second, there is **turbulence** which describes the effect of small-scale spatiotemporal fluctuations of the electric and/or magnetic potentials. It contains viscous damping, pinch and drive via wave-particle interactions.
- **Neoclassical physics** describes the effect of collisions in a non-homogeneous magnetic field. It contains both damping and drive via thermal forces.
- **MagnetoHydroDynamic (MHD)** activity describes the plasma magnetic stability.
- **External sources or sinks of momentum**, describing the momentum injections or plasma-wall interactions.

The three first channels are detailed in the following sections of this chapter. The MHD activity describes the effect of macroscopic instabilities that impact the magnetic topology. This activity can modify or even suppress magnetic surfaces. MHD can lead

## 2. Physics of flows in a 3D magnetic configuration – 2.2. Resonant surfaces in a rippled tokamak

to violent events responsible for heat and particle losses. Such events can then lead to magnetic islands or even *disruptions* that can damage the tokamak in worst cases. In this thesis, this channel is not studied as following considered simulations are here performed in the electrostatic limit.

The last channel concerns sources and sinks of momentum. External injections of momentum are numerous in tokamaks experiments. They can be done on purpose or result from indirect effects. Here is a list of different means of injection:

- Neutral Beam Injection (NBI) consists of injecting a high-energy beam of neutral particles thanks to a particle accelerator. Momentum can be transferred from the fast incident particles to the plasma, either in the poloidal or toroidal direction, depending on the angle between the beam and the magnetic axis.
- Resonant or Non-Resonant Magnetic Perturbations (RMP / nRMP) consist of destabilizing either resonant or non-resonant modes using external coils. This method, used mainly for mitigating ELMs, also transfers momentum to the plasma by amplifying the breaking of axisymmetry. This loss of symmetry is associated with a new torque in the toroidal direction (this is discussed in detail in Sec.4.1).
- Radio wave heating and current-drive consist of transferring energy from an incident electromagnetic wave to particles. Depending on the incident wave frequency and the selected mode to amplify, it is possible to heat and accelerate only one species, e.g. electrons. This generates a current and thus transfers a net momentum to the plasma.

In addition to external momentum injection, plasma-wall interactions can also play an important role in the establishment of edge plasma flows. There are many mechanisms at play like orbit losses [39], momentum flux carried by waves [40], scrape-off layer interactions, turbulence spreading [41], or the role of neutral particles. In this work, the considered boundary physics is the one that is implemented in GYSELA. The GYSELA boundary conditions are detailed in Sec.3.2 in the next chapter.

The main focus is then on stochastic, neoclassical, and turbulent flow drives. To properly describe these phenomena on the same footing, one must use kinetic formalism. Indeed, each of the studied channels of transport in this thesis requires a kinetic approach:

- the stochastic motion of particles arises when considering the possible interactions of islands that live in the phase space (see Sec.2.5);
- for neoclassical flows, the conventional fluid models do not cover the physics at low collisionality which is relevant for fusion plasmas;
- turbulence is better described with a kinetic formalism as resonant wave-particle interactions depend on particle velocity.

## 2.2. Resonant surfaces in a rippled tokamak

In this section, we show how perturbations on a system at equilibrium modify the particle trajectories through the phase space. In the first subsection, it is demonstrated

## 2. Physics of flows in a 3D magnetic configuration – 2.2. Resonant surfaces in a rippled tokamak

that a single small perturbation creates an *island* in phase space. An island describes the shape of closed iso-contours of the energy when plotted in some angle/action or position/velocity space. Particle trajectories are of course embedded in these iso-contours. A closed iso-contour then denotes a trapped trajectory in both phase and real space. Surprisingly, a single perturbation applied on an unperturbed system does not deteriorate confinement. As detailed in the following, transport arises when considering either collisions or multiple perturbations. The perturbations considered here are the  $1/R$  magnetic decay, the magnetic ripple and the turbulence. In short, what happens when multiple perturbations exist is the following. When the islands generated by the different perturbations are "far enough", the transport is only due to collisions. However, when they are "close enough", the particle motion becomes stochastic and transport appears. First, let us see how an island is formed from an analytical point of view.

### 2.2.1. Phase space island generated by resonance

Let us remind that if three invariants of motion exist, the Hamiltonian motion of a particle is integrable. In a tokamak, the motion can be described by a set of action/variables  $(\boldsymbol{\alpha}, \mathbf{J})$  from the equilibrium Hamiltonian  $\mathcal{H}_{\text{eq}}(\mathbf{J})$  such that  $d_t J_i = -\partial_{\alpha_i} \mathcal{H}_{\text{eq}} = 0$  and  $d_t \alpha_i = \partial_{J_i} \mathcal{H}_{\text{eq}} = \Omega_i$ . Roughly speaking,  $J_1$  is related to the magnetic moment  $\mu$ ,  $J_2$  to the parallel adiabatic invariant  $\oint m v_{\parallel} dl$  and  $J_3$  to the toroidal kinetic momentum  $P_{\varphi}$ . The angles  $\alpha_1$ ,  $\alpha_2$  and  $\alpha_3$  are related to the cyclotron phase, the poloidal angle and the toroidal angle respectively. This equilibrium already includes the  $1/R$  magnetic decay perturbation. Let us now consider that a perturbation  $\tilde{\mathcal{H}}$  is added to the equilibrium Hamiltonian  $\mathcal{H}_{\text{eq}}$  such that

$$\tilde{\mathcal{H}}(\boldsymbol{\alpha}, \mathbf{J}, t) = h(\mathbf{J}) \cos(\xi(t)) \quad (2.2)$$

where  $h$  is the perturbation amplitude and

$$\xi = \mathbf{n} \cdot \boldsymbol{\alpha} - \omega t \quad (2.3)$$

is the perturbation phase. The triplet  $\mathbf{n}$  represents the mode numbers with respect to angular variables of the perturbation and  $\omega$  is the perturbation frequency. Writing the total Hamiltonian  $\mathcal{H} = \mathcal{H}_{\text{eq}} + \tilde{\mathcal{H}}$ , the Hamilton equations then read

$$\frac{d\boldsymbol{\alpha}}{dt} = \frac{\partial \mathcal{H}}{\partial \mathbf{J}} = \boldsymbol{\Omega} + \frac{\partial h}{\partial \mathbf{J}} \cos(\xi) \quad (2.4)$$

$$\frac{d\mathbf{J}}{dt} = -\frac{\partial \mathcal{H}}{\partial \boldsymbol{\alpha}} = \mathbf{n} h \sin(\xi) \quad (2.5)$$

with  $\boldsymbol{\Omega} = \frac{\partial \mathcal{H}_{\text{eq}}}{\partial \mathbf{J}}$ .

If the phase is time-independent, i.e.  $\frac{d\xi}{dt} = \mathbf{n} \cdot \boldsymbol{\Omega} - \omega = 0$ , the trajectories are significantly impacted. The condition  $\mathbf{n} \cdot \boldsymbol{\Omega} - \omega = 0$  defines a *resonant surface* in the  $\mathbf{J}$

2. Physics of flows in a 3D magnetic configuration – 2.2. Resonant surfaces in a rippled tokamak

action space. The motion in the vicinity of this resonance remains integrable with the following perturbative treatment. Let us consider a small displacement  $I\mathbf{n}$  of the action near a point  $\mathbf{J}_R$  of the resonance such that  $\mathbf{J} = \mathbf{J}_R + I\mathbf{n}$ . A Taylor expansion yields

$$\mathcal{H}(\mathbf{J}) = \mathcal{H}(\mathbf{J}_R) + \mathbf{n} \cdot \left. \frac{\partial \mathcal{H}}{\partial \mathbf{J}} \right|_{\mathbf{J}_R} I + o(I) \quad (2.6)$$

and, as  $d_t \boldsymbol{\alpha} = d_J \mathcal{H} = \boldsymbol{\Omega} + d_J \tilde{\mathcal{H}}$ ,

$$\frac{d\xi}{dt} = CI \quad (2.7)$$

where  $C = n_i n_k \left. \frac{\partial^2 \mathcal{H}}{\partial J_i \partial J_k} \right|_{\mathbf{J}_R}$  is commonly referred to as the *Hamiltonian curvature*. It is then possible to define a new Hamiltonian

$$\mathcal{H}_I = \frac{CI^2}{2} + \tilde{\mathcal{H}} \quad (2.8)$$

associated with the following equations of motion <sup>1</sup>

$$\frac{d\xi}{dt} = \frac{\partial \mathcal{H}_I}{\partial I} \quad (2.9)$$

$$\frac{dI}{dt} = -\frac{\partial \mathcal{H}_I}{\partial \xi}. \quad (2.10)$$

Trajectories follow the constant  $\mathcal{H}_I$  contour in the  $(\xi, I)$  space. Analogously to banana trapped particle, they are either passing or trapped depending on whether  $I = \sqrt{(2/C)(\mathcal{H}_I - h \cos(\xi))}$  goes to zero along the particle motion or not. It then defines an island, with the characteristic shape of a cat's eye, in the angle/action  $(\xi, I)$  space, as depicted in Fig.2.1.

---

1. Here we have used the properties  $\frac{d\mathbf{J}}{dt} = \frac{d(\mathbf{J}_R + I\mathbf{n})}{dt} = \mathbf{n} \frac{dI}{dt} = -\frac{\partial \mathcal{H}}{\partial \boldsymbol{\alpha}}$  and  $\frac{\partial \mathcal{H}}{\partial \boldsymbol{\alpha}} = \frac{\partial \xi}{\partial \boldsymbol{\alpha}} \frac{\partial \mathcal{H}}{\partial \xi}$ .

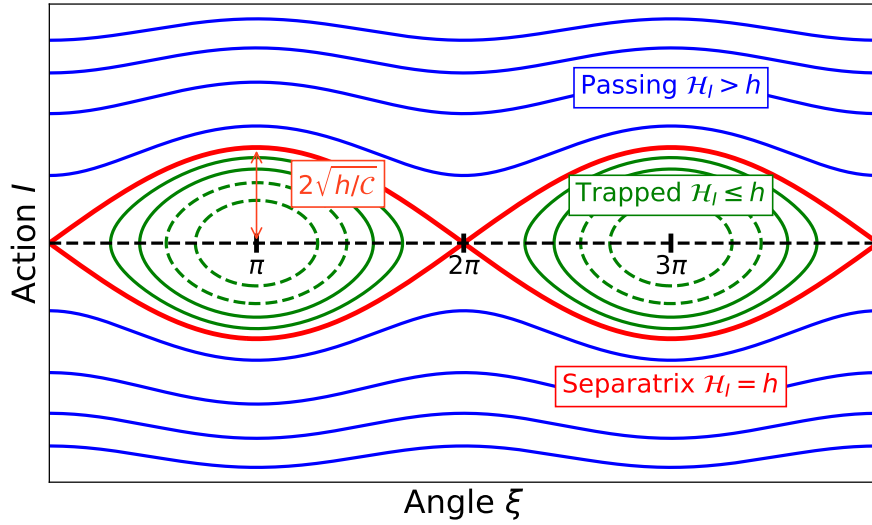


Figure 2.1. – Iso-contour in the angle/action ( $\xi, I$ ) space of the new Hamiltonian  $\mathcal{H}_I$  describing the resonance. Particles are passing (trapped) if the amplitude of the perturbation  $h$  is higher (smaller) than  $\mathcal{H}_I$ .

In this thesis, we consider two static perturbations of the magnetic field, as well as fluctuating perturbations on the electric potential which is called electrostatic turbulence. In the next subsection, we look at the associated islands. For the sake of clarity, the phase space considered will not be the angle-action space but rather the position-velocity space. It offers a better physical understanding of what the island represents in real space.

### 2.2.2. $1/R$ magnetic decay and banana trapped particles

In this study, a simplified geometry is considered where magnetic surfaces are taken circular and concentric. Using toroidal coordinates  $(r, \theta, \varphi)$ , and in the limit of large aspect ratio and small ripple magnitude, the axisymmetric magnetic field amplitude  $B$  can be approximated as follows:

$$B = \frac{B_0 R_0}{R(r, \theta)} \simeq B_0 \left( 1 - \underbrace{\varepsilon(r) \cos \theta}_{1/R \text{ decay}} \right). \quad (2.11)$$

Here,  $B_0$  is a reference magnetic field amplitude taken on the magnetic axis,  $R(r, \theta) = R_0 + r \cos(\theta)$  with  $R_0$  the major radius and  $\varepsilon = r/R_0$ . The perturbation is then simply the magnetic gradient that exists in all tokamaks.

As already discussed in the previous chapter, this perturbation is responsible for banana trapping. The representations of trajectories under such a perturbation on the real space and the phase space are depicted in Fig.2.2a and Fig.2.2b respectively.

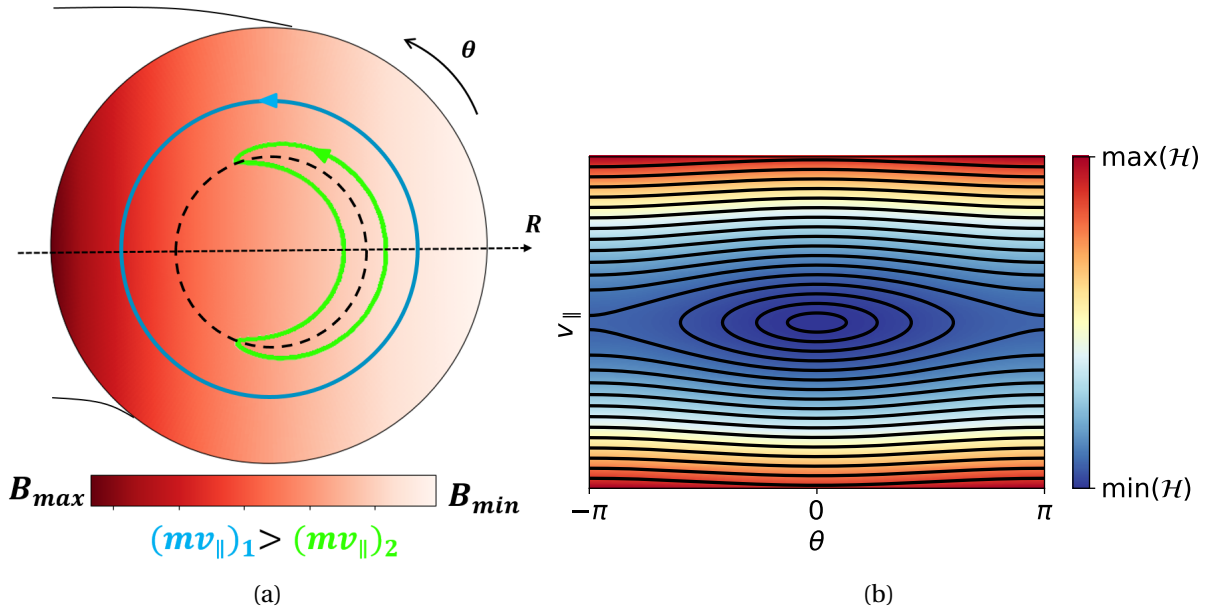


Figure 2.2. – (a) Principle of the banana trapping. For the same perpendicular momentum, the blue trajectory is passing and the green trajectory is trapped due to a different parallel momentum. (b) Island generated by the banana trapping in the  $(\theta, v_{\parallel})$  phase space.

### 2.2.3. Locally trapped particle in magnetic ripple wells

Let us now consider a tokamak without the  $1/R$  decay but only the magnetic ripple as a perturbation. The magnetic field amplitude would then read

$$B = B_0 \left( 1 + \underbrace{\delta(r, \theta) \cos(N_c \varphi)}_{\text{magnetic ripple}} \right) \quad (2.12)$$

where  $B_0$  is a reference magnetic field amplitude taken on the magnetic axis, and in between two coils,  $\delta$  is the ripple amplitude and  $N_c$  is the number of toroidal coils.

The ripple amplitude can be expressed for each radial and poloidal coordinate as a function of the minimum and maximum magnetic field amplitude encountered along the toroidal direction  $\varphi$ . It reads

$$\delta(r, \theta) = \frac{\frac{\max(B)}{\varphi} - \frac{\min(B)}{\varphi}}{\frac{\max(B)}{\varphi} + \frac{\min(B)}{\varphi}} \quad (2.13)$$

It is common to express it in percent, and this convention is used here unless specified otherwise throughout the manuscript. A ripple amplitude poloidal section - here the one in the Tore Supra tokamak - is displayed in Fig.2.3.

2. Physics of flows in a 3D magnetic configuration – 2.2. Resonant surfaces in a rippled tokamak

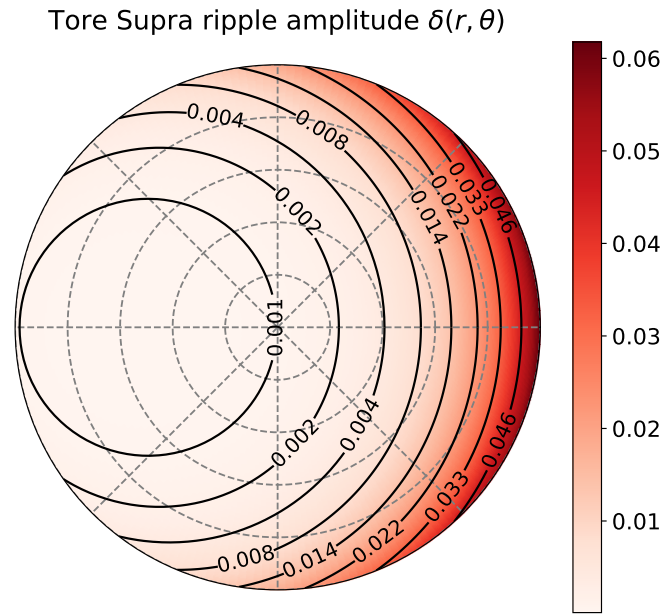


Figure 2.3. – Poloidal section of the ripple amplitude in the Tore Supra tokamak (Tore Supra and WEST contain 18 toroidal coils.) in closed flux surfaces.

All tokamaks exhibit the same shape of ripple amplitude, i.e. roughly radially exponential from an origin slightly shifted toward the high field side. The maximal value is then reached at the low field side in the midplane and seldom exceeds 1%. The Tore Supra ripple amplitude shown is then unusually high, which makes it a particularly interesting case to study the effect of magnetic perturbations. As developed in the next sections, even a ripple amplitude equal to a fraction of a percent can drastically change plasma flows.

A phenomenon similar to banana trapping occurs when accounting for the magnetic field ripple. Indeed ripple causes a modulation of the magnetic field in the toroidal direction: the magnetic field amplitude under a coil is stronger than in-between two consecutive coils. Depending on the parallel momentum of the particle, the trajectory can either be passing or trapped between two consecutive coils. This is called the *local trapping*. Trajectories in such a magnetic configuration are plotted in the real space and phase space in Fig.2.4a and Fig.2.4b respectively.

2. Physics of flows in a 3D magnetic configuration – 2.2. Resonant surfaces in a rippled tokamak

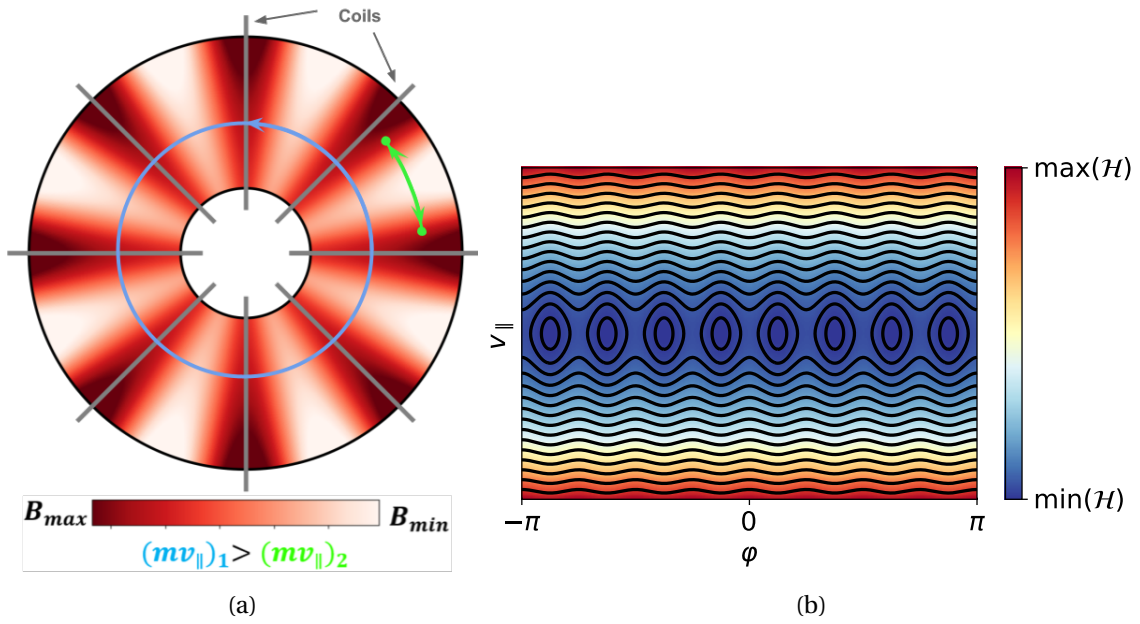


Figure 2.4. – (a) Principle of trapping induced by ripple with  $N_c = 8$ : for the same perpendicular momentum, the blue trajectory is passing and the green trajectory is trapped due to a different parallel momentum. (b) Island generated by the local trapping in the  $(\varphi, v_{\parallel})$  phase space.

### 2.2.4. Realistic magnetic configuration with two static perturbations

Both resonances due to the  $1/R$  magnetic decay perturbation and the magnetic ripple, and their associated trapping, can co-exist. The ripple wells are however not existing in all the plasma domain. Indeed, Fig.2.5 shows the shape of the kinetic energy as function of the angle  $\varphi_0 + q\theta$ . Particles travel at constant kinetic energy  $E - e\phi$ , where  $\phi$  is the electric potential, such that their trajectory is passing when  $E - e\phi > \mu B_{max}$  and banana-trapped in the other case. However in region of high ripple amplitude, the locally trapped particles are located in the multiple small wells that are particularly deep near the mid-plane at low field side  $\varphi_0 + q\theta = 0$  for a realistic ripple amplitude as shown in Fig.2.3. Then an important remark can be made: if the ripple amplitude is too weak, the magnetic wells do not exist. This can be described thanks to the trapping parameter  $Y(r, \theta) = \frac{\epsilon |\sin \theta|}{N_c q \delta}$  (see [42] p.127 for more insight) which is the condition of existence of ripple-induced magnetic wells. Magnetic wells exists only in regions where  $Y(r, \theta) < 1$ .



2. Physics of flows in a 3D magnetic configuration – 2.2. Resonant surfaces in a rippled tokamak

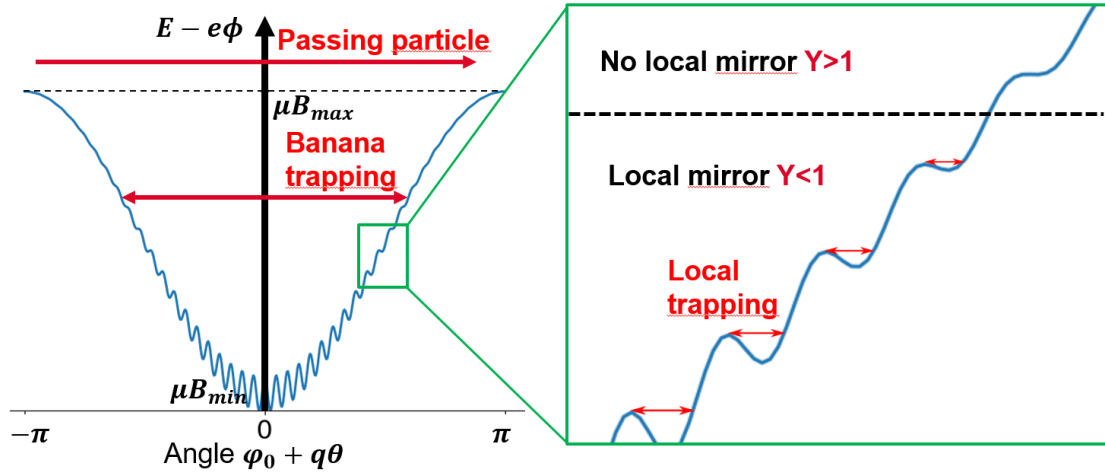


Figure 2.5. – Typical shape of the kinetic energy as function of the angle  $\varphi_0 + q\theta$  that parametrizes a particular field line for each  $\varphi_0$ . Particle trajectory follows constant energy lines.

That said, the *Kolmogorov-Arnold-Moser theorem* (KAM) [43] states that the system stays integrable as long as the islands associated with each perturbation are far enough from each other in the phase space, and their amplitude is sufficiently small. On the contrary, when the islands are too close to each other and/or their amplitude is large enough, the system becomes chaotic.

Here a subtle point should be assessed. In the previous sections, the discussed islands were described in the position/velocity  $(\mathbf{x}, \mathbf{v})$  space for clarity. However when two perturbations are accounted for, the angle/action  $(\alpha, \mathbf{J})$  space is more appropriate. The poloidal and toroidal angles  $\theta$  and  $\varphi$  are related to the unperturbed Hamiltonian angles  $\alpha_B$  and  $\varphi_0$  such that, in the deeply trapped limit, they are related through

$$\theta = \theta_B \sin(\alpha_B) \quad (2.14)$$

$$\varphi = \varphi_0 + q\theta_B \sin(\alpha_B) \quad (2.15)$$

where  $\theta_B$  is the poloidal bounce angle. Note that this choice of angle/action coordinates means that banana particles are selected. The ripple perturbation is then added, resulting in the trajectories of banana-trapped particles modified by magnetic ripple. Note that one could also have chosen the angle/action coordinates related to the particle locally trapped and then add the  $1/R$  magnetic decay perturbation. This would result in the trajectories of particles trapped between two coils perturbed by the magnetic gradient. However, the chaos resulting from this channel is expected to be way lower than for the banana-trapped particle and consequently will not be discussed in this thesis.

In this banana-related set of coordinates, and remembering that the generating

2. Physics of flows in a 3D magnetic configuration – 2.2. Resonant surfaces in a rippled tokamak

function of the first kind Bessel functions  $J_n$  of order  $n$  reads

$$\sum_{n=-\infty}^{+\infty} J_n(x) e^{in\beta} = e^{ix \sin(\beta)} \quad \forall(x, \beta) \quad (2.16)$$

then the magnetic ripple harmonic becomes

$$\cos(N_c \varphi) = \frac{1}{2} \sum_{n_B=-\infty}^{+\infty} J_{n_B}(N_c q \theta_B) \cos(N_c \varphi_0 + n_B \alpha_B) \quad (2.17)$$

meaning that these two perturbations in the real phase space actually translate into an infinite number of perturbations in the angle/action space. This will be developed in Sec.2.5.

It can be shown that chaos arises when the precession frequency  $\Omega_D$  is high enough, more precisely when  $\Omega_D > \Omega_B / N_c$  (see Sec.2.5.1). Even in this non-integrable situation, it is possible to estimate the resulting transport. In the other limit  $\Omega_D < \Omega_B / N_c$ , particle trajectories are integrable. However, integrable does not mean that there is no transport. In fact, these perturbations impact each other. The banana trajectories are indeed modified, especially near the bounce point where the rapid parallel motion vanishes. Depending on the direction of the magnetic drift, and whether the toroidal angle of the bounce point is at a coil level or between two coils, the particle bounce point position is modified. This effect is depicted in Fig.2.6 (left). However, as long as the particle is far away from the separatrix, defined as the last closed flux surface, the trajectory stays confined. The locally trapped particles are also affected by the  $1/R$  magnetic decay. Indeed, for such a trapped particle, the vertical magnetic drift is not compensated by the helicity of the magnetic field lines. These particles drift vertically out of the tokamak. This effect is depicted in Fig.2.6 (right).

2. Physics of flows in a 3D magnetic configuration – 2.2. Resonant surfaces in a rippled tokamak

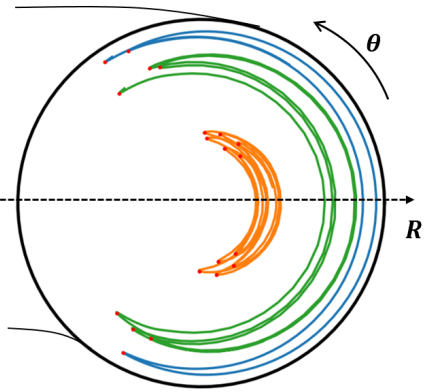
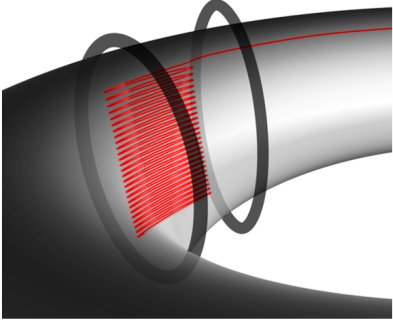
Primary perturbation	Magnetic gradient $\nabla B$	Ripple
Secondary perturbation	Ripple	Magnetic gradient $\nabla B$
		

Figure 2.6. – Trapped particle trajectories with both perturbations -  $1/R$  magnetic field decay and magnetic ripple - obtained with the GCT code [44]. (Left) Banana trapped trajectories exhibit radial and poloidal shifts of bounce points due to magnetic ripple. (Right) Locally trapped particles drift vertically due to the magnetic drift induced by the  $1/R$  magnetic decay perturbation.

On top of these effects, collisions play an important role. Collisional transport exists independently of any resonance. However, the collisional processes are enhanced by resonances, as described within the neoclassical theory. The resulting flow is assessed in Sec.2.4.

### 2.2.5. Multiple fluctuating perturbations: turbulence

The situation can become intractable when accounting for multiple time-evolving perturbations. This is the case for turbulence, which is one of the most important topics in the tokamak community<sup>2</sup> as the transport across the magnetic field is often mainly turbulent. Turbulence is a chaotic process that deserves to be treated separately from chaos induced by static perturbations because of its complexity. Indeed, compared with the magnetic perturbation discussed previously, the mechanisms at play in turbulence are not fully understood yet. In this Chapter, turbulence is described qualitatively in Sec.2.7.

2. Also in stellarators now: recent experiments in W7X showed that turbulent heat transport dominates the neoclassical transport above a certain input power.

## 2.3. Linking forces and fluxes with an entropy variational principle

In this brief section, a method to describe an equilibrium in a compact way is introduced. In particular, this method makes the link between thermodynamic forces and fluxes thanks to the *transport matrix*. The method is based on the entropy production rate  $\dot{S}$ , which must be minimum at equilibrium. The idea is that a variational principle can be built from this condition. Variational principles carry multiple benefits, but the one of use for this work is that it allows one to express all the transport equations in a compact way. Here only the main ingredients of the method are presented, but the interested reader can refer to [45–47]. First, it can be shown that the Fokker-Planck equation expressed in the angle/action coordinates  $(\boldsymbol{\alpha}, \mathbf{J})$  on a slow evolving equilibrium can take the form

$$\frac{\partial F_{\text{eq}}(\mathbf{J}, t)}{\partial t} + \frac{\partial \Gamma_i}{\partial J_i} = \mathcal{C}[F_{\text{eq}}] \quad (2.18)$$

where  $F_{\text{eq}}$  is the equilibrium distribution function,  $\Gamma_i$  the flux of action  $J_i$  and  $\mathcal{C}$  a collision operator. Note that "equilibrium" here is not a full thermodynamic equilibrium, but one that only weakly differs from it. Here fluxes are considered diffusive, such that

$$\Gamma_i = -D_{ik} \frac{\partial F_{\text{eq}}}{\partial J_k} \quad (2.19)$$

where  $D_{ik}$  is the transport matrix, i.e. the quantity of interest in this chapter, and  $\partial F_{\text{eq}}/\partial J_k$  is a measure of the departure from equilibrium and can be seen as thermodynamical gradients. Let us see the link with the entropy production rate  $\dot{S}$ .

The entropy is defined as  $S = -\int d\gamma F_{\text{eq}} \ln F_{\text{eq}}$  with  $d\gamma$  a volume element in the phase space. The considered equilibrium is of the form  $F_{\text{eq}} = \exp\left\{-\left(\frac{\mathcal{H}_{\text{eq}} - U_{\text{eq}}}{T_0}\right)\right\}$ , where  $\mathcal{H}_{\text{eq}}$  is the equilibrium Hamiltonian,  $U_{\text{eq}}$  a thermodynamical potential and  $T_0$  a constant reference temperature. Hence, the production rate at equilibrium reads

$$\dot{S} = -\frac{1}{T_0} \int d\gamma \frac{\partial F_{\text{eq}}}{\partial t} U_{\text{eq}} . \quad (2.20)$$

From this entropy production rate, it is possible to construct a functional  $\mathcal{S}(U_{\text{eq}}, U_{\text{eq}}^\dagger)$  such that

$$\mathcal{S} = \dot{S}_t + \dot{S}_{\text{res}} + \dot{S}_{\text{coll}} \quad (2.21)$$

where

2. Physics of flows in a 3D magnetic configuration – 2.3. Linking forces and fluxes with an entropy variational principle

$$\dot{S}_t(U_{\text{eq}}, U_{\text{eq}}^\dagger) = \frac{2}{T_0^2} \int d\gamma F_{\text{eq}} \left( U_{\text{eq}}^\dagger \frac{\partial U_{\text{eq}}}{\partial t} \right) \quad (2.22)$$

$$\dot{S}_{\text{res}}(U_{\text{eq}}, \partial_{\mathbf{J}} U_{\text{eq}}^\dagger) = -\frac{1}{T_0^2} \int d\gamma \left( \frac{\partial U_{\text{eq}}^\dagger}{\partial J_i} D_{ij} \frac{\partial U_{\text{eq}}^\dagger}{\partial J_j} \right) \quad (2.23)$$

$$\dot{S}_{\text{coll}}(U_{\text{eq}}, \partial_{\mathbf{J}} U_{\text{eq}}^\dagger) = -\frac{1}{T_0^2} \int d\gamma F_{\text{eq}} \left( U_{\text{eq}}^\dagger \mathcal{C}[U_{\text{eq}}^\dagger] \right). \quad (2.24)$$

This segmentation of the functional is convenient:  $\dot{S}_t$  encompasses the dynamic of  $F_{\text{eq}}$  while  $\dot{S}_{\text{coll}}$  describes the effect of collisions and  $\dot{S}_{\text{res}}$  describes the resonant behavior of the plasma as it is detailed in the next sections. Regarding the dynamic term to describe a situation out of equilibrium, minimizing  $\dot{S}_t$  with respect to  $U^\dagger$  leads to an evolution equation on  $U^\dagger$ . In the weak collisionality limit, which is of interest for core tokamak plasmas,  $\dot{S}_{\text{coll}}$  is subdominant compared to  $\dot{S}_{\text{res}}$  which is reinforced in collisionless systems (collisions actually smooth the resonance and its associated transport). The quantity of interest that describes the equilibrium is therefore  $\dot{S}_{\text{res}}$ . It can be expressed in the real space [47] as follows

$$\dot{S}_{\text{res}} = -\frac{1}{2} \int dV n \left( \frac{\Gamma}{n \mathcal{N}} \frac{d\mathcal{N}}{dr} + \frac{\mathcal{M}}{nmV_{\text{th}}} \frac{V_T}{V_{\text{th}}} + \frac{Q}{nT} \frac{1}{T} \frac{dT}{dr} \right) \quad (2.25)$$

with  $dV$  a volume element,  $\Gamma$  the particle flux,  $\mathcal{M}$  the rate of dissipated toroidal momentum,  $Q$  the heat flux and

$$\frac{1}{\mathcal{N}} \frac{\partial \mathcal{N}}{\partial r} = \frac{1}{n} \frac{dn}{dr} - \frac{eE_r}{T} \quad (2.26)$$

where  $\mathcal{N}$  is a density modified by the radial electric field. These fluxes can then be derived as

$$\Gamma = -\frac{1}{2} \frac{\partial \dot{S}_{\text{res}}}{\partial (\partial \ln \mathcal{N} / \partial r)} \quad (2.27)$$

$$\mathcal{M} = -\frac{1}{2} nmV_{\text{th}}^2 \frac{\partial \dot{S}_{\text{res}}}{\partial V_T} \quad (2.28)$$

$$Q = -\frac{1}{2} nT \frac{\partial \dot{S}_{\text{res}}}{\partial (\partial \ln T / \partial r)}. \quad (2.29)$$

For the following the resonant entropy production rate is considered to come from two mechanisms: neoclassical processes encompassed in  $\dot{S}_{\text{neo}}$  and stochastic processes encompassed in  $\dot{S}_{\text{st}}$  such that  $\dot{S}_{\text{res}} = \dot{S}_{\text{neo}} + \dot{S}_{\text{st}}$ . In the next sections, each mechanism is described and an expression is given for these terms.

## 2.4. Neoclassical contribution in presence of ripple: the role of collisions

Neoclassical transport at low collisionality is due to the resonant enhancement of collisional processes.

It owes its existence to trapped particles, for which adding collisions accounts for the *neoclassical theory*. When the collision frequency becomes comparable or smaller to the bounce frequency of the considered trapped population, a random walk with a characteristic step linked to the trajectory orbit width prevails. Considering banana trapping, for example, this step would be roughly the banana width. Subtleties also appear when accounting for the synergies between the different trappings. For example, the ripple causes banana bounce points to drift radially in such a way that they undergo a random walk process. Neoclassical theory is meant to describe all those processes. It relies on a kinetic derivation of the equilibrium distribution function for the considered species. Each population (trapped or passing) tends to relax towards a Maxwellian equilibrium under the effect of collisions. The resulting total distribution function can however be non-Maxwellian and therefore lead to finite fluxes.

This physics is captured by the gyrokinetic code GYSELA. Fig.2.7 shows the impact of the  $1/R$  magnetic field decay and magnetic ripple on the distribution function in the  $(\theta, v_{\parallel})$  and  $(\varphi, v_{\parallel})$  spaces. Magnetic ripple produces islands in the  $(\varphi, v_{\parallel})$  space corresponding to particles trapped toroidally between coils. The island in the  $(\theta, v_{\parallel})$  space, corresponding to the banana trapping, is also modified with ripple. As discussed previously, the effect is maximum at  $v_{\parallel} = 0$  where the effect of ripple is not smoothed out by the fast parallel motion. A similar mechanism also exists for particles locally trapped.

2. Physics of flows in a 3D magnetic configuration – 2.4. Neoclassical contribution in presence of ripple: the role of collisions

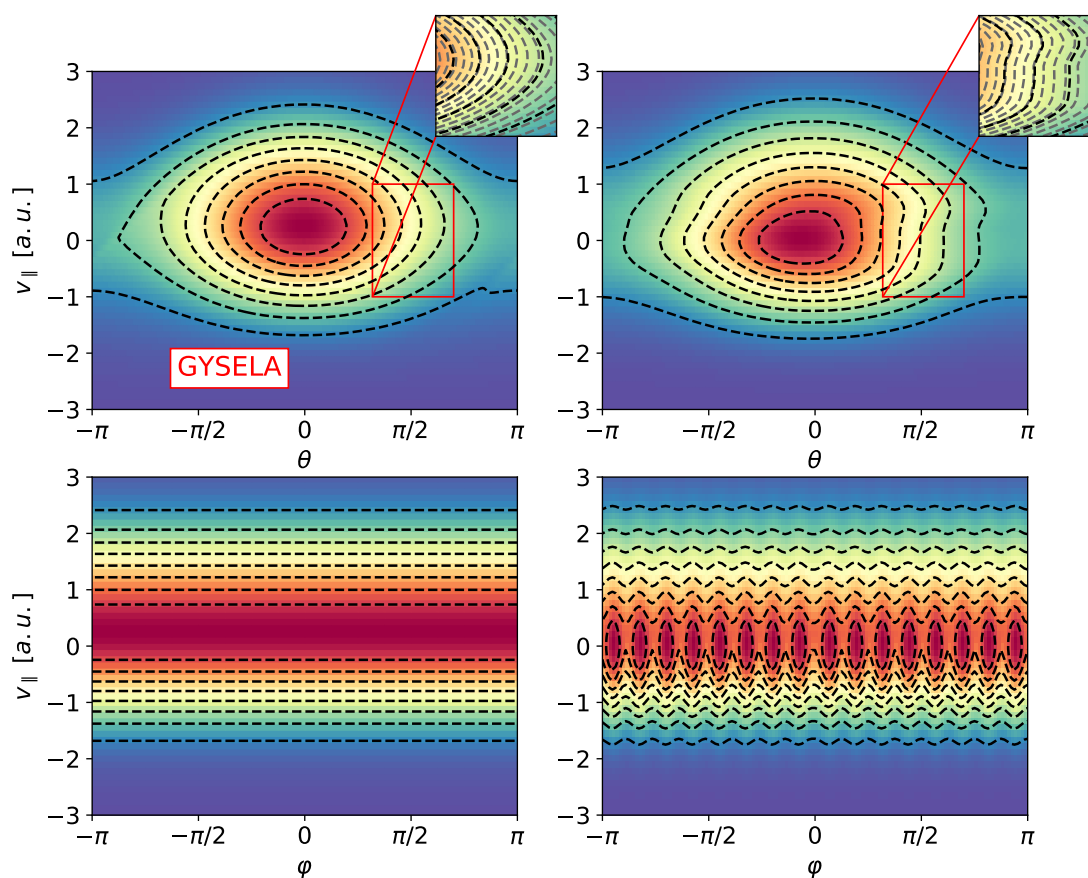


Figure 2.7. – Distribution function, taken at fixed radius and magnetic moment  $\mu$ , of trapped particles without (left) and with (right) ripple, obtained with GYSELA with  $N_c = 16$ . Ripple accounts for an additional trapping in the toroidal direction and also modifies the island of banana-trapped particles near bounce points.

To get the expression of the distribution function and associated transport, the simplest starting point is the drift kinetic equation (DKE). The first step of the derivation then relies on solving the DKE for each perturbation, i.e. the  $1/R$  magnetic field decay or ripple, independently. They are labeled ‘primary’ perturbations. Solving the DKE with the  $1/R$  magnetic field decay as primary perturbation leads to the axisymmetric neoclassical theory and the well known commonly called "neoclassical transport regimes" visible in the black curve on Fig.2.8. Doing the same for the ripple perturbation amounts to consider collisional processes in a tokamak without curvature, i.e. a rippled cylinder, with equally spaced coils that leads to local trapping. The next step is to perturb the trapped population by the primary perturbation with the other one, labeled ‘secondary’ perturbation. If ripple is the secondary perturbation, it then accounts for the radial drift of the banana bounce point induced by ripple. If the  $1/R$  magnetic field decay is the secondary perturbation, it then accounts for the bounce points of the ripple-induced trapped trajectories drifting vertically due to the magnetic

2. Physics of flows in a 3D magnetic configuration – 2.4. Neoclassical contribution in presence of ripple: the role of collisions

drift. These four contribution branches to neoclassical transport can be summed up in this list, from which the terminology comes from the stellarator community [48]:

- the *axisymmetric branch* is the neoclassical contribution of unperturbed banana particles;
- the *helically symmetric branch* is the neoclassical contribution of unperturbed ripple-induced trapping;
- the *banana drift branch* is the neoclassical contribution from ripple effect on banana trapped particles;
- the *ripple-wells drift branch* is the neoclassical contribution from the  $1/R$  magnetic field decay effect on particles trapped in ripple-induced magnetic wells.

The typical collisionality scaling in tokamaks of the radial fluxes for each of these branches is displayed in Fig.2.8. Note that when  $\nu^* \rightarrow 0$  the fluxes vanish. This is intuitive for banana-trapped particles but counter-intuitive for locally-trapped particles. Indeed, at "low" collisionality, locally trapped particles account for a  $1/\nu$  behaviour due to the fact the vertical drift of particles is not stopped by collisions. However, at even lower collisionalities, higher order magnetic and electric drifts regularize this behaviour.

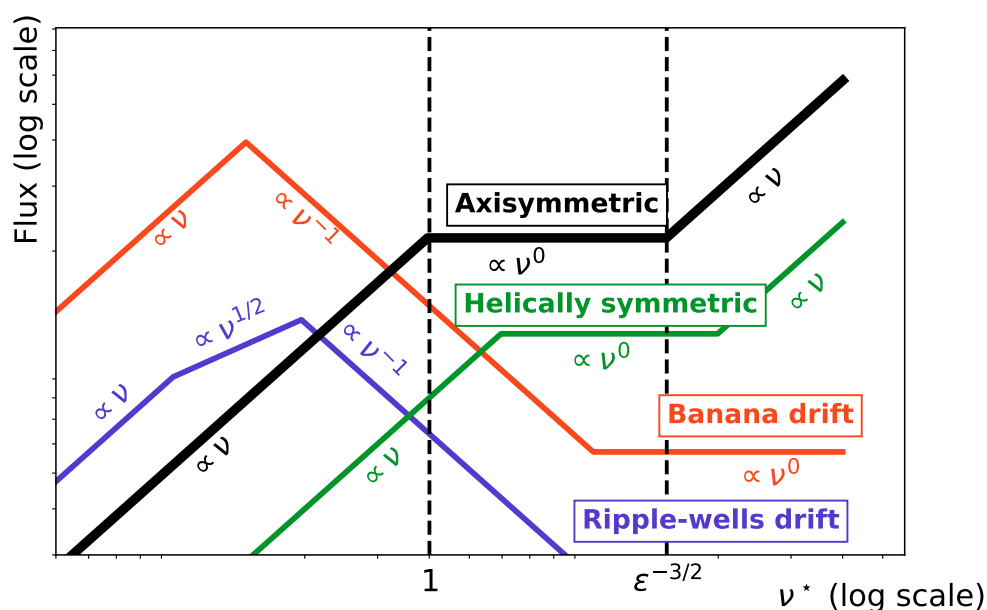


Figure 2.8. – Typical scaling of the radial neoclassical fluxes with the collisionality for each branch.

The whole analytical calculation of neoclassical transport is a formidable task that will not be detailed here. Here is however a bit of history on the development of the neoclassical theory, particularly in non-axisymmetric devices. Note that many actors shaped the current knowledge of this channel of transport, and only a handful of them are mentioned here. The following should then be considered as our specific point of view on what we consider to be the main milestones in this domain.



## 2. Physics of flows in a 3D magnetic configuration – 2.4. Neoclassical contribution in presence of ripple: the role of collisions

The foundations for the enhancement of collisional processes by the presence of trapped particles were laid in the late 60's in particular with the work of Galeev & Sagdeev [49, 50] and Kovrizhnykh [51]. From these pioneering works, a growing interest arose and several publications at the origin of the neoclassical theory appeared in the 70's. A review of this work was done by Hinton [46], and a more recent and comprehensive one has been published by Helander [52]. In that time almost all of them were devoted to axisymmetric devices<sup>3</sup> except for the work of Stringer [53] and Connor [54] that noticed the  $1/\nu$  behavior of the ripple-wells drift branch. Interest in neoclassical transport in non-axisymmetric systems peaked in the late 70's-beginning of the 80's. At that time, the impact of ripple on banana trapping has been extensively studied [55–57] and a generalized transport of banana trajectories was proposed by Yushmanov [58]. The transport due to locally trapped particles has also been detailed with, among other, an emphasis on the work by Yushmanov [59] and Shaing [60, 61]. An important review at that time was the one of Kovrizhnykh [62]. Among the numerous studies that follow, we want to emphasize on the very helpful review on transport in rippled configuration by Yushmanov [42] in the 90's. Also, the zoology of very low collisionality regimes, i.e. the  $1/\nu$ ,  $\nu - \sqrt{\nu}$  regimes, as well as the effect of lower order electric and magnetic drift making up for the superbanana regime, has known a strong development with the work by Shaing *et al.* around 2010 [63–65].

In the present work, the derivation of the neoclassical fluxes is based on the calculation included in the review by Garbet *et al.* [30], up to some minor corrections. Note that this model does not account for the  $\nu - \sqrt{\nu}$  regimes of the "banana-drift" and "ripple-wells" branches that arise at extremely low collisionality. Also, the very high collisionality regime, referred to as *Pfirsch–Schlüter* regime, is not considered. The resonant production rate of entropy  $\dot{S}_{\text{neo}}$  due to neoclassical processes can be partitioned such that

$$\dot{S}_{\text{neo}} = \dot{S}_{\text{tor,I}} + \dot{S}_{\text{rip,I}} + \dot{S}_{\text{tor,II}} + \dot{S}_{\text{rip,II}} \quad (2.30)$$

with  $\dot{S}_{\text{tor,I}}$  and  $\dot{S}_{\text{rip,I}}$  the contributions from the axisymmetric and helically symmetric branches, and  $\dot{S}_{\text{tor,II}}$  and  $\dot{S}_{\text{rip,II}}$  the contributions from the banana drift and ripple-wells drift branches respectively. They can be expressed as a function of three parameters:

- The collisionality  $\nu^*$ ;
- The product of the number of coils and the safety factor  $N_c q$ ;
- The ratio between the ripple and  $1/R$  decay magnetic perturbations  $\delta/\varepsilon$ .

These entropy productions rates are given by [30]:

---

3. The reason was not only the increased complexity when accounting for 3D magnetic perturbations, but also that the stellarator was disregarded at that time due to their poor performances back then.

2. Physics of flows in a 3D magnetic configuration – 2.4. Neoclassical contribution in presence of ripple: the role of collisions

$$\dot{S}_{\text{tor,I}} = \frac{1}{2} \sqrt{\frac{\pi}{2}} \int dV n D_p \int_0^{+\infty} du e^{-u} u^2 K_{\text{tor,I}}(r, u) \left[ \frac{1}{\mathcal{N}} \frac{d\mathcal{N}}{dr} + \left(u - \frac{3}{2}\right) \frac{1}{T} \frac{dT}{dr} + \frac{eB_p}{T} V_T \right]^2 \quad (2.31)$$

$$\dot{S}_{\text{rip,I}} = \frac{1}{2} \sqrt{\frac{\pi}{2}} \int dV n D_p (N_c q) \left(\frac{\bar{\delta}}{\varepsilon}\right)^2 \int_0^{+\infty} du e^{-u} u^2 K_{\text{rip,I}}(r, u) \left[ \frac{eB_p}{T} V_T \right]^2 \quad (2.32)$$

$$\dot{S}_{\text{tor,II}} = \frac{8}{9} \left(\frac{2}{\pi}\right)^{3/2} \int dV n D_p \left(\frac{\bar{\delta}}{\varepsilon}\right)^{3/2} \frac{G_1}{v^*} \int_0^{+\infty} du e^{-u} u^{5/2} \frac{1}{\bar{v}(u)} \left[ \frac{1}{\mathcal{N}} \frac{d\mathcal{N}}{dr} + \left(u - \frac{3}{2}\right) \frac{1}{T} \frac{dT}{dr} \right]^2 \quad (2.33)$$

$$\dot{S}_{\text{rip,II}} = \left(\frac{2}{\pi}\right)^{3/2} \int dV n D_p \frac{1}{N_c q} \left(\frac{\bar{\delta}}{\varepsilon}\right)^2 \frac{1}{v^*} \int_0^{u_c} e^{-u} u^{5/2} \frac{K_{\text{rip,II}}(r, u)}{\bar{v}(u)} \left[ \frac{1}{\mathcal{N}} \frac{d\mathcal{N}}{dr} + \left(u - \frac{3}{2}\right) \frac{1}{T} \frac{dT}{dr} \right]^2 \quad (2.34)$$

where  $\bar{\delta} = \frac{1}{2\pi} \int d\theta \delta(r, \theta)$ ,  $D_p = \frac{qR_0}{V_{\text{th}}} \left(\frac{T}{eB_0 R_0}\right)^2$  is a reference diffusion coefficient with  $V_{\text{th}} = \sqrt{T/m}$  the ion thermal velocity, and  $\bar{v}$  is the normalized collision frequency [66] defined as:

$$\bar{v}(u) = \frac{3}{4} \sqrt{2\pi} \frac{1}{u^{3/2}} (\Phi(u^{1/2}) - G(u^{1/2})) \quad \text{where} \quad \begin{cases} \Phi(u) = \frac{2}{\sqrt{\pi}} \int_0^u dx \exp(-x^2) \\ G(u) = \frac{1}{2u^2} (\Phi(u) - u \frac{d\Phi(u)}{du}) \end{cases}$$

The functions  $K$  provide smooth transitions between various collision regimes:

$$K_{\text{rip,I}}(r, u) = \min \left( G'_0, G''_0 \frac{4}{\pi} \mathcal{I} \frac{v^*}{N_c q} \left(\frac{\varepsilon}{\bar{\delta}}\right)^{3/2} \frac{\bar{v}(u)}{u^{1/2}} \right) \quad \text{with } \mathcal{I} = 1.38 \quad (2.35)$$

$$K_{\text{tor,I}}(r, u) = \min \left( 1, \frac{4}{\pi} \mathcal{I} v^* \frac{\bar{v}(u)}{u^{1/2}} \right) \quad (2.36)$$

$$K_{\text{rip,II}}(r, u) = 1 + \frac{\pi^2}{8} v^* (N_c q)^2 \frac{\bar{v}(u)}{u^{1/2}} \quad (2.37)$$

where is defined the continuous function  $\min(x, y) = \frac{xy}{x+y}$ .

The *form factors*  $G'_0$ ,  $G''_0$ ,  $G_1$ , used to discriminate banana trapped particles and magnetic wells, are given by the relations:

$$\begin{aligned} G'_0(r) &= \int_{Y < 1} \frac{d\theta}{2\pi} \tilde{\delta}^2(r, \theta) \\ G''_0(r) &= \int_{Y < 1} \frac{d\theta}{2\pi} \tilde{\delta}^{1/2}(r, \theta) \\ G_1(r) &= \int_{Y < 1} \frac{d\theta}{\pi} \tilde{\delta}^{3/2}(r, \theta) \sin^2 \theta \end{aligned} \quad (2.38)$$

2. *Physics of flows in a 3D magnetic configuration – 2.5. Chaos and transport: the stochastic motion of particles*

where  $Y(r, \theta) = \frac{\epsilon |\sin \theta|}{N_c q \delta} < 1$  is the condition of existence of ripple-induced magnetic wells (see Sec.2.2.4) and  $\tilde{\delta}(r, \theta) = \frac{\delta(r, \theta)}{\int \frac{d\theta}{2\pi} \delta(r, \theta)}$ . Note that the entropy production rate for the banana drift branch is carrying an upper limit  $u_c$  in the energy integral. The reason is that, over this limit, the trajectories of banana-trapped particles become stochastic such that the nature of transport is not neoclassical anymore. This limit as well as the entropy production rate associated with the stochastic transport are assessed in the next section.

## 2.5. Chaos and transport: the stochastic motion of particles

### 2.5.1. Physical origin

Stochastic transport refers to a collisionless diffusion that can arise in the presence of ripple for some banana-trapped particles. Here is the principle. As detailed in Appendix B, ripple causes a radial jump  $\Delta r$  of the banana-trapped particles at the bounce point locations. This jump is either inward or outward depending on the bounce point position relative to the nearest coil. It can be expressed<sup>4</sup> as

$$\Delta r = \lambda \rho_i \delta \cos(N_c \varphi_B - \pi/4) \quad (2.39)$$

where  $|\lambda| \sim \sqrt{N_c} (q/\epsilon)^{3/2}$  [67] with  $q$  the safety factor,  $\rho_i$  is the ion Larmor radius and  $\varphi_B$  the toroidal angle of bounce points. In most tokamaks, an estimate at the edge is  $\sqrt{\langle \Delta r^2 \rangle_\varphi} \sim 2 - 3 \rho_i$  where  $\langle . \rangle_\varphi$  is the toroidal average. If  $\Delta r > 0$  (outward) in between two coils, then  $\Delta r < 0$  (inward) in the vicinity of the coils. As trapped particles drift toroidally at the precession frequency  $\Omega_D$ , they undergo a different radial shift at each bounce point. After each bounce period  $2\pi/\Omega_B$ , one can define a toroidal phase shift  $\Delta\varphi_B = \varphi_B(t + 2\pi/\Omega_B) - \varphi_B(t)$ . If  $\Delta\varphi_B$  is small with respect to the toroidal angle span separating two coils  $\Delta\varphi_C = 2\pi/N_C$ , the consecutive radial shifts exerted on the particle are expected to be as often inward as outward, resulting in a zero mean radial displacement. However, in the other limit, namely  $N_C \Omega_D \gg \Omega_B$ ,  $\Delta\varphi_B$  becomes comparable to  $\Delta\varphi_C$ . In this scenario, consecutive bounce point positions follow no particular order and stochasticity appears. This mechanism is illustrated in Fig.2.9.

---

4. This form is obtained by taking Eq.(72) and neglecting terms of order  $\sim 1$ .

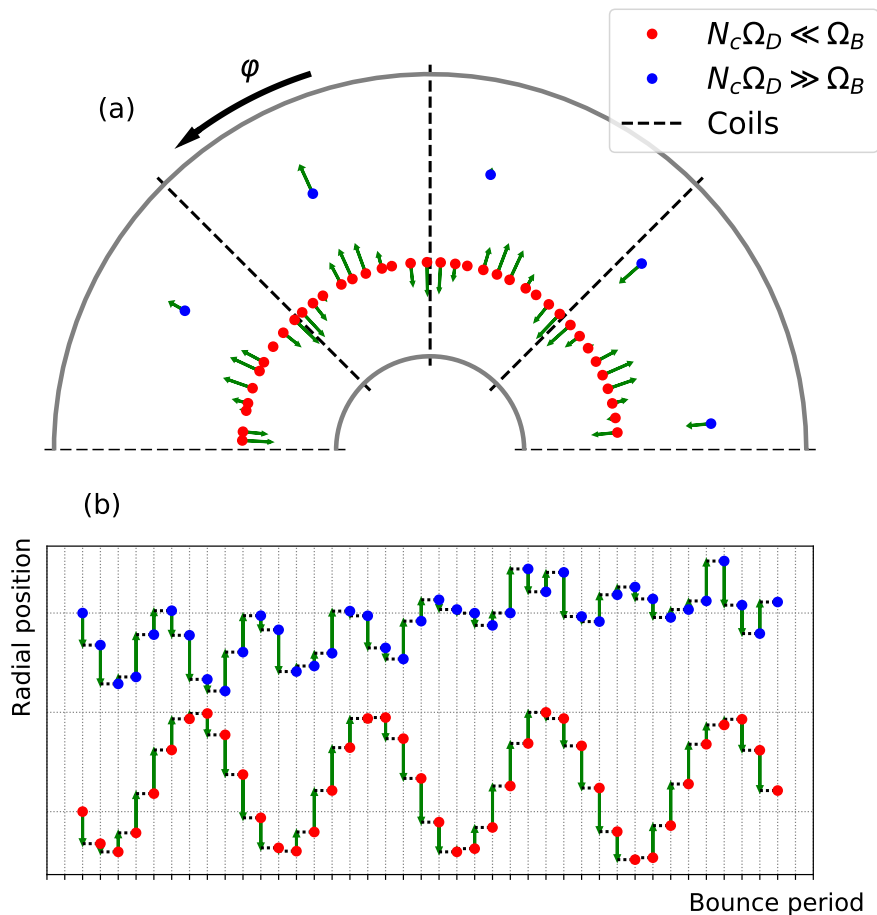


Figure 2.9. – (a) Schematic view in toroidal section of bounce point for trapped particles either below the stochasticity limit (red) or above (blue). The green arrow shows the direction and amplitude of the radial shift  $\Delta r$  exerted on the particle by ripple. (b) Successive radial positions of the bounce point for each case.

Surprisingly, we found little documentation [67–69] on this important channel of transport. In the following sections, we will see under which circumstances the perturbation of the Hamiltonian due to ripple can lead to chaos.

### 2.5.2. Resonance due to magnetic ripple

This section aims at finding a threshold in ripple amplitude above which the trajectory of particles becomes chaotic. The following derivation is heavily inspired from [68].

2. Physics of flows in a 3D magnetic configuration – 2.5. Chaos and transport: the stochastic motion of particles

In a large-aspect ratio (circular-concentric) tokamak, the axisymmetric equilibrium Hamiltonian reads

$$\mathcal{H}_{\text{eq}} = \frac{1}{2} m v_{\parallel}^2 + \mu B_0 [1 - \varepsilon \cos(\theta)] . \quad (2.40)$$

Magnetic ripple adds a perturbation  $\tilde{\mathcal{H}}$  to this Hamiltonian that is written

$$\tilde{\mathcal{H}} = \mu B_0 \delta \cos(N_c \varphi) . \quad (2.41)$$

As discussed in Sec.2.2.4, magnetic ripple adds an infinite number of perturbations such as Eq(2.2) in the angle/action space. Using Eq(2.17), the perturbed Hamiltonian can be written <sup>5</sup>

$$\tilde{\mathcal{H}} = \sum_{n_B=-\infty}^{+\infty} h_{n_B} \cos(\xi_{n_B}) \quad (2.42)$$

with

$$h_{n_B} = \frac{\mu B_0 \delta}{2} J_{n_B}(N_c q \theta_B) \quad (2.43)$$

$$\xi_{n_B} = N_c \varphi_0 + n_B \alpha_B . \quad (2.44)$$

According to the KAM theorem, motion stays integrable as long as the resonant islands linked to each of these single perturbations are "far" from each other. If they are too "close", the motion becomes stochastic. A useful criterion can be used to quantify this transition: the *Chirikov overlap parameter*  $S$ . This parameter is a dimensionless quantity often used to describe the level of chaos in a dynamic system. It is also called the resonance-overlap criterion, as it describes the relative proximity between two unperturbed resonances in the phase space. Above a critical Chirikov parameter, i.e. when the resonances overlap, a deterministic trajectory will travel between the resonances in an unpredictable way. The particle trajectory is considered to be chaotic when  $S \geq 1$ . Let us obtain an expression for this parameter.

For this purpose, we first restrain the analysis to a single  $n_B$  to select one single Hamiltonian perturbation  $\mathcal{H}_{n_B} = h_{n_B} \cos(\xi_{n_B})$ . The resonant surface associated with  $\mathcal{H}_{n_B}$  yields

$$\omega_{n_B} = \frac{d\xi_{n_B}}{dt} = n_B \Omega_B + N_c \Omega_D \quad (2.45)$$

where we recall that  $\Omega_B$  is the banana bounce frequency and  $\Omega_D$  is the precession frequency. As done in Sec.2.2.1, one can write a new invariant

$$\mathcal{H}_{I,n_B} = \frac{C_{n_B} I^2}{2} + h_{n_B} \cos(\xi_{n_B}) \quad (2.46)$$

with

$$C_{n_B} = n_B \left. \frac{\partial \omega_{n_B}}{\partial J_2} \right|_{\mathbf{J}_R} + N_c \left. \frac{\partial \omega_{n_B}}{\partial J_3} \right|_{\mathbf{J}_R} \quad (2.47)$$

---

5.  $J_{n_B}$  is the modified Bessel function of order  $n_B$ .

2. Physics of flows in a 3D magnetic configuration – 2.5. Chaos and transport: the stochastic motion of particles

where we recall that  $J_2$  is the longitudinal invariant and  $J_3$  is the canonical toroidal momentum.

Recalling Eq(2.7), i.e.  $\omega_{n_B} = \frac{d\xi_{n_B}}{dt} = C_{n_B} I$ , it is convenient to manipulate the normalized Hamiltonian  $\mathcal{H}_{\omega, n_B} = C_{n_B} \mathcal{H}_{I, n_B}$  such that

$$\mathcal{H}_{\omega, n_B} = \frac{\omega_{n_B}^2}{2} + (\delta\omega_{n_B})^2 \cos(\xi_{n_B}) \quad (2.48)$$

where  $\delta\omega_{n_B} = \sqrt{C_{n_B} h_{n_B}}$ . Regarding Eq(2.45), for any  $n_B$  the distance between two resonant surfaces reads

$$\Delta\omega = \omega_{n_B+1} - \omega_{n_B} = (n_{B+1}\Omega_B + N_c\Omega_D) - (n_B\Omega_B + N_c\Omega_D) = \Omega_B \quad (2.49)$$

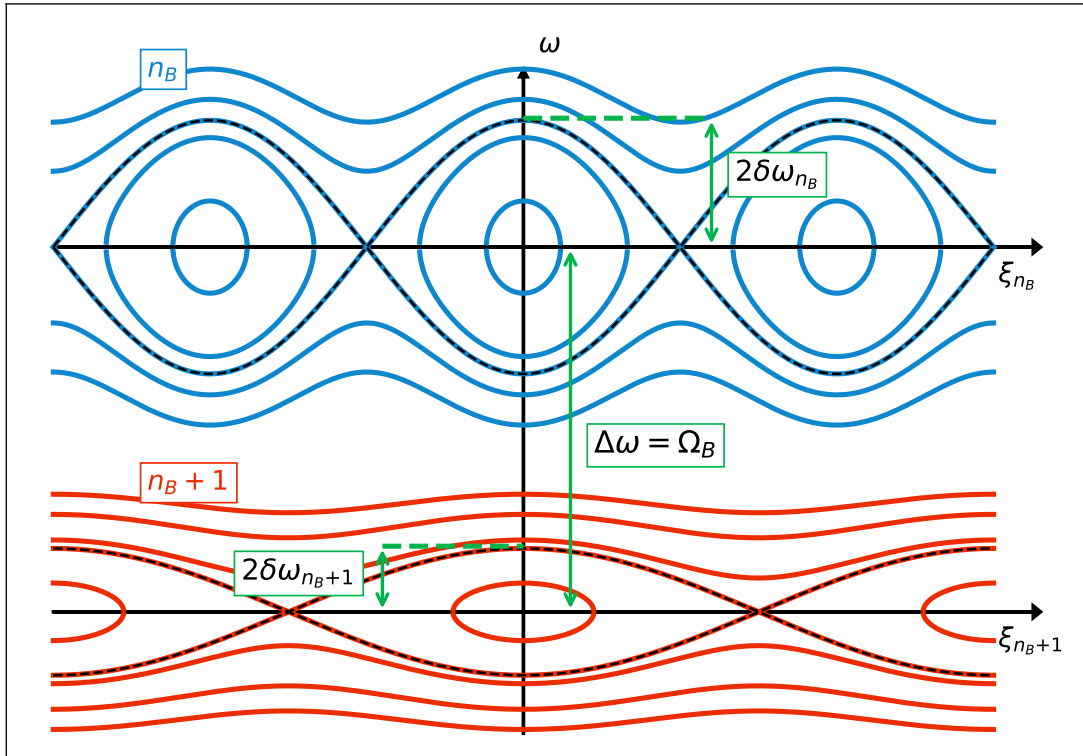


Figure 2.10. – Iso-contour at constant  $\mathcal{H}_{\omega, n_B}$  for 2 distinct  $n_B$  (so for 2 different resonant surfaces).

The sketch in Fig.2.10 can then be drawn, giving more sense to the Chirikov overlap criterion  $S$ : two islands "overlap" when the distance  $\Delta\omega$  between the islands is inferior to the sum of their respective half-width  $2\delta\omega_{n_B}$  (taken at the separatrix). The Chirikov parameter is then expressed as

$$S = 2 \frac{\delta\omega_{n_B} + \delta\omega_{n_B+1}}{\Delta\omega} . \quad (2.50)$$

2. Physics of flows in a 3D magnetic configuration – 2.5. Chaos and transport: the stochastic motion of particles

However, with ripple, things in fact are a bit more complicated. Trouble arises when accounting for the  $\theta_B$  dependence in  $h_{n_B}$ . Indeed, one has to deal with the Bessel function  $J_{n_B}(N_c q \theta_B)$  that appears in the perturbation amplitude  $h_{n_B}$  Eq(2.43). This is important because it is possible to relate  $\theta_B$  to  $\omega_{n_B}$ . To do this, a Taylor expansion is done on the bounce angle such that  $\theta_B(\mathbf{J}) = \theta_B(\mathbf{J}_R) + C'_{n_B} I$  where

$$C'_{n_B} = n_B \left. \frac{\partial \theta_B}{\partial J_2} \right|_{\mathbf{J}_R} + N_c \left. \frac{\partial \theta_B}{\partial J_3} \right|_{\mathbf{J}_R}. \quad (2.51)$$

The Bessel function can then be recast as  $J_{n_B}(N_c q \theta_B) = J_{n_B}(N_c q (\theta_B(\mathbf{J}_R) + C'_{n_B} I))$ . As  $\omega_{n_B} = C_{n_B} I$ , the Hamiltonian then reads

$$\mathcal{H}_{\omega, n_B} = \frac{\omega_{n_B}^2}{2} + C_{n_B} \frac{\mu B_0 \delta}{2} J_{n_B}(N_c q \theta_B(\mathbf{J}_R) + \tau_{n_B} \omega_{n_B}) \cos(\xi_{n_B}) \quad (2.52)$$

where  $\tau_{n_B} = N_c q C'_{n_B} / C_{n_B}$  is a characteristic time that describes the dependence of the perturbed Hamiltonian with the action  $I$ , or equivalently with the frequency  $\omega_{n_B}$ . It is also important to note that in most cases the offset due to  $N_c q \theta_B(\mathbf{J}_R)$  in the Bessel function is not negligible, as in most tokamaks the product  $N_c q$  is high (in general  $N_c > 15$  and  $q > 2$ ). It can be understood in Fig.2.11, which displays the iso-contour of the perturbed Hamiltonian defined in Eq(2.52) for different values of  $n_B$  and  $\tau_{n_B}$ . If  $\tau_{n_B} \rightarrow 0$ , the Bessel function then tends toward a finite value, which would not have been the case for  $n_B \neq 0$  without the offset<sup>6</sup>. In this limit, the classical cat's eye shape of  $\mathcal{H}_{\omega, n_B}$  iso-contour is retrieved for each  $n_B$ . If  $\tau_{n_B}$  is finite though, structures a bit more complex than typical islands appear. Indeed, increasing enough  $\tau_{n_B}$  results in iso- $\mathcal{H}_{\omega, n_B}$  structures with multiple separatrices.

It then appears that two asymptotic regimes of transport emerge and depend on the value of the characteristic time  $\tau_{n_B}$ :

- The **weak perturbation regime** where a single separatrix exists;
- The **strong perturbation regime** where multiple separatrices exist.

The next step is then to obtain a practical expression for the Chirikov overlap parameters and diffusion coefficients associated with each of these regimes.

---

6. Indeed,  $\lim_{x \rightarrow 0} J_{n_B}(x) = 0$  for all  $n_B$  except  $n_B = 0$ .

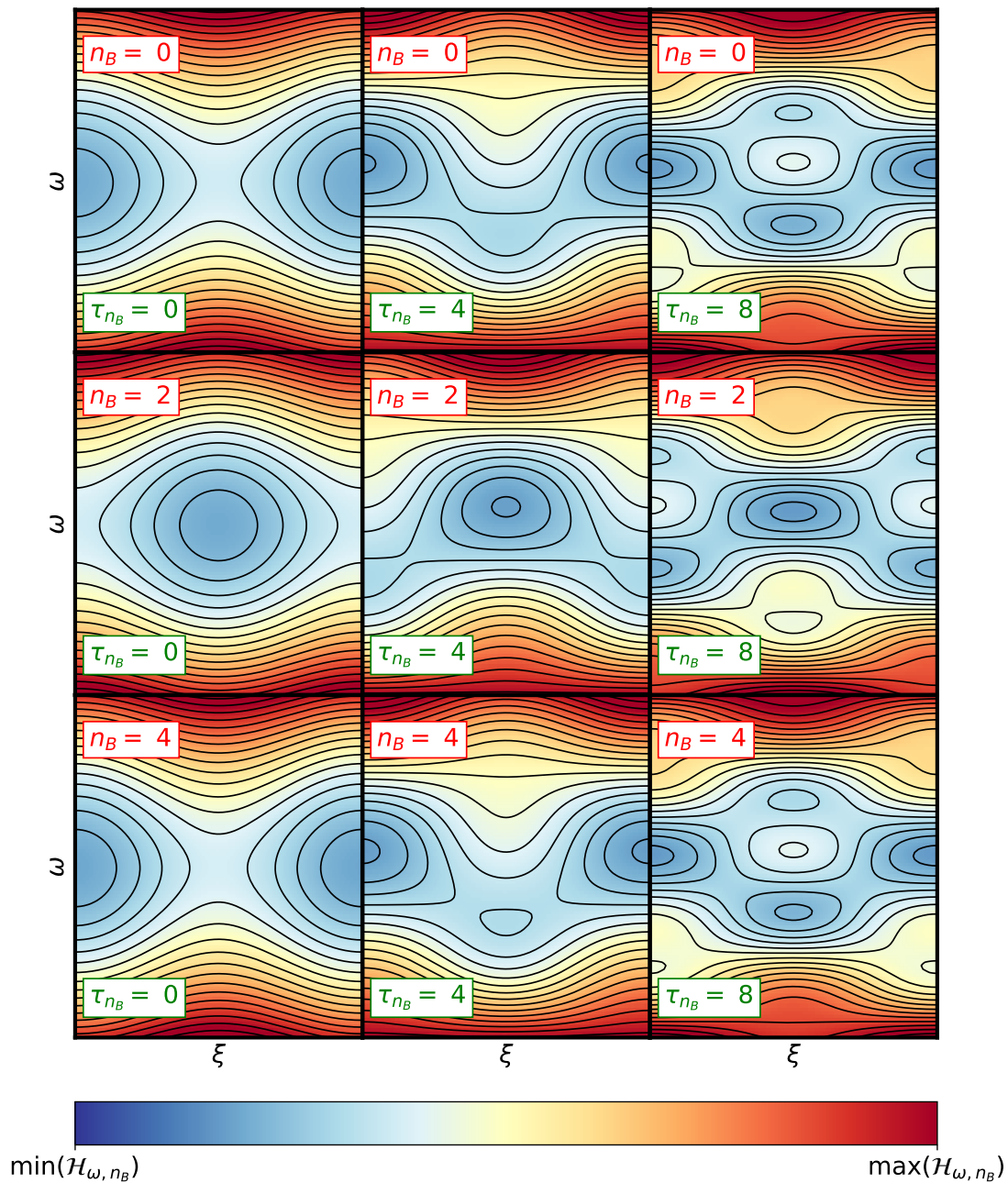


Figure 2.11. – Iso-contour at constant  $\mathcal{H}_{\omega, n_B}$  (with the Bessel function dependence) for different  $n_B$  and  $\tau_{n_B}$  with  $N_c = 18$ ,  $q = 3$  and  $\theta_B(\mathbf{J}_R) = \pi/2$ . Units are arbitrarily chosen.

### 2.5.3. Chirikov overlap criteria and diffusion coefficients

The detail of the derivation to obtain the Chirikov overlap parameters and diffusion coefficients of each regime is detailed in Appendix C.

Introducing the weak perturbation regime Chirikov overlap criterion  $S_{\text{weak}}$ , which is



2. Physics of flows in a 3D magnetic configuration – 2.5. Chaos and transport: the stochastic motion of particles

the lower limit for chaos to arise, it reads (Eq.(83))

$$S_{\text{weak}} = 2\sqrt{\frac{2}{\pi\theta_B} s^{1/2} \frac{q\rho_i}{R_0} \frac{\delta^{1/2}}{\varepsilon^2} u^{1/2}} \quad (2.53)$$

where  $u = v_{\perp}^2 / V_{\text{th}}^2$ ,  $s = \frac{r}{q} \frac{dq}{dr}$  is the magnetic shear and  $\rho_i$  is the Larmor radius.

This criterion makes it possible to estimate the critical normalized energy  $u_c$  for which the trajectories become stochastic (this is the upper limit of the energy integral in Eq(2.34) calculated within the neoclassical theory). It reads

$$u_c = \frac{\pi}{8} \frac{1}{s} \left( \frac{R_0}{q\rho_i} \right)^2 \frac{\varepsilon^4}{\delta} . \quad (2.54)$$

This threshold is commonly associated with energetic particles, as the r.h.s. of Eq(2.54) is large in most tokamak discharges. In particular, the ratio  $\frac{\varepsilon^4}{\delta}$  is really high in most of tokamaks for typical ripple amplitudes. This is why "ripple losses" of particles are usually attributed to fast particles.

The particle diffusion coefficient  $D_{\text{weak}}$  in this regime is the quasilinear coefficient  $D_{\text{QL}}$ . After some algebra, detailed in Appendix C, it yields the following expression (Eq.(91))

$$D_{\text{weak}} = D_{\text{QL}} = \frac{1}{8\theta_B} N_c q u^{3/2} D_P \frac{\delta^2}{\varepsilon^{5/2}} \quad (2.55)$$

with  $D_P = \frac{qR_0}{V_{\text{th}}} \left( \frac{T}{eB_0R_0} \right)^2$ .

The Chirikov criterion  $S_{\text{strong}}$  in the strong perturbation regime reads (Eq.(86))

$$S_{\text{strong}} \approx \frac{1}{2} \sqrt{\frac{2\theta_B}{\pi}} s (N_c q)^{3/2} \frac{\delta}{\varepsilon^{5/2}} \frac{q\rho_i}{R_0} u^{1/2} . \quad (2.56)$$

In this regime, as the resonance shape is more complex than the classical cat-eye, the quasi-linear expression for the diffusion coefficient is not valid. A solution is to add a correction to  $D_{\text{QL}}$  with a form factor  $\Xi$ . The idea is here to fit the diffusion coefficient to the one obtained by Goldston [67] which is based on a random walk argument on the radial shift of particles in the banana bounce point vicinity due to ripple. This diffusion coefficient is actually the one in the strong perturbation regime. This gives the form factor  $\Xi = 2/S_{\text{strong}}$ . The resulting diffusion coefficient in the strong perturbation regime  $D_{\text{strong}}$  then reads

$$D_{\text{strong}} = \Xi D_{\text{QL}} \quad (2.57)$$

With these diffusion coefficients, it is then possible to obtain an expression for the entropy production rate  $\dot{S}_{\text{st}}$  associated with the stochastic transport.

The following expression is found

2. Physics of flows in a 3D magnetic configuration – 2.6. An analytical model to predict flows in presence of magnetic ripple

$$\begin{aligned} \dot{S}_{\text{st}} = & \frac{1}{2} \sqrt{\frac{\pi}{2}} \int dV n D_P N_c q \left( \frac{\delta}{\varepsilon} \right)^2 \\ & \int_{u_c}^{+\infty} du e^{-u} u^2 K_{\text{st}}(r, u) \left[ \frac{1}{N} \frac{dN}{dr} + \left( u - \frac{3}{2} \right) \frac{1}{T} \frac{dT}{dr} \right]^2 \end{aligned} \quad (2.58)$$

with  $K_{\text{st}}(r, u) = \min(1, S_{\text{strong}}(r, u))$ .

This entropy production rate, when added to the ones obtained considering neoclassical processes (Eq(2.31-2.34)), gives the last ingredient to obtain the transport matrix that gives the link between fluxes and forces. We should mention that, actually, this stochastic regime of transport is subdominant for the studies of the next chapters with gyrokinetic simulations. The reason is that the velocity threshold for a trajectory to become stochastic is quite high and we do not consider fast particle population throughout this thesis. However, there was no real way to predict this without actually deriving this threshold and hopefully, this will be helpful for future studies accounting for fast particles.

## 2.6. An analytical model to predict flows in presence of magnetic ripple

### 2.6.1. Explicit form of the reduced model

Using the two previous sections (Sec.2.4 & 2.5), it is now possible to construct a reduced model taking into account both neoclassical and stochastic physics to get the resulting flows without turbulence. The total resonant entropy production rate can now be calculated using Eq(2.31), Eq(2.32), Eq(2.33), Eq(2.34) and Eq(2.58). It leads to a transport matrix that links the equilibrium fluxes of particles  $\Gamma$  and heat  $Q$  as well as the magnetic drag force  $\mathcal{M}$ , with the thermodynamic gradient forces, the mean toroidal velocity  $V_T$  and the radial electric field  $E_r$ . For a single ion species, it can be expressed in a compact way:

$$\begin{pmatrix} \Gamma_N \\ \Gamma_{V_T} \\ \Gamma_T \end{pmatrix} = -D_P \begin{pmatrix} d_0 + \tilde{d}_0 & d_0 & d_1 + \tilde{d}_1 \\ d_0 & d_0 + \hat{d}_0 & d_1 \\ d_1 + \tilde{d}_1 & d_1 & d_2 + \tilde{d}_2 \end{pmatrix} \cdot \begin{pmatrix} A_N \\ A_{V_T} \\ A_T \end{pmatrix} \quad (2.59)$$

where  $\Gamma_N = \frac{\Gamma}{n}$ ,  $\Gamma_{V_T} = \frac{\mathcal{M}}{neB_p}$ ,  $\Gamma_T = \frac{Q}{nT}$ ,  $A_N = \frac{1}{n} \frac{dn}{dr} - \frac{eE_r}{T}$ ,  $A_{V_T} = \frac{eB_p}{T} V_T$ ,  $A_T = \frac{1}{T} \frac{dT}{dr}$  with  $n$  the density,  $T$  the temperature,  $e$  the electric charge and  $B_p$  the poloidal component of the magnetic field. We also recall that  $D_P = \frac{qR_0}{V_{\text{th}}} \left( \frac{T}{eB_0R_0} \right)^2$  is a reference diffusion coefficient.

The transport matrix coefficients are detailed in Appendix D. They only depend on three dimensionless parameters:  $v^*$ ,  $\delta/\varepsilon$  and  $N_c q$ . The coefficients  $d_i$  are independent of  $\delta/\varepsilon$ . Without ripple,  $\tilde{d}_i = 0$  and  $\hat{d}_i = 0$ , such that one recovers the classic

2. Physics of flows in a 3D magnetic configuration – 2.6. An analytical model to predict flows in presence of magnetic ripple

coefficients resulting from the axisymmetric neoclassical theory at lower order in  $\varepsilon$ . In that case, it is clear that the two first lines of the transport matrix are identical. This degeneracy explains why axisymmetric neoclassical theory cannot predict  $A_N$  and  $A_{V_T}$  independently, and hence treats a combination of the radial electric field and the toroidal velocity as a single unknown.

### 2.6.2. Assessing the equilibrium flows with the model

This model is now used to predict meaningful quantities relevant to the plasma flow and is compared with common asymptotic regimes. Let us first define these "meaningful quantities". First, there are thermal drive coefficients that link the equilibrium toroidal velocity  $V_{T,\text{eq}}$ , poloidal velocity  $V_{P,\text{eq}}$  and the radial electric field  $E_{r,\text{eq}}$  to the temperature gradient, labelled  $k_{V_T}$ ,  $k_N$  and  $k_{V_P}$  respectively. The thermal drive coefficient expressions are obtained when considering that both  $\Gamma_N$  and  $\Gamma_{V_T}$  go to zero at equilibrium (without external sources of particles and momentum).

Under these conditions, Eq(2.59) gives the equalities

$$k_{V_T} \frac{\nabla T_{\text{eq}}}{eB_P} = V_{T,\text{eq}} \quad (2.60)$$

$$k_{V_P} \frac{\nabla T_{\text{eq}}}{eB_T} = V_{P,\text{eq}} \quad (2.61)$$

$$k_N \frac{\nabla T_{\text{eq}}}{T_{\text{eq}}} = \frac{eE_{r,\text{eq}}}{T_{\text{eq}}} - \frac{\nabla n_{\text{eq}}}{n_{\text{eq}}} \quad (2.62)$$

where the "eq" subscript denotes values taken at equilibrium and  $B_T, B_P$  are the toroidal and poloidal components of the magnetic field  $\mathbf{B}$ .

These equations can also be written in a dimensionless form:

$$A_{V_T} = k_{V_T} A_T \quad (2.63)$$

$$A_{V_P} = k_{V_P} A_T \quad (2.64)$$

$$A_N = -k_N A_T \quad (2.65)$$

The explicit expressions of the thermal drives when these two fluxes vanish are

$$k_{V_T} = \frac{d_0 \tilde{d}_1 - d_1 \tilde{d}_0}{(d_0 + \tilde{d}_0)(d_0 + \hat{d}_0) - d_0^2} \quad (2.66)$$

$$k_N = \frac{(d_0 + \hat{d}_0)(d_1 + \tilde{d}_1) - d_0 d_1}{(d_0 + \tilde{d}_0)(d_0 + \hat{d}_0) - d_0^2} \quad (2.67)$$

$$k_{V_P} = 1 + k_{V_T} - k_N \quad (2.68)$$

where the thermal drive  $k_{V_P}$  has been obtained with the force balance equation  $A_{V_P} = \frac{eB_T}{T} V_P = A_N + A_{V_T} + A_T$ . Knowing those thermal drive coefficients as well as the temperature gradient, one can make predictions on the final flow.

2. Physics of flows in a 3D magnetic configuration – 2.6. An analytical model to predict flows in presence of magnetic ripple

These coefficients have a fixed value in some asymptotic regimes of collisionality and ripple amplitude. These regimes depend among others on the trapping parameter  $Y(r, \theta) = \frac{\varepsilon |\sin \theta|}{\delta N_c q}$  introduced in Sec.2.2.4 Regions with  $Y < 1$  are characterized by local magnetic wells in between two toroidal field coils. Conversely, for  $Y > 1$ , such magnetic wells do not exist so there is no ripple-induced trapping in those regions.

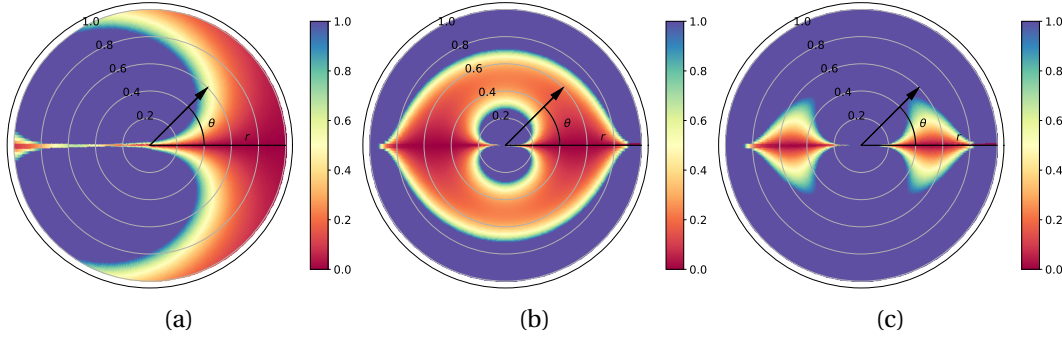


Figure 2.12. – Condition of existence of ripple-induced magnetic wells in the Tore Supra tokamak (a) a radially gaussian ripple (see next Chapter for the reasons to consider such a shape) centered at mid-radius and poloidally symmetric with a  $\delta = 3\%$  peak (b) and a  $\delta = 0.5\%$  peak (c). There are no magnetic wells in  $Y > 1$  areas (blue) so no local trapping can occur.

This subtle point is worth discussing as predictions are significantly different between regions with or without ripple-induced magnetic wells. It indicates that a poloidal dependence must be taken into account. Indeed, one could construct an academic case in which  $\delta$  has no poloidal dependency but then  $Y$  does (as displayed in Fig.2.12a and Fig.2.12b), and inversely one could impose a poloidally symmetric  $Y$  but then  $\delta$  would be proportional to  $|\sin(\theta)|$ . Still, for numerical convenience explained below, the considered ripple perturbation for this academic work is poloidally symmetric. Fig.2.12 displays the poloidal map of  $Y$  for the Tore Supra tokamak and for radially gaussian ripple  $\delta(r)$  profiles centered at mid-radius such that  $\delta(r) = \delta_0 e^{-32(r/a-0.5)^2}$  with  $\delta_0$  the mid-radius ripple amplitude. This latter unrealistic shape of ripple amplitude is useful for numerical simulations as detailed in next Chapter. That said, the asymptotic regimes of  $k_{V_T}$ ,  $k_N$  and  $k_{V_P}$  are summarized in Tab.2.1.

	$Y > 1$		$Y < 1$ (Local mirrors)		$\forall Y$
	$\forall \delta/\varepsilon$		$\delta/\varepsilon < 1$	$\delta/\varepsilon > 1$	$\forall \delta/\varepsilon$
	$v^* \ll (N_c q)^{-2}$	$(N_c q)^{-2} \ll v^* \ll 1$	$v^* < (\delta/\varepsilon)^{3/2}$	$v^* < 1$	$v^* \gg 1$
$k_N$	3.37	1.5	3.37	3.37	1.5
$k_{V_P}$	1.17	1.17	1.17	-2.37	-0.5
$k_{V_T}$	3.54	1.67	3.54	0.0	0.0

Table 2.1. – Asymptotic values of  $k_{V_T}$ ,  $k_N$  and  $k_{V_P}$  for different ranges of  $\delta/\varepsilon$ ,  $v^*$  and  $N_c q$ .

## 2. Physics of flows in a 3D magnetic configuration – 2.6. An analytical model to predict flows in presence of magnetic ripple

In this table, one can observe that thermal drive coefficients change substantially depending on collisionality regimes. For example,  $k_{V_T}$  can double in regions without magnetic wells under the sole effect of collisionality. It means that for a given temperature gradient, the toroidal velocity can change drastically when the collisionality evolves (due to heating for example). Similar effects can be observed for  $k_N$  and  $k_{V_p}$ . However, this table can easily be misleading for several reasons. First, the model is poloidally averaged so the resulting thermal drive can be a mix between their predictions in  $Y > 1$  regions and  $Y < 1$  regions. Then, those asymptotic regimes hide that those thermal drives actually depend non-linearly on  $\delta/\varepsilon$  and  $v^*$ .

Although less accurate than simulation codes, the reduced model has the advantage over simulation codes to provide transport coefficients effortlessly. In other words, it can be used to perform scans on wide ranges of  $\delta/\varepsilon$ ,  $v^*$  and  $N_c q$ . Now and for the remaining of this section, a fixed  $N_c q = 16 \times 1.4$  is considered. The thermal drive coefficients  $k_{V_T}$ ,  $k_N$  or  $k_{V_p}$  are scanned for the ranges of  $\delta/\varepsilon$  and  $v^*$  as shown in Fig.2.13.

2. Physics of flows in a 3D magnetic configuration – 2.6. An analytical model to predict flows in presence of magnetic ripple

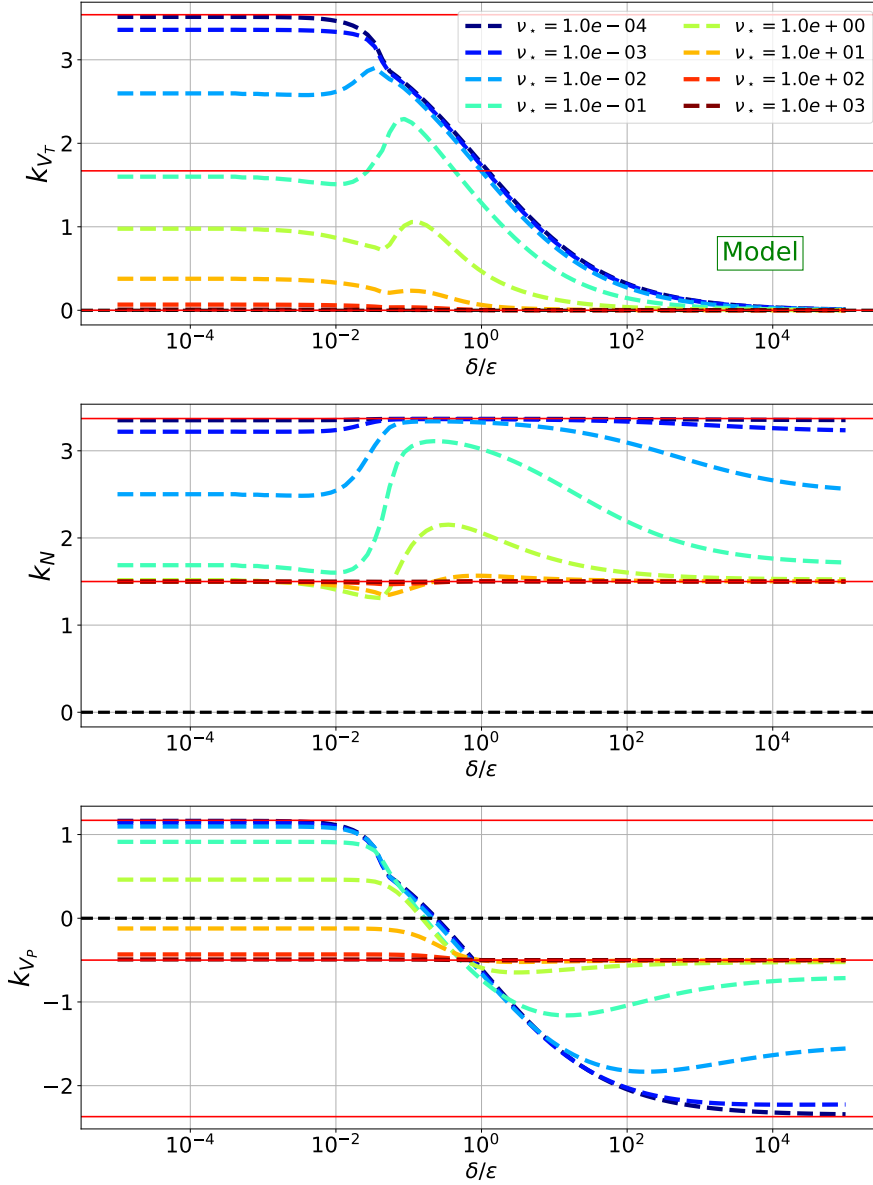


Figure 2.13. – Scan in ripple amplitude of thermal drives  $k_{VT}$ ,  $k_N$  and  $k_{VP}$  for a wide range of  $\nu^*$ . Red plain lines represent the asymptotic values that appear in Tab.2.1.

All asymptotic regimes are recovered. It should be mentioned however that the *Pfirsch–Schlüter* regime, expected to play a role for  $\nu^* \gg 10$ , is not included in the model and is expected to change  $k_{VP}$  towards even more negative values [70] (indeed the prediction in axisymmetric configuration is  $k_{VP} \rightarrow -2.1$ ). The transitions between the different regimes are mainly due to the  $(\delta/\epsilon)^{-1}$  dependence of  $Y$ . Indeed, as  $(\delta/\epsilon)$  increases, the size of the regions where ripple-induced magnetic wells exist also increases. In the range of the  $(\delta/\epsilon)$  parameter where the  $Y < 1$  regions become dominant compared with  $Y > 1$  regions, important variations of  $k_{VT}$ ,  $k_N$  and  $k_{VP}$  are

2. Physics of flows in a 3D magnetic configuration – 2.6. An analytical model to predict flows in presence of magnetic ripple

observed. In particular,  $k_{V_p}$  decreases toward negative values with increasing ripple amplitude. It means that the poloidal velocity changes sign when increasing the ripple amplitude. A physical explanation could be the following. At high ripple amplitude and low collisionality, particles are locally trapped and undergo the vertical drift due to the  $1/R$  magnetic decay. These toroidally trapped particles do not carry any toroidal velocity so  $k_{V_T} = 0$ . The vertical drift account for non-ambipolar diffusion resulting in a finite electric field such that  $k_N = 3.37$ . The poloidal velocity drive has to adapt to fulfill the force balance equation, and is then negative.

### 2.6.3. Assessing the dynamics of the flows with the model

Another interesting quantity can be defined: the neoclassical toroidal friction  $v_\varphi$ . It corresponds to the characteristic damping rate – set by ripple-induced neoclassical processes – of the toroidal flow toward its predicted equilibrium value (governed by  $k_{V_T}$ ). The idea is that, if the toroidal momentum conservation is dominated by the magnetic braking  $\mathcal{M}$  force, then

$$nm \frac{\partial V_T}{\partial t} = \mathcal{M} \quad (2.69)$$

or equivalently

$$\Gamma_{V_T} = \frac{m}{eB_p} \frac{\partial V_T}{\partial t} . \quad (2.70)$$

Developing the two first lines of Eq(2.59) yields

$$\Gamma_{V_T} = -D_P (-d_0 A_N + \hat{d}_0 A_{V_T} - \tilde{d}_1 A_T) + \Gamma_N . \quad (2.71)$$

The neoclassical toroidal friction  $v_\varphi$  is the coefficient that multiplies  $A_{V_T}$ . Its expression significantly changes depending on the assumptions taken on the fluxes. Indeed, if one considers that neither the particle flux nor the momentum flux vanishes in this out-of-equilibrium situation, i.e.  $\Gamma_N \neq 0$  and  $\Gamma_{V_T} \neq 0$ , the neoclassical friction then simply reads

$$v_\varphi = \hat{d}_0 . \quad (2.72)$$

However, keeping the zero particle flux constraint  $\Gamma_N = 0$  but with a finite momentum flux, i.e.  $\Gamma_{V_T} \neq 0$ , Eq(2.59) gives

$$\Gamma_{V_T} = -D_P v_\varphi^{\Gamma_N=0} (A_{V_T} - k_{V_T} A_T) \quad (2.73)$$

where the thermal drive  $k_{V_T}$  is same as derived in Eq(2.66). The neoclassical friction  $v_\varphi^{\Gamma_N=0}$  in this case then reads

$$v_\varphi^{\Gamma_N=0} = \hat{d}_0 + \frac{d_0 \tilde{d}_0}{d_0 + \tilde{d}_0} . \quad (2.74)$$

Notice that, since  $\hat{d}_0$  and  $\tilde{d}_0$  go to zero when  $\delta/\varepsilon \rightarrow 0$ , the neoclassical friction always

(i.e. regardless of the assumption on the fluxes) vanishes in the axisymmetric case as a consequence of the well known neoclassical degeneracy: without ripple, the toroidal velocity cannot be separated from  $E_r$ . Furthermore,  $\hat{d}_0$  and  $\tilde{d}_0$  increase with  $\delta/\varepsilon$  so that the system relaxes faster with higher ripple amplitude, as one would expect on the basis of qualitative physical arguments.

In Sec.3.3.4, the neoclassical friction is assessed with the GYSELA code. References on this neoclassical friction addressing the impact of externally applied magnetic perturbations can be found in [71–74]. However, none of the references known to the author clearly addresses this neoclassical toroidal friction due to magnetic ripple in tokamaks, neither through analytical study nor numerical simulations.

This reduced model that gives predictions on flows without turbulence is assessed in GYSELA simulations in Chapter 4. The next section is meant to describe qualitatively the turbulence in fusion plasmas.

## 2.7. Turbulence: a short introduction

Turbulence is a rich and complex phenomenon that is still not fully understood. It describes a chaotic state that appears above an instability threshold, depending on thermodynamical gradients, where several modes are destabilized and are non-linearly coupled. The resulting turbulent flow exhibits a large number of degrees of freedom<sup>7</sup> and, as such, is difficult to assess with a predictive theory. Turbulence manifests as swirly flows, with mixing eddies covering a wide range of spatiotemporal scales. In magnetized plasmas, the underlying mechanisms of turbulence are not the same as in neutral fluids. One of the main differences is the presence of a fluctuating electromagnetic field, which is required to be consistent with the density and current fluctuations. The resulting physics includes, inter-alia, particle-wave resonant interactions, mode-coupling, and stochasticity of the magnetic field, which are not present in neutral fluid turbulence. Also, in hydrodynamics, the dissipation of kinetic energy into heat occurs at small scales while the excitation sets at large scales. In between, the "free" spectral region is said to be "inertial". In plasmas, the collisionless dissipation comes from the Landau resonances over a broad range of scales and the excitation comes from instabilities that develop at all scales such that there is no true inertial region. A typical wavenumber spectrum in a tokamak discharge, here in Tore Supra, is displayed in Fig.2.14 and shows the broad range of scales involved as well as excitation and dissipative regions.

---

7. In hydrodynamics, this number of degrees of freedom is evaluated with the Reynolds number which is defined as the ratio between the non-linear advection to the viscous dissipation. In plasmas, other dimensionless numbers relevant to turbulence also play a role.



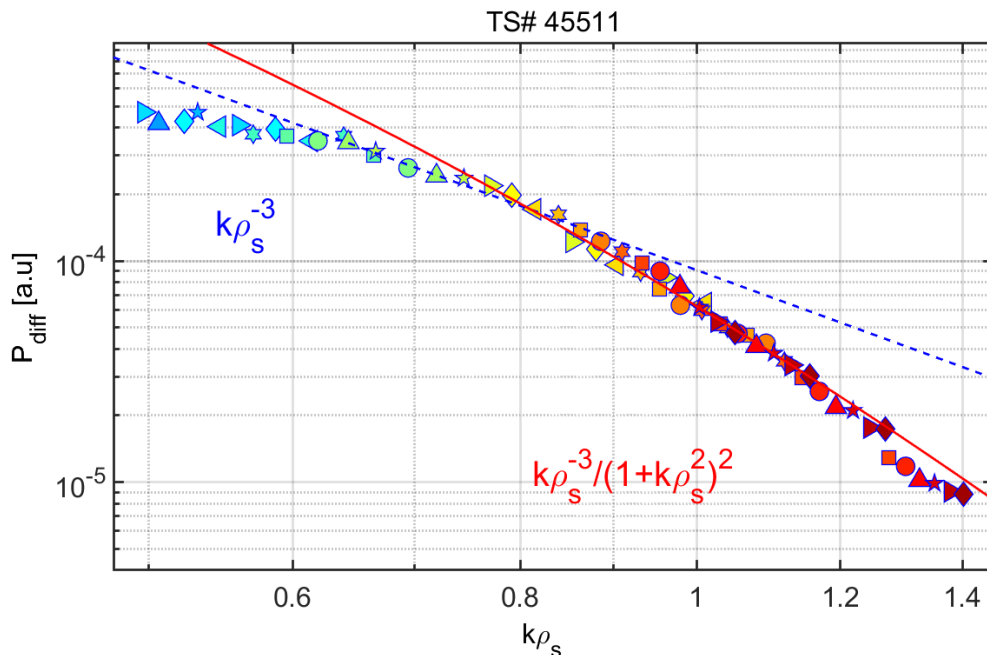


Figure 2.14. – Wavenumber spectrum of density fluctuations in the #45511 discharge of the Tore Supra tokamak. The region with a  $k^{-3}$  scaling is the region of energy injection, and the region with a  $k^{-3}/(1+k^2)^2$  scaling is the energy transfer region. Extracted from [75].

So why is the turbulence of interest for fusion? Historically, in the '80-90s, one realized that the observed heat diffusion measured in experiments was in fact way higher than what was predicted with neoclassical theory. This discrepancy was called *anomalous transport*, which is now understood to originate from turbulence<sup>8</sup>. It is then of prime importance to understand this mechanism in order to possibly reduce the resulting transport. A visual representation of turbulence in magnetized plasma is displayed in Fig.2.15, where one can see turbulent structures through a colormap on the electric potential fluctuations  $\tilde{\phi}$ .

8. Note that "anomalous" now designates non-diffusive flows.

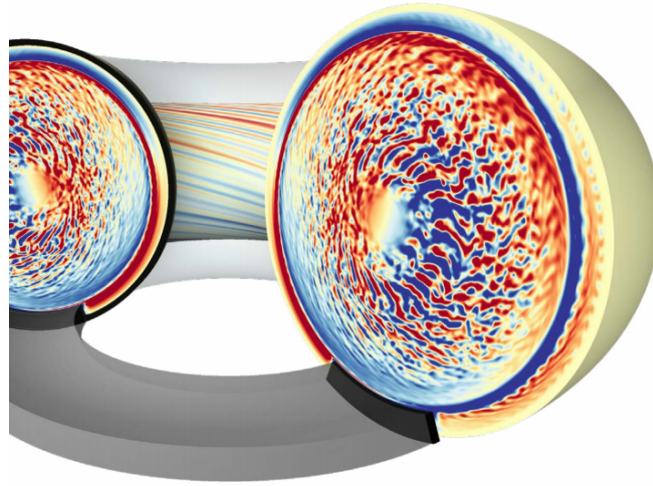


Figure 2.15. – Fluctuation of the electric potential  $\tilde{\phi}$  seen through a colormap in the whole tokamak, simulated with the GYSELA code [76].

These mixing eddies are bound to induce radial transport of heat and particles. Indeed, in the direction perpendicular to the magnetic field lines, the particles undergo the effect of turbulence through the perturbed electric drift velocity  $\tilde{v}_{ExB} = \frac{\mathbf{B} \times \nabla \tilde{\phi}}{B^2}$ . With this expression, it is clear that iso-contours of  $\tilde{\phi}$  are also the particle trajectory projected on the plane perpendicular to the direction of  $\mathbf{B}$ , as illustrated in Fig.2.16.

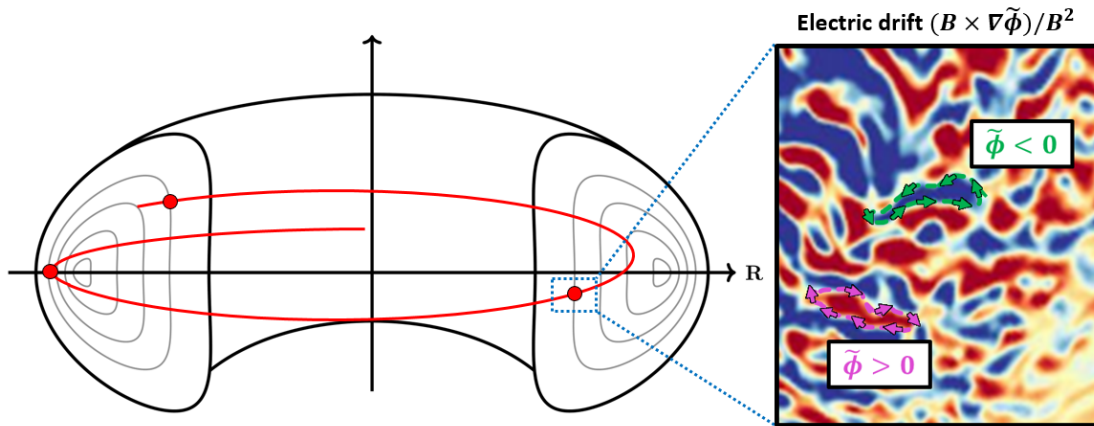


Figure 2.16. – Sketch of turbulence impact on the fluctuating part of the electric drift in a poloidal section (magnetic drift is neglected here). This drift adds to the parallel motion of the guiding center represented in red.

These structures are elongated in the toroidal direction due to the fast parallel transit of particles. As the main interest is transport, we will focus on turbulent radial motion of particles. In that projection, the spatial scale of the main turbulent structure responsible for transport is of the order of the ion Larmor radius  $l_c \sim \rho_i \sim 1\text{ mm}$  and the correlation time is about  $\tau_c \sim R/v_{\parallel} \sim 10\mu\text{s}$ .

## 2. Physics of flows in a 3D magnetic configuration – 2.7. Turbulence: a short introduction

In this thesis, the instability of interest is the "interchange-like instability" driven by the main ion temperature gradient. The resulting turbulence is called "Ion Temperature Gradient (ITG) driven turbulence". The interchange instability principle is illustrated in Fig.2.17. The idea is the following. Let us assume that a perturbation causes the emergence of vertically aligned charged structures near the equatorial plane, represented as red and blue circles in the figure for positive and negative charges respectively. The electric field resulting from these convective cells causes a horizontal electric drift directed left - resp. right - when considering the up-down dipole with the negative cell on top - resp. below. The advected quantity, i.e. particles or heat (particles on the figure), also undergoes the vertical magnetic drift  $\mathbf{v}_D = \frac{mv_{\parallel}^2 + \mu B}{eB} \frac{\mathbf{B} \times \nabla B}{B^2}$  which depends on the particle charge. The advection coming from the right then tends to neutralize the cell while the one from the left tends to amplify the total charge of the cell. The instability happens when the total advection benefits more to the amplification than the neutralization. This happens when the density (i.e. number of particles) or temperature is higher on the left of the cells than on the right. In other words, this occurs when the pressure gradient is aligned with the gradient of magnetic field modulus. In tokamaks, the high-field side is then locally stable regarding the interchange instability, while the low-field side is unstable. Due to the helicity of the magnetic field lines, particles explore both these regions. Thus the plasma parallel current, which carries electric charges between stable and unstable regions, has a stabilizing effect. This will be developed further in Chapter 5.

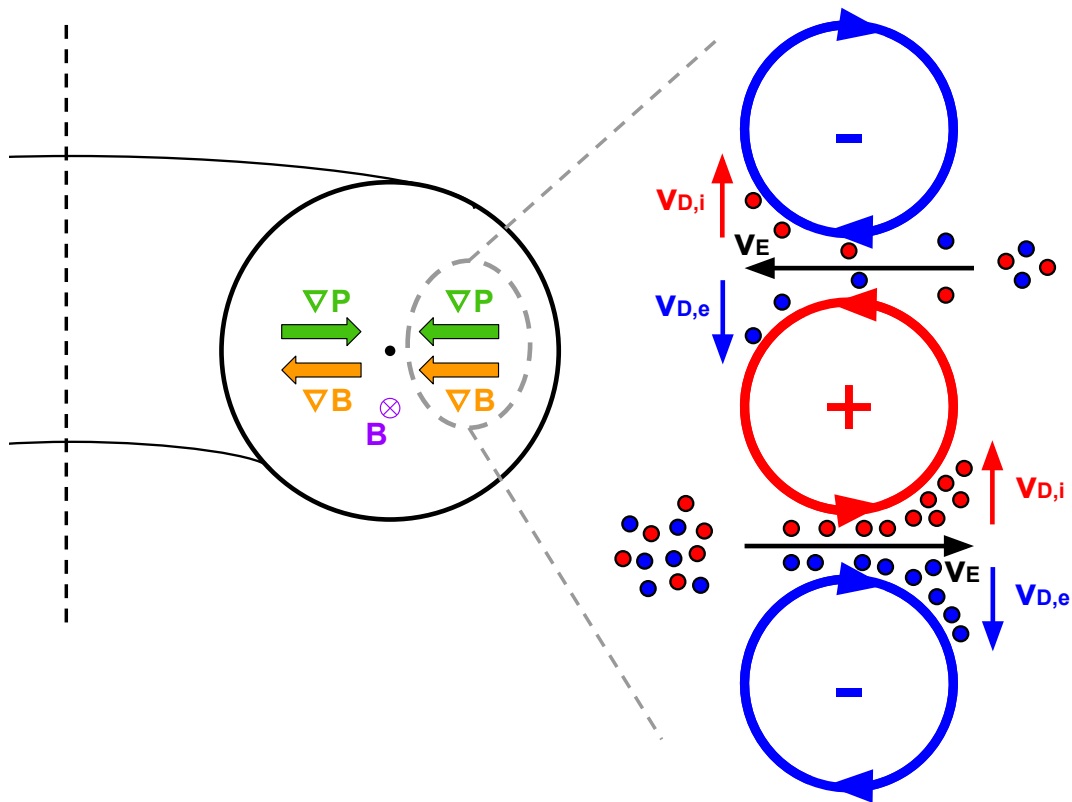


Figure 2.17. – Illustration of the interchange instability. A positive (negative) convective cell tends to become even more positive (negative) when the magnetic field gradient and the pressure gradient are aligned, thus causing an instability on the electric field.

## 2.8. Conclusion of chapter 2

In this Chapter, intrinsic channels of transport in a non-axisymmetric system have been introduced. To model this disparity from axisymmetry, the magnetic ripple is considered. The effect of the static perturbations of the magnetic field on the trajectory of particles is described: the  $1/R$  magnetic decay is responsible for the banana trapping and the magnetic ripple for the local trapping between two consecutive toroidal coils. The transport is assessed using a variational principle that separates the channel into two categories: the neoclassical (collisional) processes and the stochastic (collisionless) particle motion. When the precession frequency is negligible with respect to the banana bounce frequency, neoclassical physics is well described. The magnetic ripple breaks the degeneracy of axisymmetric system where neoclassical theory cannot predict the radial electric field and the toroidal velocity separately.

In presence of this perturbation, four branches of neoclassical transport exist. The two 'primary' ones refer to the random walk of the orbit width of the banana and the locally trapped particles. The two 'secondary' ones refer to the impact of one

## *2. Physics of flows in a 3D magnetic configuration – 2.8. Conclusion of chapter 2*

perturbation on the other: ripple is responsible for the radial displacement of banana bounce points and vice-versa.

When the precession frequency is comparable with the banana bounce frequency, the stochasticity of particle trajectories arise. The Chirikov overlap parameter is derived, as well as the resulting diffusion and the threshold velocity for a particle trajectory to become chaotic.

Both of these transport channels are included in a compact reduced model that predicts the fluxes as a function of the thermodynamical gradients (i.e. density and temperature), the toroidal velocity and the radial electric field.

# 3. The GYSELA code

## Table of contents

3.1. Gyrokinetic model . . . . .	85
3.2. Code description . . . . .	86
3.3. Implementation of magnetic ripple . . . . .	89
3.3.1. GYSELA geometry . . . . .	89
3.3.2. Method of implementation . . . . .	89
3.3.3. Verification through toroidal angular momentum conservation . . . . .	92
3.3.4. Comparison of GYSELA global simulations with neoclassical predictions and NEO . . . . .	94
3.3.4.1. Computing neoclassical coefficients with GYSELA . . . . .	95
3.3.4.2. Computing neoclassical coefficients with NEO . . . . .	96
3.3.4.3. Benchmark . . . . .	99
3.4. Conclusion of chapter 3 . . . . .	101

The purpose of this chapter's is twofold. First, it briefly describes the simulation code GYSELA which is a tool extensively used in the studies of this thesis. Second, the way the magnetic ripple has been implemented in the code and further benchmarked is explained in detail. The chapter is organized as follows: Sec.3.1 gives the set of equations solved by GYSELA that constitutes the gyrokinetic model, Sec.3.2 explains the basic features of GYSELA (the numerical model, the accessible spatio-temporal scales ...) and Sec.3.3 is a comprehensive description of the magnetic ripple implementation, verification and validation.

## 3.1. Gyrokinetic model

This section aims to present briefly the *gyrokinetic model* equations that are solved in the GYSELA code. The gyrokinetic model describes strongly magnetized plasmas for which typical frequencies are less than the cyclotron frequency. Hence, it is well designed to characterize collisional and turbulent processes. This model aims to reduce the dimensionality of the 6D kinetic approach by averaging the dynamics over the cyclotron motion (this is called the *gyroaverage*), while still accounting for finite Larmor radius effects. It leads to the building of a new adiabatic invariant of motion, the magnetic moment  $\mu_s$ , related to a virtual particle: the gyrocenter. It differs weakly from the particle guiding center but is more adapted to describe small-scale fluctuations. Compared to the guiding center, the gyrocenter takes into account

the effect of electromagnetic perturbations during the gyromotion. Consequently, polarization and magnetization of the plasma are well described even in this 5D description. The derivation of the *gyrokinetic theory* is a formidable task that will not be detailed in this thesis, but the interested reader can refer to [77, 78]. Here only the resulting equations are given.

The first one is the gyrokinetic Fokker-Planck equation . It describes the evolution of the gyrocenter distribution function  $\bar{F}_s$  of each species  $s$  in a 5D phase space  $(\mathbf{x}_G, v_{G\parallel}, \mu_G)$  where  $\mathbf{x}_G$  is the gyrocenter position,  $v_{G\parallel}$  is the gyrocenter velocity parallel to the magnetic field line and  $\mu_G$  is the gyrocenter magnetic moment. It reads

$$\frac{\partial \bar{F}_s}{\partial t} + \frac{d\mathbf{x}_G}{dt} \cdot \nabla \bar{F}_s + \frac{dv_{G\parallel}}{dt} \frac{\partial \bar{F}_s}{\partial v_{G\parallel}} = \mathcal{C}(\bar{F}_s) + S \quad (3.1)$$

where  $\mathcal{C}$  is a collision operator [79] and  $S$  a source (of particles, moment and/or heat).

The second is the electrostatic quasi-neutrality equation Eq(3.2), here expressed in the case of adiabatic electrons and in the limit of long wavelengths (with respect to the thermal ion Larmor radius):

$$\frac{e[\phi - \langle \phi \rangle]}{T_e} - \sum_s \frac{1}{n_{\text{eq},s}} \nabla_{\perp} \cdot \left[ \frac{m_s n_{\text{eq},s}}{e_s B^2} \nabla_{\perp} \phi \right] = \sum_s \frac{1}{n_{\text{eq},s}} \iint \frac{2\pi B_{\parallel,s}^*}{m_s} dv_{G\parallel} d\mu \mathcal{J}(\bar{F}_s - \bar{F}_{\text{eq},s}) \quad (3.2)$$

with  $\langle \cdot \rangle$  denotes a flux-surface average,  $\mathcal{J}$  is the gyroaverage operator.  $\phi$  is the electric potential,  $T_e$  is the electron temperature and  $e$  the ion charge. For each ion species  $s$ ,  $m_s$  is the mass,  $e_s$  is the charge and  $B_{\parallel,s}^*$  is the Jacobian of the phase space coordinate transform. The density  $n_{\text{eq},s}$  is calculated with the equilibrium Maxwellian gyroaveraged distribution function  $\bar{F}_{\text{eq},s}$ .

This is the set of equations solved in the simulation code GYSELA.

## 3.2. Code description

GYSELA is a full-f, non-linear, global 5D gyrokinetic code based on a backward semi-Lagrangian numerical scheme. Let us decipher each of these terms.

- **5D** means that the code evolves the distribution function in a 5D phase-space, which is a reduction from the real 6D phase space as mentioned in the previous section.
- **Full-f** means that the total distribution functions are evolved, as opposed to the “ $\delta f$ ” codes which only describe the departure from a reference distribution function.
- **Backward semi-Lagrangian scheme** [15] is a hybrid scheme that incorporates specificities from both Eulerian and Lagrangian schemes. An Eulerian scheme is based on a fixed grid in phase space where the distribution function  $F$  is evaluated at time  $t + \Delta t$  through finite differences or finite elements knowing  $F$  at

### 3. The GYSELA code – 3.2. Code description

time  $t$ . A Lagrangian scheme, mainly used in *Particle-In-Cell* (PIC) codes, rather relies on the invariance of  $F$  along trajectories when solving the Fokker-Planck equation Eq(3.1). This method tracks the orbit of *markers*<sup>1</sup> in phase-space. The backward semi-Lagrangian scheme used in GYSELA then starts from a point of a fixed grid (Eulerian) at time  $t + \Delta t$  and solves the trajectory equation (Lagrangian) to obtain this same point's position at time  $t$ . In general, the computed position at time  $t$  doesn't match a grid point, so an interpolation is done from nearby mesh points. The main advantages of semi-Lagrangian schemes are their immunity against *Courant-Friedrichs-Lewy* (CFL) conditions (comparing to explicit Eulerian schemes) and reduced numerical noise (compared to PIC schemes). The major drawbacks are the costly interpolations (often simplified at the cost of precision) and that particle conservation is not guaranteed. GYSELA is the only gyrokinetic code at *High-Performance Computing* (HPC) scale that uses this numerical scheme.

- **Flux-driven** means that gradients evolve self-consistently, unlike in *gradient-driven* simulations. Flux-driven simulations then require a source (of heat in most cases) to reach an equilibrium with gradients. Consequently, they also inevitably require a sink at the edge. Gradient-driven simulations are useful to estimate the fluxes for given plasma parameters. Flux-driven simulations allow the study of bursty behaviors of some essential transport mechanisms (like avalanches, Edge Localised Modes ...).
- **Electrostatic** means that only the electrostatic potential  $\phi$  is evolved at the expense of the perturbed vector potential  $\tilde{\mathbf{A}}$ . Hence the magnetic field remains static in the simulations. This approximation is made given that taking electromagnetic effects into account drastically increases the cost of simulations, as some of the associated mechanisms are characterized by frequencies higher than the electrostatic ones, and also because the electron response is needed to compute the perturbed current  $\mu_0 \tilde{\mathbf{J}} = \nabla \times \tilde{\mathbf{B}}$ . The validity of this simplification is questionable for the edge plasma, but reasonable for the core region. Note that the electromagnetic version of GYSELA is in the testing phase.
- **Global** means that the plasma is simulated over the whole tokamak - from core to edge - contrary to *local* codes that usually treat one or few magnetic surfaces. Global simulations are way more costly than local ones. They are however essential to take non-local effects into account, e.g. turbulence spreading, avalanches or profile shearing.
- **Non-linear** means the term  $(\mathbf{v}_E \cdot \nabla)F$  in Eq(3.1) is not linearized.

Put simply, GYSELA is a code designed to simulate turbulence, as well as its interaction with other phenomena in the same scale range. An overview picture of the captured physical mechanisms is displayed in Fig.3.1.

---

1. Individual particle, fluid element, mesoscopic plasma volume ...



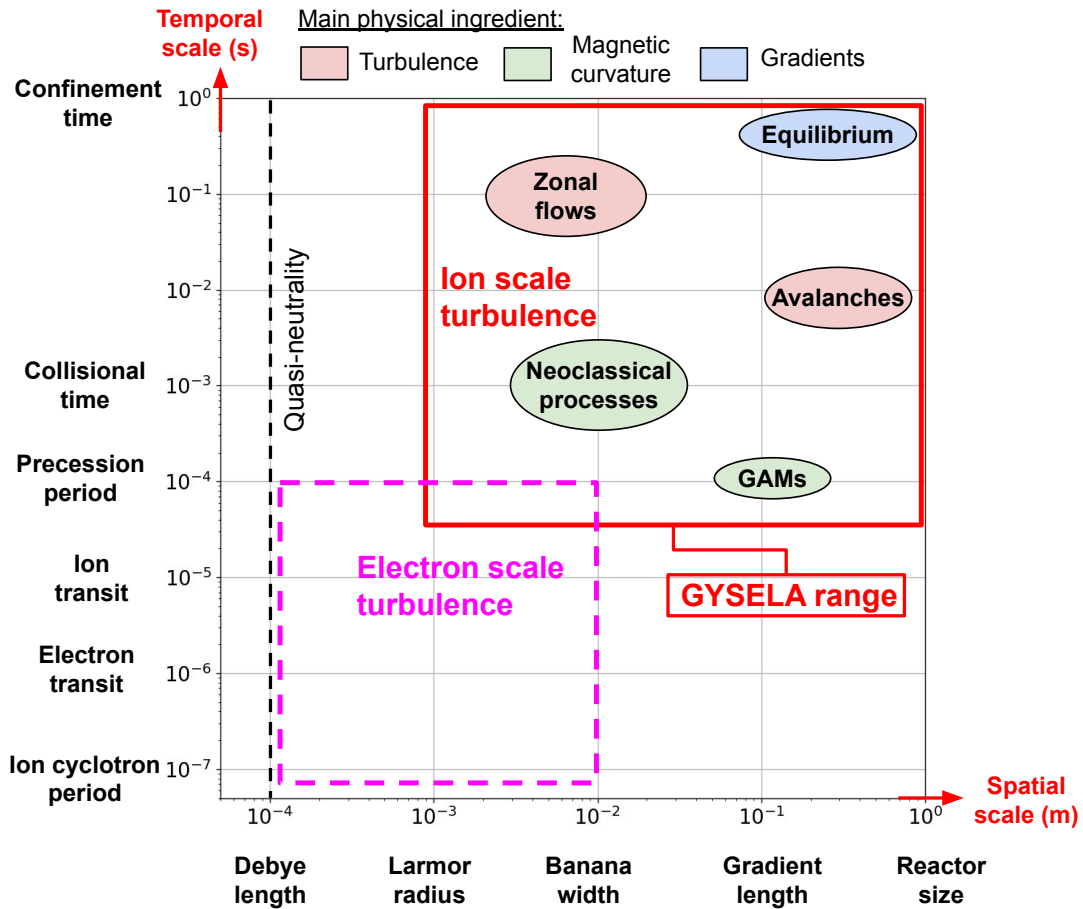


Figure 3.1. – Spatiotemporal scales range described by the GYSELA code and the captured mechanisms. Inspired from Y. Sarazin presentation at Festival de théorie 2022.

GYSELA has been developed since the beginning of the 2000s. It has been evolving continuously to include more and more physics, taking advantage of the development of more powerful computers and by using state-of-the-art high-performance computing<sup>2</sup>. Despite access to a large amount of numerical resources (hundreds of millions of CPU hours per year), it is currently impossible to describe all the physics happening in a tokamak with a single code. In GYSELA, the major missing physics at the time of this thesis are:

- Fluctuations are electrostatic: the magnetic field  $B$  doesn't evolve in time. As a consequence, there is no retro-action of the pressure gradient on  $B$ , either at the equilibrium scale (i.e. the Grad-Shafranov shift) or at fluctuating scale (i.e. electromagnetic turbulence). MHD events are also dismissed.
- Adiabatic electrons<sup>3</sup>: the electron dynamics exhibit a thermodynamical re-

2. In particular regarding the OpenMP/MPI parallelism (with plans to port parts of the code on GPUs)

3. It should be noted that kinetic electrons are implemented in the code, but this version was not

### 3. The GYSELA code – 3.3. Implementation of magnetic ripple

response such that the electron density reads  $n_e = n_0(1 + \frac{e}{T_e}(\phi - \langle\phi\rangle))$ . Turbulence developing at electron scale is then not described<sup>4</sup>.

A detailed description of the GYSELA code can be found in Grandgirard *et al.* [76]. In the frame of this thesis, magnetic ripple has been added to the code.

## 3.3. Implementation of magnetic ripple

### 3.3.1. GYSELA geometry

The current version of the GYSELA code uses a set of orthogonal toroidal coordinates labeled  $\{x^i\} = (r, \theta, \varphi)$ , where  $r$  is the radial position,  $\theta$  the geometric poloidal geometric angle, and  $\varphi$  the toroidal angle. This is a choice among many others such as Hamada coordinates, Boozer coordinates, or other intrinsic coordinates. The metric tensor  $g_{ik}$  is defined via the distance element  $ds$  such that

$$ds^2 = g_{ik}dx^i dx^k = g^{ik}dx_i dx_k$$

The Jacobian in space  $\mathcal{J}_x$  is defined as  $\mathcal{J}_x = \sqrt{g}$  with  $g$  the determinant of the metric tensor. It is calculated as  $\mathcal{J}_x = [(\nabla x^1 \times \nabla x^2) \cdot \nabla x^3]^{-1}$ . The element of the contravariant metric tensor verifies the relation  $g^{ij} = \nabla x^i \cdot \nabla x^j$ . With these notations, each vector  $\mathbf{A}$  can be defined in terms of its covariant components  $A_i$  as  $\mathbf{A} = A_i \nabla x^i$ . In the specific case of circular concentric magnetic surfaces considered in GYSELA, it is straightforward to show that

$$g_{ij} = \begin{pmatrix} 1 & 0 & 0 \\ 0 & r^2 & 0 \\ 0 & 0 & R^2 \end{pmatrix}$$

and, as the tensor  $\{g^{ij}\}$  is the inverse of  $\{g_{ij}\}$ ,

$$g^{ij} = \begin{pmatrix} 1 & 0 & 0 \\ 0 & \frac{1}{r^2} & 0 \\ 0 & 0 & \frac{1}{R^2} \end{pmatrix}$$

where  $R(r, \theta) = R_0 + r \cos\theta$  with  $R_0$  the major radius of the torus at the magnetic axis. The Jacobian in space is then  $\mathcal{J}_x = rR$ . Note that work is currently done by the GYSELA team to implement an arbitrary magnetic geometry in the code.

### 3.3.2. Method of implementation

This section aims to explain how magnetic ripple is implemented in GYSELA. The axisymmetric magnetic field  $\mathbf{B}$  is defined as

---

used for the present work.

4. Note that the version of GYSELA with trapped kinetic electrons has been recently benchmarked successfully and is ready for production runs.

### 3. The GYSELA code – 3.3. Implementation of magnetic ripple

$$\mathbf{B} = \frac{B_0 R_0}{R(r, \theta)} \left[ \frac{r}{q(r) R_0} \hat{\mathbf{e}}_\theta + \hat{\mathbf{e}}_\varphi \right] \quad (3.3)$$

where  $\hat{\mathbf{e}}_\theta = r \nabla \theta$  and  $\hat{\mathbf{e}}_\varphi = R \nabla \varphi$  are unit vectors in the poloidal and toroidal periodic direction respectively, and  $q$  is the safety factor.

In the axisymmetric case, the electrostatic gyrokinetic equations of motion for species  $s$  solved in GYSELA are

$$B_{\parallel s}^* \frac{d\mathbf{x}_G}{dt} = v_{G\parallel} \mathbf{B}^* + \frac{\mathbf{b}}{e_s} \times \nabla \mathcal{H} \quad (3.4)$$

$$B_{\parallel s}^* m_s \frac{dv_{G\parallel}}{dt} = -\mathbf{B}^* \cdot \nabla \mathcal{H} \quad (3.5)$$

where  $\mathbf{b} = \mathbf{B}/B$  is the unit vector parallel to the magnetic field direction,

$$\mathbf{B}^* = \mathbf{B} + \frac{m_s v_{G\parallel}}{e_s} \nabla \times \mathbf{b}$$

and

$$\mathcal{H} = \frac{m_s}{2} v_{G\parallel}^2 + \mu_s B + e_s \mathcal{J}[\phi] \quad (3.6)$$

is the axisymmetric Hamiltonian, with  $\phi$  the electric potential.

In principle, the ripple perturbation  $\delta \mathbf{B}$  should be included by modifying both the magnetic field vector  $\mathbf{B}$  and its modulus. Modifying the vector  $\mathbf{B}$  in such a heavy code is very challenging. Indeed, adding a toroidal component to the magnetic field would change the magnetic surface shape such that the metrics would become 3D. This tremendous work is unnecessary, as modifying only the Hamiltonian is sufficient for acceptable accuracy<sup>5</sup>.

The new effective Hamiltonian reads

$$\mathcal{H}_{\text{eff}} = \frac{m_s}{2} v_{G\parallel}^2 + \mu_s (B + \delta B) + e_s \mathcal{J}[\phi] \quad (3.7)$$

where

$$\delta B = B_0 \delta(r, \theta) \cos(N_c \varphi). \quad (3.8)$$

The magnetic drift  $\mathbf{v}_{\mathbf{D}s}$ , the electric drift  $\mathbf{v}_{\mathbf{E} \times \mathbf{B}s}$  and the parallel force  $f_{\parallel s}$  appear when developing Eq(3.4) and Eq(3.5) such that

---

5. It can be shown that this simplification changes the expression of the magnetic braking torque  $T_{\mathcal{M},s}$ , which is the main effect of ripple, from  $T_{\mathcal{M},s} = -\int d^3 \mathbf{v} F_s \left\{ (m_s v_{G\parallel}^2 + \mu_s B) R \frac{(\hat{\mathbf{e}}_\varphi \cdot \nabla) B}{B} \right\}$  to  $T_{\mathcal{M},s} = -\int d^3 \mathbf{v} F_s \left\{ \mu_s R (\hat{\mathbf{e}}_\varphi \cdot \nabla) B \right\}$ . At low collisionality, magnetic ripple impacts mainly the trapped particles so the error on  $T_{\mathcal{M},s}$  can not exceed  $\varepsilon$  for banana trapped particles and  $\delta$  for locally trapped particles. This reasonable assumption is detailed in reference [80] that discusses the non-axisymmetric perturbation implementation in the gyrokinetic code GT5D.

### 3. The GYSELA code – 3.3. Implementation of magnetic ripple

$$\mathbf{v}_{D_s} = \frac{m_s v_{G\parallel}^2 + \mu_s B \mathbf{B} \times \nabla B}{e_s B_{\parallel s}^*} \frac{\mathbf{B} \times \nabla B}{B^2}, \quad (3.9)$$

$$\mathbf{v}_{\mathbf{E} \times \mathbf{B}_s} = \frac{\mathbf{B} \times \nabla \bar{\phi}}{B B_{\parallel s}^*}, \quad (3.10)$$

$$f_{\parallel s} = -\mu_s (\mathbf{b}_s^* \cdot \nabla) B, \quad (3.11)$$

the motion equations of GYSELA are then modified as follows

$$\frac{d\mathbf{x}_G}{dt} = v_{G\parallel} \mathbf{b}_s^* + \mathbf{v}_{D_s} + \delta \mathbf{v}_{D_s} + \mathbf{v}_{\mathbf{E} \times \mathbf{B}_s} \quad (3.12)$$

$$m_s \frac{dv_{G\parallel}}{dt} = f_{\parallel s} + \delta f_{\parallel s} - e \mathbf{b}_s^* \cdot \nabla \bar{\phi} + \frac{m_s v_{G\parallel}}{B} \mathbf{v}_{\mathbf{E} \times \mathbf{B}_s} \cdot \nabla B \quad (3.13)$$

where  $\mathbf{b}_s^*$  is defined as

$$\mathbf{b}_s^* = \frac{1}{B_{\parallel s}^*} \left( \mathbf{B} + \frac{m_s v_{G\parallel}}{e_s B} \nabla \times \mathbf{B} \right). \quad (3.14)$$

The new terms due to ripple are displayed in red and yield

$$\delta \mathbf{v}_{D_s} = \frac{\mu_s B \mathbf{B} \times \nabla \delta B}{e_s B_{\parallel s}^* B^2} \quad (3.15)$$

$$\delta f_{\parallel s} = -\mu_s (\mathbf{b}_s^* \cdot \nabla) \delta B \quad (3.16)$$

such that the magnetic ripple only adds a term  $\delta \mathbf{v}_D$  to the magnetic drift and a parallel force  $f_{\parallel s}$  in the parallel momentum conservation.

With the notation  $w_{D_s} = \frac{\mu_s}{e_s B_{\parallel s}^* \mathcal{J}_x B}$ , the contravariant components of the new magnetic drift term  $\delta \mathbf{v}_D$  are

$$\delta v_{D_s}^r = w_{D_s} \left( B_\theta \frac{\partial \delta B}{\partial \varphi} - B_\varphi \frac{\partial \delta B}{\partial \theta} \right) \quad (3.17)$$

$$\delta v_{D_s}^\theta = w_{D_s} B_\varphi \frac{\partial \delta B}{\partial r} \quad (3.18)$$

$$\delta v_{D_s}^\varphi = -w_{D_s} B_\theta \frac{\partial \delta B}{\partial r} \quad (3.19)$$

The parallel force  $f_{\parallel s}$  reads

$$f_{\parallel s} = -\mu_s \left( \frac{\partial \delta B}{\partial r} b_s^{*r} + \frac{\partial \delta B}{\partial \theta} b_s^{*\theta} + \frac{\partial \delta B}{\partial \varphi} b_s^{*\varphi} \right)$$

where the contravariant coordinates of  $\mathbf{b}_s^*$  read

### 3. The GYSELA code – 3.3. Implementation of magnetic ripple

$$b_s^{*i} = (\mathbf{b}_s^* \cdot \nabla) x_G^i = \frac{1}{B_{\parallel s}^*} \left( B^i + \frac{m_s v_{G\parallel}}{e_s} \frac{(\nabla \times \mathbf{B})^i}{B} \right)$$

or more specifically

$$b_s^{*r} = 0 \quad ; \quad b_s^{*\theta} = \frac{B^\theta}{B_{\parallel s}^*} \quad ; \quad b_s^{*\varphi} = \frac{1}{B_{\parallel s}^*} \left( B^\varphi + \frac{m_s v_{G\parallel}}{e_s} \frac{(\nabla \times \mathbf{B})^\varphi}{B} \right) .$$

In practice,  $\frac{\partial \delta B}{\partial r}$  and  $\frac{\partial \delta B}{\partial \theta}$  are negligible compared to  $\frac{\partial \delta B}{\partial \varphi}$ . Consequently, only  $\frac{\partial \delta B}{\partial \varphi}$  has been added to the code to avoid unnecessary additional calculations and increased simulation time. The following sections are dedicated to the verification and validation of this implementation.

In the future, if the modification of the magnetic field vector  $\mathbf{B}$  appears of use, it will be sufficient to add to the present field the perturbed one

$$\delta \mathbf{B} = \delta B_r \nabla r + \delta B_\theta \nabla \theta + \delta B_\varphi \nabla \varphi \quad . \quad (3.20)$$

The contravariant components of  $\delta \mathbf{B}$  are easily deduced from the metric tensor  $B^i = g^{ik} B_k$ . For the current GYSELA geometry, they read

$$\delta B^r = \frac{B_0 R_0}{N_c} \frac{\partial \delta(r, \theta)}{\partial r} \sin(N_c \varphi) \quad (3.21)$$

$$\delta B^\theta = \frac{1}{r^2} \frac{B_0 R_0}{N_c} \frac{\partial \delta(r, \theta)}{\partial \theta} \sin(N_c \varphi) \quad (3.22)$$

$$\delta B^\varphi = \frac{1}{R^2} B_0 R_0 \delta(r, \theta) \cos(N_c \varphi). \quad (3.23)$$

#### 3.3.3. Verification through toroidal angular momentum conservation

From now on, only a single ion species is considered so the subscript  $s$  is omitted. To verify the implementation of the ripple perturbation in GYSELA, a scan in ripple amplitude is considered to check the conservation of toroidal angular momentum. One of the major effects of a non-axisymmetric magnetic perturbation is an additional toroidal torque  $T_{\mathcal{M}}$ , which is called "magnetic braking torque" (or just "magnetic braking" when referring to the associated force  $\mathcal{M}$ ). The flux surface averaged, i.e. radially local, momentum conservation relation [81] involves this new term:

$$\underbrace{m \frac{\partial \langle n R V_T \rangle}{\partial t}}_{\text{Temporal evolution}} = - \underbrace{\langle \nabla \cdot \Pi_\varphi \rangle}_{\text{Reynolds stress}} - \underbrace{\langle T_\varphi \rangle}_{\text{Polarisation}} + \underbrace{\langle \mathcal{J} \cdot \nabla \psi \rangle}_{\text{Radial currents}} + \underbrace{\langle T_{\mathcal{M}} \rangle}_{\text{Magnetic braking torque}} \quad (3.24)$$

where  $V_T = \frac{1}{n} \int d^3 v \{ v_{G\parallel} (B_T / B) F \}$  is the gyrocenter mean toroidal velocity ( $B_T$  is

### 3. The GYSELA code – 3.3. Implementation of magnetic ripple

the toroidal component of the magnetic field),  $\Pi_\phi$  the toroidal Reynolds stress,  $T_\phi$  a polarization term and  $\mathcal{J}$  the sum of the radial currents due to the magnetic and electric drifts respectively.

Boundary physics, inevitably present either in global codes or experiments, acts as a momentum sink that is not included in the analytical model. For this reason, the considered profile of the ripple amplitude in the following simulations is taken radially gaussian and maximum at mid-radius. Also, no poloidal dependence is accounted for. It reads  $\delta_{\text{sim}}(r) = \delta_0 e^{-32(r/a-0.5)^2}$  with  $\delta_0$  the mid-radius ripple amplitude. The usual way to perform simulations for neoclassical studies is to artificially filter out all toroidal Fourier modes of the electric potential  $\phi$  except the axisymmetric component. This cannot be done here as ripple adds toroidal harmonics with  $N_c$  periodicity. The chosen solution to avoid turbulence is then to initiate the simulations below the instability threshold, i.e. with a sufficiently weak temperature gradient and high density gradient. It is also verified that ripple-induced mode amplitudes are low enough such that the inequality on Fourier modes  $e\phi_{kN_c} \ll \mu B_{kN_c}$ , with  $k = 1, 2, \dots$ , is satisfied, which ensures that the Hamiltonian is not affected by fluctuations of the electric potential. The parameters of the simulations are summarized in Tab.3.1.

Species	Deuterium
Aspect ratio $R_0/a$	3.2
Safety factor	$q = 0.854 + 2.184(r/a)^2$
Density gradient	$R_0/L_N = 6$
Temperature gradient	$R_0/L_T = 6$
Collisionality at $r/a = 0.5$	$\nu^* = 0.1$
$\rho_i/a$ at $r/a = 0.5$	$\rho^* = 1/150$
Number of coils	$N_c = 16$

Table 3.1. – Simulation parameters.  $L_N$  and  $L_T$  are the density and temperature gradient's lengths,  $\rho_i$  is the ion Larmor radius.

Four simulations using different ripple amplitudes are analyzed. The l.h.s of Eq(3.24), which is a standard output of GYSELA, is compared with the sum of the contributions in the r.h.s for each simulation. The radial profiles of these quantities are plotted in Fig.3.2 and show a satisfactory agreement for all ripple amplitudes attesting to proper momentum conservation in the code.

### 3. The GYSELA code – 3.3. Implementation of magnetic ripple

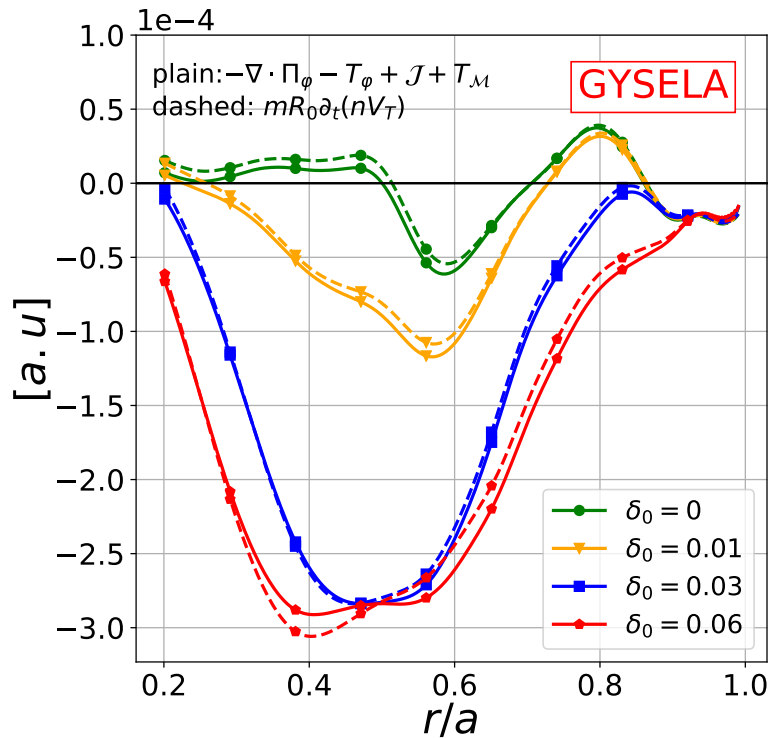


Figure 3.2. – Radial profile of the total toroidal momentum (dashed) and the sum of the expected contributions (plain) for different ripple amplitudes  $\delta_0$ .

Without turbulence, magnetic braking quickly becomes the dominant contribution and determines the mean toroidal velocity. This torque is negative, which in the GYSELA convention means that magnetic braking pushes the toroidal velocity toward the counter-current direction, as expected. The implementation of a ripple magnetic perturbation being successful, the GYSELA code can be confronted to the analytical neoclassical reduced model presented in Sec.2.6 and the reference code NEO.

#### 3.3.4. Comparison of GYSELA global simulations with neoclassical predictions and NEO

In this section, the ability of the GYSELA code to assess neoclassical processes is tested against two different tools. The first one is the reduced model developed in Chapter 2. The other one is the 3D version of the drift kinetic solver NEO which captures all the neoclassical physics with ripple. Commonly, the neoclassical theory in axisymmetric configurations is benchmarked by comparing the thermal drive coefficient  $k_{V_P}$  of the poloidal velocity  $V_P$  such that its equilibrium value reads  $V_{P,eq} = k_{V_P} \frac{\sqrt{T}}{eB_T}$ . This exercise has already been done to benchmark GYSELA against the axisymmetric neoclassical theory [82].

In the case of a non-axisymmetric magnetic perturbation, the transport matrix is not degenerate so this exercise can be extended to other quantities. It could be

### 3. The GYSELA code – 3.3. Implementation of magnetic ripple

tempting to perform a benchmark on each of the transport matrix coefficients ( $d_{ij}$ ) that appear in the reduced model Eq(2.59) and which only depend on  $\delta/\varepsilon$ ,  $v^*$  and  $N_c q$ . Given the structure of Eq(2.59), one could determine those coefficients if a sufficient number of  $(A_N, A_{V_T}, A_T)$  and associated  $(\Gamma_N, \Gamma_{V_T}, \Gamma_T)$  sets were known. Let us remind that  $A_{V_T}$  and  $A_T$  can be seen as the normalized mean toroidal velocity and normalized temperature gradient. Also,  $A_N$  is a dimensionless quantity that varies with the density gradient and the radial electric field. In theory, only 3 sets would suffice for a given  $(\delta/\varepsilon, v^*, N_c q)$  set to determine the transport matrix from simulations. However, the least-square method used as a linear solver proved to be inefficient and would probably need more statistics. In addition, the benchmark aims at verifying the validity range of the theory for a wide range of ripple amplitudes and collisionalities. As discussed below, obtaining a set  $(A_N, A_{V_T}, A_T, \Gamma_N, \Gamma_{V_T}, \Gamma_T)$  linked to one combination of  $(\delta/\varepsilon, v^*, N_c q)$  basically amounts to run one simulation. The number of simulations required to retrieve all the matrix coefficients for a wide range of  $(\delta/\varepsilon, v^*, N_c q)$  values would then be enormous. As the ripple's primary effect is a toroidal torque, the focus is here on the thermal drive of the toroidal velocity  $k_{V_T}$  and the neoclassical toroidal friction  $v_\phi$ .

The methodologies to retrieve these coefficients in GYSELA and NEO are described in detail in the following subsections.

#### 3.3.4.1. Computing neoclassical coefficients with GYSELA

In GYSELA, the main difficulty lies in the boundary conditions that can add extra effects not taken into account in the reduced model like orbit losses, momentum flux carried by waves or scrape-off layer interactions. For this reason, a radially gaussian ripple, as defined in Sec.3.3.3, is considered. The radial location of interest is then chosen at  $r/a = 0.5$ . In GYSELA,  $(A_{V_T}, A_T)$  are inputs and  $\Gamma_{V_T}$  is an output. The temperature gradient  $A_T$  evolves slowly compared with  $A_{V_T}$  and  $\Gamma_{V_T}$ . In all simulations,  $A_T$  is then fixed at the same value and only the initial  $A_{V_T}$  profile is changed. This makes the numerical resolution even simpler and more robust, as linear regression on  $\Gamma_{V_T}(A_{V_T})$  gives  $v_\phi$  and  $k_{V_T}$  which according to Eq(2.73) are respectively associated with the slope and intersection with the x-axis. A  $(A_{V_T}, \Gamma_{V_T})$  set is retrieved after the GAM phase which is here longer than a few collision times in each simulation, i.e. the characteristic time needed for neoclassical effects to establish. This method for extracting  $k_{V_T}$  from the slope of the  $\Gamma_{V_T}(A_{V_T})$  is illustrated in Fig.3.3. This figure is the result of 16 simulations with four different ripple amplitudes, four toroidal velocities, and a single  $v^*$  profile.



### 3. The GYSELA code – 3.3. Implementation of magnetic ripple

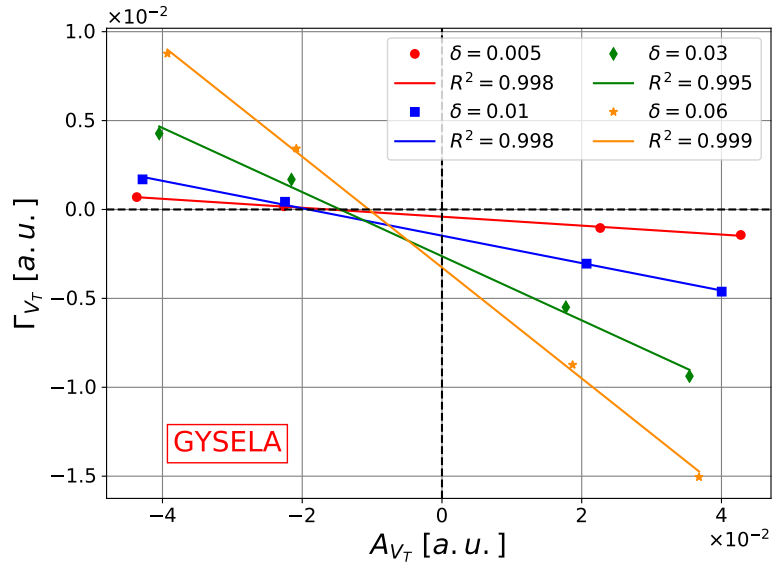


Figure 3.3. – Magnetic braking force  $\Gamma_{V_T}$  versus  $A_{V_T}$  for different ripple amplitudes  $\delta$ . Each point corresponds to a simulation with different initial toroidal velocity profiles and represents the  $(A_{V_T}, \Gamma_{V_T})$  retrieved at  $r/a = 0.5$  after the GAMs phase, here at  $v^* = 0.1$ .

This exercise has been done with four collisionality profiles for a total of 48 gyrokinetic simulations. All the input profiles are shown in Fig.3.4.

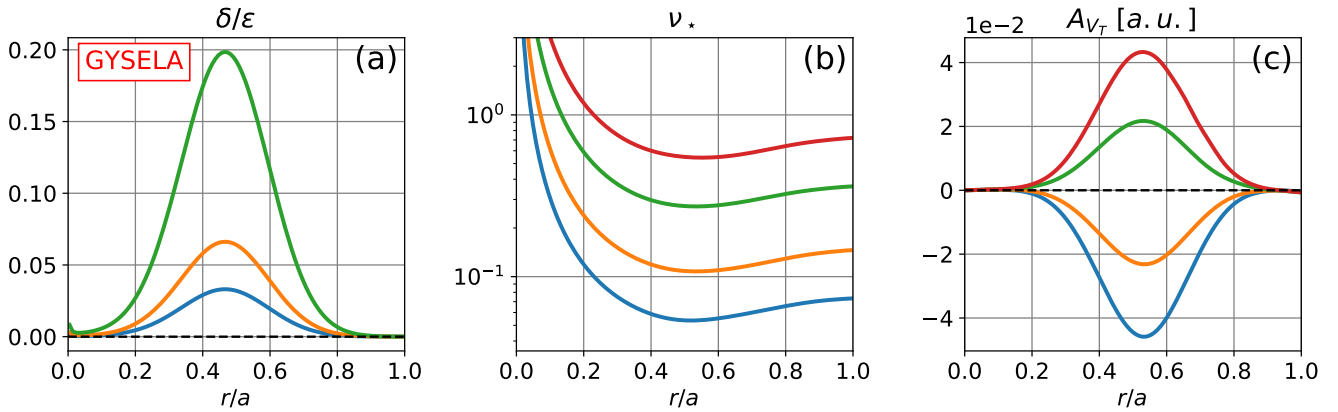


Figure 3.4. – Initial radial profiles of the effective ripple amplitudes  $\delta/\epsilon$  (a), the collisionalities  $\nu^*$  (b) and the normalized toroidal velocities  $A_{V_T}$  (c) used for the scan.

#### 3.3.4.2. Computing neoclassical coefficients with NEO

NEO is an Eulerian local code that solves the drift-kinetic equation with a linearized full Fokker-Planck collision operator [83, 84]. It is considered as  $k_{\perp} \rho_i \ll 1$  where  $k_{\perp}$  is the characteristic wave number of the distribution function. The only approximation

### 3. The GYSELA code – 3.3. Implementation of magnetic ripple

is the *drift-ordering*  $\rho^* \ll 1$  [85]. As NEO is able to handle non-axisymmetric flux surfaces (see [86] for more details), the following simulations use the same ripple perturbations used in GYSELA. NEO has to be benchmarked in the same conditions as in GYSELA. This requires zero particle flux  $\Gamma_N = 0$ , as imposed by the adiabatic electron response in GYSELA. However, contrary to the axisymmetric version, here NEO does not enforce ambipolarity so that  $\Gamma_N \neq 0$  in the general case. Notice that, at equilibrium, both  $\Gamma_N$  and  $\Gamma_{V_T}$  go to zero. Hence  $V_T = k_{V_T} \nabla T / e B_P$ , as stated in Eq(2.60), which is an output in NEO. It follows that, in such a regime, this methodology does not allow one to retrieve the neoclassical toroidal friction  $v_\phi$  with NEO. To retrieve  $k_{V_T}$ , one must first find an input set of  $(A_N, A_T)$  for which  $\Gamma_N = 0$ . There is no quasi-neutrality constraint in NEO, and consequently no onset of non-linearity, even small, due to the electric potential as in GYSELA. For this reason, the relation between  $(A_N, A_T)$  and  $(\Gamma_N, \Gamma_{V_T}, \Gamma_T)$  is linear in NEO. Taking advantage of this,  $A_N$  is set to a constant value while a scan on  $A_T$  is performed<sup>6</sup>. The resulting outputs of interest, i.e.  $\Gamma_N$ ,  $\Gamma_{V_T}$  and  $A_{V_T}$  then exhibit a linear dependency with respect to  $A_T$ , as depicted in Fig.3.5. Note that this method could also have been done by performing a scan on  $A_N$  at fixed  $A_T$ . The  $\Gamma_N = 0$  condition is then obtained by drawing the  $\Gamma_N(A_T)$  line using a few points, each obtained with one simulation, and by retrieving the  $A_T$  value that cancels the particle flux. At this value  $\Gamma_{V_T} = 0$  as expected and already discussed, so the output toroidal velocity is equal to  $A_{V_T} = k_{V_T} A_T$ . This provides the value of  $k_{V_T}$ . Fig.3.6 illustrates this procedure, that is repeated for each  $v^*$  considered for a given ripple amplitude  $\delta$ .

---

6. We here remind that the transport coefficients  $k_N$ ,  $k_{V_T}$  and  $k_{V_p}$  depends only on  $\delta/\varepsilon$ ,  $v^*$  and  $N_c q$ . It means that the scan could have been performed on  $A_N$  and this would give the same results.

3. The GYSELA code – 3.3. Implementation of magnetic ripple

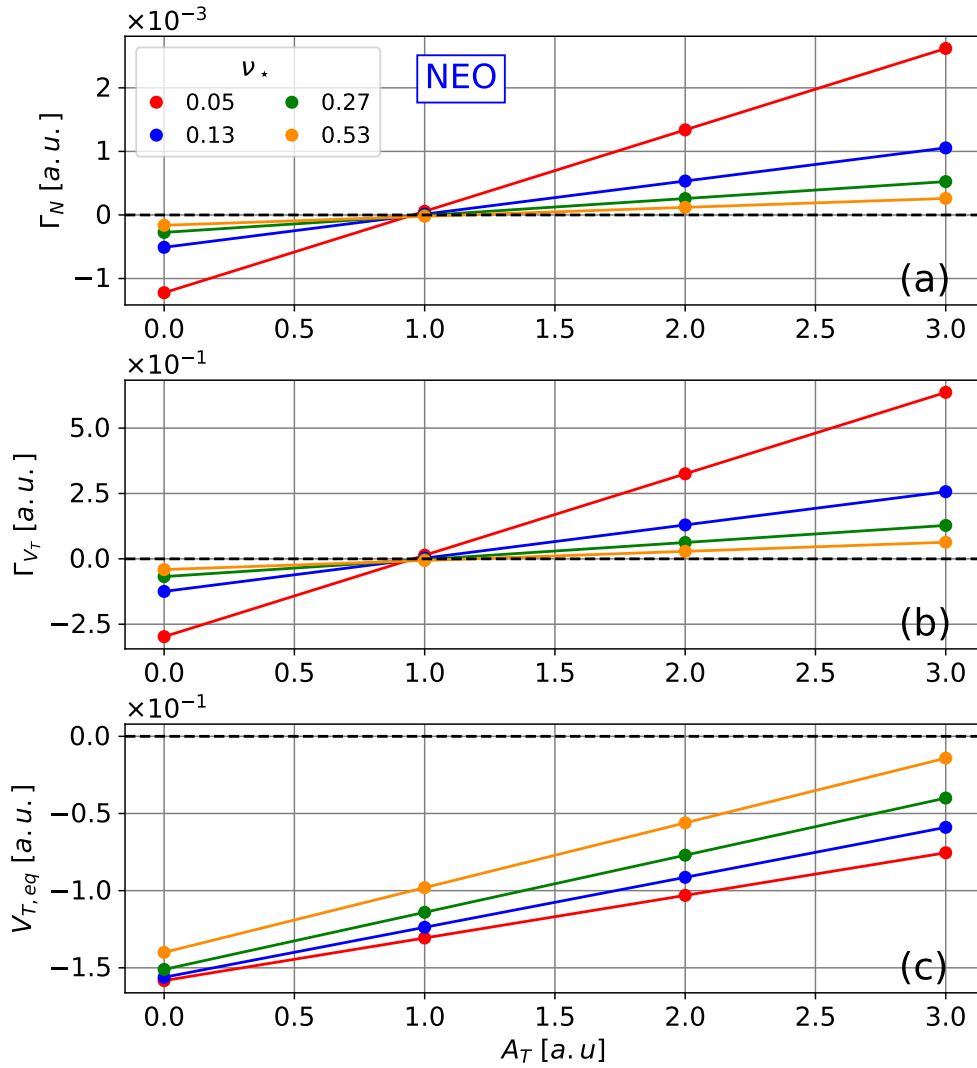


Figure 3.5. – From NEO simulations: Equilibrium particle flux  $\Gamma_N$  (a), equilibrium magnetic braking force  $\Gamma_{V_T}$  (b) and equilibrium mean toroidal velocity  $V_T$  (c) for different collisionalities  $\nu_*$  at fixed  $\delta/\varepsilon = 0.03/0.16$  and  $N_c q = 16 \times 1.4$  over a wide range of  $A_T$ .

### 3. The GYSELA code – 3.3. Implementation of magnetic ripple

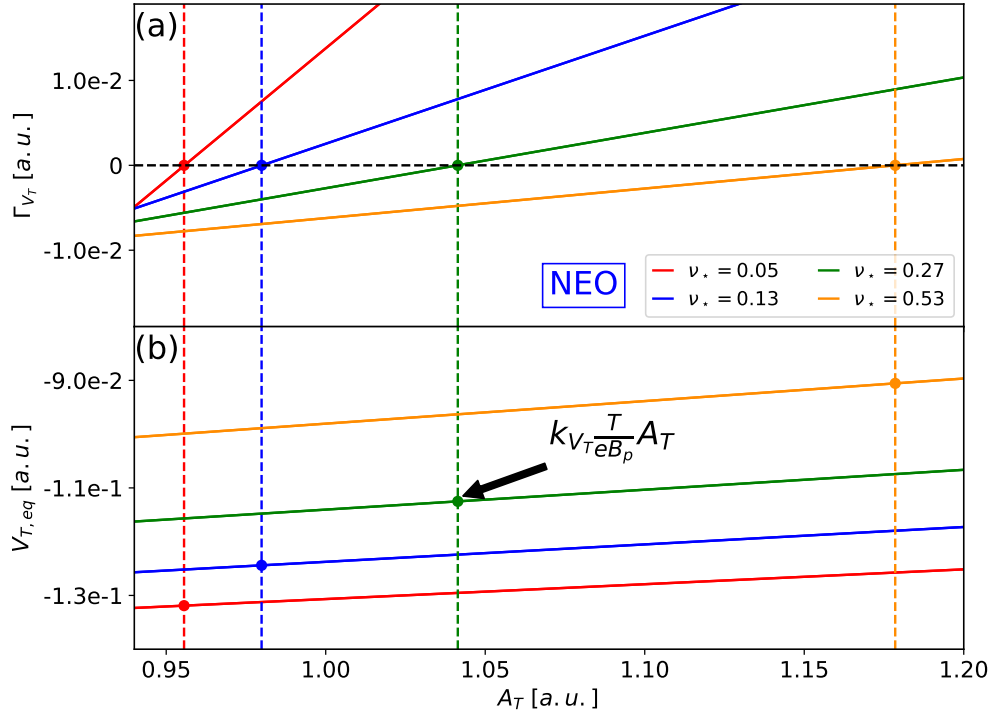


Figure 3.6. – Zoom-up of Fig.3.5 in range of  $A_T$  where  $\Gamma_N = \Gamma_{V_T} = 0$ . The value of  $V_T$  at  $A_T$  for which  $\Gamma_{V_T}$  cancels is directly linked to the neoclassical thermal drive  $k_{V_T}$ .

#### 3.3.4.3. Benchmark

The comparison between the reduced model, GYSELA and NEO is performed in the range of collisionalities  $\nu^* \in [0.05 - 0.5]$  and for three ripple amplitudes:  $\delta = 0.5\%$ ,  $\delta = 1\%$  and  $\delta = 3\%$  at  $\varepsilon = 0.16$  and at a fixed  $N_c q = 1.4 \times 16$ . Fig.3.7 shows the  $k_{V_T}$  obtained with GYSELA, NEO by the procedure explained above for a  $\nu^*$  scan and for those three ripple amplitudes. The value of  $k_{V_T}$  given by the reduced model is also plotted. A fair agreement is found between GYSELA and NEO, where the average relative error is less than 10%, even though it can reach  $\sim 50\%$  at combined high collisionality  $\nu^* = 0.5$  and low ripple  $\delta = 0.5\%$ . These results show that the model collision operator used in GYSELA is well designed to describe neoclassical processes in the collisionality range  $\nu^* \in [0.05, 0.5]$ . Agreement between both codes and the neoclassical model in non-axisymmetric configurations is also obtained regarding the thermal drives. However, the  $\delta = 0.5\%$  case with GYSELA does not seem to undergo the  $1/\nu^*$  trend followed by the model and NEO. One possible explanation is that this is the only case not dominated by  $Y < 1$  regimes (cf. Sec.2.6). In other words, only this case is dominated by the effect of banana-trapped particles. The point is that at low  $\nu^*$ , other regimes affecting only banana trapped particles exist [63, 65, 73]. They are sometimes labeled *super-banana* regimes and correspond to the effect of higher order electric and magnetic drifts at bounce points, negligible at higher collisionalities.

### 3. The GYSELA code – 3.3. Implementation of magnetic ripple

These regimes are not included in the present reduced model, nor in the present NEO simulations. However, they are treated by GYSELA, which could explain this discrepancy at low collisionality. Note that NEO can actually compute those drifts [86]. This option was not switched on as the methodology here used to retrieve  $k_{V_T}$  in NEO is not compatible if those drifts are activated. However, a few tests with reasonable parameters for those drifts were performed in NEO and showed a reduction of  $k_{V_T}$  even for collisionality around  $\nu^* \approx 0.1$ . At high  $\nu^*$ , a larger discrepancy is observed at  $\delta = 0.5\%$  between GYSELA and both NEO and the model. While these later agree, the discrepancy with GYSELA remains unexplained, but is still in an acceptable agreement with NEO and the reduced model. Overall, the model which is derived in the large aspect ratio limit  $\varepsilon \ll 1$  is showing a fair agreement with NEO. Alleviating this latter limit actually already modifies neoclassical predictions in the axisymmetric case quite substantially. In fact, for the axisymmetric neoclassical theory, i.e. without ripple, the finite aspect-ratio corrections [87] can change  $k_{V_p} = 1.17$  to  $k_{V_p} \sim 0.6$  for  $\varepsilon = 0.17$  as observed in GYSELA [82]. To our knowledge, there is no analytical derivation of the aspect ratio correction for the neoclassical theory with ripple. The agreement is then unexpectedly good, especially at high  $\delta/\varepsilon$  where the condition  $Y < 1$  dominates.

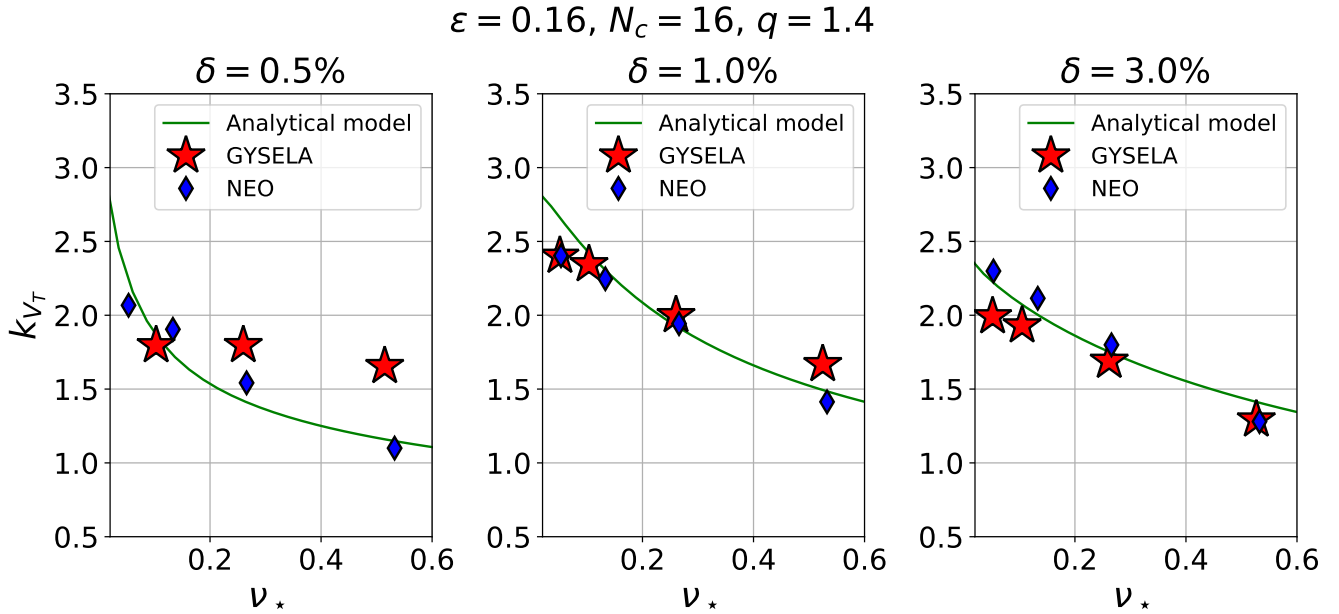


Figure 3.7. – Collisionality scan of  $k_{V_T}$  obtained with the reduced model, GYSELA and NEO for  $\delta = 0.5\%$  (left),  $\delta = 1\%$  (middle) and  $\delta = 3\%$  (right) at fixed  $\varepsilon = 0.16$  and  $N_c q = 16 \times 1.4$ .

The benchmark on the toroidal friction is shown in Fig.3.8. Both expressions derived in Sec.2.6, i.e.  $\nu_\phi$  and  $\nu_\phi^{\Gamma_{N=0}}$  are displayed on this figure. It was expected that the expression with the zero particle flux assumption, i.e.  $\nu_\phi^{\Gamma_{N=0}}$ , should be the best approximation as the electron are adiabatic in these simulations. However, it appears that the toroidal friction obtained in GYSELA is about 5 to 10 times lower than  $\nu_\phi^{\Gamma_{N=0}}$ .

The expression of the neoclassical friction obtained by considering a finite particle flux is however in reasonable agreement with GYSELA. The reason for this behavior is still an open issue.

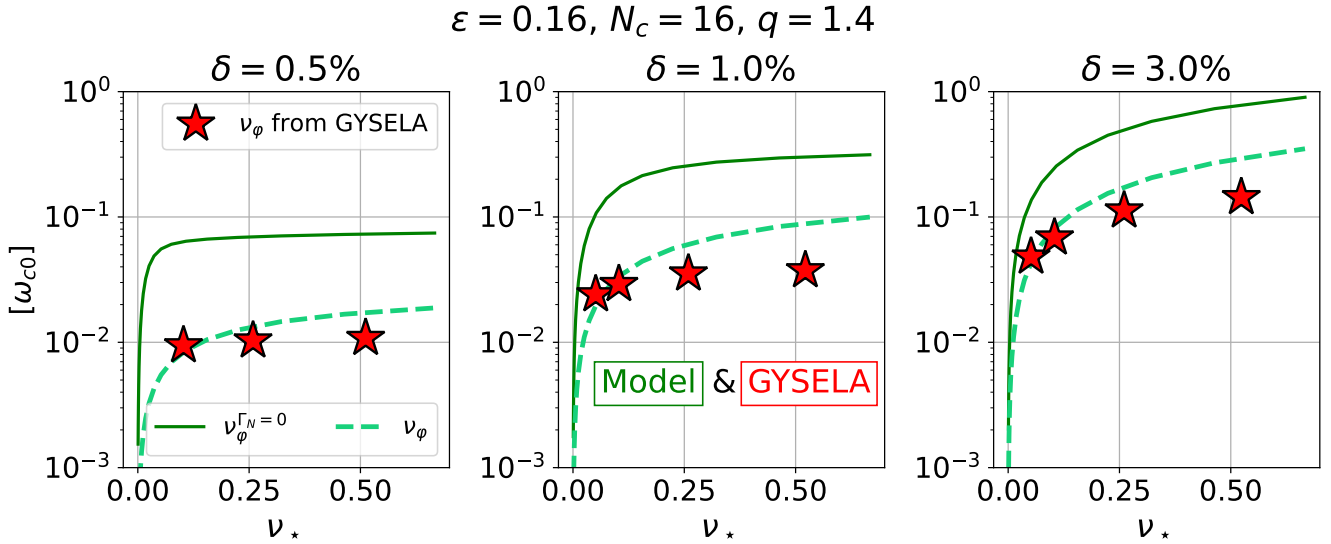


Figure 3.8. – Collisionality scan of  $\nu_\phi$  and  $\nu_\phi^{\Gamma_N=0}$  obtained with the reduced model and GYSELA for  $\delta = 0.5\%$  (left),  $\delta = 1\%$  (middle) and  $\delta = 3\%$  (right) at fixed  $\varepsilon = 0.16$  and  $N_c q = 16 \times 1.4$ .

### 3.4. Conclusion of chapter 3

Magnetic ripple perturbations have been successfully implemented in GYSELA by modifying the effective Hamiltonian. Key verification has been achieved through toroidal momentum conservation where a new term, the magnetic drag due to the ripple perturbation, becomes the dominant contribution at large ripple amplitude. GYSELA results have been benchmarked regarding the neoclassical processes occurring in presence of ripple thanks to an analytical neoclassical model and the NEO code. Good agreement with the NEO code is found, meaning GYSELA is able to properly describe ripple-induced neoclassical processes down to relatively low collisionality  $\nu^* \sim 0.05$ . GYSELA results are also found to well agree with the analytical model presented in Chapter 2 which is derived in the low collisionality and large aspect ratio limit.

# 4. Effect of magnetic ripple on toroidal rotation in presence of turbulence

## Table of contents

4.1. Introduction . . . . .	102
4.2. Reduced model for the competition between neoclassical effects and turbulence . . . . .	103
4.2.1. Turbulent coefficients using GYSELA simulations without ripple	106
4.2.2. Assessing the competition thanks to simulations with ripple . .	109
4.2.3. An heuristic expression for the critical ripple amplitude . . . . .	110
4.3. Interplay mechanisms between ripple and turbulence . . . . .	112
4.3.1. Ripple impact on the turbulent intensity . . . . .	114
4.3.2. Impact of ripple on the shear of radial electric field . . . . .	118
4.4. Conclusion of chapter 4 . . . . .	120

In this chapter, the turbulence is considered in addition to the neoclassical and stochasticity effects due to the magnetic ripple alone (as studied in the previous chapter). Particular attention is paid to the resulting toroidal velocity, even though the magnetic ripple also impacts the radial electric field and the poloidal velocity. The reason is that the main effect of ripple is to add a new force in the toroidal direction, forcing the mean toroidal velocity toward a finite value. The objective is then to see what is the effective drive of this rotation when turbulence is also accounted for, as it also acts as a rotation drive. The content of the following is published in [88].

## 4.1. Introduction

Toroidal rotation plays a key role in the confinement properties of tokamak plasmas. Indeed, numerous experiments have highlighted the link between plasma rotation and improved plasma performance [21, 26, 89–91]. On most medium size tokamaks, rotation is controllable using the external torque exerted by tangential neutral beam injection. However in reactor-size tokamaks, including ITER, external torque is expected to be small [22], so the plasma rotation will likely be driven by intrinsic plasma mechanisms. Intrinsic generation of rotation results from symmetry breaking [92]. Therefore, toroidal asymmetry of the magnetic field plays a leading role in rotation

#### 4. Effect of magnetic ripple on toroidal rotation in presence of turbulence – 4.2. Reduced model for the competition between neoclassical effects and turbulence

drive, as realistic magnetic configurations always include non-axisymmetric perturbations. They result from error fields due to coil misalignment, magnetohydrodynamic instabilities, externally applied perturbations, or magnetic field modulations due to the finite number of toroidal coils, called *ripple*. We here focus on the latter. Toroidal magnetic ripple constrains the toroidal torque through magnetic braking, i.e. the force resulting from the magnetic field inhomogeneity on particle magnetic moments. This force substantially changes the plasma rotation even for small amplitude perturbations [24]. The resulting torque, called *Neoclassical Toroidal Viscosity*, and its impact on toroidal rotation have been experimentally observed [25, 73, 93–95] and widely studied theoretically [30, 42, 54, 56–59, 61, 62, 96–99] as well as numerically [72, 80, 100–102]. Turbulence can also be responsible for intrinsic rotation of the plasma. However a symmetry-breaking mechanism is also required, which can be either a background  $E \times B$  shear [103], an up-down asymmetry [104] or a shear of turbulent intensity [105]. While this turbulent drive has also been extensively studied [92, 103–116], the possible competing and/or synergetic effects of extrinsic (ripple) versus self-generated (turbulence) asymmetries on rotation has drawn little [117] attention so far. Consequences are of prime importance, since any modification of mean flows impacts the radial electric field, and therefore also the transition toward improved confinement regimes [118]. In this thesis, the ripple amplitude threshold  $\delta_c$  below which turbulence governs plasma flows is estimated theoretically, first without any cross-talk between ripple and turbulence. This estimation is in agreement with non-linear gyrokinetic simulations using the GYSELA code [76] and leads to a proposed simple expression. Secondly, the interplay between turbulence and ripple regarding the toroidal velocity is studied thanks to comprehensive gyrokinetic GYSELA simulations. As main results, it is found that the modification of the spectral intensity by ripple through mode-coupling is found negligible. However, ripple is found to modify the toroidal Reynolds stress through the shear of radial electric field.

## 4.2. Reduced model for the competition between neoclassical effects and turbulence

Based on the complete toroidal angular momentum conservation [81, 107], one can write a simplified expression of the toroidal momentum evolution keeping the dominant terms (cf. Appendix E). Expressed within the large aspect ratio limit, i.e.  $\varepsilon = r/R_0 \ll 1$  with  $R_0$  the tokamak major radius<sup>1</sup>, the ripple and turbulent contributions to the toroidal velocity  $V_T$  evolution read as follow:

$$\partial_t V_T = \mathcal{M} - r^{-1}(r\Pi)' \quad (4.1)$$

where a prime stands for the derivative along the radial coordinate  $r$ ,  $\mathcal{M}$  is the magnetic braking force and  $\Pi$  is the turbulent radial flux of toroidal momentum, called toroidal Reynolds stress. Each contribution deserves some attention.

1. For a reminder of the toroidal coordinates and geometrical main quantities, see Fig.1.8.



4. Effect of magnetic ripple on toroidal rotation in presence of turbulence – 4.2.  
Reduced model for the competition between neoclassical effects and turbulence

Magnetic braking is derived within neoclassical theory, i.e. a kinetic derivation describing the resonant enhancement of collisional transport processes. A well-established result of this theory in axisymmetric configurations is the degeneracy between the toroidal velocity  $V_T$  and the radial electric field  $E_r$ . Ripple breaks axisymmetry, leading to non-ambipolar diffusion of particles and heat [30]. The resulting radial electric field constrains the toroidal torque through magnetic braking  $\mathcal{M}$ , removing the degeneracy. Magnetic braking is defined as the following fluid moment of the ion distribution function  $F$ :

$$\mathcal{M} = \frac{-1}{nm} \left\langle \int d^3v R \nabla \varphi \cdot \nabla (\mu \tilde{B}) F \right\rangle \quad (4.2)$$

where  $\langle \cdot \rangle$  denotes a flux surface average,  $\varphi$  the toroidal angle,  $\mu$  the magnetic moment,  $m$  the particle mass,  $n$  the density and  $R = R_0 + r \cos(\theta)$ . The toroidal perturbation of the magnetic field amplitude due to ripple reads  $\tilde{B} = B(r, \theta) \delta(r, \theta) \cos(N_c \varphi)$ , where  $\theta$  is the poloidal angle,  $B$  the axisymmetric magnetic field amplitude,  $\delta$  the ripple amplitude and  $N_c$  the number of toroidal coils.  $\mathcal{M}$  is thus the force due to toroidal asymmetry of the magnetic field, which is related to the torque  $T_{\mathcal{M}}$  defined in 3.3.3 by the relation  $T_{\mathcal{M}} \simeq mnR\mathcal{M}$ . It takes the form of a friction [30]:

$$\mathcal{M} = -v_\varphi (V_T - V_{\text{neo}}) \quad (4.3)$$

where  $V_{\text{neo}}$  is the target velocity fixed by collisional processes (see Sec.2.6.2 and Eq(2.60)) and  $v_\varphi$  is the magnetic drag coefficient (see Sec.2.6.3). The former, roughly independent of  $\delta$  as reflected by results in Fig.3.7, is in the counter-current direction as the non-ambipolar particle flux results in a negative  $E_r$  [54, 58]. Both  $V_{\text{neo}}$  and  $v_\varphi$  are predicted by neoclassical theory. In the absence of turbulence,  $V_T$  dynamic is then governed by the magnetic drag coefficient  $v_\varphi$  which depends on the ripple amplitude  $\delta$ .

The other drive mechanism is turbulence through the toroidal Reynolds stress  $\Pi$ . It is defined as a fluid moment of the distribution function:

$$\Pi = \frac{1}{n} \left\langle \int d^3v (v_\varphi v_{E_r}) F \right\rangle \quad (4.4)$$

where  $v_\varphi = R(\mathbf{b} \cdot \nabla \varphi) v_{\parallel}$  with  $\mathbf{b} = \mathbf{B}/B$  and  $v_{E_r} = -B^{-1} \partial_\theta \phi$  with  $\phi$  the electric potential. Keeping only turbulent contributions, the toroidal component of the stress tensor can be expressed as follow [105, 111, 112]:

$$\Pi = -\chi V_T' + \mathcal{V} V_T + \Pi_{\text{res}} \quad (4.5)$$

where  $\chi$  is a turbulent viscosity coefficient,  $\mathcal{V}$  a momentum pinch coefficient and  $\Pi_{\text{res}}$  the residual stress. The latter describes the momentum exchange between waves and particles, which acts as the only source of intrinsic plasma rotation in the axisymmetric case.

4. *Effect of magnetic ripple on toroidal rotation in presence of turbulence – 4.2. Reduced model for the competition between neoclassical effects and turbulence*

We want to gain insight into flows at equilibrium, which we here define as a quasi-stationary turbulent state. Combining previous mechanisms, i.e. magnetic braking and turbulence, the equilibrium toroidal velocity  $V_{T\text{eq}}$  reads:

$$V_{T\text{eq}} = \frac{v_\phi V_{\text{neo}} - r^{-1}(r\Pi_{\text{res}})'}{v_\phi + \chi\lambda_\nu + \mathcal{V}\kappa_\nu} \quad (4.6)$$

with  $\lambda_\nu = -(r\chi V'_{T\text{eq}})/(r\chi V_{T\text{eq}})$  and  $\kappa_\nu = (r\mathcal{V}V'_{T\text{eq}})/(r\mathcal{V}V_{T\text{eq}})$ . As discussed below, this equation allows one to estimate the ripple amplitude for which magnetic braking overcomes turbulence. Note that any interplay between ripple and turbulence is not considered here, but will be discussed later. Since  $v_\phi$  is an increasing monotonic function of the ripple amplitude  $\delta$  (as reflected by results in Fig.3.8), neoclassical terms vanish at low ripple, i.e.  $\delta \rightarrow 0$ , so that  $V_{T\text{eq}} \rightarrow V_{\text{turb}} = -\frac{r^{-1}(r\Pi_{\text{res}})'}{\chi\lambda_\nu + \mathcal{V}\kappa_\nu}$ . At high ripple, i.e.  $\delta \rightarrow \infty$ , turbulent terms become negligible so that  $V_{T\text{eq}} \rightarrow V_{\text{neo}}$ . Computing  $V_{T\text{eq}}$  as a function of the ripple amplitude requires solving a transport equation, i.e. the use of kinetic simulation codes. However a “critical ripple” amplitude  $\delta_c$  can be devised such that magnetic braking is dominant when  $\delta > \delta_c$ . As shown Fig.4.1, this critical value can be defined as  $V_{T\text{eq}}(\delta_c) = (V_{\text{neo}} + V_{\text{turb}})/2$ . This value is then the ripple amplitude above which the toroidal velocity becomes closer to its neoclassical prediction than its turbulent prediction. The critical ripple amplitude  $\delta_c$  is then defined by

$$v_\phi(\delta_c) = |\lambda_\nu|\chi_{\text{eff}} \quad (4.7)$$

with the effective viscosity defined as  $\chi_{\text{eff}} = \chi + (\kappa_\nu/\lambda_\nu)\mathcal{V}$ .

4. Effect of magnetic ripple on toroidal rotation in presence of turbulence – 4.2.  
 Reduced model for the competition between neoclassical effects and turbulence

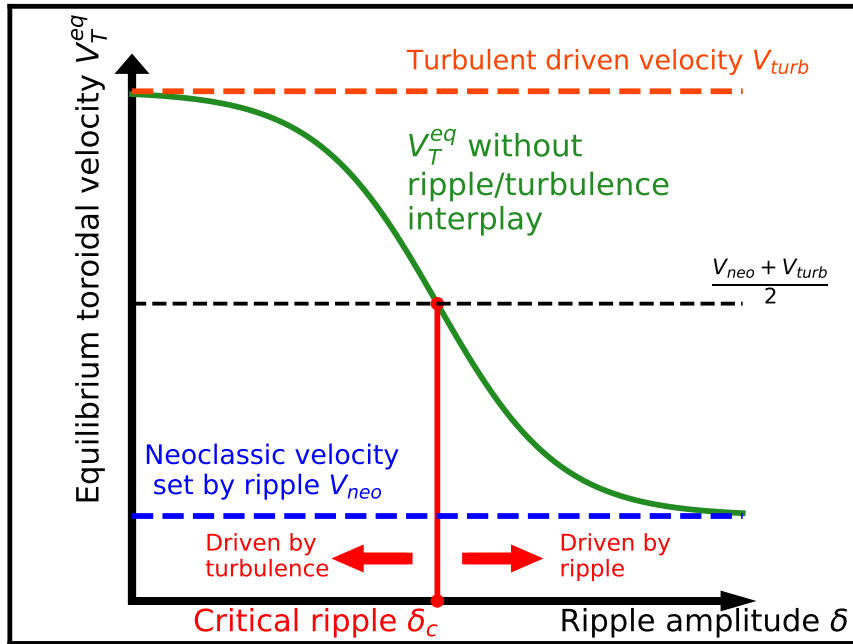


Figure 4.1. – Sketch of the proposed simplified definition for the critical ripple amplitude describing the neoclassical/turbulence competition. The synergistic effects are not accounted for here, but are detailed further below.

#### 4.2.1. Turbulent coefficients using GYSELA simulations without ripple

As already mentioned, predictions on  $v_\phi$  and its dependence on  $\delta$  are known (see Sec.2.6.3). Conversely, there are so far no reliable analytical predictions about  $\chi$  and  $\mathcal{V}$ . For given plasma parameters, determining those coefficients is actually an active topic of both experimental and theoretical research. Here they are determined with four gyrokinetic simulations of ITG turbulence with four different initial toroidal velocity profiles, performed with adiabatic electrons, of a typical Tore Supra discharge [119] without ripple (i.e.  $\delta = 0$ ).

The main input parameters and initial profiles used in GYSELA flux-driven simulations in this chapter are presented in Tab.4.1 and Fig.4.2.

4. Effect of magnetic ripple on toroidal rotation in presence of turbulence – 4.2.  
Reduced model for the competition between neoclassical effects and turbulence

Turbulence	ITG only
Electron response	Adiabatic
Aspect ratio	3.2
$\nabla n$ at $\rho = 0.65$	$R_0/L_N = 2.2$
$\nabla T$ at $\rho = 0.65$	$R_0/L_T = 8$
Collisionality at $\rho = 0.65$	$\nu^* = 0.14$
$\rho_i/a$ at $\rho = 0.65$	$\rho^* = 1/250$

Table 4.1. – Simulation parameters.  $L_N$  and  $L_T$  are the density and temperature gradient length and  $\rho_i$  the ion Larmor radius.

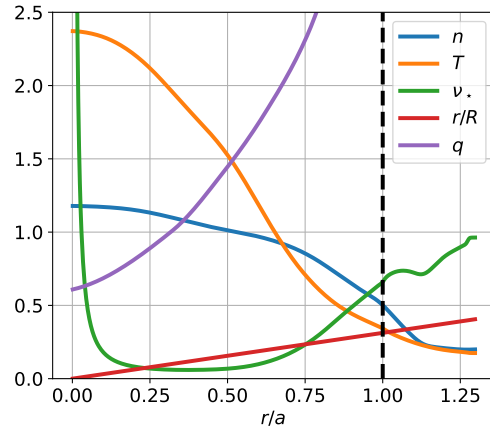


Figure 4.2. – Initial profiles in simulations.

Taking advantage of the  $\Pi$  structure Eq(4.5),  $\chi$  and  $\mathcal{V}$  are determined for each radius using a least square method on the resulting  $V_T$ ,  $V_T'$  and  $\Pi$  profiles, displayed on Fig.4.3, and initialized with different toroidal velocities. Note that such analysis is done after saturation of turbulence. As indicated by the clear correlation between Reynolds stress and toroidal velocity shear, the viscosity term is dominant. The viscosity resulting from this least square regression is plotted in Fig.4.4. As  $\Pi$  cancels near midradius for each simulation, the evaluation near this radial area is incorrect. Invoking continuity properties, the viscosity in this zone is reconstructed using splines and gives the final profile of  $\chi$  (plotted in orange). In addition, at  $r/a \approx 0.5$ ,  $V_T'$  vanishes and  $\Pi$  reaches the same value for each simulation. Since  $V_T$  is extremal at this radial position, while the pinch contribution is linear with  $V_T$ , it can be concluded that the pinch term in these simulated cases is negligible. This has already been observed in gyrokinetic simulations with adiabatic electrons [92]. The Reynolds stress  $\Pi$  is then dominated by the residual stress at vanishing  $V_T'$ . Note however that in experiments, the pinch contribution can be significant and actually plays an important role in determining the radial profile of  $V_T$ . In the following we then consider  $\chi_{\text{eff}} = \chi$  with  $\chi$  the turbulent viscosity of Fig.4.4 (orange curve).

4. Effect of magnetic ripple on toroidal rotation in presence of turbulence – 4.2.  
Reduced model for the competition between neoclassical effects and turbulence

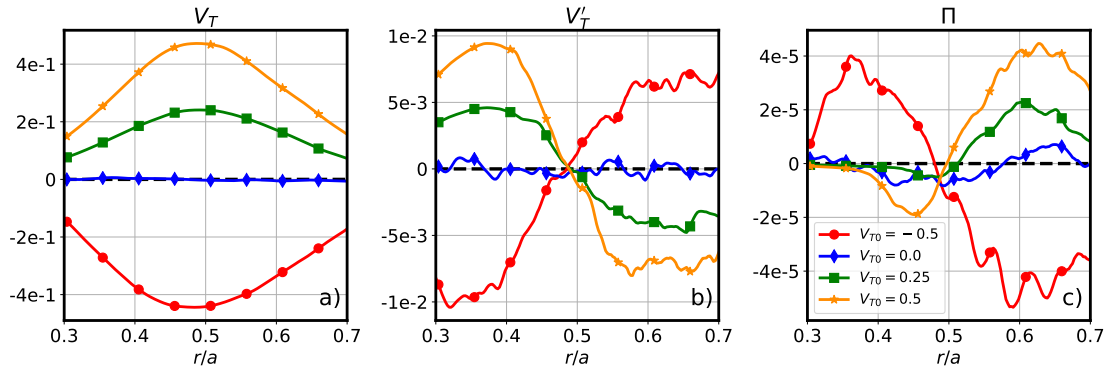


Figure 4.3. – Radial profiles of the toroidal velocity  $V_T$  **(a)** and its shear  $V'_T$  **(b)**, as well as the stress tensor  $\Pi$  **(c)**, taken at turbulent saturation for simulations without ripple and with different initial toroidal velocity profiles  $V_T(t=0) = V_{T0} \exp((-32(r/a - 0.5)^2)$  with  $a$  the minor radius. Velocities are normalized to a reference ion thermal velocity  $V_{T0}$  and lengths to a reference ion Larmor radius  $\rho_0$ .

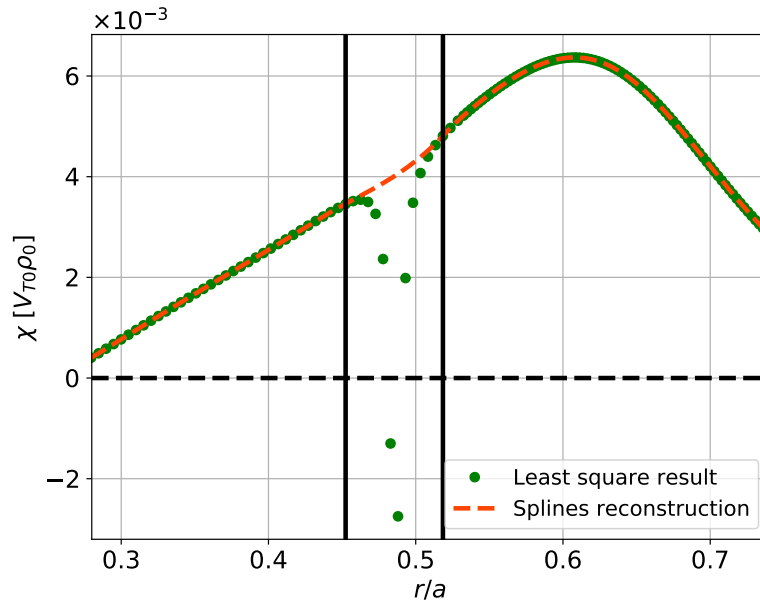


Figure 4.4. – Evaluation of the turbulent viscosity  $\chi$  by the least square method using profiles of Fig.4.3 obtained using GYSELA simulations without ripple for plasmas parameters summarized in Tab.4.1 (green). The incorrect points due to a lack of proper statistics at midradius are removed and this zone is reconstructed using splines, giving the final  $\chi$  profile (orange). Distances are normalized to a reference Larmor radius  $\rho_0$ .

### 4.2.2. Assessing the competition thanks to simulations with ripple

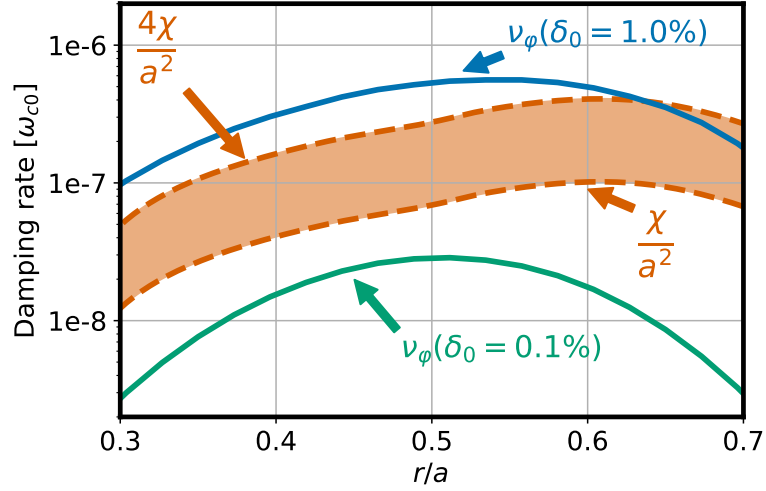


Figure 4.5. – Comparison of the theoretical prediction of  $v_\phi$  in presence of ripple of different amplitude (green and blue lines) and the turbulent viscous contribution  $\chi|\lambda_\nu|$  (orange) to assess Eq(4.7). The orange zone represents  $\chi|\lambda_\nu|$  for  $a/2 \leq |\lambda_\nu|^{-1/2} \leq a$ . Time is normalized to the cyclotron period  $\omega_{c0}^{-1}$ .

In order to determine  $\delta_c$  in the specific plasma conditions studied in this work (Tab.4.1) and test its proposed definition Eq(4.7), two additional simulations with finite ripple (and consequently finite magnetic drag) such that  $v_\phi \ll \chi|\lambda_\nu|$  and  $v_\phi \gg \chi|\lambda_\nu|$  were run. Since the physics of the boundary acts as a complex momentum sink, controlled by orbit losses, momentum flux carried by waves [120] and scrape-off layer interactions, a model ripple amplitude is chosen with a radially Gaussian envelope centered at midradius:  $\delta(r) = \delta_0 \exp\{-32(r/a - 0.5)^2\}$  and a number of coils  $N_c = 16$ . This ensures a disentanglement between boundary conditions and intrinsic physics in a controlled way. With this ripple amplitude structure, and the knowledge of the turbulent viscosity  $\chi$ , an estimation for the peak ripple amplitude  $\delta_0$  such that  $\delta_0 = \delta_c(r/a = 0.5)$  is possible. As  $|\lambda_\nu|$  is difficult to estimate, it is approximated that  $|\lambda_\nu|^{-1/2}$  scales as the system size such that the true value is expected in the wide range  $a/2 \leq |\lambda_\nu|^{-1/2} \leq a$ . This is consistent with experimental measurements in Tore Supra [28]. It then appears that the critical ripple amplitude at midradius for this particular turbulence is  $\delta_c(r/a = 0.5) \approx 0.5\%$ . In these two additional simulations, the midradius ripple amplitudes are  $\delta_0 = 0.1\%$  and  $\delta_0 = 1\%$ . Fig.4.5 displays the magnetic drag  $v_\phi$ , from model presented in Sec.2.6.3, associated to these simulations (blue and green lines) as well as the turbulent contribution  $\chi|\lambda_\nu|$ .

The time evolution near midradius of the toroidal velocity  $V_T$  and the radial electric field  $E_r$  for each case - without ripple and the  $\delta_0 = [0.1\%, 1\%]$  cases - is shown in

4. Effect of magnetic ripple on toroidal rotation in presence of turbulence – 4.2. Reduced model for the competition between neoclassical effects and turbulence

Fig.4.6. The  $\delta_0 = 0.1\%$  case exhibits no significant difference with the axisymmetric case  $\delta_0 = 0\%$ , neither regarding  $V_T$  nor  $E_r$ . Conversely, the toroidal velocity in the  $\delta_0 = 1\%$  case, evolving deeply in the counter-current direction, suggests that  $V_T$  is driven by magnetic braking. Also,  $E_r$  increases roughly by a factor 1.5.

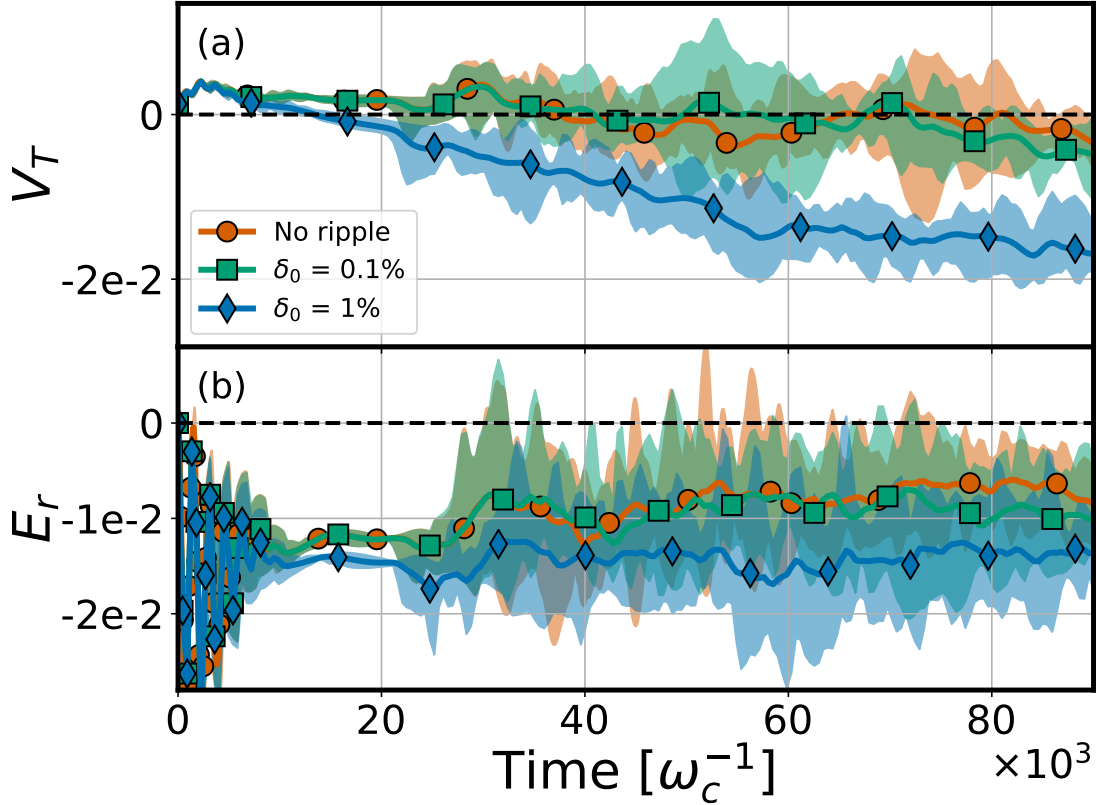


Figure 4.6. – Time traces of the toroidal velocity  $V_T$  (a) and the radial electric field  $E_r$  (b) in  $0.45 < r/a < 0.55$  (shaded areas, mean: solid lines) for different ripple amplitudes. Markers are only here for better visibility.

### 4.2.3. An heuristic expression for the critical ripple amplitude

The critical ripple amplitude stands out as a practical landmark to determine the main driving flow mechanism. All the elements of the relation  $v_\varphi(\delta_c) = |\lambda_\nu| \chi_{\text{eff}}$  may not be known, in particular because the viscosity and pinch profiles are difficult to obtain experimentally. Here a rule of thumb is proposed to evaluate the order of magnitude of  $\delta_c$ . Let us address the approximations used to obtain it. First, one can fairly approximate the magnetic drag to its asymptotic value in the *ripple-plateau* regime of collisionality [30]. In most tokamaks, including ITER, this regime is the most relevant and states that  $v_\varphi^{\text{RP}} \sim \frac{N_c V_{\text{th}}}{R} \delta^2$  where  $V_{\text{th}}$  is the ion thermal velocity. There is more uncertainty regarding a proxy for the effective viscosity. Nevertheless, one can consider a gyroBohm scaling  $\chi_{\text{eff}} \sim \frac{\rho_i^2 V_{\text{th}}}{L_T}$  where  $L_T$  is the temperature gradient length

4. Effect of magnetic ripple on toroidal rotation in presence of turbulence – 4.2.  
Reduced model for the competition between neoclassical effects and turbulence

and  $\rho_i$  the ion Larmor radius.

The validity of these approximations was verified with GYSELA simulations. On the one hand, the turbulent viscosity  $\chi$  was checked in the simulations without ripple described previously. A radial profile of the ratio  $\chi/\chi_{GB}$  is presented in Fig.4.7a (blue line). For further validation, the Prandtl number  $\chi/\chi_{HF}$ , where  $\chi_{HF}$  is the heat diffusivity, is also plotted (orange line). Indeed,  $\chi_{HF}$  is also expected to follow the gyroBohm scaling and simulations show good agreement in order of magnitude. The gyroBohm scaling then stands out as a proper proxy for the turbulent viscosity. On the other hand, the neoclassical friction  $v_\phi$  has been tested in GYSELA in dedicated simulations without turbulence, presented in Sec.3.3.4, with radially gaussian ripple amplitude equal to 0.5%, 1% and 3% at maximum. The radial profile for the 1% case of the resulting friction  $v_\phi^{GYS}$  is presented in Fig.4.7b (red lines) and compared with the asymptotic prediction for the ripple-plateau regime  $v_\phi^{RP}$  (blue). It appears that  $v_\phi^{GYS} \sim v_\phi^{RP}$  for a wide range of collisionalities. It should be stressed that the prediction on  $v_\phi$  used in the Fig.4.5 of the manuscript for validating the critical ripple amplitude is not this asymptotic value but rather from the reduced model developed in Chapter 2.

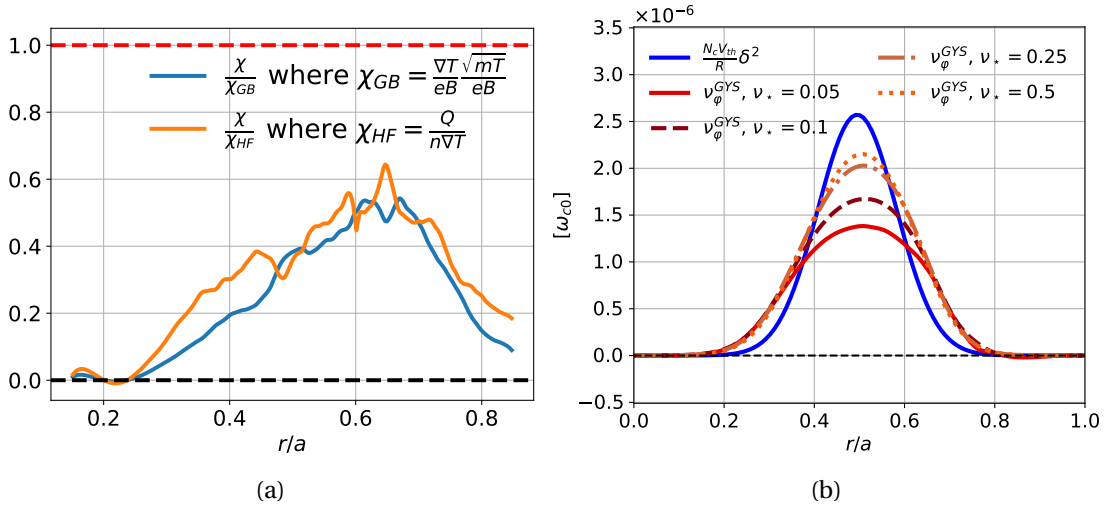


Figure 4.7. – (a) Radial profiles obtained in GYSELA of the turbulent viscosity  $\chi$  normalized to the gyroBohm viscosity  $\chi^{GB}$  (blue) and heat diffusivity  $\chi^{HF}$  (orange). (b) Radial profiles obtained in GYSELA (red) of the neoclassical friction at  $\delta_0 = 1\%$  for different  $\nu^*$  (estimated at  $r/a = 0.5$ ) and its asymptotic prediction (blue).

Finally, Fig.4.8 shows the ratios  $v_\phi^{GYS}/\chi$  and  $v_\phi^{RP}/\chi^{GB}$  for different ripple amplitudes, here taken at  $r/a = 0.5$  in simulations. Each red point on this plot is the result of 8 gyrokinetic simulations. It is found that these estimates become less accurate with increasing ripple amplitude but hold remarkably well for  $\delta$  up to a 1%, which is hardly



#### 4. Effect of magnetic ripple on toroidal rotation in presence of turbulence – 4.3. Interplay mechanisms between ripple and turbulence

exceeded in most tokamaks.

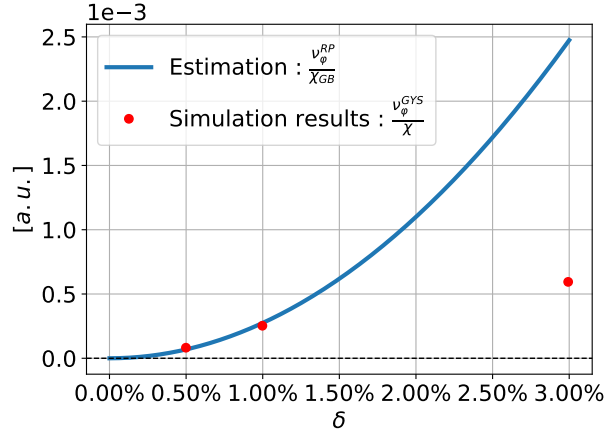


Figure 4.8. – Ripple amplitude scan of  $v_\phi^{GYS}/\chi$  (red points) and  $v_\phi^{RP}/\chi^{GB}$  (blue line).

In short, magnetic braking follows the standard neoclassical theory and the gyroBohm scaling fits the turbulent viscosity in magnitude. It indicates that the proposed approximations hold in the parameter range of our simulations. Under these hypotheses, i.e.  $v_\phi^{RP} \sim |\lambda_\nu| \chi^{GB}$ , the critical ripple amplitude can be estimated as

$$\delta_c \sim \rho_\star \mathcal{E} \left( \frac{1}{N_c} \frac{R}{L_T} R^2 |\lambda_\nu| \right)^{1/2} \quad (4.8)$$

where  $\mathcal{E} = a/R_0$  is the inverse aspect ratio and  $\rho_\star = \rho_i/a$ . An application on a Tore Supra ohmic discharge at  $r/a = 0.8$  with  $\rho_\star^{-1} = 700$ ,  $R/L_T = 12$ ,  $N_c = 18$ ,  $\mathcal{E} = 3.2$  and  $R_0 |\lambda_\nu|^{1/2} \sim 11.25$  [28] gives  $\delta_c \approx 0.4\%$  which is way lower than the actual ripple amplitude in Tore Supra at this location (see Fig.2.3). Consistently the equilibrium rotation and radial electric field are found to be ruled by ripple [29]. One could argue that such a critical ripple could only be reached in Tore Supra as its ripple is significantly higher than in most other tokamaks. However, the ripple in ITER is actually expected to exceed 1% at the edge in some scenarios according to the recent [ITER Research Plan within the Staged Approach](#) (see Appendix F.3 therein). With the ferritic inserts meant to decrease the peak ripple amplitude from  $\delta \sim 1.2\%$  to  $\delta \sim 0.3\%$  for discharges at  $B = 5.3T$ , for the discharges at  $B = 1.8T$  these inserts will overcompensate the ripple amplitude that will peak at  $\delta \sim 1.3\%$ . The critical ripple amplitude could then be crossed near the edge for future fusion devices.

### 4.3. Interplay mechanisms between ripple and turbulence

So far, magnetic braking and turbulent stress were computed separately in the model, ignoring any cross-talk. In this section, the interplay between turbulence

4. Effect of magnetic ripple on toroidal rotation in presence of turbulence – 4.3.  
Interplay mechanisms between ripple and turbulence

and magnetic braking is addressed. This study relies on three simulations performed with different ripple amplitudes, which are the  $\delta_0 = 0\%$  (i.e. without ripple) and  $\delta_0 = 1\%$  cases discussed in the previous section, as well as a new  $\delta_0 = 3\%$  very high ripple amplitude case. On the one hand, based on Eq(4.2), the effect of turbulence on magnetic braking  $\mathcal{M}$  is observed to be negligible as ripple wave numbers are non-resonant with wavelengths related to turbulence, hence hardly generated via mode-coupling. On the other hand, magnetic braking is found to impact the turbulent momentum transport  $-r^{-1}(r\Pi)'$ . It is known that the residual stress is predicted to depend on the radial shear of the turbulent intensity and the  $E \times B$  drift radial shear [105, 111] whilst turbulent viscosity depends only on the former.

At this point, it is worth making a little digression on the nature of the considered turbulent viscosity and residual stress obtained with GYSELA simulations. A common expression of the residual stress is  $\Pi_{\text{res}}^{\text{tot}} = -C\chi_{\text{turb}}\partial_r V_E$  where  $\chi_{\text{turb}}$  is a turbulent viscosity that slightly differs from the one obtained in simulations,  $C$  is a constant depending on geometrical parameters and  $V_E = -E_r/B$ . The force balance states that  $E_r = \frac{\partial_r P}{Ne} + V_T B_P - V_P B_T$ . The residual stress can then be split into a diamagnetic part and another part proportional to  $\partial_r V_T$ . Assuming  $\partial_r \ln(B_P/B) \ll \partial_r \ln V_T$ , one could then rewrite the total toroidal stress tensor [115] as

$$\Pi = - \underbrace{\left( \chi_{\text{turb}} - C\chi_{\text{turb}} \frac{B_P}{B} \right)}_{\chi} \partial_r V_T + \frac{C\chi_{\text{turb}}}{B} \partial_r \left( \frac{\partial_r P}{Ne} - V_P B_T \right) \quad (4.9)$$

meaning that the part of the residual stress proportional to  $\partial_r V_T$  can be included in the viscous term by defining the viscosity  $\chi = \chi_{\text{turb}}(1 - C\frac{B_P}{B})$  which is actually the one obtained with simulations. Indeed, to recover the viscosity a scan in  $\partial_r V_T$  was done (see Fig.4.3). It gave the contribution proportional to  $\partial_r V_T$  which we called viscosity  $\chi$ , and the contribution not proportional to  $\partial_r V_T$  which we called  $\Pi_{\text{res}}$  that can then only come from the diamagnetic part. Note that "our" viscosity  $\chi$  is the right quantity for this particular study, as separating the toroidal Reynolds stress in contributions proportional to  $V_T$  and  $\partial_r V_T$  is necessary to make use of Eq(4.6) which is the starting point for obtaining the critical ripple amplitude expression Eq(4.7).

For the following, we call "residual stress" only this diamagnetic part. This residual stress can be expressed as:

$$\Pi_{\text{res}} = \sum_k k_{\parallel} k_{\theta} \left| \frac{e\phi_k}{T} \right|^2 \tau_k \quad (4.10)$$

where  $\phi_k$  are the Fourier components of the electric potential,  $T$  the thermal energy,  $k_{\parallel}$  and  $k_{\theta}$  the parallel and poloidal wave numbers and  $\tau_k$  a form factor [121]. Ripple can impact the residual stress by retro-acting on the turbulent spectral amplitude  $|\phi_k|^2$ , which is related to the turbulent intensity  $\mathcal{I}$ , or the radial shear of  $E_r$  through the parallel wave number  $k_{\parallel}$ .

This model for  $\Pi_{\text{res}}$  comes from a mean-field theory which holds when  $E_r$  and  $\mathcal{I}$  are

#### 4. Effect of magnetic ripple on toroidal rotation in presence of turbulence – 4.3. Interplay mechanisms between ripple and turbulence

averaged over multiple turbulent structure lengths and correlation times, defining the coarse-grain average labeled  $\langle \cdot \rangle_{CG}$ . This is done by time averaging over  $10^5$  cyclotron periods, i.e. about 50 correlation times, and performing a sliding radial average with a  $50\rho_i$  window, i.e. about 5-6 correlation lengths. The residual stress profile is calculated as  $\Pi_{res} = \Pi + \chi V_T'$  using the previously obtained viscosity (see Fig.4.4). Since the initial toroidal velocity in these simulations is zero, the viscous term is subdominant, as displayed in Fig.4.9 showing the radial profile of coarse-grained total toroidal Reynolds stress and calculated residual stress.

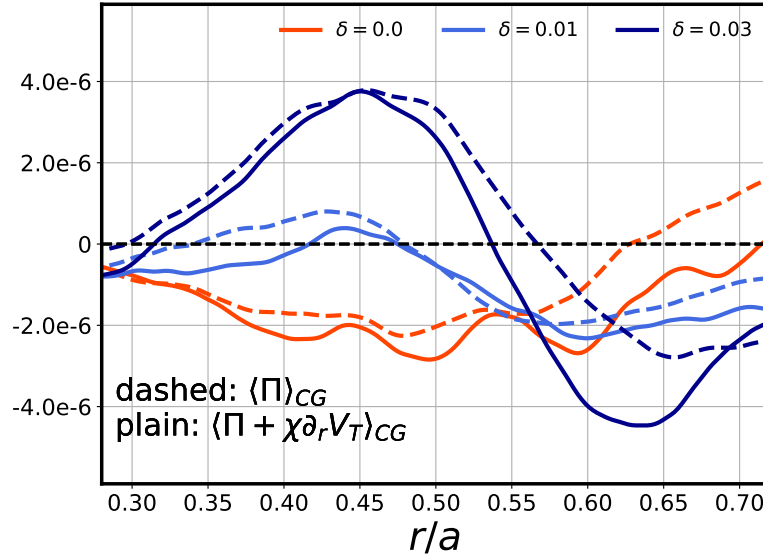


Figure 4.9. – Radial profile of the coarse-grained total toroidal stress tensor  $\langle \Pi \rangle_{CG}$  (dashed) and the coarse-grained diamagnetic part of the residual stress  $\langle \Pi + \chi \partial_r V_T \rangle_{CG}$  (plain).

In this same figure, it appears that  $\Pi_{res}$  grows monotonically with  $\delta$  and changes sign. As mentioned above, the next step consists in linking this behavior with an impact of ripple on either the turbulent intensity shear  $\mathcal{I}'$  or the radial electric field shear  $E_r'$ .

##### 4.3.1. Ripple impact on the turbulent intensity

The modification of the spectral intensity  $|\phi_k|^2$  is expected through toroidal mode coupling between turbulence and electric potential fluctuations induced by the magnetic toroidal perturbation due to ripple. Turbulent resonant modes of the electric potential are located around  $n = -m/q$  line, forming a *resonance cone*, in the  $(m, n)$  space where  $m$  and  $n$  are the poloidal and toroidal mode numbers respectively. These mode numbers are related to the wave numbers by  $k_{\parallel} = R^{-1}(n + m/q)$  and  $k_{\theta} = m/r$ .

Magnetic ripple also accounts for destabilization of poloidally uniform modes, i.e.  $m = 0$ , with a toroidal periodicity equal to a harmonic of the number of coils, i.e.

4. Effect of magnetic ripple on toroidal rotation in presence of turbulence – 4.3.  
*Interplay mechanisms between ripple and turbulence*

$n = kN_c$ ,  $k \in \mathbb{Z}^*$ . These modes  $(0, kN_c)$  can then couple to a resonant one  $(m_0, n_0)$  to form a non-zero  $(m_0, n_0 + kN_c)$  mode, and vice versa. A visual representation of this coupling is presented in Fig.4.10 which displays the  $(m, n)$  spectra of  $|\phi_{m,n}|^2$  for different ripple amplitudes in simulations. An increasing ripple amplitude translates into a more populated spectrum in the  $m = 0$  vicinity. These new modes are coupled to modes in the resonant cone, accounting for the checkerboard structure near the ripple harmonics due to the relatively low resolution for the toroidal modes. Whilst visually impressive, one has to notice the logarithmic scale.

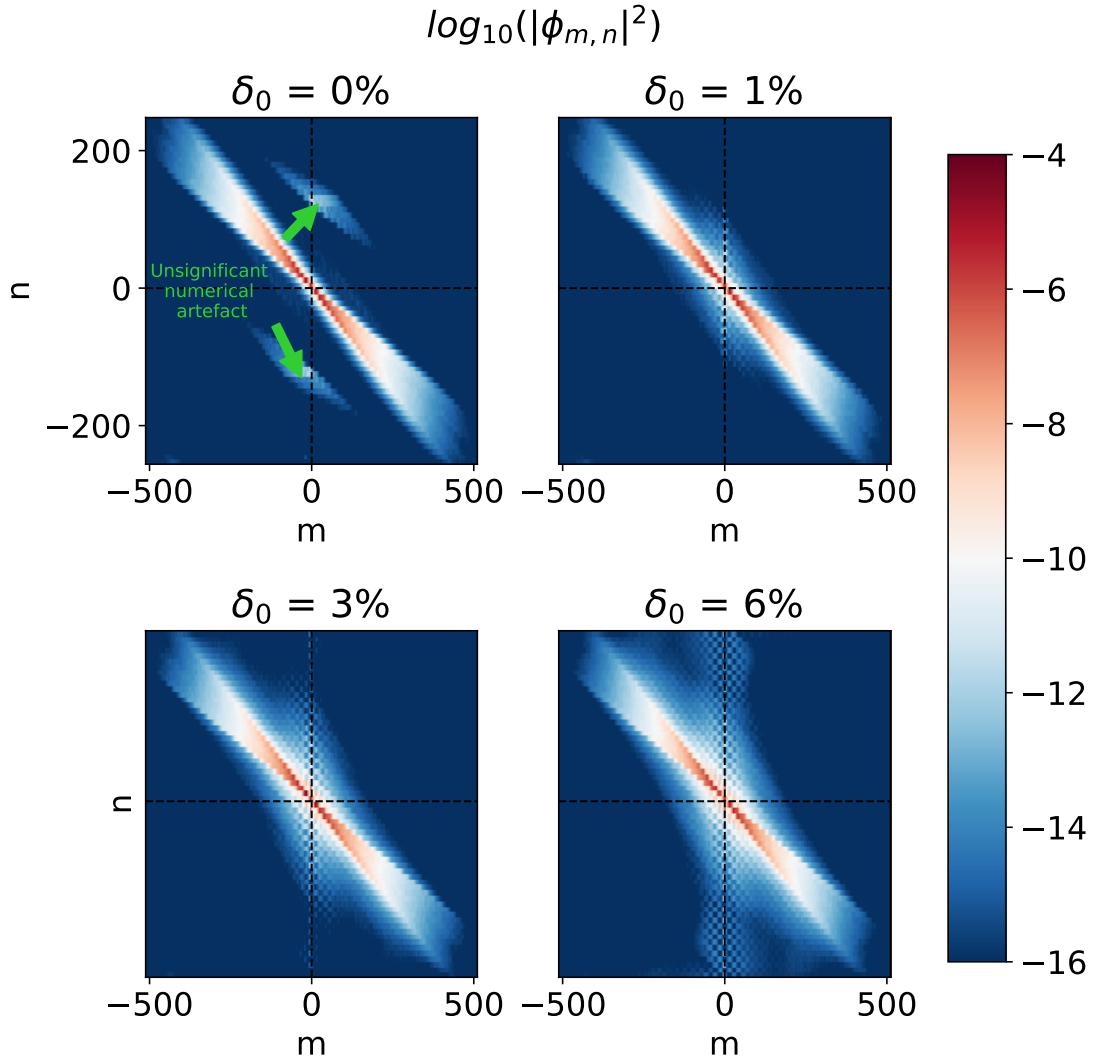


Figure 4.10. – Spectra of  $|\phi_{m,n}|^2$  in the  $(m, n)$  space taken at  $r/a = 0.65$ .

There are some reasons to think that ripple can significantly modify the residual stress through mode coupling. In simulations, ripple is responsible for lowering the amplitude of modes in the resonant cone. Indeed, as defined in Fig.4.11, one can choose an arbitrary  $\delta r = 0.1a$  (with  $a$  the minor radius) such that the cone is delimited

4. Effect of magnetic ripple on toroidal rotation in presence of turbulence – 4.3.  
Interplay mechanisms between ripple and turbulence

by the lines  $n = -m/q_{in}$  and  $n = -m/q_{out}$  where  $q_{out}, q_{in} = q(r \pm \delta r)$ .

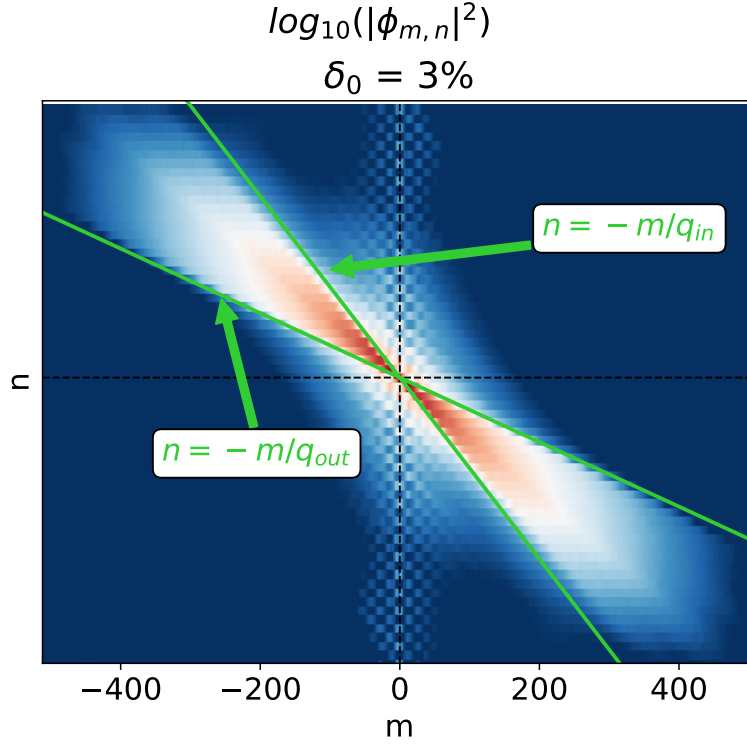


Figure 4.11. – Spectra of  $|\phi_{m,n}|^2$  in the  $(m, n)$  space taken at  $r/a = 0.65$  for the  $\delta_0 = 3\%$  case. The resonance cone is defined by the lines  $n = -m/q_{in}$  and  $n = -m/q_{out}$  where  $q_{out}/q_{in} = q(r \pm \delta r)$  with an arbitrary  $\delta r = 0.1a$

One can then consider the quantity  $S(m) = \frac{\sum_{n \in C(m)} |\phi_{m,n}|^2}{m(q_{out}^{-1} - q_{in}^{-1})}$  where  $C(m) = \left[ -\frac{m}{q_{in}}; -\frac{m}{q_{out}} \right]$  is containing all the modes in between the two green lines in Fig.4.11 and a vertical line at abscissa  $m$  (not represented on the figure). It represents the turbulent spectral intensity associated with a mode number  $m$ . Fig.4.12 displays  $S$  versus the poloidal wave number  $k_\theta$  for different ripple amplitudes and its relative difference with the case without ripple  $\delta_0 = 0\%$ . Adding ripple then tends to diminish the spectral intensity in the resonant cone, especially for high mode numbers. There is however no clear effect for the large-scale modes (i.e. low  $k_\theta \rho_i$ ).

4. Effect of magnetic ripple on toroidal rotation in presence of turbulence – 4.3.  
Interplay mechanisms between ripple and turbulence

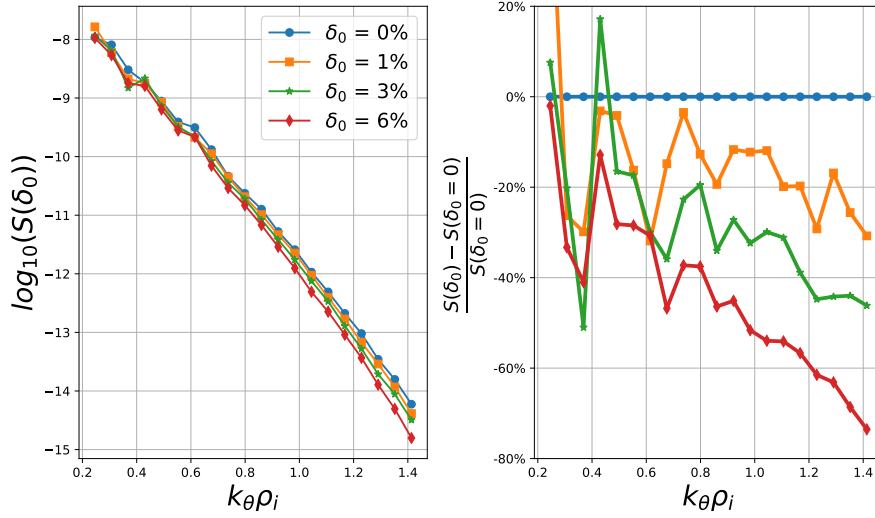


Figure 4.12. – Power spectrum  $S$  at  $r/a = 0.65$  of the turbulent modes for different ripple amplitudes  $\delta_0$  (left) and the relative difference with the axisymmetric case (right).

In addition, ripple tends to broaden the spectrum through mode coupling with  $(0, kN_c)$  modes as already mentioned above and visible in Fig.4.10, giving additional importance to the  $k_\parallel k_\theta$  product for modes outside the resonant cone. The turbulent intensity consequently cannot be simply obtained by taking the sum of the modes in the resonance cone. In presence of a 3D magnetic perturbation, one has then to define carefully the turbulent intensity  $\mathcal{I}$ .

Here the adopted solution is to consider all poloidal and toroidal modes, except the  $n = 0$  and  $m = 0$  modes. For the  $m = 0$  modes, the reason is that the new finite modes due to ripple are not due to turbulence but rather non-axisymmetric neoclassical effects. This is similar for the  $n = 0$  modes, except that the considered neoclassical modes are due to the  $1/R$  magnetic field decay.

The considered turbulent intensity is then  $\mathcal{I} = e\tilde{\phi}_{RMS}/T$  with

$$\tilde{\phi}_{RMS} = \sqrt{\sum_{m \neq 0, n \neq 0} |\phi_{m,n}|^2} . \quad (4.11)$$

Fig.4.13a displays the radial profile of time-averaged and coarse-grained turbulent intensity for different ripple amplitudes. It appears that  $\langle \mathcal{I} \rangle_{CG}$  actually increases monotonically with the ripple amplitude, gaining in average 2 – 3% between the axisymmetric case and the  $\delta_0 = 3\%$  case. Compared with the opposite behaviour seen in Fig.4.12, this means that ripple tends to amplify modes outside of the resonant cone. This modest increase is associated with an enhancement of the turbulent intensity shear, especially in the core, as displayed in Fig.4.13b. However, as already observed in Fig.4.9, this modification of  $\langle \mathcal{I} \rangle_{CG}$  does not seem correlated with the impact of ripple on  $\Pi_{res}$  which is maximum nearer to the midradius. This either indicates that

4. Effect of magnetic ripple on toroidal rotation in presence of turbulence – 4.3.  
Interplay mechanisms between ripple and turbulence

the turbulent intensity shear is too weakly impacted by ripple<sup>2</sup> or that this effect is negligible compared with the one coming from the  $E_r$  shear (as discussed in the next section).

In any case, it indicates 1) that the turbulent viscosity could be only mildly affected by ripple and 2) that it cannot explain the observed modification of the residual stress with ripple. As mentioned previously, the other natural candidate to explain the ripple effect on  $\Pi_{\text{res}}$  is through the  $E_r$  shear.

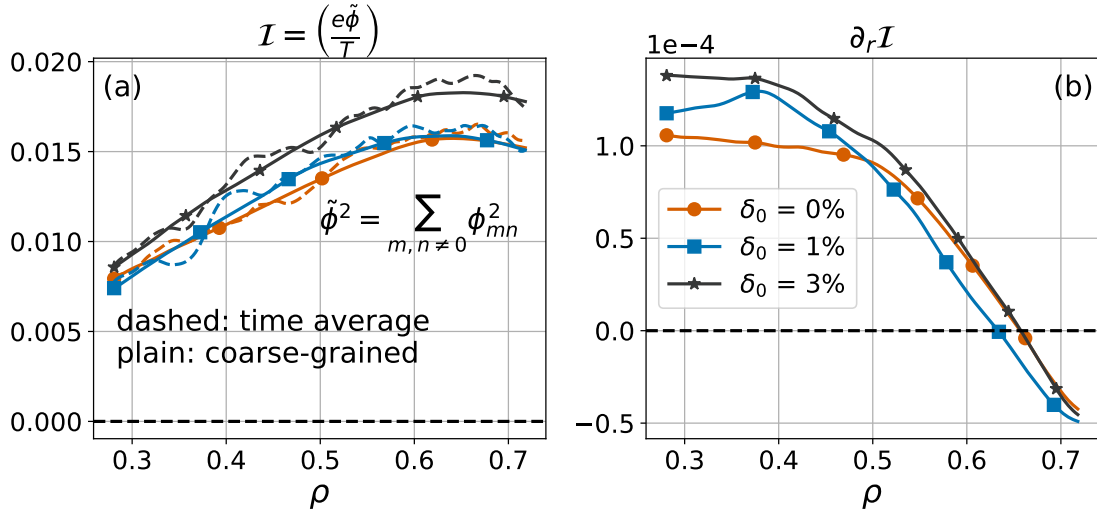


Figure 4.13. – Radial profile of the turbulent intensity (left) and its coarse-grained radial shear (right).

### 4.3.2. Impact of ripple on the shear of radial electric field

The  $E \times B$  shear modifies the parallel wave number by introducing radial asymmetry [113]. Ripple increases the radial electric field amplitude through neoclassical effects, as detailed in Sec.2.4, so the  $E_r$  shear depends among others on the radial shape of the ripple amplitude. Mean  $E_r$  and associated shear are plotted in Fig.4.14a and 4.14b. The effect of ripple on these profiles is clear: both  $\langle E_r \rangle_{\text{CG}}$  and  $\langle E_r' \rangle_{\text{CG}}$  increase in amplitude with  $\delta$  near the core region.

2. The relative gain between  $\delta_0 = 0\%$  and  $\delta_0 = 3\%$  at  $r/a = 0.3$  is about 30%.

4. Effect of magnetic ripple on toroidal rotation in presence of turbulence – 4.3.  
 Interplay mechanisms between ripple and turbulence

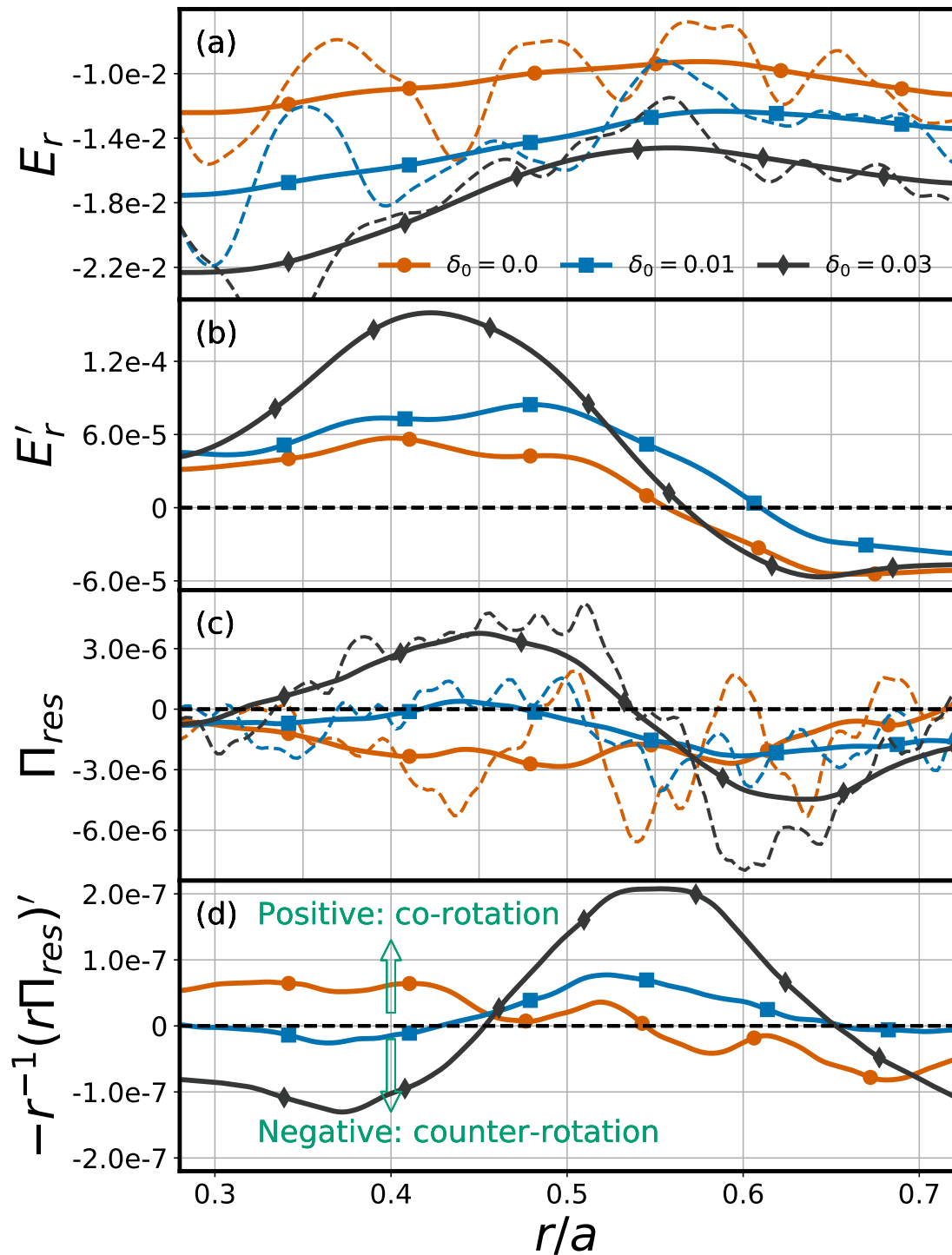


Figure 4.14. – Solid lines: radial profile of coarse-grained (temporally and spatially for plain lines and only temporally for dashed lines) radial electric field (a) and its shear (b), as well as residual stress (same as Fig.4.9 for full lines) (c) and the opposite of its divergence (d) for different ripple amplitudes.



#### 4. Effect of magnetic ripple on toroidal rotation in presence of turbulence – 4.4. Conclusion of chapter 4

$\langle \Pi_{\text{res}} \rangle_{\text{CG}}$ , shown in Fig.4.14c, is correlated with the increase of  $\langle E_r' \rangle_{\text{CG}}$ , shown in Fig.4.14b, up to an offset, consistently with the numerical study [122]. The offset is likely explained by the impact of turbulent intensity shear, which for each simulation is about the same as displayed in Fig.4.13, and significant near the region in between the core and the midradius where this offset is particularly visible. Note that this offset can also be impacted by the effect of diamagnetism [105]. Finally, Fig.4.14d shows the averaged  $-r^{-1}(r\Pi)'$  that appears in the momentum conservation equation Eq(4.1). Regarding plasma rotation, the increment of the toroidal velocity due to turbulence, i.e. the opposite of toroidal Reynolds stress divergence, is modified. Under the effect of an increasing radially gaussian ripple, it goes from co- to counter-current rotation drive in the plasma core and from an about-vanishing to deeply co-current rotation drive past the midradius. All in all, it is reasonable to conclude that, in these simulations, magnetic ripple impacts the residual stress significantly through the radial electric field shear and only weakly through the turbulent intensity shear. The critical ripple expression, derived without interplay, is still valid as it does not depend on the residual stress.

## 4.4. Conclusion of chapter 4

In summary, the effect of turbulent drive and magnetic braking has been studied on the same footing thanks to comprehensive gyrokinetic simulations. The critical ripple amplitude for which magnetic braking overcomes turbulence has been estimated theoretically and agrees with gyrokinetic simulations. An evaluation of this threshold is proposed and its value in Tore Supra agrees with experimental measurements. A quick estimate suggests that this threshold could be crossed in ITER. However, an open question remains about the validity of this threshold near the plasma edge when boundary conditions, not included in the presented model, could play a role.

Ripple also modifies the toroidal velocity by changing the turbulent toroidal Reynolds stress through the residual stress. In fact, the residual stress is observed to vary monotonically with the ripple amplitude in simulations. The residual stress is expected to depend on the turbulent intensity radial shear and the radial electric field radial shear. It is observed in simulations that the turbulent intensity shear is only weakly impacted by the magnetic ripple. However, the radial electric field shear is enhanced in presence of ripple and is clearly correlated with the residual stress modification due to ripple.

The sketch in Fig.4.15 acts as a summary of this chapter.

4. Effect of magnetic ripple on toroidal rotation in presence of turbulence – 4.4.  
Conclusion of chapter 4

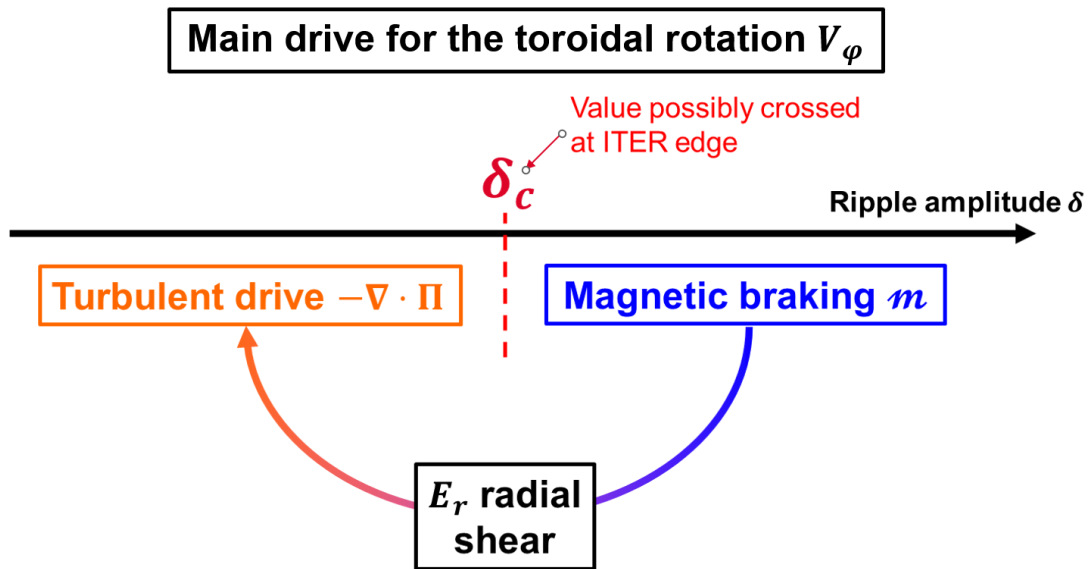


Figure 4.15. – Sketch summarizing Chapter 4.

Robust knowledge of this intrinsic physics provides means to control the rotation. Indeed, recent work [123] demonstrated that restoring the magnetic symmetry is actually possible, giving some leverage on the magnetic braking strength.

# 5. Influence of the safety factor on the radial electric field

## Table of contents

5.1. Introduction . . . . .	122
5.2. Experimental observations . . . . .	123
5.2.1. Doppler back-scattering diagnostic . . . . .	123
5.2.2. Scan of velocity profiles with plasma current . . . . .	125
5.3. Effect of the safety factor in dedicated GYSELA simulations . . . . .	127
5.3.1. Isolating the safety factor effect . . . . .	127
5.3.2. GYSELA simulations parameters . . . . .	127
5.3.3. Observations of the safety factor impact in GYSELA simulations . . . . .	128
5.3.4. Generalized vorticity conservation and force balance . . . . .	134
5.4. Mechanisms impacting flows carrying a $q$ dependence . . . . .	137
5.4.1. Neoclassical processes . . . . .	138
5.4.2. Zonal flows (ZFs) and Geodesic Acoustic Modes (GAMs) . . . . .	141
5.4.3. Reduced model of energy transfer between turbulence, zonal flows and GAMs . . . . .	144
5.4.4. Synergy between turbulence and neoclassical effects . . . . .	152
5.5. Conclusion of chapter 5 and discussion . . . . .	155

## 5.1. Introduction

As discussed in Chapter 1, the radial electric field is a key element for the confinement of a tokamak plasma, as it is expected to play a major role in turbulence quenching and is presumed to be a necessary ingredient for transitions toward enhanced confinement modes. Knowing the mechanisms at play in the establishment of this field is then of prime importance in order to get robust predictions and means of control of a reactor's performance.

In this Chapter, we focus on the effect of the safety factor on the radial electric field. The motivation for this study comes from experimental observations on the Tore supra, WEST, and MAST tokamaks, which show a deepening of the well in radial electric field, i.e. the  $E \times B$  flow, near the edge of the plasma with high plasma current. Once again, we will make use of gyrokinetic simulations. The plasma current is not an input in the GYSELA code. However, the edge safety factor, which is inversely proportional to the plasma current, is an input. The idea is then to see if changing the

safety factor does impact the radial electric field in the same way as experiments. The premise of this study is that  $q$  is the main player regarding the establishment of  $E_r$  in this plasma current scan. Looking at this particular dependence is interesting for at least two reasons:

- The plasma current is bound to increase in future reactors, and toward values never encountered before. ITER for example is expected to operate as high as  $I_p = 15\text{MA}$ , which is to be compared to the maximum current of existing tokamaks which is about  $I_p = 5\text{MA}$ . This study then gives insight into the radial electric field behavior of next-generation tokamaks.
- The aforementioned experimental studies on the effect of the plasma current on WEST and Tore Supra are great frameworks for developing theoretical models and testing numerical codes. As we will see in this Chapter, several mechanisms are expected to shape the radial electric field and depend sensitively on the safety factor, which we recall is inversely proportional to the plasma current near the edge. Simulation codes and reduced models can then be used to identify the main mechanisms, and can be compared with the experimental measurements.

## 5.2. Experimental observations

### 5.2.1. Doppler back-scattering diagnostic

The experimental profiles shown in the next section rely on a diagnostic called *Doppler Back-Scattering* (DBS) using a reflectometry-like method. The reflectometry principle relies on probing a plasma with high-frequency electromagnetic waves, usually in the microwave range ( $\sim 30 - 150$  GHz), and studying the wave that is reflected by the plasma. The incident wave propagates in the plasma as long as the refractive index is strictly positive. If the refractive index cancels along the propagation direction, the wave is then reflected at the *cut-off layer* where the index is zero. This refractive index depends on the plasma characteristics, in particular its density<sup>1</sup>, but also the wave frequency. Knowing the medium characteristics, one can then choose the frequency such that the reflection occurs at a chosen cut-off layer position. The specificity of the DBS diagnostic [124, 125] is to detect only the electric field that is back-scattered by density fluctuations of a given spatial scale at the cut-off layer location. The probing wave is launched with a finite incident angle with respect to the direction normal to the iso-index-of-refraction surfaces. The principle of back-scattering is illustrated in Fig.5.1, here considering the probing waves in O-mode polarization where the iso-index-of-refraction surfaces are also iso-density surfaces. During its propagation, the incident probing wave of wavevector  $\mathbf{k}_i$  is scattered in all directions with a large enhancement in the cut-off layer vicinity. The DBS antenna then selects only the back-scattered part  $\mathbf{k}_{bs} = -\mathbf{k}_i$ . This diagnostic carries the emitter and the receptor at the same location, such that only the back-scattered part is measured. The back-scattering technique

---

1. Depending on the probing wave polarization, it may also depend on the electric field or, in X-mode polarization, it also depends on the magnetic field.

is then actually not a reflectometry method as it uses the scattered wave and not the reflected one. The density fluctuations such that the wavevector  $\mathbf{k}_f$  matches the Bragg rule  $\mathbf{k}_f = -2\mathbf{k}_i$  are selected through this method.

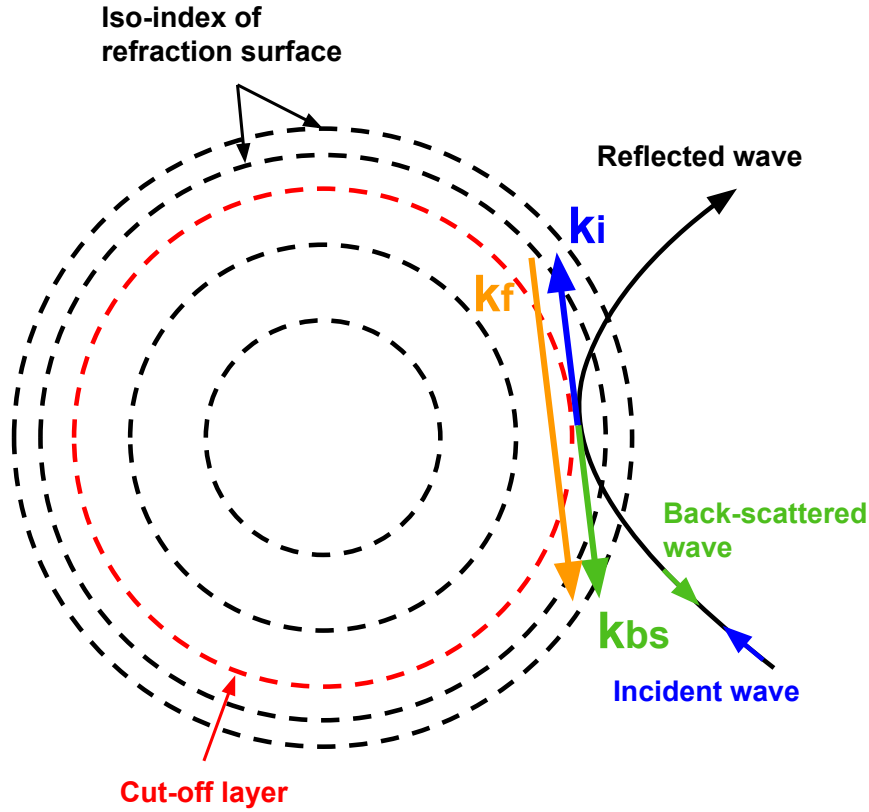


Figure 5.1. – Principle of back-scattering reflectometry. For probing wave in O-mode polarization, the iso-index-of-refraction surfaces are also the iso-density surfaces. The backscattered wave carries the plasma density fluctuations characteristics associated with the  $k_f = -2k_i$  wavenumber.

The back-scattered signal gives the power spectral density of the fluctuations of a given spatial scale. The name "Doppler" back-scattering comes from the Doppler-shift  $\Delta f = \mathbf{k}_f \cdot \mathbf{v}_f$  where  $\mathbf{v}_f$  is the velocity of density fluctuations. The velocity of the associated fluctuations can then be determined from the detected signal using a ray-tracing code to evaluate the wavenumber  $k_f$  at the location of the cut-off layer [126]. As a result, this method gives access to the velocity  $v_f$  of density fluctuations in the direction bi-normal to the magnetic field. It reads  $v_f = v_{E \times B} + v_{ph}$  where  $v_{E \times B}$  is the electric drift velocity and  $v_{ph}$  is the phase velocity of the fluctuations, which can be significant in some cases [119] but appears negligible at the extreme edge of confined plasmas. Actually, in the experimental results presented in the next section, the phase velocity at the very edge of the plasma ( $r/a > 0.9$ ) is assessed as negligible compared with the electric drift: the DBS gives the same velocity regardless of the wavenumber  $k_f$  chosen. Thus we can consider that the measurements give the  $E \times B$  velocity.

### 5.2.2. Scan of velocity profiles with plasma current

This section presents the experimental observations related to the impact of plasma current on the radial electric field. A dedicated experimental study in the WEST tokamak can be found in [33]. To summarize and focus on the part of interest for our work: it has been found that the  $E_r$  amplitude increases significantly near the edge of the plasma with the plasma current  $I_P$ , which is inversely proportional to the safety factor near the edge. Indeed, edge safety factor  $q$  and plasma current  $I_P$  are linked through Ampère's law  $I_P = \frac{2\pi a \epsilon B_\phi}{\mu_0 q}$  (where  $\mu_0$  is the vacuum permeability). Increasing  $q$  then translates into decreasing  $I_P$ . In Chapter 1, in Fig.1.12, we already showed the radial profile of the transverse velocity, mainly due to the  $E \times B$  drift, obtained through DBS diagnostic for different plasma currents at the edge in WEST discharges. This experiment has been done in the *Lower Single Null* (LSN) and *Upper Single Null* (USN) configurations. They refer to discharges where one of the magnetic X-points is inside the vessel, either at the bottom (LSN) or top (USN) of the plasma. Regardless of the configuration, a monotonic behavior is observed where  $E_r$  increases in amplitude when  $I_P$  increases, even though the effect is more pronounced in the USN configuration.

An interesting remark is that this trend with the plasma current has already been observed in Tore Supra [34], as shown in Fig.5.2 that displays radial profiles of the velocity measured by DBS for different plasma current values. The experimental safety factor profiles of the discharges shown in this figure are displayed in Fig.5.3. It appears that the magnetic shear stays constant between each discharge. Tore Supra had circular magnetic surfaces which means that the triangularity and elongation are not necessary ingredients to witness the sensibility of the radial electric field to the plasma current. In these discharges, there are no USN or LSN configurations but the plasma is in contact with the wall, either at the top or bottom of the vessel. This is reassuring in the idea that the following GYSELA simulations, performed with circular magnetic surfaces, should be able to catch the physics at play in the establishment of the radial electric field well.

## 5. Influence of the safety factor on the radial electric field – 5.2. Experimental observations

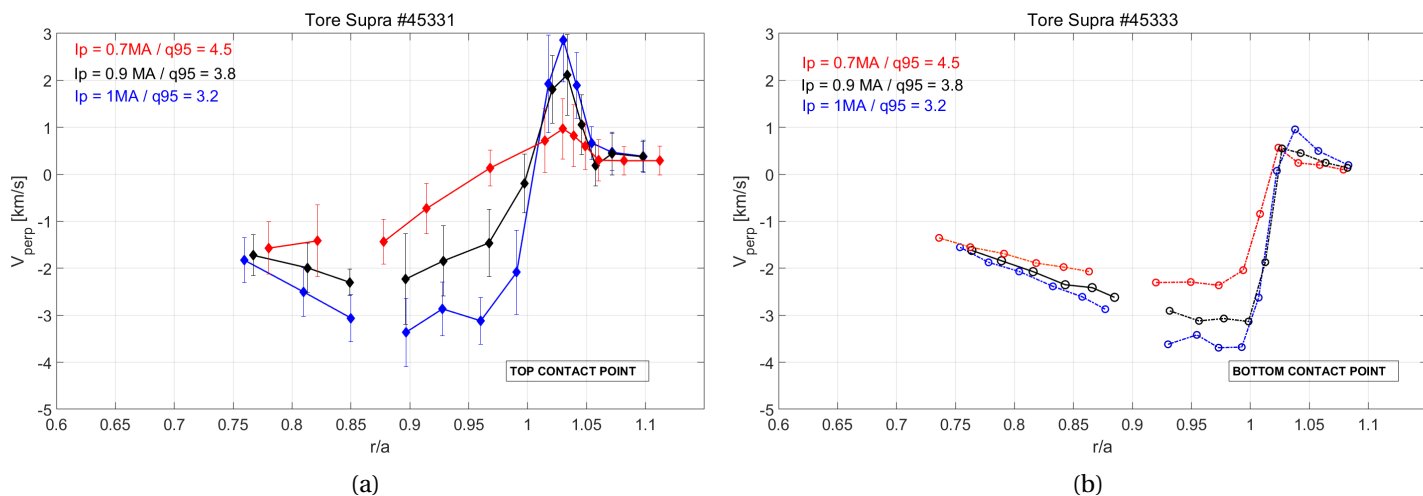


Figure 5.2. – Radial profiles, near the edge of the plasma, of the  $V_{E \times B}$  velocity measured in the Tore Supra tokamak for different plasma current values. The plasma is in contact with the wall at the top (left) / bottom (right).

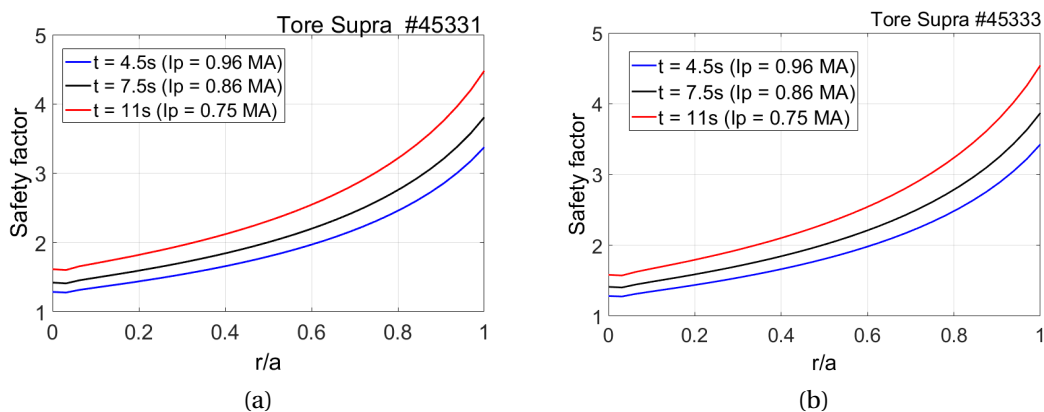


Figure 5.3. – Radial profiles of the experimental safety factor in the Tore Supra tokamak for the discharges of Fig.5.2.

The  $I_p$  scan performed in these experiments is physically complex: it mingles plasma-wall interactions, the effect of different magnetic configurations, asymmetric gas puff and pumping, orbit-losses in presence of an X-point ... One must simplify the problem to obtain a reduced model and run relevant simulations that discriminate various processes.

## 5.3. Effect of the safety factor in dedicated GYSELA simulations

### 5.3.1. Isolating the safety factor effect

Running simulations with experimental plasma parameters seems attractive. They provide a precise estimation of all wanted quantities that are not retrievable with the diagnostics available during the experiments. However, this is a risky way to proceed. The reason is that in general all profiles tend to evolve in the experiments as it is challenging to increase the plasma current while keeping steady density and temperature<sup>2</sup> in the plasma. Comparing simulations with several different varying parameters makes post-processing extremely challenging. Indeed, let's say a quantity of interest changes between two of these simulations: how to be sure that this modification is due to the difference in plasma current? or in temperature gradient? or a synergy between the two? It is in general more reasonable to perform a scan with only one parameter of interest. For this reason, carefully tailored simulations are designed to isolate the sole effect of the safety factor.

If a similar effect on the perpendicular velocity is observed in these simulations, as in the experimental  $I_p$  scans, it then gives a good hint as to the role of the safety factor in building these edge radial electric field profiles. As this study only considers turbulence driven by the ion temperature gradient in a plasma with adiabatic electron response, this would also imply that kinetic physics of electrons is not mandatory to explain this effect. The considered simulation profiles are now detailed.

### 5.3.2. GYSELA simulations parameters

For convenience, the reference simulation considered in this study is the same as the one without ripple in Chapter 4. The main advantages are that it saves the cost of one (expensive) simulation, and that the associated heat source has already been adjusted to maintain a quasi-steady temperature profile<sup>3</sup>. Note also that this reference simulation is actually shaped to mimic the Tore Supra discharge #45511, which is not related to the ones shown in Fig.5.2, but that exhibits realistic shapes of thermodynamical gradients. The input profiles are those plotted in Fig.4.2 in the previous Chapter. The main initial parameters are summarized in Tab.4.1. The magnetic ripple is switched off as it causes simulations to consume more CPU hours, and is observed to play a subdominant role in the  $q$  effect on the radial electric field a posteriori.

The only varying input parameter between simulations is the safety factor. Two cases, in addition to the reference one, have been run. To leave the magnetic shear  $s = \frac{r}{q} \frac{dq}{dr}$  unchanged, as in the WEST and Tore Supra experiments, the safety factor from

---

2. Especially for the ohmic discharges considered where the only heating channel is through the plasma current.

3. This adjustment is actually a tremendous task.



## 5. Influence of the safety factor on the radial electric field – 5.3. Effect of the safety factor in dedicated GYSELA simulations

the reference simulation is simply multiplied by a constant factor. This is important as some studies [127] (see the first figure) suggest that  $q$  and  $s$  can have opposite effects regarding the turbulent spectra which may play a role in the final  $E_r$  profile. The reference case is labeled  $q_{1.0}$ , the "low"  $q$  case is labeled  $q_{0.5}$  and corresponds to the reference safety factor multiplied by 0.5 while the "high"  $q$  case is labeled  $q_{1.5}$  and correspond to the reference safety factor multiplied by 1.5. The resulting radial profile of each safety factor is displayed in Fig.5.4.

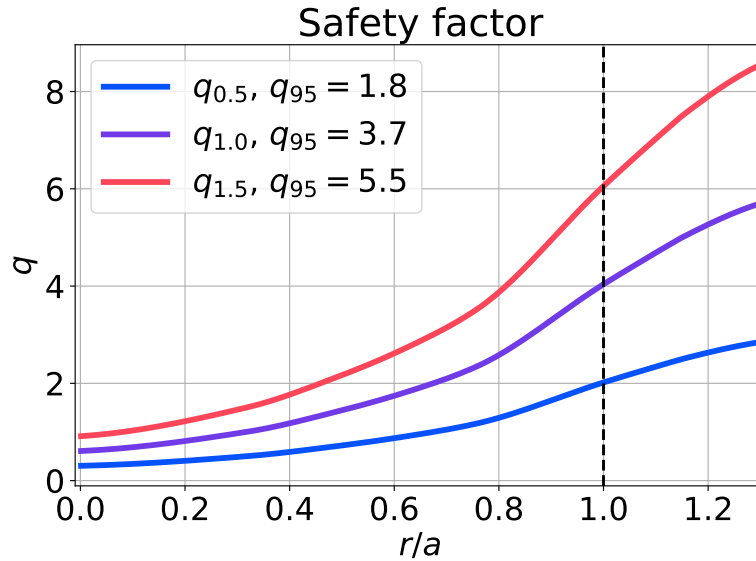


Figure 5.4. – Radial profiles of the safety factor used in each simulation.

Finally, note that these simulations are all run with a bottom limiter. They can then be assimilated to the Tore Supra discharge with the bottom contact point described in Fig.5.2. Note that a discharge with limiter (unpublished #48208), not shown here, has shown the same trend with  $I_p$  on the radial electric field.

### 5.3.3. Observations of the safety factor impact in GYSELA simulations

Simulations have been run for about  $\sim 150000$  reference cyclotron periods  $\omega_{c0}^{-1}$ . As they are flux-driven, the equilibria reached are not perfectly stationary as thermodynamical gradients are free to evolve. However, the provided heat source identical for each simulation maintains temperature profiles in a quasi-steady state. Note that the tuning (location, amplitude and shape) of this heat source is a tremendous work. It partly justifies the choice of the reference simulation  $q_{1.0}$  for which this exercise was already done. We add that the heat flux is expected to vary with the safety factor [128] A verification must then be made in the turbulent phase of the simulations to verify that profiles are similar in each case. The temperature and temperature gradient profiles for each case at  $t = 140000\omega_{c0}^{-1}$  are depicted in Fig.5.5.

5. Influence of the safety factor on the radial electric field – 5.3. Effect of the safety factor factor in dedicated GYSELA simulations

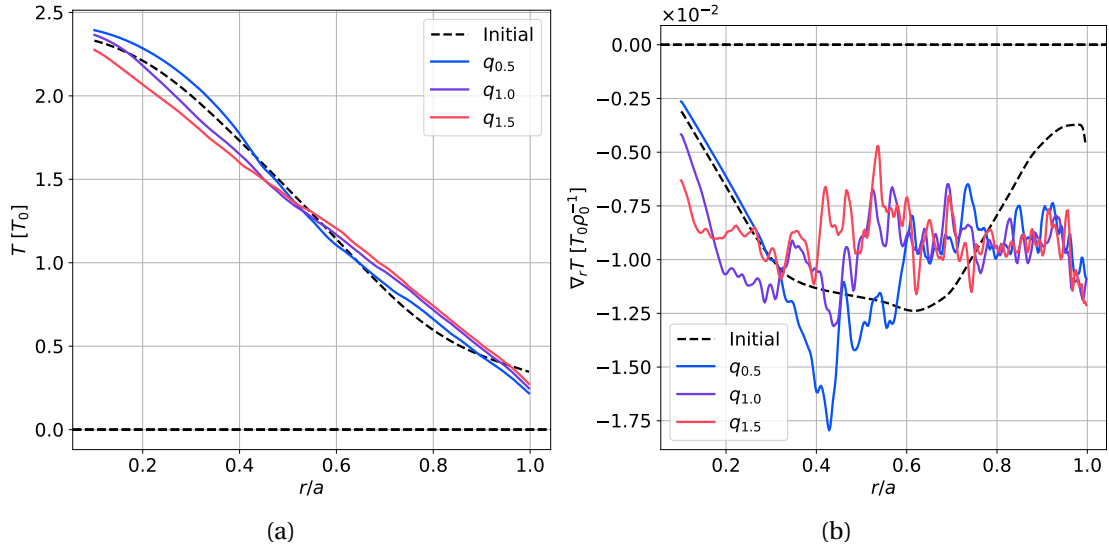


Figure 5.5. – Radial profile of the temperature **(a)** and its radial gradient **(b)** for each safety factor profiles at  $t = 140000\omega_{c0}^{-1}$ .

The relative disparity in temperature is less than 10% for all the safety factors considered. The temperature gradients are also of similar amplitude, especially near the edge. The density profile has also been studied and is the same for each simulation. These simulations are then well designed to isolate the sole effect of the safety factor.

The radial profile of the radial electric field in the turbulent equilibrium obtained with the aforementioned simulations is displayed in Fig.5.6. There is a clear relationship between the  $E_r$  amplitude and the increase of the safety factor. Indeed, near the plasma edge  $0.75 < r/a < 0.85$ , the radial electric field amplitude increases substantially and monotonically when the safety factor decreases. The trend is then the same as in the experimental measurements.

5. Influence of the safety factor on the radial electric field – 5.3. Effect of the safety factor in dedicated GYSELA simulations

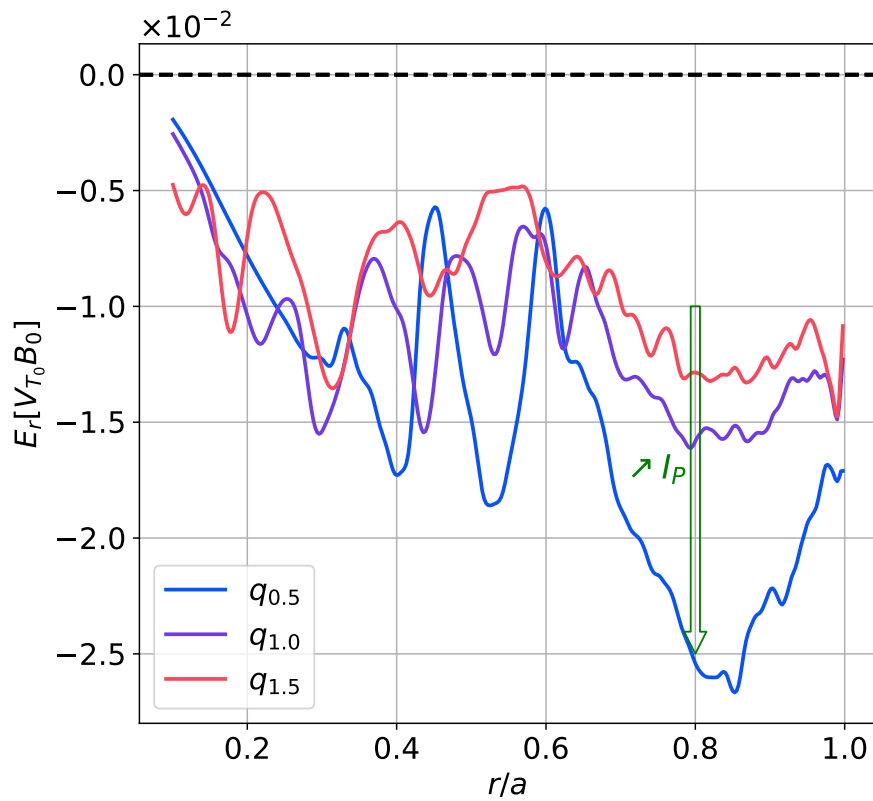


Figure 5.6. – Radial profile of the radial electric field  $E_r$  for each safety factor profile averaged between  $100000 < t[\omega_{c0}^{-1}] < 145000$ .

Interesting observations can be made when looking at the spatiotemporal evolution of  $E_r$  displayed in Fig.5.7 for the  $q_{0.5}$  and  $q_{1.5}$  cases.

5. Influence of the safety factor on the radial electric field – 5.3. Effect of the safety factor in dedicated GYSELA simulations

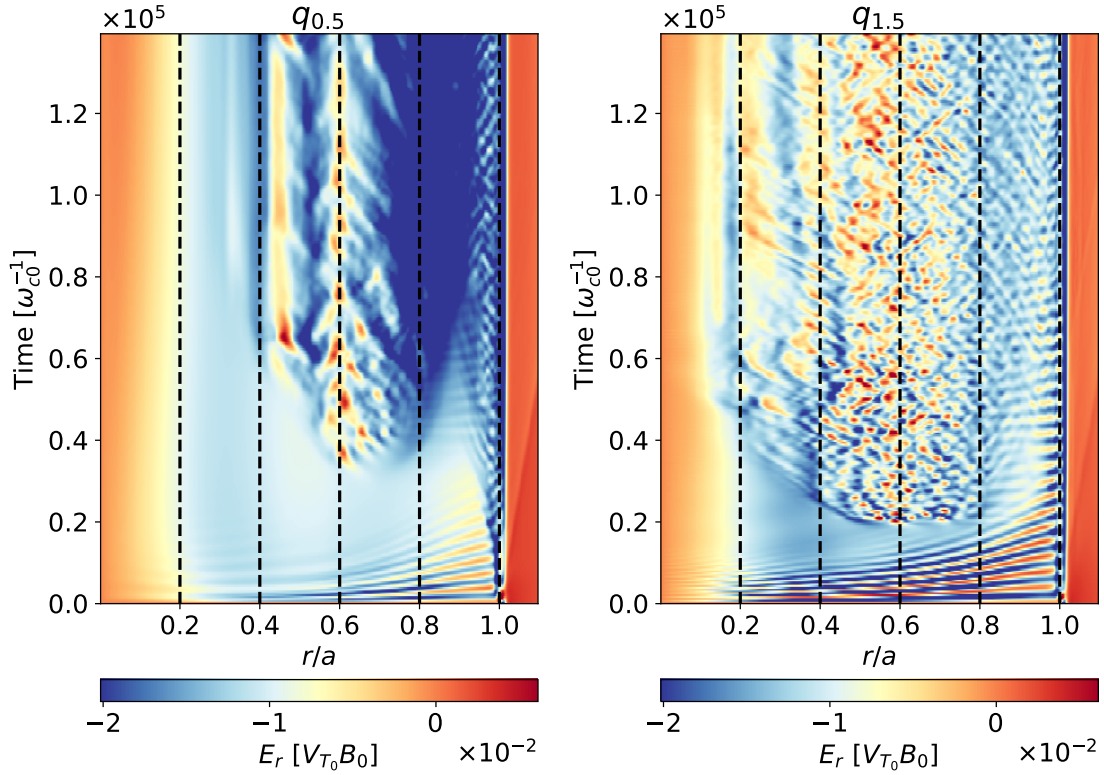


Figure 5.7. – Spatiotemporal map of the radial electric field  $E_r$  for extremal safety factor profiles.

It appears that radial structures in the  $q_{0.5}$  case are steady, or at the very least slowly drifting. These zonal flows have already been observed and assessed in GYSELA [19, 129]. Their impact on ITG-driven turbulence reduction is well-known [18], which partly explains why they are of great interest in the fusion community. The interested reader may take a look at [20] for a comprehensive review of zonal flows by Diamond *et al.* On the contrary, the  $q_{1.5}$  exhibits short-lasting structures that drift radially. Also, the *Geodesic Acoustic Modes* (GAMs) behavior is quite different between these two cases. The  $q_{1.5}$  case exhibits stronger GAMs amplitudes and their attenuation is weaker.

Another interesting quantity is the turbulent intensity  $\mathcal{I}$ . Here<sup>4</sup> it is written as  $\mathcal{I} = \sqrt{\langle (\delta n/n)^2 \rangle}$  with  $\langle \cdot \rangle$  the flux surface average and  $\delta n = e(\phi - \phi_{00})/T$ , where  $\phi_{00}$  is the  $(n = 0, m = 0)$  mode of the electric potential with  $m$  and  $n$  the poloidal and toroidal mode numbers. This quantity is basically the energy allocated to turbulence, up to the normalization with the ion temperature. For each safety factor profile, the radial profile of  $\mathcal{I}$  is displayed Fig.5.8.

4. In chapter 4, the definition was slightly different to exclude the modes induced by magnetic ripple which are non-turbulent.

5. Influence of the safety factor on the radial electric field – 5.3. Effect of the safety factor in dedicated GYSELA simulations

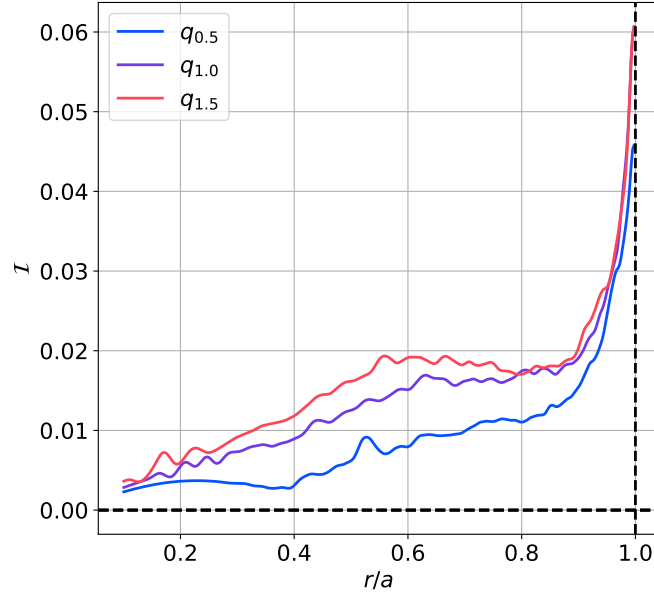


Figure 5.8. – Radial profile of the turbulent intensity  $\mathcal{I}$  time-averaged between  $100000 < t[\omega_{c0}^{-1}] < 145000$  for each safety factor profile.

It appears that the turbulent intensity grows with  $q$ , with a more pronounced increase at low safety factor value. This behavior is reported in several publications both theoretically, numerically and experimentally. On the experimental side, the effect of  $q$  has been isolated and shown that turbulent heat transport, which increases with turbulent intensity, in the DIII-D tokamak [128] increases with  $q$ . On the theoretical and numerical sides, it is shown in [127] and [130] that the linear growth rate  $k_\theta$ -spectra (with  $k_\theta$  the poloidal mode number) of the electric potential is weaker for low  $q$ . When looking at the electric potential fluctuations Fig.5.9, one can observe that the turbulent structures in the  $q_{0.5}$  case are more tilted poloidally than the  $q_{1.5}$  case. This is characteristic of a flow shear, that is consistent with both the observation of zonal structures in Fig.5.7 and the reduction of turbulent intensity for the  $q_{0.5}$  case displayed Fig.5.8.

5. Influence of the safety factor on the radial electric field – 5.3. Effect of the safety factor in dedicated GYSELA simulations

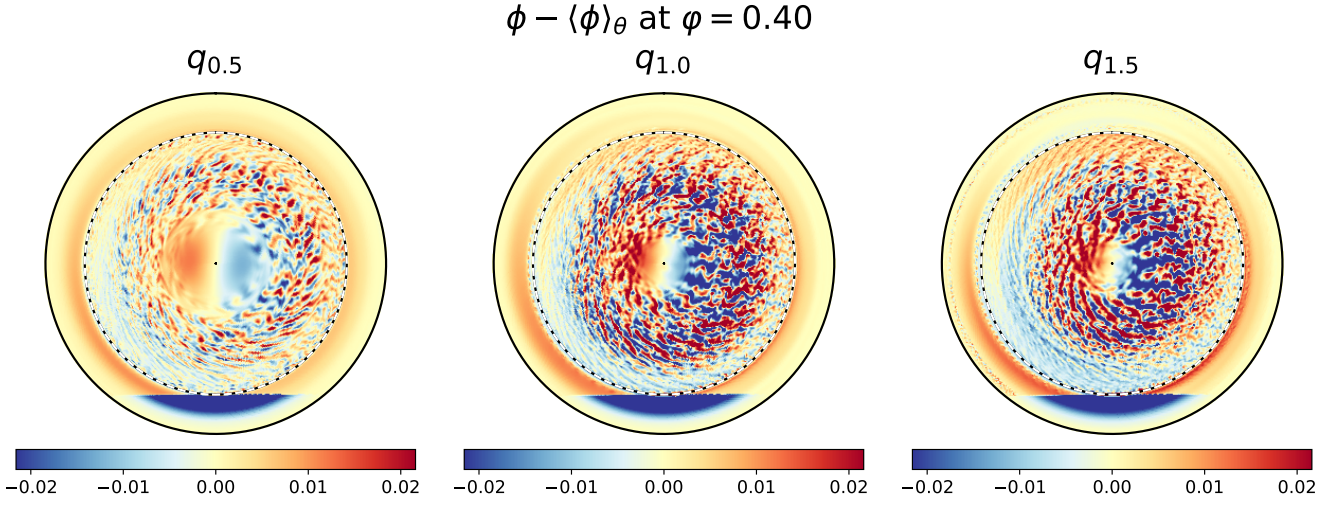


Figure 5.9. – Fluctuations of the electric potential at  $t=93600 \omega_{c0}^{-1}$  at a toroidal angle  $\varphi = \pi/8$  for each case.

Another lead for this reduction of turbulent intensity with the plasma current is the transition between the excitation and dissipative spectral regions that is expected to occur at a wavenumber  $k_{\theta, \text{cutoff}} \sim L_T / (qR\rho_i)$ , where  $L_T$  is the temperature gradient's length, which depends on the safety factor value [131]. To assess this point, Fig.5.10 shows the  $k_\theta$ -spectra of non-zonal modes of the normalized squared electric potential for each case, at  $r/a = 0.8$  where the effect on  $E_r$  is maximum according to Fig.5.6. It appears that the low safety factor case exhibits a spectral density of the electric potential lower than the higher ones at all scales. In addition, these spectra exhibit a non-linear trend with  $q$ , which is in agreement with the spectra in [127]. However, the transition between driving and dissipative regions is not clearly visible in any case. The reason could be that this transition occurs at very high wavenumbers that are not resolved in our simulations. Anyway, as the effect on the radial electric field is recovered, we conclude that this mechanism is then not necessary for its establishment.

5. Influence of the safety factor on the radial electric field – 5.3. Effect of the safety factor in dedicated GYSELA simulations

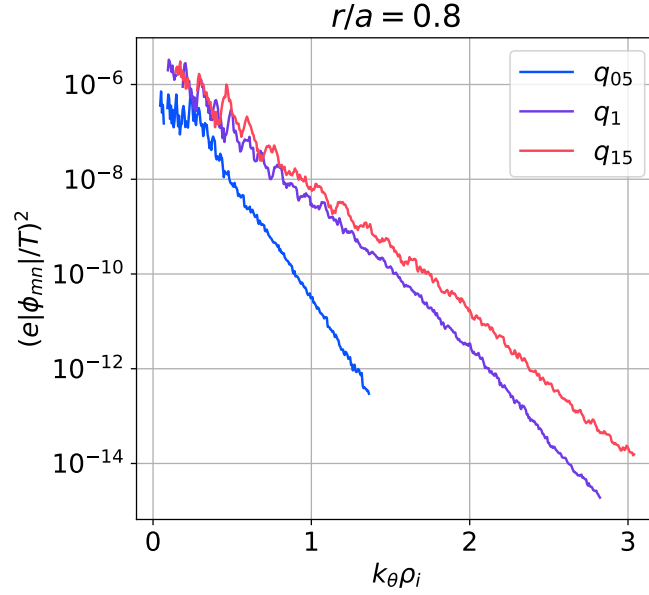


Figure 5.10. –  $k_\theta$ -spectra of the electric potential spectral density for each safety factor profile at  $r/a = 0.8$  and averaged between  $100000 < t[\omega_{c0}^{-1}] < 140000$ . The maximal accessible  $k_\theta$  decreases with  $q$  since the resonant modes follow the  $n = -m/q$  line so low  $q$  means a steeper line that fastly reaches the limit of the  $(m, n)$  box, fixed by the poloidal and toroidal resolution.

All of these observations are important clues to understand the main mechanisms responsible for the formation of the radial electric field.

#### 5.3.4. Generalized vorticity conservation and force balance

As in Chapter 4, it would be convenient to use a conservation equation on the radial electric field  $E_r$  to see the different contributions and their nature. Unfortunately, the radial electric field is not a conservative field, in the sense that one cannot write an equation as  $\partial_t E_r + \nabla \cdot \Gamma = 0$  with  $\Gamma$  a flux. However, one can show that another quantity close to the  $E_r$  shear is conserved. Labeled *generalized vorticity* and noted  $\Omega$ , it is defined for one species, and for  $k_\perp \rho_i \ll 1$ , as

$$\Omega = -\nabla \cdot \left( \frac{mn}{B} \nabla_\perp \phi + \frac{1}{2} \frac{m}{eB^2} \nabla_\perp P_\perp \right) \quad (5.1)$$

with  $P_\perp$  the perpendicular pressure. This vorticity is related to the shear of  $E_r$  through its dependence on  $\nabla_\perp^2 \phi$ . The related conservation equation [81] reads

$$\partial_t \Omega + \nabla \cdot (\mathbf{J}_E + \mathbf{J}_D) = 0 \quad (5.2)$$

5. Influence of the safety factor on the radial electric field – 5.3. Effect of the safety factor in dedicated GYSELA simulations

where  $\mathbf{J}_E$  and  $\mathbf{J}_D$  are the current densities due to the electric and magnetic drift respectively. This equation is valid in the gyrokinetic formalism and with the following Taylor expansion<sup>5</sup> of the gyroaverage operator  $\mathcal{J}[\phi] \simeq \phi + \frac{1}{2} \nabla \cdot \left( \frac{m\mu}{e^2 B} \nabla_{\perp} \phi \right)$ .

First, let us actually check if this conservation is fulfilled in the aforementioned GYSELA simulations. Each term in the flux surface averaged equation Eq(5.2) is composed of quantities that are standard outputs of GYSELA. The generalized vorticity conservation can then be visualized by comparing the radial profile<sup>6</sup> of the terms  $\partial_t \langle \Omega \rangle$  and  $-\langle \nabla \cdot (\mathbf{J}_E + \mathbf{J}_D) \rangle$  where  $\langle \cdot \rangle$  is the flux surface average operator. This is displayed in Fig.5.11 in the turbulent phase of each simulation.

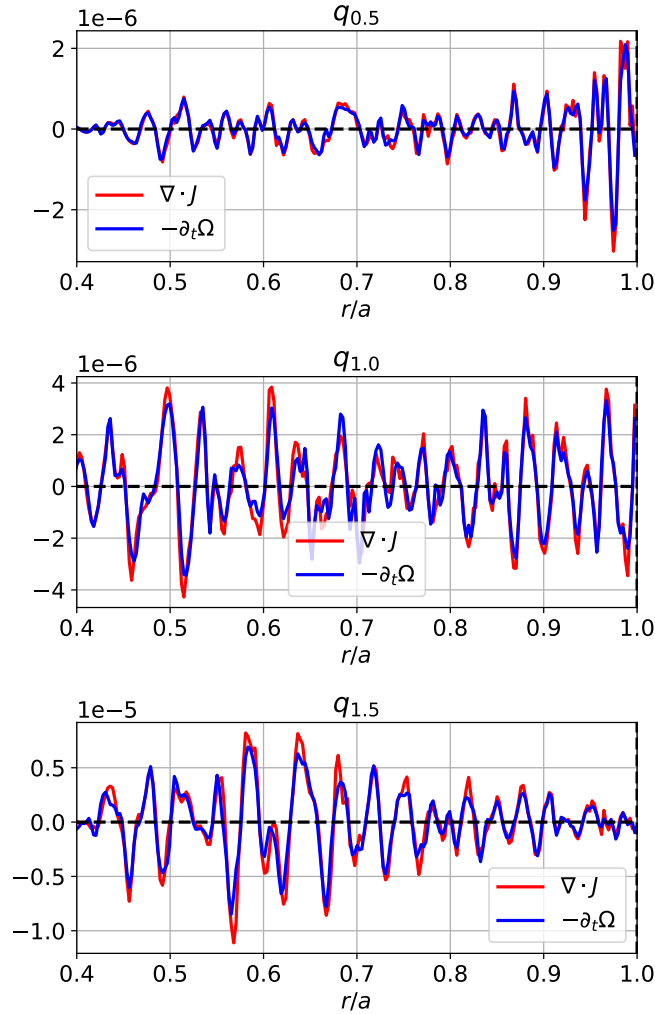


Figure 5.11. – Radial profile of each term appearing in the generalized vorticity equation Eq(5.2) at  $t = 130000\omega_{c0}^{-1}$  for each case.

5. Note that, in GYSELA, no approximation is made on the gyro-averaging.

6. The relative difference is usually more appropriate to compare two quantities, but here they are fluctuating around 0.



5. Influence of the safety factor on the radial electric field – 5.3. Effect of the safety factor in dedicated GYSELA simulations

Fair agreement is found between these terms indicating robust conservation in the code, especially since the plotted terms contain some second-order radial derivatives as well as a time derivative. It could be tempting to integrate spatially the generalized vorticity conservation as each term is the spatial divergence of some quantity. It reads

$$\partial_t \mathcal{P} + \mathbf{J}_E + \mathbf{J}_D = \mathbf{0} \quad (5.3)$$

with  $\mathcal{P} = \frac{mn}{B} \nabla_{\perp} \phi + \frac{1}{2} \frac{m}{eB^2} \nabla_{\perp} P_{\perp}$ . This equation is attractive as it gives the evolution of a quantity that depends on the radial electric field and not its shear. However, as shown in Fig.5.12, the resulting conservation, cast on the radial direction, is not as good as for the vorticity.

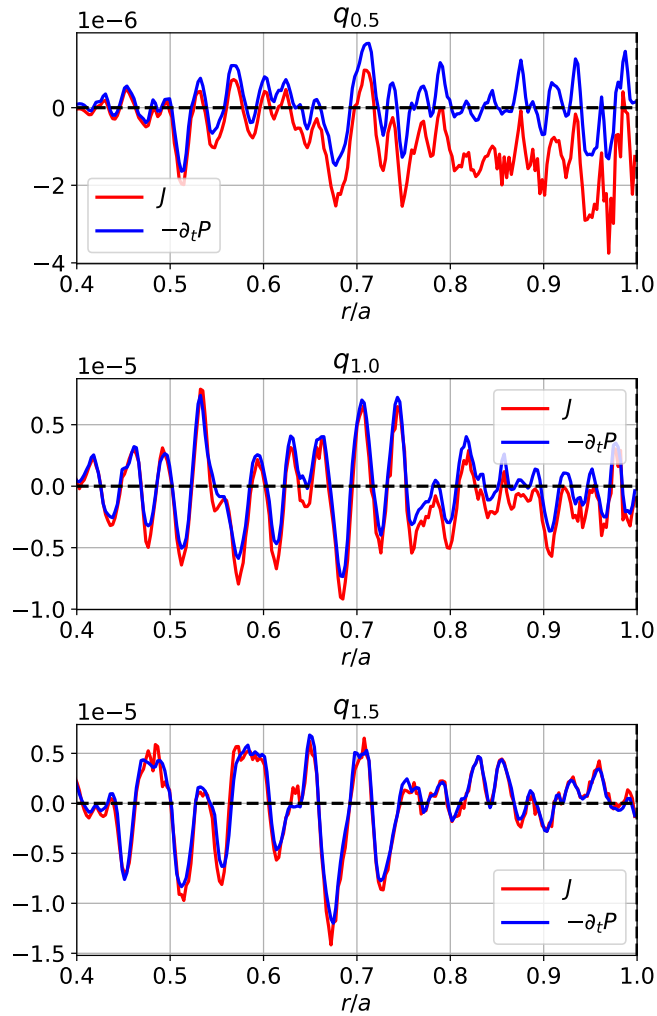


Figure 5.12. – Radial profile of each term appearing in the spatially integrated generalized vorticity equation at  $t = 130000\omega_{c0}^{-1}$  for each case.

This error could come from the approximation on the gyroaverage, which could eventually lead to a current that could be written as  $\nabla \times \mathbf{X}$  such that the equation on

## 5. Influence of the safety factor on the radial electric field – 5.4. Mechanisms impacting flows carrying a $q$ dependence

the vorticity still holds<sup>7</sup> as verified in GYSELA. Another reason for this disparity could be that the limit in numerical precision is reached. It is still unclear whether or not this impacts the simulation results in any way. We will thus proceed assuming accuracy is sufficient.

Another interesting verification is the force balance equation that can be expressed through the poloidal velocity  $V_P$  such that

$$V_P = \frac{\nabla_r P}{neB_T} - \frac{E_r}{B_T} + \frac{\varepsilon}{q} V_T . \quad (5.4)$$

In Fig.5.13, for each simulation, the radial profile of each term is plotted as well as their sum which is compared to the  $V_P$  GYSELA output. A good agreement is found between the sum of all terms on the r.h.s of Eq(5.4) (in black dashed line) and the poloidal velocity  $V_P$  GYSELA output.

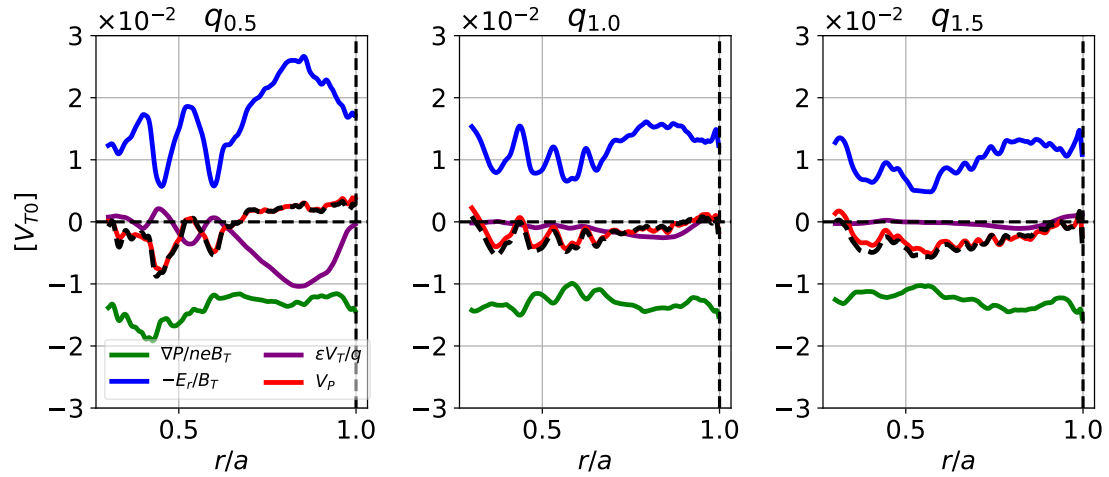


Figure 5.13. – Radial profile of each term appearing in the force balance Eq(5.4) time averaged in the range  $100000 < t[\omega_c^{-1}] < 145000$ . The black dashed curve represent the sum  $\frac{\nabla_r P}{neB_T} - \frac{E_r}{B_T} + \frac{\varepsilon}{q} V_T$ .

An interesting observation is that the toroidal velocity  $V_T$  partially balances the strong radial electric field in the  $q_{0.5}$  case. Also, the poloidal velocity is strongly impacted by the radial electric field. In the following section, different mechanisms that could explain the effect of  $q$  on the radial electric field are explored.

### 5.4. Mechanisms impacting flows carrying a $q$ dependence

There is a variety of mechanisms that impact flows, including the radial electric field, and which depend on the safety factor. Here is a list of the ones that are well

7. As  $\nabla \cdot (\nabla \times \mathbf{X}) = 0 \quad \forall \mathbf{X}$

5. Influence of the safety factor on the radial electric field – 5.4. Mechanisms impacting flows carrying a  $q$  dependence

described by the GYSELA code:

- **Neoclassical processes;**
- Turbulence, through an **energy transfer** to either the **Geodesic Acoustic Modes (GAMs)**, which are oscillations of the electric potential due to the geodesic magnetic curvature, or the **zonal flows (ZFs)** which are quasi-stationary radial structures of the  $n = 0$  and  $m = 0$  modes of the electric potential.
- **A synergy between neoclassical processes and turbulence;**

Note that some authors call "zonal flows" all the dynamics related to  $\phi_{00}$ , such that GAMs are just the high-frequency branch of ZFs. In this thesis, "zonal flows" are associated with the low-frequency events on  $\phi_{00}$  only.

### 5.4.1. Neoclassical processes

The previous observations showed that the turbulent intensity is substantially lower in the  $q_{0.5}$  case than in the  $q_{1.0}$  and  $q_{1.5}$  cases, in conjunction with the radial electric field which is mostly impacted in the  $q_{0.5}$  case. It then suggests that the neoclassical effects could play a role.

In absence of 3D magnetic perturbations, the neoclassical processes only impact the poloidal velocity  $V_P$  as there is a degeneracy between the toroidal velocity  $V_T$  and the radial electric field  $E_r$ . However, a radial shear of the poloidal velocity can lead to a reduction of the turbulent intensity. This shear could be driven by neoclassical mechanisms. Without turbulence, the equilibrium poloidal velocity  $V_{P,eq}^{neo}$  is set by neoclassical processes and is predicted as

$$V_{P,eq}^{neo} = k_{V_P} \frac{\nabla_r T}{eB_T} \quad (5.5)$$

with  $k_{V_P}$  the amplitude of the thermal force exerted by collisional processes on  $V_P$ . GYSELA has already been benchmarked [82] regarding these neoclassical effects.

In order to quantify the weight of neoclassical processes regarding the equilibrium poloidal velocity, non-turbulent versions of the simulations with the  $q_{0.5}$  and  $q_{1.5}$  safety factor profiles were run. In these new simulations, all the toroidal modes except  $n = 0$  are artificially killed, i.e. set to zero. This is a way to prevent most turbulent modes to grow while keeping the neoclassical ones which are contained in the modes  $n = 0$ . In Fig.5.14 and Fig.5.15 are compared the time evolutions of  $E_r$  and  $V_P$  for the  $q_{0.5}$  and  $q_{1.5}$  cases with and without turbulence at  $r/a \sim 0.8$  where the effect on  $E_r$  in the turbulent simulations is maximum.

5. Influence of the safety factor on the radial electric field – 5.4. Mechanisms impacting flows carrying a  $q$  dependence

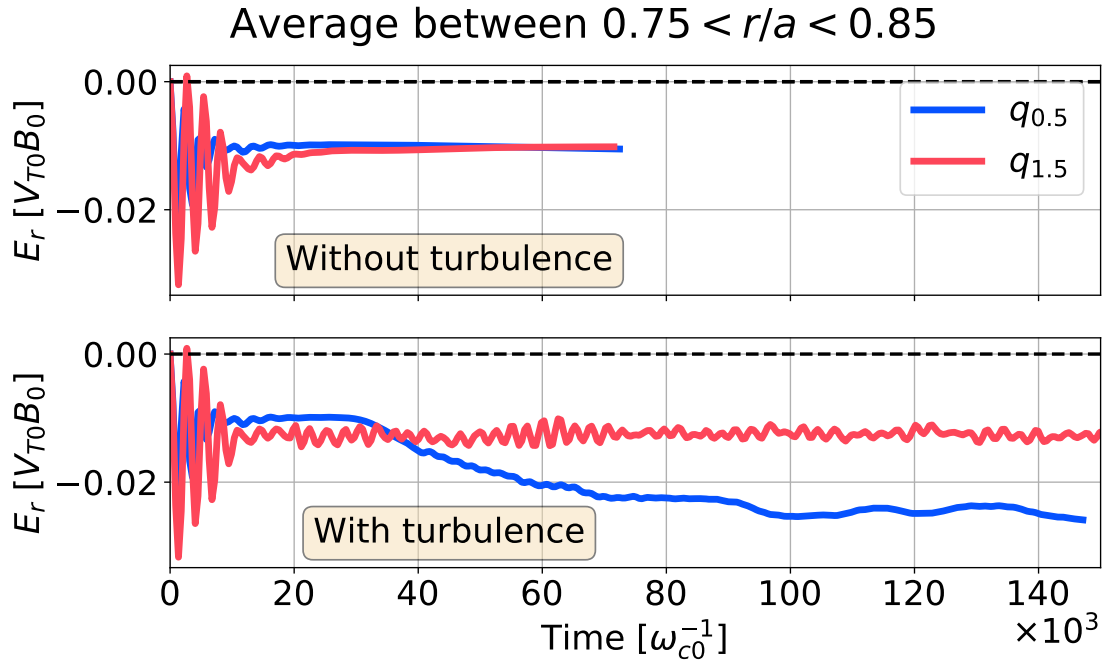


Figure 5.14. – Time evolution of the radial electric field for the  $q_{0.5}$  and  $q_{1.5}$  cases with only the  $n = 0$  mode (top) and all toroidal modes (bottom).

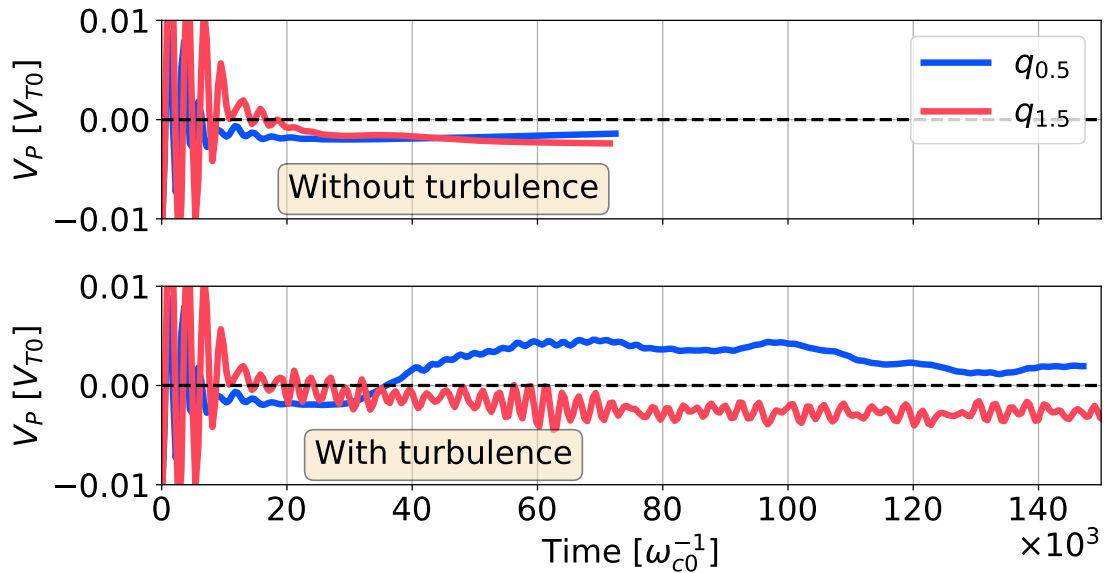


Figure 5.15. – Time evolution of the poloidal velocity for the  $q_{0.5}$  and  $q_{1.5}$  cases with only the  $n = 0$  mode (top) and all toroidal modes (bottom).

For both  $E_r$  and  $V_p$ , there is no significant difference for the  $q_{0.5}$  and  $q_{1.5}$  cases without turbulence. Regarding the radial electric field, this is not a surprise as the degeneracy between  $E_r$  and  $V_T$  predicted by the axisymmetric neoclassical theory

5. Influence of the safety factor on the radial electric field – 5.4. Mechanisms impacting flows carrying a  $q$  dependence

states that  $E_r$  is unchanged when  $V_T$  is unchanged (the initial toroidal velocity is the same in each simulation). Regarding the low dependence of the poloidal velocity with the safety factor, this is consistent with the heuristic fit on  $k_{Vp}$  taking all collisionality regimes into account [46] (See Eq(6.135) and Eq(6.136)). It reads

$$k_{Vp} = \left( \frac{1.17 - 0.35v^{\star 1/2}}{1 + 0.7v^{\star 1/2}} - 2.1v^{\star 2}\epsilon^3 \right) \frac{1}{1 + v^{\star 2}\epsilon^3} \quad (5.6)$$

and thereby does not depend on the safety factor, provided that the normalized collisionality  $v^{\star}$  does not change, which is the case in these simulations. More precisely, the value of the collisionality  $v^{\star}$  in our simulation is specified at  $r/a = 0.625$ . As  $v^{\star} = v_i \frac{qR_0}{V_{th}\epsilon^{3/2}}$ , it means that the ion collision frequency  $v_i$  adapts to keep  $v^{\star} = 0.14$  at  $r/a = 0.625$ . As proof Fig.5.16 shows the radial profile of  $v_i$  for each case, and demonstrates the  $1/q$  variation of this collision frequency between each simulation.

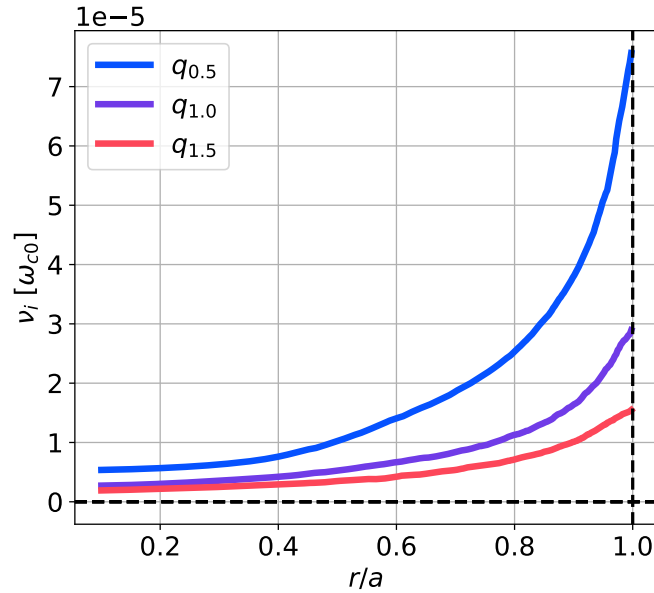


Figure 5.16. – Radial profile of ion collision frequency for each case.

However, the simulations including turbulence are similar to the ones without turbulence only at the initial time steps (when the amplitude of the turbulent mode is still negligible). Multiple pieces of information are then given by these new simulations without turbulence. First, that turbulence is an indispensable ingredient to explain the  $E_r$  dependence on  $q$  in these simulations. Second, the GAMs are strongly damped early in both neoclassical simulations: they become negligible from  $\sim 20000\omega_{c0}^{-1}$ . However, in the simulation with all modes, the GAMs are driven by turbulence. This is particularly visible for the  $q_{1.5}$  case and is detailed in the next subsection. Lastly, the radial electric field in the  $q_{1.5}$  case with turbulence is actually really close to the one obtained in the non-turbulent simulation whereas this is the case that exhibits the highest turbulent intensity.

### 5.4.2. Zonal flows (ZFs) and Geodesic Acoustic Modes (GAMs)

Looking at Fig.5.7, it appears that the dynamic of  $E_r$  is quite different between the low and high safety factor cases. Indeed, in the  $q_{0.5}$  case one can observe steady zonal structures on the radial electric field forming once turbulence sets on. The  $q_{1.5}$  case exhibits higher frequency events and especially lasting GAMs at the edge.

Both of these mechanisms, i.e. ZFs and GAMs, are known to be sensitive to the safety factor profile. The question is: how do these mechanisms modify the radial electric field? The physics of ZFs and GAMs is actually quite different:

- GAMs manifest as fast oscillations of the radial electric field and the associated  $E \times B$  drift. They are due to the plasma compressibility and the geodesic magnetic curvature, ubiquitous in toroidal devices such as tokamaks. A full review of GAMs by Conway *et al.* can be found in [132]. The principle is the following: the magnetic curvature translates into a  $(m, n) = (1, 0)$  pressure perturbation, which couples with the diamagnetic velocity  $\mathbf{v}_{\text{dia}} = \frac{\mathbf{B} \times \nabla P}{neB^2}$  to induce a  $(m = 0)$  mode of the radial electric field. GAMs are known to play a role in turbulence regulation, first by the establishment of sheared  $E \times B$  flows and second by acting as a sink for the energy carried by turbulence (that then acts as a source for the GAMs). However GAMs oscillate at high frequency, such that the turbulence mitigation through corresponding sheared  $E \times B$  flow is expected to be small compared with steady flows<sup>8</sup>.
- Zonal flows are low-frequency flows driven by turbulence. Contrary to GAMs, they can exist even without magnetic curvature. In fact, zonal flows are not restricted to magnetized plasmas: Jupiter jet streams are an example. However, like GAMs, they also act as a reservoir that can pump energy from turbulence. Zonal structures can be associated with strong shearing flow regions. The stationary feature of these structures allows efficient mitigation of turbulence.

Some publications [133, 134] on the effect of the safety factor on flows invoke the argument that  $q$  affects the way turbulent energy is distributed among ZFs and GAMs (scalings of associated damping rates with the safety factor are given in upcoming section Sec.5.4.3). The principle is quite simple: at low  $q$ , the GAMs are strongly damped but not the ZFs so the excess of turbulent energy is transferred to ZFs. In turn, the radial structures associated with these ZFs increase the sheared flows, i.e. the radial electric field, and by doing so lower the turbulent intensity. On the contrary, at high  $q$ , the GAMs are not damped. The oscillatory nature of GAMs makes the effective flow shear lower than ZFs, and so is the associated radial electric field. At intermediate  $q$  values, ZFs and GAMs coexist.

Quantifying these processes is complicated, even with comprehensive gyrokinetic simulations. The approach here is to find "clues" that support this idea of energy transfer between turbulence, ZFs and GAMs. Fig.5.17 shows frequency spectra of the  $q_{0.5}$  and  $q_{1.5}$  cases, averaged in the region of interest  $0.75 < r/a < 0.85$ , and obtained

8. Indeed, if the direction of the shearing flows oscillates fast in time, turbulent structures perpendicular stretch is limited.

5. Influence of the safety factor on the radial electric field – 5.4. Mechanisms impacting flows carrying a  $q$  dependence

in two different time ranges in the simulation. The first time range is plotted in Fig.5.17a and corresponds to the beginning of the simulations. These simulations are run from an initial distribution function that always differs from the equilibrium distribution function. During the transition to this equilibrium, GAMs are driven. This phase is shown in order to identify the GAMs frequency, and is further assessed by a comparison with the Winsor prediction<sup>9</sup> [136] of the GAMs frequency that reads

$$\omega_{\text{GAM}}^{\text{theo}} = \frac{2}{R_0} \sqrt{\frac{5}{3} \frac{T}{m} \left(1 + \frac{1}{2q^2}\right)}. \quad (5.7)$$

The bump in the frequency spectra of  $E_r$  is then clearly identified as GAMs and can be compared with Fig.5.17b showing the same quantity in the turbulent phase<sup>10</sup>. In this phase, the GAMs amplitude is more than 10 times lower in the  $q_{0.5}$  case than the  $q_{1.5}$ . This behavior is expected, as the damping rate of the GAMs is known to decrease with the safety factor in the collisionless case which is relevant in these simulations. The interesting part of these simulations is that GAMs can only be driven by turbulence, itself driven by the thermodynamical gradients which are the same in each simulation. As seen previously in Fig.5.8, the energy in the  $q_{0.5}$  case is not fed substantially to the turbulent intensity (relative to the other cases). Here we observe that the energy is not fed to the GAMs either. The remaining channel is an energy transfer to static zonal flows.

---

9. The first paper with an explicit form is actually [135].

10. The effect is less clean than Fig.5.17a due to the undersized time resolution fixed by the rate at which data are saved  $\Delta t_{\text{diag}} = 450\omega_{c0}^{-1}$ .

5. Influence of the safety factor on the radial electric field – 5.4. Mechanisms impacting flows carrying a  $q$  dependence

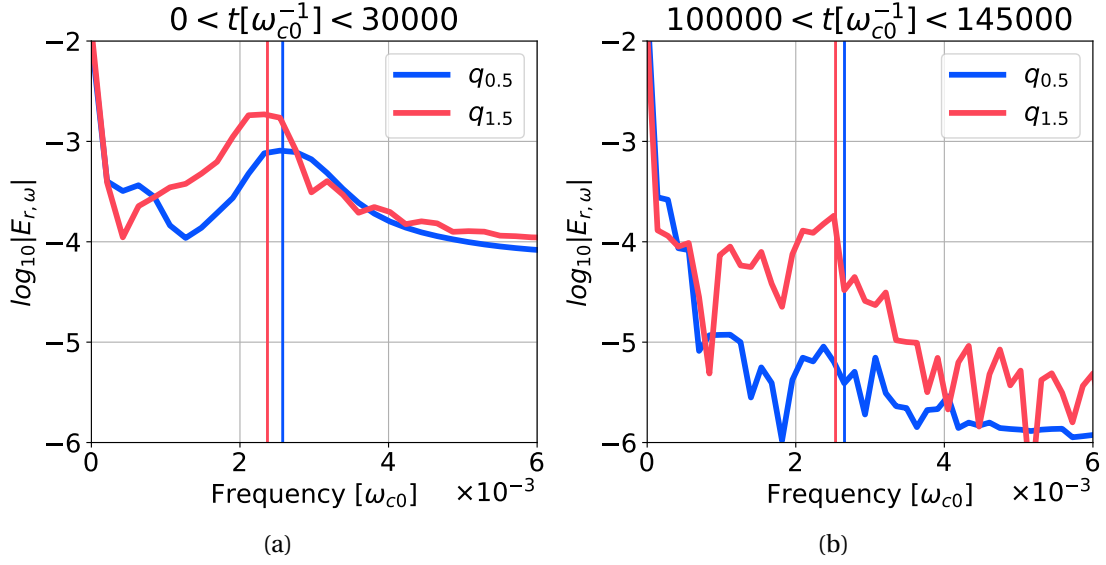


Figure 5.17. – Frequency-spectra of the radial electric field averaged in the range  $0.75 < r/a < 0.85$  and taken at the beginning of the simulations (left) and in the turbulent phase (right) for the  $q_{0.5}$  and  $q_{1.5}$  cases. The vertical lines represent the theoretical GAMs frequency  $\omega_{\text{GAM}}^{\text{theo}}$ .

Another interesting clue is the radial profile of the poloidal Reynolds stress divergence which can be seen as the drive for zonal flows and GAMs drives.

Fig.5.18 shows the spatiotemporal evolution of the radial electric field  $E_r$  in the turbulent phase and the coarse-grained poloidal Reynolds stress divergence  $\nabla \cdot \langle \Pi_{r\theta} \rangle_{\text{CG}}$  radial profile for the  $q_{0.5}$  and  $q_{1.5}$  cases. The coarse-grain procedure is the same as described in Sec.4.3: it consists of a time average of  $10^5 [\omega_{c0}^{-1}]$ , i.e. about 50 turbulent correlation times and a sliding radial average with a  $\sim 50\rho_i$  window, i.e. about 5-6 correlation lengths. The poloidal Reynolds stress is estimated in the code as a fluid moment of the distribution function  $F$ :

$$\Pi_{r\theta} = \frac{1}{n} \left\langle \int d^3\mathbf{v} (v_\theta v_{Er}) F \right\rangle \quad (5.8)$$

where  $v_\theta$  is the poloidal component of the particle's velocity and  $v_{Er} = -B^{-1} \partial_\theta \phi$  with  $\phi$  the electric potential.

For the  $q_{0.5}$  case, there is a clear correlation between the radial zonal structures of  $E_r$  and the turbulent drive. For the  $q_{1.5}$  case, there is also a quite clear correlation between the turbulent source and the radial electric field: high amplitude events of  $E_r$  are mostly located at a radial position that matched the peaks of  $\nabla \cdot \langle \Pi_{r\theta} \rangle_{\text{CG}}$ . Between the two cases, there is about an order of magnitude of difference in the Reynolds stress divergence. This matches the idea that the turbulent source, by feeding zonal flows, reduces efficiently the turbulent intensity and consequently itself.



5. Influence of the safety factor on the radial electric field – 5.4. Mechanisms impacting flows carrying a  $q$  dependence

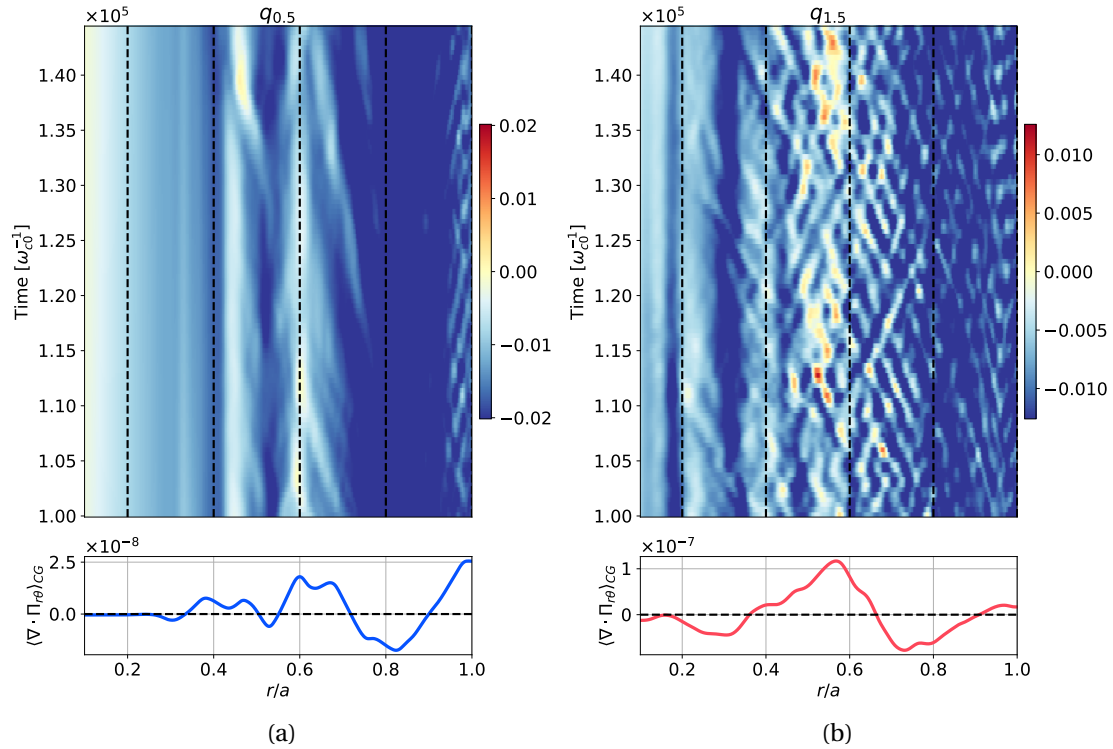


Figure 5.18. – Spatiotemporal evolution of the radial electric field (top) and the coarse-grained electric Reynolds stress divergence radial profile (bottom) for the  $q_{0.5}$  case (a) and  $q_{1.5}$  case (b).

Given all these observations, the mechanisms of energy transfer from turbulence to ZFs and GAMs are further developed with a 0D reduced model.

### 5.4.3. Reduced model of energy transfer between turbulence, zonal flows and GAMs

Based on the previous observations, the main mechanism retained for the formation of a steep radial electric field near the edge is the plasma safety factor dependence on the flow generated by turbulence. The idea is that turbulence can transfer energy to ZFs and GAMs, which themselves retroact on turbulence. This transfer favors either GAMs or ZFs depending on the safety factor value. To assess this idea, a simplified version of the 0D model proposed by Miki & Diamond [137] is first described and further utilized. The original model is meant to study the L-H transition. Here, it is complemented by restoring the safety factor dependence of the main parameters. The objective of this model is not to obtain a quantification of energy transfer but rather to have a rough idea of how the energy is distributed based on both observations and well-known scalings. Any assumptions and simplifications made, most of them arguable, are mentioned. This section should be treated as a preliminary attempt toward a more detailed description of turbulent energy transfer. Fig.5.19 shows a

5. Influence of the safety factor on the radial electric field – 5.4. Mechanisms impacting flows carrying a  $q$  dependence

sketch of the model's key features. The principal difference with the Miki & Diamond model is that the energy transfer between ZFs and GAMs is not considered here. This choice is done as it does not seem necessary to obtain the  $q$  scaling of interest, and it greatly simplifies the problem.

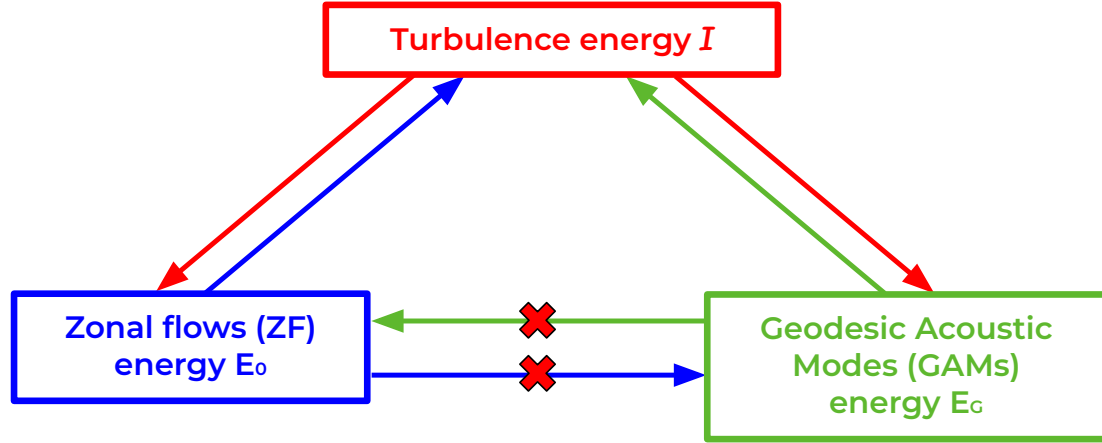


Figure 5.19. – Sketch summarizing the 0D model for the energy exchanges between turbulence, zonal flows and GAMs. Note that the possible direct interplay between GAMs and zonal flows is not considered, which constitutes the main difference with the model of Miki & Diamond [137].

Defining the turbulent intensity  $\mathcal{I}$ , the ZFs energy  $E_0$  and the GAMs energy  $E_G$ , the model equations are

$$\partial_t \mathcal{I} = \gamma_L \mathcal{I} - \Delta\omega \mathcal{I}^2 - \alpha_0 \mathcal{I} E_0 - \alpha_G E_G \mathcal{I} \quad (5.9)$$

$$\partial_t E_0 = \alpha_0 \mathcal{I} E_0 - \nu_0 E_0 - \gamma_0 E_0^2 \quad (5.10)$$

$$\partial_t E_G = \alpha_G \mathcal{I} E_G - \nu_G E_G - \gamma_G E_G^2 \quad (5.11)$$

where each of the parameters is defined in Tab.5.1.

	Description	Expected $q$ dependence
$\gamma_L$	Linear growth rate	Yes
$\Delta\omega$	Non-linear saturation	Unknown
$\alpha_0, \alpha_G$	Turbulence coupling coefficients to ZFs, GAMs	Unknown
$\nu_0, \nu_G$	Linear damping of ZFs, GAMs	Yes
$\gamma_0, \gamma_G$	2nd order saturation of ZFs, GAMs	Unknown

Table 5.1. – Parameters appearing in the system of equations.

In this same table is indicated whether or not a  $q$ -dependence is accounted for each parameter. If unknown, no dependence with  $q$  is considered in the following.

5. Influence of the safety factor on the radial electric field – 5.4. Mechanisms impacting flows carrying a  $q$  dependence

Expressed in words, these equations can be described as follow. Eq(5.9) states that the turbulent energy  $\mathcal{I}$  grows linearly at a rate  $\gamma_L$  but saturates non-linearly at a rate  $\Delta\omega$ , while allowing energy transfer with zonal flows and GAMs through the two last quadratic terms. Eq(5.10) states that the zonal flow energy  $E_0$  can only grow when turbulent energy is transferred, but is damped linearly as observed in experiments. A quadratic saturation  $\gamma_0 E_0^2$  is added for the stability of the model<sup>11</sup>, which is another difference with the model in [137]. Eq(5.11) is analogous to Eq(5.10) for the GAMs. Note that the total energy  $\mathcal{I} + E_0 + E_G$  is conserved when all the drive/damping rates are set to zero.

Handy normalizations allow the rewriting of these equations such that

$$\partial_\tau \mathcal{I} = \mathcal{I}(\mathcal{I}_L - \mathcal{I} - C_0 \mathcal{E}_0 - C_G \mathcal{E}_G) , \quad (5.12)$$

$$a_0 \partial_\tau \mathcal{E}_0 = \mathcal{E}_0(\mathcal{I} - \mathcal{I}_0 - \mathcal{E}_0) , \quad (5.13)$$

$$a_G \partial_\tau \mathcal{E}_G = \mathcal{E}_G(\mathcal{I} - \mathcal{I}_G - \mathcal{E}_G) \quad (5.14)$$

with the new terms defined in Tab.5.2.

$\tau = \Delta\omega t$	Normalized time
$\mathcal{E}_0 = \frac{\gamma_0}{\alpha_0} E_0, \mathcal{E}_G = \frac{\gamma_G}{\alpha_G} E_G$	Normalized energies of ZFs, GAMs
$\mathcal{I}_0 = \frac{\gamma_0}{\alpha_0}, \mathcal{I}_G = \frac{\gamma_G}{\alpha_G}$	Normalized dampings of ZFs, GAMs
$\mathcal{I}_L = \frac{\gamma_L}{\Delta\omega}$	Normalized turbulent growth rate
$C_0 = \frac{\alpha_0^2}{\Delta\omega\gamma_0}, C_G = \frac{\alpha_G^2}{\Delta\omega\gamma_G}$	Coupling parameters of ZFs, GAMs
$a_0 = \frac{\Delta\omega}{\alpha_0}, a_G = \frac{\Delta\omega}{\alpha_G}$	Normalized evolution rate of ZFs, GAMs

Table 5.2. – Normalization parameters

One can now calculate the fixed points, i.e. the  $(\overline{\mathcal{I}}, \overline{\mathcal{E}_0}, \overline{\mathcal{E}_G})$  sets such that  $\partial_\tau(\mathcal{I}, \mathcal{E}_0, \mathcal{E}_G) = 0$ . In order to describe interesting equilibria, we consider a finite turbulent intensity such that  $\overline{\mathcal{I}} > 0$ . Four different equilibria can then be found:

1. The "No flows" case where  $\mathcal{E}_0 = \mathcal{E}_G = 0$ . In that case, the solutions are simply

$$\overline{\mathcal{I}}^{\text{NF}} = \mathcal{I}_L , \quad (5.15)$$

$$\overline{\mathcal{E}_0}^{\text{NF}} = 0 , \quad (5.16)$$

$$\overline{\mathcal{E}_G}^{\text{NF}} = 0 . \quad (5.17)$$

2. The "ZFs only" case where  $\mathcal{E}_G = 0$  and  $\mathcal{E}_0 > 0$ . The solutions are

11. And also because the choice  $\gamma_0 = \gamma_G = 0$  does not allow an equilibrium "GAMs only" or a "Mixed ZFs/GAMs" when a "ZFs only" equilibrium exists, as presented further.

5. Influence of the safety factor on the radial electric field – 5.4. Mechanisms impacting flows carrying a  $q$  dependence

$$\overline{\mathcal{I}}^{\text{ZF}} = \frac{\mathcal{I}_L + C_0 \mathcal{I}_0}{1 + C_0} , \quad (5.18)$$

$$\overline{\mathcal{E}}_0^{\text{ZF}} = \frac{\mathcal{I}_L - \mathcal{I}_0}{1 + C_0} , \quad (5.19)$$

$$\overline{\mathcal{E}}_G^{\text{ZF}} = 0 . \quad (5.20)$$

3. The "GAMs only" case where  $\mathcal{E}_0 = 0$  and  $\mathcal{E}_G > 0$ . By analogy with the previous case, the solutions are

$$\overline{\mathcal{I}}^{\text{GAM}} = \frac{\mathcal{I}_L + C_G \mathcal{I}_G}{1 + C_G} , \quad (5.21)$$

$$\overline{\mathcal{E}}_0^{\text{GAM}} = 0 , \quad (5.22)$$

$$\overline{\mathcal{E}}_G^{\text{GAM}} = \frac{\mathcal{I}_L - \mathcal{I}_G}{1 + C_G} . \quad (5.23)$$

4. The "mixed ZFs/GAMs" case where each parameter is strictly positive. The solutions are

$$\overline{\mathcal{I}}^{\text{MIX}} = \frac{1}{1 + C_0 + C_G} (\mathcal{I}_L + \mathcal{I}_G C_G + \mathcal{I}_0 C_0) , \quad (5.24)$$

$$\overline{\mathcal{E}}_0^{\text{MIX}} = \frac{1}{1 + C_0 + C_G} (\mathcal{I}_L - \mathcal{I}_0(1 + C_G) + C_G \mathcal{I}_G) , \quad (5.25)$$

$$\overline{\mathcal{E}}_G^{\text{MIX}} = \frac{1}{1 + C_0 + C_G} (\mathcal{I}_L - \mathcal{I}_G(1 + C_0) + C_0 \mathcal{I}_0) . \quad (5.26)$$

Each equilibrium's stability is assessed in Appendix F.

Let us take the normalized growth rate  $\mathcal{I}_L$  as a parameter control. Increasing it from zero, the first stable equilibrium is the "No flows" case. Then two cases can occur.

In one case, when  $\mathcal{I}_0 < \mathcal{I}_G$ , then the "ZFs only" equilibrium is satisfied when  $\mathcal{I}_L$  reaches  $\mathcal{I}_0$  and the zonal flow energy  $\overline{\mathcal{E}}_0$  is allowed to grow. In this situation, the "GAMs only" and "mixed ZFs/GAMs" equilibria are not allowed as  $\overline{\mathcal{E}}_G < 0$  when  $\mathcal{I}_0 \leq \mathcal{I}_L < \mathcal{I}_G$ . By continuity, the "mixed ZFs/GAMs" equilibrium is reached when  $\mathcal{I}_L = \mathcal{I}_G + C_0(\mathcal{I}_G - \mathcal{I}_0)$  where  $\overline{\mathcal{E}}_0 = \mathcal{I}_G - \mathcal{I}_0$ .

In the other case, i.e.  $\mathcal{I}_G < \mathcal{I}_0$ , then the "GAMs only" equilibrium is satisfied when  $\mathcal{I}_L$  reaches  $\mathcal{I}_G$  and the GAMs energy  $\overline{\mathcal{E}}_0$  is allowed to grow. The "mixed ZFs/GAMs" equilibrium is reached when  $\mathcal{I}_L = \mathcal{I}_0 + C_G(\mathcal{I}_0 - \mathcal{I}_G)$  and then  $\overline{\mathcal{E}}_G = \mathcal{I}_0 - \mathcal{I}_G$ .

Let us look at the results given by this model when accounting for the safety factor scaling of the main parameters. The three main parameters with a safety factor dependence are expected to be:

- The **linear growth rate**  $\gamma_L$  of turbulence, for which a prediction is not available.

5. Influence of the safety factor on the radial electric field – 5.4. Mechanisms impacting flows carrying a  $q$  dependence

However, in our simulation as well as other numerical results [127],  $\gamma_L$  increases monotonically with  $q$  in a non-linear fashion. As the increase is slower when  $q$  increases, here it is arbitrarily modeled with a  $q^{1/3}$  scaling;

- The **damping rate of zonal flows**  $\nu_0$ , for which the choice is delicate. On the one hand, it should be chosen as the collisional damping rate of ZFs as calculated by Hinton & Rosenbluth [138]. On the other hand, it is clear that observations are related to the mean flow, which can be seen as the zero frequency limit of ZFs. In this case, the damping rate is the one predicted by neoclassical theory. The second path is adopted here, where  $\nu_0$  is then the neoclassical friction  $\nu_{\theta,neo}$ . Here it is estimated that it follows the *plateau* regime<sup>12</sup> of collisionality where the prediction is  $\nu_{\theta,neo} = 2.21 q V_{th} / R$ ;
- The **damping rate of GAMs**  $\nu_G$ , which has different predictions regarding the magnetic surface shape, the orbit width effects or the collisional regime. They are all available in [132] (check p.22 for a table with all damping rates predictions). Here we consider two different scalings for the collisional and collisionless cases. For the collisionless case, the simplest prediction is the one of Landau that scales like  $\nu_G \propto q^5 \exp(-q^2)$ . However, this simple prediction is not valid for low values of  $q$ , which are of interest here. Indeed the Landau prediction states that  $\nu_G \rightarrow 0$  when  $q \rightarrow 0$  when actually it should go toward very high values. Fig.5.20 shows typical GAMs damping rates compared with a precise theoretical prediction from Gao [139] and some simulations codes. In all cases, the damping rate increases substantially when  $q$  approaches unity. To account for this, an arbitrary prefactor  $1 + q^{-6}$  is added to the Landau prediction.

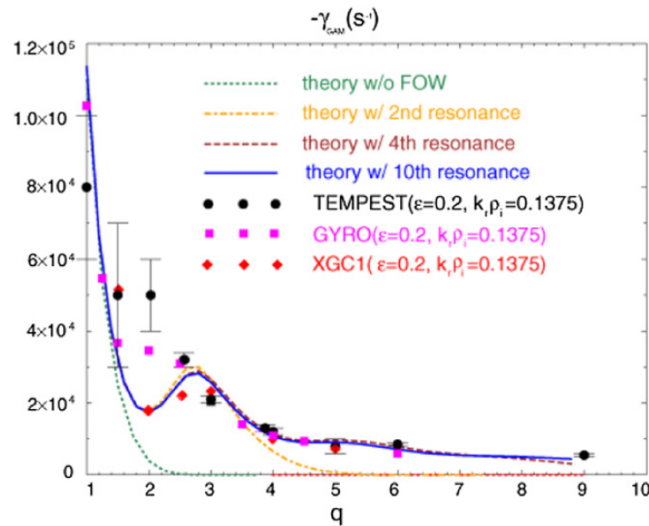


Figure 5.20. – GAMs damping rate obtained with the Gao theoretical prediction (lines) and obtained with several simulation codes (points). Extracted from [132].

12. Note that in the *banana* regime of collisionality the prediction is  $\nu_{\theta,neo} = 0.66 q^2 v_i / \epsilon^{3/2}$

5. Influence of the safety factor on the radial electric field – 5.4. Mechanisms impacting flows carrying a  $q$  dependence

For the collisional case, we consider the Novakoskii prediction  $\nu_G = (4/7)\nu_i$  that scales as  $q^{-1}$  at fixed collisionality  $\nu^*$  (as discussed in 5.4.1).

These scalings give the following expressions

$$\mathcal{I}_L = A_L q^{1/3}, \quad (5.27)$$

$$\mathcal{I}_0 = A_0 q, \quad (5.28)$$

$$\mathcal{I}_G = A_G(1 + q^{-6})q^5 \exp(-q^2) \quad (\text{Collisionless}), \quad (5.29)$$

$$\mathcal{I}_G = A_G q^{-1} \quad (\text{Collisional}). \quad (5.30)$$

Where  $A_L$ ,  $A_0$  and  $A_G$  are constant control parameters. In order to obtain physically relevant results, the ordering  $A_0 \ll A_L, A_G$  must be considered. If this ordering on  $A_L$  is an assumed gamble, we believe that it does make sense for  $A_0$  and  $A_G$  because it is expected that the dissipation  $\nu_0$  of ZFs is weak while the non-linear coupling  $\alpha_0$  is expected to be strong, such that  $I_0 = \nu_0/\alpha_0$  is small. The coupling parameters,  $C_0$  and  $C_G$  are set arbitrarily to unity.

Considering the collisionless case first, the  $q$  dependence of  $\mathcal{I}_L$ ,  $\mathcal{I}_0$  and  $\mathcal{I}_G$  is displayed in Fig.5.21. In this same figure is displayed the boundary between each equilibrium. Increasing the safety factor from  $q = 0$ , the first equilibrium is the "Zonal flows only", then the "Mixed ZFs/GAMs" and for very high values of  $q$  the "GAMs only" equilibrium is reached.

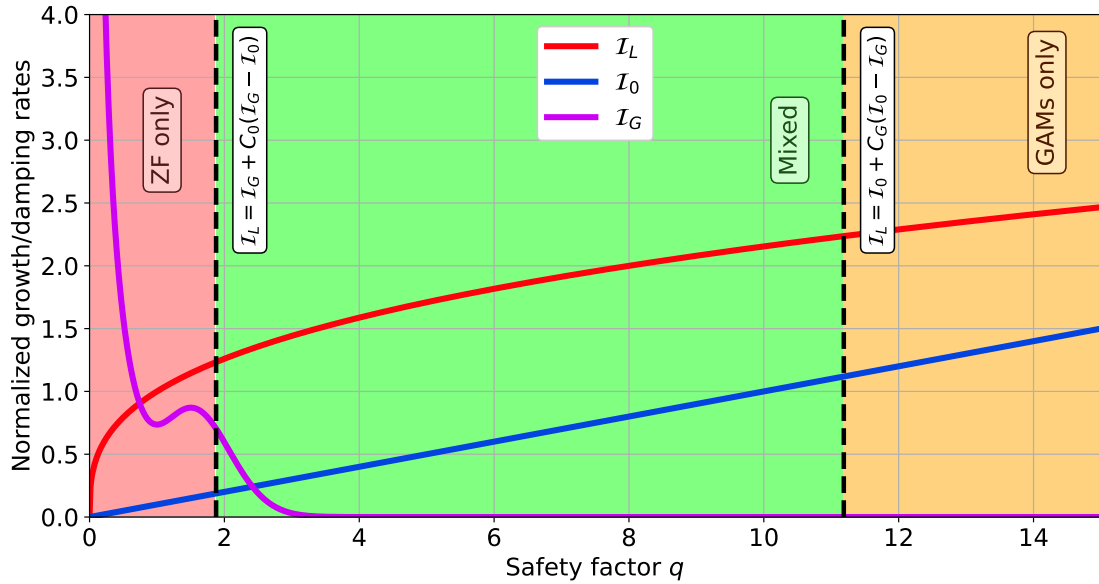


Figure 5.21. – Safety factor dependence of the normalized damping rates  $\mathcal{I}_0$  (ZFs) and  $\mathcal{I}_G$  (GAMs) and the normalized turbulent growth rate  $\mathcal{I}_L$  in the collisionless case. The parameters of control are  $A_0 = 0.1$ ,  $A_L = 1$  and  $A_G = 1$ .

The resulting turbulent, zonal flows and GAMs energies are displayed in Fig.5.22. As

5. Influence of the safety factor on the radial electric field – 5.4. Mechanisms impacting flows carrying a  $q$  dependence

expected, the zonal flow energy is maximum at low  $q$  and decays with an increasing safety factor, for the benefit of the GAMs energy that increases in the meantime. The turbulent intensity keeps a roughly  $q^{1/3}$  profile. This sequence is in line with what is observed in simulations. The abrupt transition from "ZFs only" to "Mixed ZFs/GAMs" is due to the steep scaling of the GAMs damping rate with the safety factor.

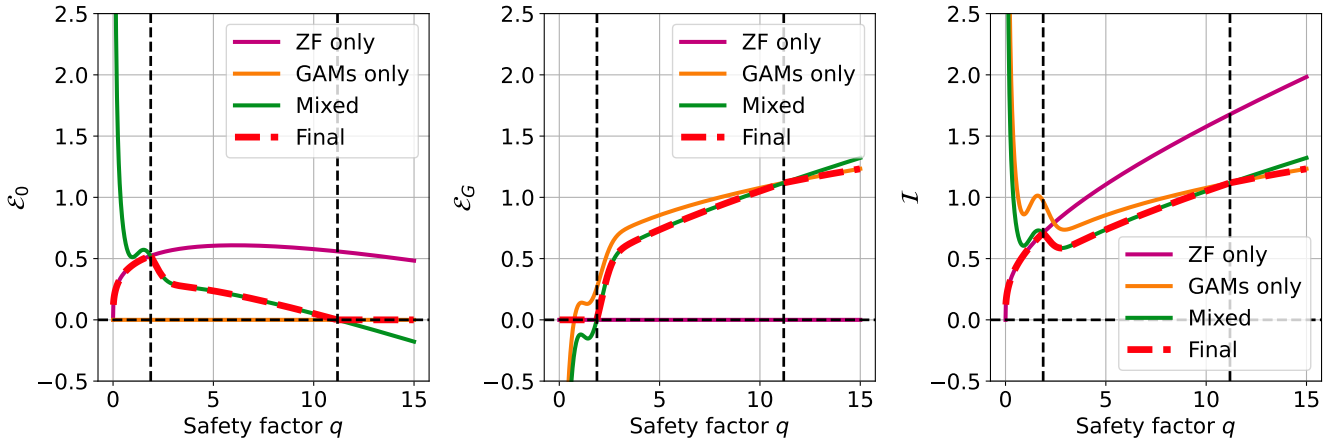


Figure 5.22. – Zonal flows (left), GAMs (middle) and turbulent (right) energy in the situation described in Fig.5.21.

In the collisional case, the scaling with the safety factor of  $\mathcal{I}_L$ ,  $\mathcal{I}_0$  and  $\mathcal{I}_G$  is displayed in Fig.5.23. The resulting turbulent, zonal flows and GAMs energies are displayed in Fig.5.24. Behavior similar to the collisionless case is retrieved.

5. Influence of the safety factor on the radial electric field – 5.4. Mechanisms impacting flows carrying a  $q$  dependence

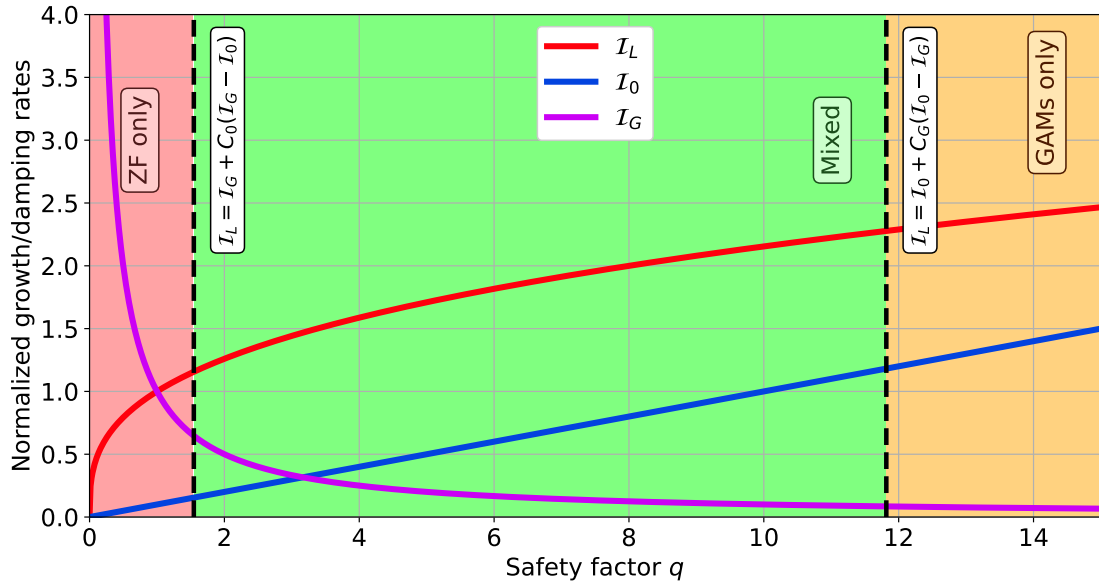


Figure 5.23. – Safety factor dependence of the normalized damping rates  $\mathcal{I}_0$  (ZFs) and  $\mathcal{I}_G$  (GAMs) and the normalized turbulent growth rate  $\mathcal{I}_L$  in the collisional case. The parameters of control are  $A_0 = 0.1$ ,  $A_L = 1$  and  $A_G = 1$ .

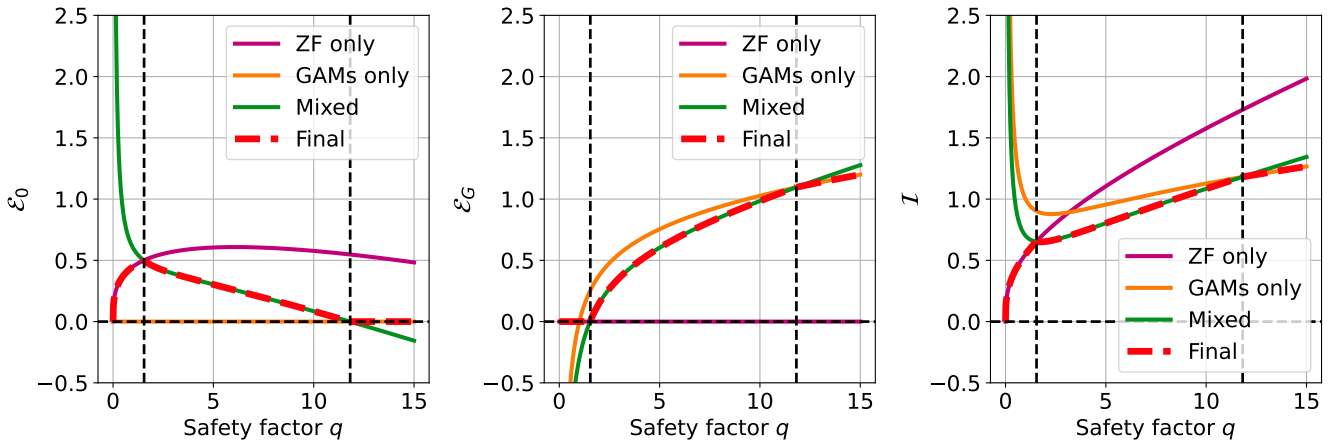


Figure 5.24. – Zonal flows (left), GAMs (middle) and turbulent (right) energy in the situation described in Fig.5.23.

All in all, this simple model that includes the minimal physical ingredients carrying a safety factor dependence is comforting in the idea of an energy transfer from turbulence to zonal flows and GAMs. It should be taken with a grain of salt, as many parameters are set ad-hoc. However, it gives some bricks to build a more precise description of the role of the safety factor in turbulence regulation.



#### 5.4.4. Synergy between turbulence and neoclassical effects

We already assessed neoclassical effects without turbulence in Sec.5.4.1. Nevertheless, this does not rule out the effect of neoclassical processes on  $E_r$  when there is also turbulence. To assess this synergy, the vorticity conservation equation is not suitable as the neoclassical and turbulent effects are challenging to discriminate in terms that constitute it.

Instead, we use an approximate expression for the evolution of the poloidal velocity  $V_P$ , which is a proxy for the radial electric field  $E_r$ , that reads

$$\frac{\partial V_P}{\partial t} = -\nabla \cdot (\Pi_{r\theta} + \Pi_{r\theta}^*) - \nu_\theta (V_P - V_0) \quad (5.31)$$

with  $\Pi_{r\theta}$  the poloidal Reynolds stress due to the electric drift,  $\Pi_{r\theta}^*$  the diamagnetic Reynolds stress and  $\nu_\theta$  a friction.

Let us give sense to the physical meaning of these terms. The divergence of the electric and diamagnetic Reynolds stress can be seen as the turbulent source. The term  $\nu_\theta (V_P - V_0)$  states that the poloidal velocity is pushed toward a value  $V_0$  at a rate  $\nu_\theta$ . The structure of this term comes from the fact that, without turbulence, the axisymmetric component  $n = 0$  of the terms in the integrated vorticity conservation Eq(5.3) can be expressed in this fashion, with  $\nu_\theta$  equal to the neoclassical poloidal friction<sup>13</sup>  $\nu_{\theta,neo}$  and  $V_0 = V_{P,eq}^{neo}$  given in Eq(5.5).

Even this simplified form comes with its share of complexities. The first difficulty is to calculate the diamagnetic Reynolds stress, which requires the knowledge of the pressure fluctuations in the 3D real space, unfortunately only saved at some time steps in these simulations. It has been shown [140] that this diamagnetic term  $\Pi_{r\theta}^*$  can be of the same order of magnitude, and on average even two times higher, than the electric Reynolds stress  $\Pi_{r\theta}$  in GYSELA simulations of ITG turbulence. This diamagnetic term is also expected to be in phase with the electric Reynolds stress. Here a rough assessment of this quantity is made using the 3D data at time  $t = 93600\omega_{c0}^{-1}$ , for which the radial profile is displayed in 5.25 and compared with the electric Reynolds stress for each simulation. As expected, it appears that the diamagnetic Reynolds stress is indeed in phase with the electric Reynolds stress, and with the same order of magnitude.

---

13. This quantity is analogous to the toroidal friction  $\nu_\phi$  discussed in Chapter 2 but in the poloidal direction

5. Influence of the safety factor on the radial electric field – 5.4. Mechanisms impacting flows carrying a  $q$  dependence

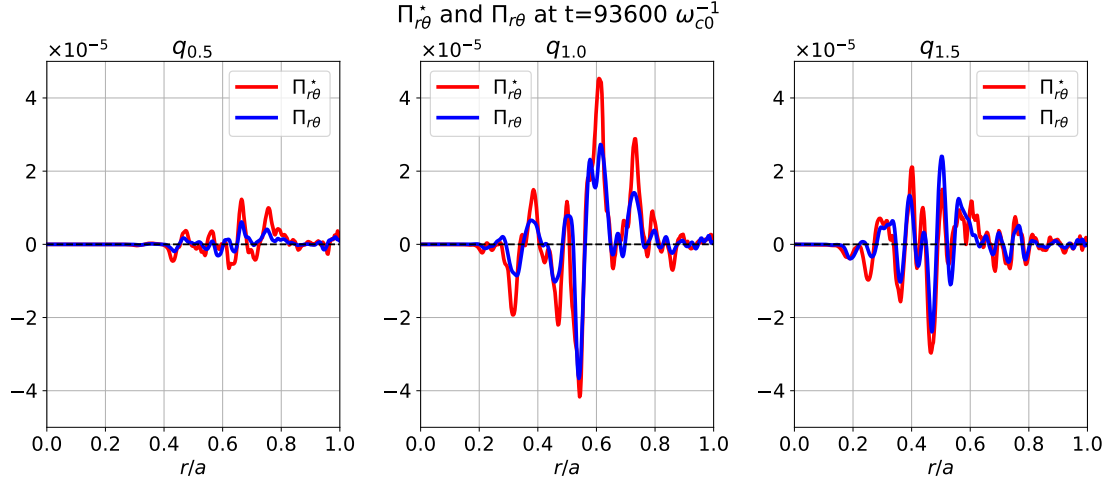


Figure 5.25. – Radial profile of the diamagnetic stress tensor  $\Pi^*$  and the electric Reynolds stress  $\Pi_{r\theta}$  for each simulation at  $t = 93600\omega_{c0}^{-1}$ .

In the following, we define the quantity  $\Pi = \Pi_{r\theta} + \Pi_{r\theta}^*$  will be reasonably approximated to  $\Pi \approx 2\Pi_{r\theta}$ .

The second complexity comes from the friction  $v_\theta$  and the target velocity  $V_0$  that are unknowns of the problem. The neoclassical effects are expected to be fully included in these terms. A first step consists to consider that  $v_\theta$  and  $V_0$  are only due to neoclassical effects. Then, at equilibrium, Eq(5.31) becomes

$$V_{P,eq} \simeq V_{P,eq}^{neo} - \frac{\nabla \cdot \Pi}{v_{\theta,neo}} . \quad (5.32)$$

Compared with the case with neoclassical processes only, a new term appears and depends both on collisional effects through  $v_{\theta,neo}$  and turbulence through  $\Pi$ . A problem is that the collisional friction  $v_\theta$  is not a GYSELA output. Estimating this friction precisely would require a whole study similar to what has been done in Chapter 3 for obtaining the toroidal neoclassical friction  $v_\varphi$ . Here, we use the heuristic expression taking into account all collisional regimes in the axisymmetric case given in [141] (See Eq(C.15)) that reads

$$v_{\theta,neo} = \mu_i (q/\varepsilon)^2 \quad (5.33)$$

with

$$\mu_i = \frac{0.452 f_t v_i}{(1 + 1.03 v^{*1/2} + 0.31 v^*)(1 + 0.66 v^* \varepsilon^{3/2})} \quad (5.34)$$

where  $v_i$  is the ion-ion collision frequency and  $f_t$  is the fraction of trapped particles estimated as  $\sqrt{2\varepsilon}$ .

The equilibrium velocity  $V_{P,eq}^{neo}$  is given by the simulations without turbulence discussed in Sec.5.4.1. The contribution of each of these terms, for the  $q_{0.5}$  and  $q_{1.5}$  cases, is given in Fig.5.26.

5. Influence of the safety factor on the radial electric field – 5.4. Mechanisms impacting flows carrying a  $q$  dependence

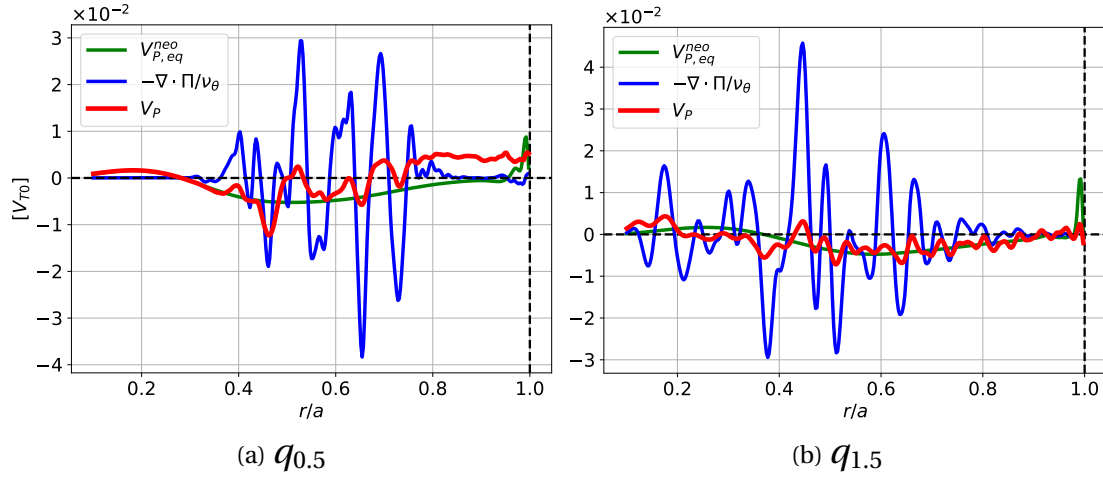


Figure 5.26. – Radial profile of  $V_{P,eq}^{neo}$  obtained with the "neoclassical" simulations (green),  $-\frac{\nabla \cdot \Pi}{\nu_{\theta,neo}}$  obtained with the electric Reynolds stress from turbulent simulations and the heuristic neoclassical friction Eq(5.33) (blue) and the poloidal velocity from turbulent simulations (red) for the  $q_{0.5}$  and  $q_{1.5}$  cases. These profiles are also temporally averaged between  $65000 < t[\omega_{c0}^{-1}] < 70000$ .

It appears that the proxy of the heuristic neoclassical friction  $\nu_{\theta,neo}$  is unsatisfactory for predicting the equilibrium poloidal velocity. Indeed, the term  $-\nabla \cdot \Pi / \nu_{\theta,neo}$  is overestimated. However, we already assessed that the edge poloidal velocity in the  $q_{0.5}$  case is not retrieved with the contribution of the neoclassical prediction  $V_{P,eq}^{neo}$  (as seen in Sec.5.4.1). Then, if the simplified expression of the poloidal momentum conservation Eq(5.31) is accurate enough, the effect observed on  $E_r$  and  $V_P$  can only be due to the turbulent/neoclassic synergistic term  $-\nabla \cdot \Pi / \nu_{\theta,neo}$ .

If this is true, a source of disagreement between the simulation's results and the model is that the neoclassical friction in the code is different from the one given by the heuristic formula Eq(5.33). Another is that turbulence can modify the equilibrium poloidal velocity  $V_0$ , which would be consistent with the establishment of zonal flows in the  $q_{0.5}$  case. It would also explain the relatively low amplitude of the Reynolds stress divergence near the edge: if turbulence transfers most of its energy to zonal flows that then quench turbulence, the turbulent source is expected to drop consequently.

Based on rough scalings estimate, the synergistic term  $-\nabla \cdot \Pi / \nu_{\theta,neo}$  must decrease with the safety factor to explain the behavior of  $V_P$  and ultimately  $E_r$ . It means that  $\nu_{\theta,neo}$  should increase faster with  $q$  than  $-\nabla \cdot \Pi$ . Fig.5.27a shows the opposite of coarse-grained divergence of poloidal Reynolds stress  $-\langle \nabla \cdot \Pi_r \rangle_{CG}$  for each simulation case. Taking the value of  $-\langle \nabla \cdot \Pi_r \rangle_{CG}$  in the vicinity of  $r/a = 0.8$ , we can estimate a rough scaling of this turbulent drive with the safety factor as shown in Fig.5.27b. As shown with the green curve on this figure,  $-\langle \nabla \cdot \Pi_r \rangle_{CG}$  in the radial range of interest follows a rough  $q^{1/3}$  scaling. Regarding the collisional friction  $\nu_{\theta,neo}$ , as the collisionality at  $r/a = 0.8$  for each case is about  $\nu^* \simeq 0.25$ , it is reasonable to claim that  $\nu_{\theta,neo}$

## 5. Influence of the safety factor on the radial electric field – 5.5. Conclusion of chapter 5 and discussion

follows the  $q$ -scaling of the *plateau* collisionality regime which is linear with  $q$ . These rough estimates support the idea that the synergetic term  $-\nabla \cdot \Pi / \nu_{\theta, \text{neo}}$  decreases in amplitude with the safety factor.

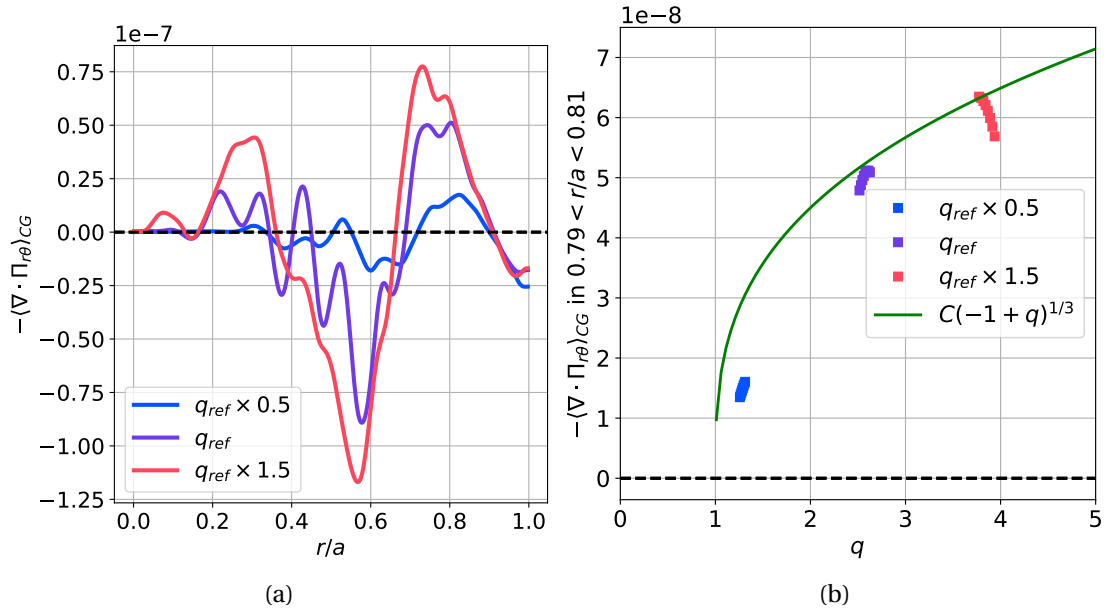


Figure 5.27. – Radial profile of coarse-grained  $-\nabla \cdot \Pi_r$  in range  $100000 < t[\omega_c^{-1}] < 145000$  with a sliding radial average with a  $50\rho_i$  window (a) for each simulation. Safety factor scan of  $-\langle \nabla \cdot \Pi_r \rangle_{\text{CG}}$  taken in simulation in radial range  $0.79 < r/a < 0.81$  ( $C$  is a constant) (b).

## 5.5. Conclusion of chapter 5 and discussion

In this Chapter, the impact of safety factor  $q$  on flows and especially the edge radial electric field in simulations of ITG turbulence has been assessed. The safety factor is a parameter of interest as it is inversely proportional to the plasma current near the edge. Recent experimental measurements on the WEST tokamak, and previous ones on Tore Supra and MAST, demonstrated that the radial electric field amplitude near the edge of the plasma increases when the plasma current increases, i.e. when the safety factor decreases. Using GYSELA simulations with different safety factor profiles, this trend has been retrieved.

The effect of neoclassical processes, without their possible synergy with turbulence, in the establishment of the flow has been assessed as negligible.

The flow, directly related to the radial electric field, induced by turbulence is of different nature depending on the safety factor value. For high  $q$  values, turbulence generates intermittent flows at GAMs frequency while for low  $q$  values, turbulence feeds quasi-steady zonal flows. As the turbulent intensity is observed to increase with the safety factor, the idea is that zonal flows in the low  $q$  case are efficient to quench

the turbulence but the GAMs in the high  $q$  case are not. Several clues in simulations point to this phenomenon. In addition, a 0D reduced model that keeps the main safety factor dependency on key model parameters determining the turbulent intensity, the zonal flow energy, and the GAMs energy, is developed and is in agreement with this idea. To go further, one could use advanced signal processing to assess the transfer of information from one quantity to another, e.g. Reynolds stress to the low-frequency zonal mode of the electric potential for the zonal flows, or the turbulent intensity to the  $(m, n) = (1, 0)$  mode of the pressure for the GAMs. The usual tools to quantify the energy transferred from one mode to another are the bispectrum and bicoherence which are used to quantify the correlation between signals. They have been used here and there [142–144] for magnetized plasmas-related studies, and especially to study the energy transfer between zonal flow and turbulence. These tools are quite tricky to use, especially as reliable results only emerge given proper statistics. In our simulations, the available statistics are unfortunately too low as the time step  $\Delta t_{\text{diag}} = 450\omega_{c0}^{-1}$  at which the data have been saved is too large.

The synergy between neoclassical effects and turbulence assessment with GYSELA revealed as a complex task. First, the fluctuating nature of the poloidal Reynolds stress in addition to the missing data to reconstruct the diamagnetic tensor make the estimation of the turbulent source challenging to assess. Secondly, it appears that the common predictions on the neoclassical friction and neoclassical equilibrium poloidal velocities are unable to explain the effect on the radial electric field. It could indicate that turbulence actually modifies these terms. However, estimates based on the available scalings with the safety factor indicate that the synergy between neoclassical effects and turbulence is encouraging to explain the observation on the radial electric field.

The sketch in Fig.5.28 acts as a summary of this chapter.

5. Influence of the safety factor on the radial electric field – 5.5. Conclusion of chapter 5 and discussion

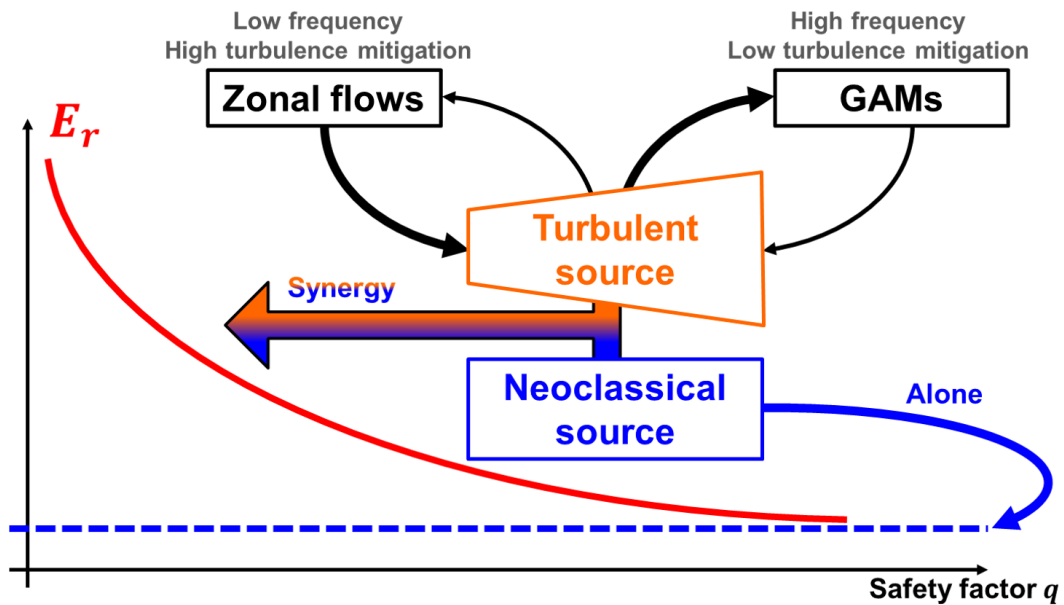


Figure 5.28. – Sketch summarizing Chapter 5.

Let us end this chapter with a conundrum. In this study, we emphasized on the behavior of GAMs, and especially on their damping which is theoretically expected to decrease with the safety factor as observed in the simulations. However experimentally, on both WEST and Tore Supra, the oscillations of the mean perpendicular velocity detected by the DBS, with a frequency in the range of expected frequency for GAMs, are found to decrease when the safety factor increases. An example of the #45333 Tore Supra discharge is displayed on Fig.5.29. It shows the amplitude of the velocity oscillations at the GAMs frequency as a function of the safety factor, effectively decreasing when  $q$  increases.

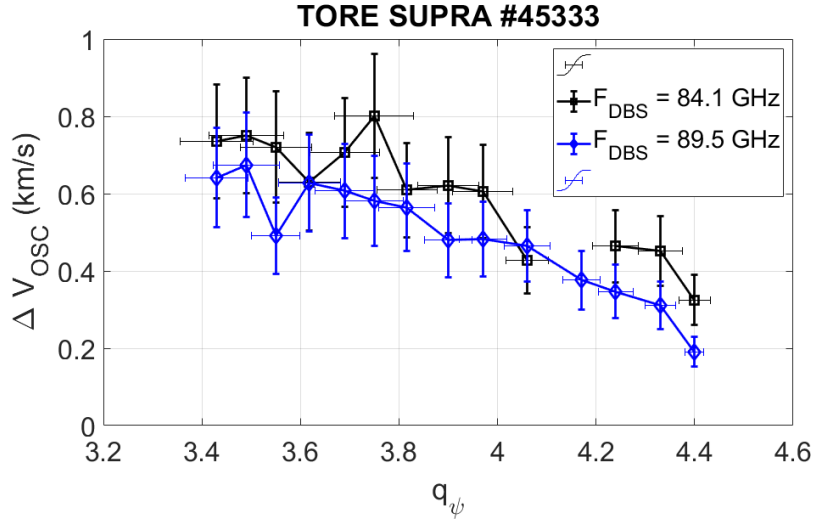


Figure 5.29. – Amplitude of the fluctuations associated with frequencies in the range of GAMs in the #45333 discharge of Tore Supra as a function of the safety factor.

Note that this trend is observed at low ( $\nu^* < 0.5$ ) and high ( $\nu^* \gg 1$ ) collisionality. This behavior remains unexplained. A reason could be that the simulations and theories come with their share of approximations, e.g. adiabatic electrons, electrostatic field or simplified boundary condition, which may impact the GAMs damping. Regarding the 0D model developed in Sec.5.4.3, it is possible to find a sequence that matches this observation, i.e. a turbulent energy transfer that favors GAMs at low  $q$  but not at high  $q$ . For this, one must consider that the GAMs damping is subdominant compared with the ZFs damping at low  $q$ , but that it increases faster. An example is shown in Fig.5.30 which shows the safety factor dependence of the normalized damping rates and growth rate in such a situation. The associated safety factor dependence of the ZFs, GAMs and turbulence energies is shown in Fig.5.31. In this case, one can observe that the GAMs energy decreases with  $q$  but at the expense of an enhancement of the zonal flows energy that is weaker than in observations/gyrokinetic simulations.

This indicates the tremendous task that remains is to obtain a robust scaling between these damping and growth rates, as well as their safety factor dependence.

5. Influence of the safety factor on the radial electric field – 5.5. Conclusion of chapter 5 and discussion

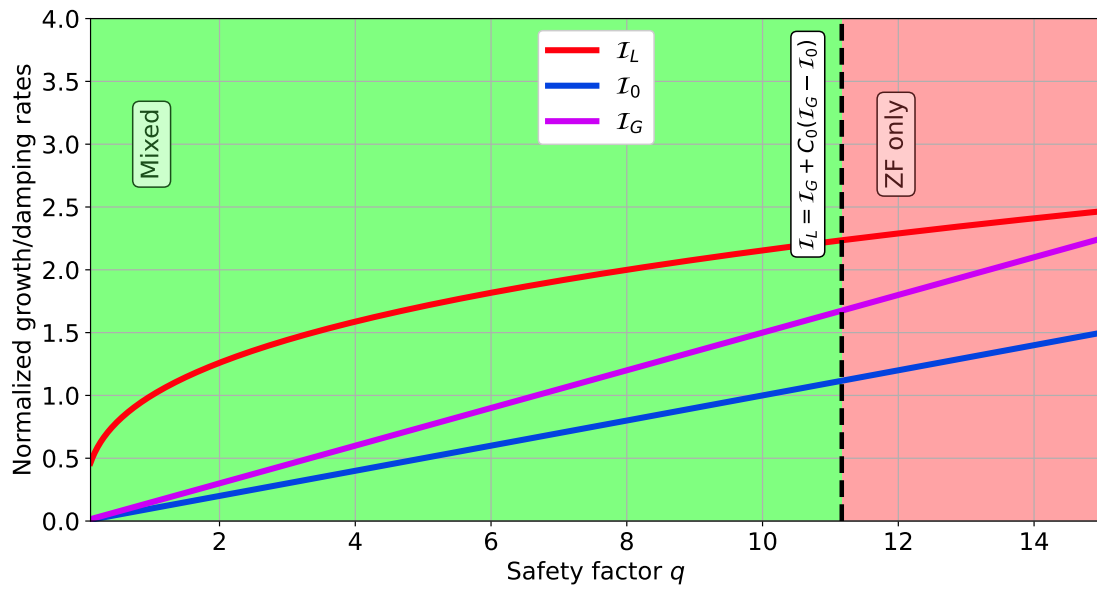


Figure 5.30. – Safety factor dependence of the normalized damping rates  $\mathcal{I}_0 = A_0 q$  (ZFs) and  $\mathcal{I}_G = A_G q$  (GAMs) and the normalized growth rate  $\mathcal{I}_L = A_L q^{1/3}$  in the collisional case. The parameters of control are  $A_L = 1$ ,  $A_0 = 0.1$  and  $A_G = 0.15$ .

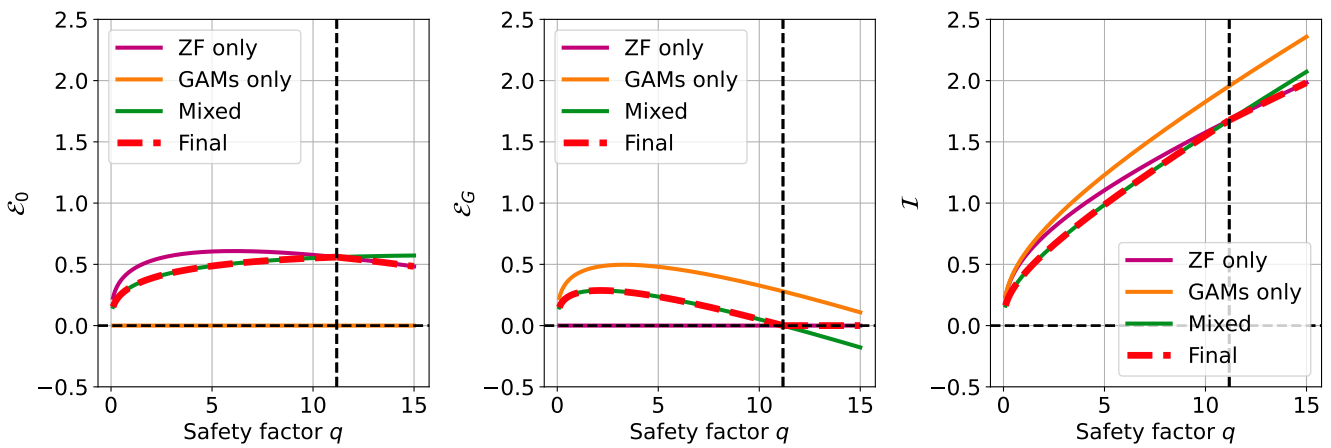


Figure 5.31. – Zonal flows (left), GAMs (middle) and turbulent (right) energy in the situation described in Fig.5.30.



# Conclusion

Flow generation in tokamak plasmas plays a key role in confinement and plasma stability. A new record on the K-STAR tokamak has been set at the time these lines are written: 20 seconds of sustained plasma at a temperature of 100 million Kelvin [145]. Such a milestone is attributed to the fast ion flow that reduces core plasma turbulent transport. This is an example among many others that illustrates the need to understand the plasma behavior in order to design new reactors and optimize the operation of the present generation of tokamaks. This thesis aims to give insight into two important unanswered questions regarding the establishment of flows.

The first question is: "How does magnetic ripple, due to the finite number of toroidal coils, impact flows in a turbulent magnetized plasma?" Several experiments have shown that 1) an enhanced magnetic ripple amplitude is correlated with an increment of the toroidal velocity in the counter-current direction and 2) toroidal velocity is also driven by turbulence. Magnetic ripple is known to impact collisional processes and to stochastize trajectories of a class of particles even in the absence of turbulence. All of this put together, the main effect of ripple is to produce a new force in the toroidal direction: the magnetic braking, which is also sometimes referred to as *Neoclassical Toroidal Viscosity*. The strategy to understand this competition/synergy between magnetic braking and turbulent drive is the following. A kinetic model including the neoclassical theory for a non-axisymmetric perturbation as well as the stochastic motion of particles has first been developed in order to predict the magnetic braking scaling with key parameters, such as the collisionality or the ripple amplitude. Adding turbulence crushes all possible dreams of integrability for this problem. The resulting flow can only be assessed with gyrokinetic codes due to the kinetic nature of mechanisms associated with both ripple and turbulence. The magnetic ripple has then been implemented in the gyrokinetic simulation code GYSELA. Using non-turbulent simulations, this implementation was first verified by testing toroidal momentum conservation where now magnetic braking appears. It has then been successfully benchmarked with the non-axisymmetric version of the reference drift-kinetic code NEO. A further comparison against the kinetic analytical model also showed reasonable agreement. The way was opened to add turbulence in simulations. Before this, a simple model of the toroidal momentum evolution has been devised, where only appears the magnetic braking and turbulent drive. This simple model states that magnetic braking becomes the main drive for the toroidal velocity above a predictable critical ripple amplitude. Simulations showed that this threshold is a good landmark to characterize the main drive of toroidal velocity. Furthermore, a simple expression giving the order of magnitude of this threshold is given. A step further is an assessment

of the synergy between these two drives, which is reachable as GYSELA simulations treat both of these effects on the same footing. The only channel of synergy found is from magnetic braking on the turbulent drive. It has been shown that neoclassical effects due to ripple modify the shear of the radial electric field, which in turn impacts the source term of the turbulent drive.

Future perspectives opened by this work include:

- Implementing the kinetic electron physics in the source term of the turbulent drive of the toroidal rotation, in order to assess the impact of momentum pinch;
- Considering the momentum source/sink induced by the boundary physics in the expression of the critical ripple amplitude;
- Gyrokinetic simulations of planned ITER discharges in presence of magnetic ripple and error fields, in order to predict if magnetic braking is competitive with the turbulent rotation drive;

The second question is: "Can we find mechanisms that deepen the well of the radial electric field when the safety factor decreases near the edge of the plasma?" The aim of this study is to explain the experimental measurements on the WEST and Tore Supra tokamak where a scan in plasma current, which is inversely proportional to the edge safety factor, has been performed. It was found that the radial electric field near the edge is enhanced for high plasma current. This study is quite relevant as the physics that governs this radial electric field is expected to impact the formation and the sustainment of transport barriers which reduce turbulent transport. For this assessment, GYSELA gyrokinetic simulations have been run with different safety factor profiles. This approach is not meant to replicate the experiments in which profiles are different from one discharge to the other. Instead, these simulations are run with the exact same parameters, including the magnetic shear, except for the safety factor. It has been observed that the radial electric field amplitude indeed increases near the edge when the safety factor decreases, i.e. the plasma current increases. The influence of neoclassical effects, without accounting for their possible synergy with turbulence, is found negligible. The main effect seems to come from turbulence which transfers energy in a way that favors zonal flows or GAMs depending on the value of the safety factor. First, the GAMs are only damped in the low safety factor case while clearly fed by turbulence in higher safety factor cases. Second, the radial shape dependence of the poloidal Reynolds stress divergence, which is the source of zonal flows, is correlated with the enhancement of the radial electric field at the edge. Regarding the poloidal velocity, which is a proxy for the radial electric field, this turbulence source amplitude added to the standard neoclassical predictions is too weak to explain the final poloidal velocity profile at the edge. This behaviour of the velocity is consistent with an energy transfer from turbulence to the mean flow, in which case the neoclassical predictions are not applicable, and would then explain this disparity. In order to reconcile all these aspects, this energy transfer is further assessed with a 0D reduced model taking into account the safety factor scaling of the damping of zonal flow and GAMs, as well as the turbulence growth rate. This scaling matches our simulations. Such results indicate that the observed gain in confinement in high plasma current experiment could be

*5. Influence of the safety factor on the radial electric field – 5.5. Conclusion of chapter 5 and discussion*

linked to the turbulence self-regulation through zonal flow establishment.

Future perspectives opened by this work include:

- A new plasma current scan with gyrokinetic simulations with proper statistics in order to use advanced signal processing and quantify the energy transfer from turbulence to zonal flows and GAMs;
- Assessing the order of magnitude of the damping and growth rates of turbulence, GAMs and zonal flows in order to strengthen the reduced 0D model.

# Appendices

## A. Derivation of the guiding center equations of motion

This appendix is meant to give the detail of derivation of the motion equations of the guiding center that are shown in Sec.1.4.4 in Chapter 1.

Starting from the Lagrangian in the set of variables  $(\mathbf{X}, v_{\parallel}, \mu, \varphi_c)$

$$\mathcal{L}(\mathbf{X}, v_{\parallel}, \mu, \varphi_c, t) = e\mathbf{A}^*(\mathbf{X}, t) \cdot \dot{\mathbf{X}} + \frac{m\mu}{e}\dot{\varphi}_c - \mathcal{H}(\mathbf{X}, v_{\parallel}, \mu, t) \quad (.35)$$

where the Hamiltonian is

$$\mathcal{H}(\mathbf{X}, v_{\parallel}, \mu, t) = \frac{mv_{\parallel}^2}{2} + \mu B(\mathbf{X}, t) + e\phi(\mathbf{X}, t) \quad (.36)$$

and

$$\mathbf{A}^*(\mathbf{X}, t) = \mathbf{A}(\mathbf{X}, t) + \frac{mv_{\parallel}}{e}\mathbf{b}(\mathbf{X}, t) \quad (.37)$$

the motion equations are obtained from the Euler-Lagrange equation

$$\frac{d}{dt} \left( \frac{\partial \mathcal{L}}{\partial \dot{x}_i} \right) = \frac{\partial \mathcal{L}}{\partial x_i} \quad (.38)$$

### A.1. $x_i = \varphi_c$

This gives the evolution equation of the magnetic moment  $\mu$ . Indeed, as  $\frac{\partial \mathcal{L}}{\partial \varphi_c} = 0$  and  $\frac{\partial \mathcal{L}}{\partial \dot{\varphi}_c} = \frac{m\mu}{e}$  then it comes

$$\boxed{\frac{d}{dt} \left( \frac{m\mu}{e} \right) = 0} \quad (.39)$$

which confirms that  $\mu$  is an invariant of motion.

### A.2. $x_i = \mu$

This gives the evolution equation of the cyclotron phase angle  $\varphi_c$ . Indeed, as  $\frac{\partial \mathcal{L}}{\partial \mu} = 0$  and  $\frac{\partial \mathcal{L}}{\partial \dot{\mu}} = \frac{m\dot{\varphi}_c}{e} - B$

$$\boxed{\dot{\varphi}_c = \frac{eB}{m}} \quad (.40)$$

which is the cyclotron frequency, as expected.

### A.3. $x_i = v_{\parallel}$

It is straightforward to show  $\frac{\partial \mathcal{L}}{\partial v_{\parallel}} = 0$  and  $\frac{\partial \mathcal{L}}{\partial \dot{v}_{\parallel}} = \mathbf{e}_{\parallel} \cdot \dot{\mathbf{X}} - v_{\parallel}$ . This equation then gives the following constraint:

$$\boxed{v_{\parallel} = \mathbf{e}_{\parallel} \cdot \dot{\mathbf{X}}} \quad (.41)$$

5. Influence of the safety factor on the radial electric field – A. Derivation of the guiding center equations of motion

**A.4.**  $x_i = X_i$

This calculation is a bit heavier. It gives the last evolution equations on  $\mathbf{X}$  and  $v_{\parallel}$ . Let us calculate the l.h.s and r.h.s of Eq..38 separately.

First, it is direct to obtain

$$\frac{\partial \mathcal{L}}{\partial \dot{\mathbf{X}}} = e\mathbf{A}^* . \quad (42)$$

It then appears when calculating the only non-vanishing term of the lagrangian derivative in the l.h.s are

$$e \frac{d\mathbf{A}^*}{dt} = e \left( \frac{\partial \mathbf{A}^*}{\partial t} + (\dot{\mathbf{X}} \cdot \nabla) \mathbf{A}^* \right) . \quad (43)$$

Let us now calculate the r.h.s

$$\frac{\partial \mathcal{L}}{\partial \mathbf{X}} = e \nabla (\mathbf{A}^* \cdot \dot{\mathbf{X}}) - \mu \nabla B - e \nabla \phi \quad (44)$$

where

$$\nabla (\mathbf{A}^* \cdot \dot{\mathbf{X}}) = (\mathbf{A}^* \cdot \nabla) \dot{\mathbf{X}} + (\dot{\mathbf{X}} \cdot \nabla) \mathbf{A}^* + \mathbf{A}^* \times (\nabla \times \dot{\mathbf{X}}) + \dot{\mathbf{X}} \times (\nabla \times \mathbf{A}^*) . \quad (45)$$

As  $\mathbf{X}$  and  $\dot{\mathbf{X}}$  are independent, the non-vanishing terms are

$$\nabla (\mathbf{A}^* \cdot \dot{\mathbf{X}}) = (\dot{\mathbf{X}} \cdot \nabla) \mathbf{A}^* + \dot{\mathbf{X}} \times \mathbf{B}^* \quad (46)$$

with

$$\mathbf{B}^* = \nabla \times \mathbf{A}^* = \nabla \times \mathbf{A} + \frac{mv_{\parallel}}{e} \nabla \times \mathbf{b} . \quad (47)$$

Combining Eq.(43) and Eq.(44) yield

$$e \frac{\partial \mathbf{A}^*}{\partial t} = e \dot{\mathbf{X}} \times \mathbf{B}^* - (\mu \nabla B - e \nabla \phi) . \quad (48)$$

Developing the l.h.s with  $\mathbf{A}^* = \mathbf{A} + \frac{mv_{\parallel}}{e} \mathbf{b}$  yield

$$m \frac{dv_{\parallel}}{dt} \mathbf{b} = e \dot{\mathbf{X}} \times \mathbf{B}^* - \mu \nabla B - e \left[ \nabla \phi + \frac{\partial \mathbf{A}}{\partial t} \right] . \quad (49)$$

Note that the partial derivative on  $v_{\parallel}$  became a lagrangian derivative as  $v_{\parallel}$  does not depend on other coordinates. From Eq.49, the motion equation on  $\mathbf{X}$  is obtained through a cross-product with  $\mathbf{b}$  and the one on  $v_{\parallel}$  through a projection on  $\mathbf{B}^*$ .

Defining  $B_{\parallel}^* = \mathbf{b} \cdot \mathbf{B}^*$ , applying the vectorial product with  $\mathbf{b}$  then gives

$$\boxed{B_{\parallel}^* \frac{d\mathbf{X}}{dt} = v_{\parallel} \mathbf{B}^* + \frac{\mathbf{b}}{e} \times \left( \mu \nabla B + e \left[ \nabla \phi + \frac{\partial \mathbf{A}}{\partial t} \right] \right)} . \quad (50)$$

5. Influence of the safety factor on the radial electric field – B. Radial jump of banana trapped particles due to ripple

where we took advantage of the relation

$$\mathbf{b} \times (\dot{\mathbf{X}} \times \mathbf{B}^*) = \dot{\mathbf{X}}(\mathbf{b} \cdot \mathbf{B}^*) - \mathbf{B}^*(\mathbf{b} \cdot \dot{\mathbf{X}}) \quad (.51)$$

$$= \dot{\mathbf{X}} B_{\parallel}^* - \mathbf{B}^* v_{\parallel} \quad (.52)$$

and the projection on  $\mathbf{B}^*$  of Eq.49 gives directly

$$\boxed{B_{\parallel}^* m \frac{dv_{\parallel}}{dt} = -\mathbf{B}^* \cdot \left( \mu \nabla B + e \nabla \phi + e \frac{\partial \mathbf{A}}{\partial t} \right)} . \quad (.53)$$

The electrostatic form of these equations is simply obtained by removing the  $\frac{\partial \mathbf{A}}{\partial t}$  term.

## B. Radial jump of banana trapped particles due to ripple

This appendix is meant to give a derivation of the radial displacement of banana bounce point when magnetic ripple is considered.

For banana trapped particles, the action  $J_3 = P_{\phi}$  can be seen as a magnetic surface label as it only depends on the poloidal magnetic flux  $\psi$ . In presence of ripple,  $J_3$  invariance is broken so the radial position of the particle evolves in time. Consequently, the angle  $\varphi_0$  associated with  $J_3$  becomes a variable of the problem.

With the change of variable  $(\mu, J_2, J_3, \varphi_0) \rightarrow (\mu', \mathcal{H}, J'_3, \varphi'_0)$  where  $\mathcal{H}$  is the Hamiltonian,  $J_2$  the longitudinal invariant,  $\mu = \mu'$ ,  $J_3 = J'_3$  and  $\varphi_0 = \varphi'_0$ , one can define a function  $\mathcal{J}$  such that:

$$\mathcal{J}(\mu', \mathcal{H}(\mu, J_3, \varphi_0, J_2), J'_3, \varphi'_0) = J_2 . \quad (.54)$$

Deriving with respect to  $\varphi_0$  reads:

$$\frac{d\mathcal{J}}{d\varphi_0} = \left( \frac{\partial \mathcal{J}}{\partial \mathcal{H}} \right)_{\mu', J'_3, \varphi'_0} \left( \frac{\partial \mathcal{H}}{\partial \varphi_0} \right)_{\mu, J_2, J_3} + \left( \frac{\partial \mathcal{J}}{\partial \varphi'_0} \right)_{\mu', \mathcal{H}, J'_3} \underbrace{\left( \frac{\partial \varphi'_0}{\partial \varphi_0} \right)_{\mu, J_2, J_3}}_{=1} = 0 . \quad (.55)$$

The Hamilton equations give  $\frac{dJ_3}{dt} = -\frac{\partial \mathcal{H}}{\partial \varphi_0}$ .

Replacing in Eq(.55) holds:

$$\frac{dJ_3}{dt} = - \underbrace{\left( \frac{\partial \mathcal{H}}{\partial \mathcal{J}} \right)_{\mu, J_3, \varphi_0}}_{\equiv \Omega_B} \left( \frac{\partial \mathcal{J}}{\partial \varphi_0} \right)_{\mathcal{H}, \mu, J_3} \quad (.56)$$

with  $\Omega_B$  the banana bounce frequency. For circular and concentric magnetic surfaces,  $\frac{d\bar{\Psi}}{dr} = \frac{rB_0}{q}$  so

$$\frac{dr}{dt} = -\frac{q}{eB_0 r} \Omega_B \frac{\partial J_2}{\partial \varphi_0} . \quad (.57)$$

5. Influence of the safety factor on the radial electric field – B. Radial jump of banana trapped particles due to ripple

The next step is to obtain an expression for  $J_2$ .

The longitudinal invariant is expressed  $J_2 = \oint_{\text{banana}} m v_{\parallel} \frac{dl}{2\pi}$ , where the integral is taken along a banana trajectory.

Ignoring the banana width,  $dl$  is then given by the magnetic field line expression :

$$\frac{dl}{B} = \frac{rd\theta}{B_{\theta}} \Rightarrow dl \simeq qR_0 d\theta . \quad (.58)$$

With the energy  $E$  invariance, the parallel component of the particle velocity reads:

$$v_{\parallel}(\theta, \varphi) = \sqrt{\frac{2}{m}} \sqrt{E - \mu B(\theta, \varphi)} = \sqrt{\frac{2\mu}{m}} \sqrt{B(\theta_B) - B(\theta, \varphi)} \quad (.59)$$

with  $\theta_B$  the poloidal angle of the bounce point where  $v_{\parallel} = 0$ .  $J_2$  then reads:

$$J_2 = \frac{m}{\pi} \sqrt{\frac{2\mu}{m}} \int_{-\theta_B}^{\theta_B} qR_0 d\theta \left\{ \sqrt{B(\theta_B) - B(\theta, \varphi)} \right\} . \quad (.60)$$

With the expression of the magnetic field amplitude  $B(r, \theta, \varphi) = B_0 (1 - \varepsilon \cos \theta - \delta(r, \theta) \cos(N_c \varphi))$  one obtains:

$$\begin{aligned} \sqrt{B(\theta_B) - B(\theta, \varphi)} &= \sqrt{B_0 \left\{ \varepsilon(\cos \theta - \cos \theta_B) \left( 1 + \frac{\delta(r, \theta) \cos N_c \varphi}{\varepsilon(\cos \theta - \cos \theta_B)} \right) \right\}} \\ &\simeq \sqrt{B_0 \varepsilon (\cos \theta - \cos \theta_B)} \left( 1 + \frac{\delta(r, \theta) \cos N_c \varphi}{2\varepsilon(\cos \theta - \cos \theta_B)} \right) . \end{aligned} \quad (.61)$$

Defining  $\sqrt{\frac{2\mu B_0}{m}} = v$ , the  $J_2$  dependant of the ripple amplitude becomes:

$$J_2 = \underbrace{\frac{mqR_0 v}{2\pi} \int_{-\theta_B}^{\theta_B} d\theta \left\{ 2\sqrt{\varepsilon(\cos \theta - \cos \theta_B)} \right\}}_{\tilde{J}_2} + \underbrace{\frac{mqR_0 v}{2\pi\sqrt{\varepsilon}} \int_{-\theta_B}^{\theta_B} d\theta \left\{ \frac{\delta(r, \theta) \cos N_c \varphi}{\sqrt{\cos \theta - \cos \theta_B}} \right\}}_{\tilde{J}_2} \quad (.62)$$

where  $J_2$  corresponds to the ripple contribution to the longitudinal invariant of motion.

It is useful to decompose the integral as follows:

$$\tilde{J}_2 = \frac{mqR_0 v}{2\pi\sqrt{\varepsilon}} \left[ \int_{-\theta_B}^0 d\theta \left\{ \frac{\delta(r, \theta) \cos(N_c \varphi)}{\sqrt{\cos \theta - \cos \theta_B}} \right\} + \int_0^{\theta_B} d\theta \left\{ \frac{\delta(r, \theta) \cos(N_c \varphi)}{\sqrt{\cos \theta - \cos \theta_B}} \right\} \right] . \quad (.63)$$

The fundamental point of this development is based on the fact that a trapped particle spends much more time in the vicinity of the bounce point than at the equatorial plane. This has multiple consequences regarding the derivation:

- As  $\delta$  is weakly dependant of  $\theta$ , the approximation  $\int_{-\theta_B}^{\theta_B} \delta(r, \theta) X d\theta \simeq \delta(r, \theta_B) \int_{-\theta_B}^{\theta_B} X d\theta$  is reasonable;



5. Influence of the safety factor on the radial electric field – B. Radial jump of banana trapped particles due to ripple

- It allows a Taylor expansion of the cosine function about the bounce angle;
- Finally, replacing the bounds of the integral from  $[0, \theta_B]$  (resp.  $[-\theta_B, 0]$ ) to  $]-\infty, \theta_B]$  (resp.  $[-\theta_B, \infty[$ ) only has a limited impact and is useful to make appear Fresnel integrals.

With these simplifications, adding the  $\theta$  dependence of the toroidal angle  $\varphi = \varphi_0 + q\theta$ , the ripple contribution becomes:

$$J_2 = \frac{mqR_0 v \delta(r, \theta_B)}{2\pi \sqrt{\varepsilon |\sin \theta_B|}} \int_{-\theta_B}^{+\infty} d\theta \left\{ \frac{\cos(N_c \varphi_0 + N_c q \theta)}{\sqrt{\theta_B + \theta}} + \frac{\cos(N_c \varphi_0 - N_c q \theta)}{\sqrt{\theta_B + \theta}} \right\} . \quad (.64)$$

A first change of variable  $\theta \rightarrow x - \theta_B$  gives:

$$\begin{aligned} J_2 &= \frac{mqR_0 v \delta(r, \theta_B)}{2\pi \sqrt{\varepsilon |\sin \theta_B|}} \int_0^{+\infty} \frac{dx}{\sqrt{x}} \left\{ \cos(N_c \varphi_0 + N_c q x - N_c q \theta_B) + \cos(N_c \varphi_0 - N_c q x + N_c q \theta_B) \right\} \\ &= \frac{mqR_0 v \delta(r, \theta_B)}{2\pi \sqrt{\varepsilon |\sin \theta_B|}} 2 \cos(N_c \varphi_0) \int_0^{+\infty} \frac{dx}{\sqrt{x}} \left\{ \cos(N_c q \theta_B - N_c q x) \right\} \end{aligned} \quad (.65)$$

and another one  $x \rightarrow \frac{t^2}{N_c q}$  gives:

$$J_2 = \frac{2mR_0 v \delta(r, \theta_B)}{\pi \varepsilon N_c \sqrt{|\sin \theta_B|}} \cos(N_c \varphi_0) \int_0^{+\infty} dt \left\{ \cos(N_c q \theta_B - t^2) \right\} . \quad (.66)$$

Using the Euler expression for cosinus:

$$\int_0^{+\infty} dt \left\{ \cos(N_c q \theta_B - t^2) \right\} = \frac{1}{2} \left[ e^{iN_c q \theta_B} \int_0^{+\infty} dt \left\{ e^{-it^2} \right\} + e^{-iN_c q \theta_B} \int_0^{+\infty} dt \left\{ e^{it^2} \right\} \right] \quad (.67)$$

and with the Fresnel formula reading

$$\int_0^{+\infty} dt \left\{ \cos(t^2) \right\} = \int_0^{+\infty} dt \left\{ \sin(t^2) \right\} = \frac{1}{2} \sqrt{\frac{\pi}{2}} \quad (.68)$$

then one can write:

$$\begin{cases} \int_0^{+\infty} dt \left\{ e^{-it^2} \right\} = \int_0^{+\infty} dt \left\{ \cos t^2 \right\} - i \int_0^{+\infty} dt \left\{ \sin t^2 \right\} = \frac{\sqrt{\pi}}{2} e^{-i\frac{\pi}{4}} \\ \int_0^{+\infty} dt \left\{ e^{it^2} \right\} = \int_0^{+\infty} dt \left\{ \cos t^2 \right\} + i \int_0^{+\infty} dt \left\{ \sin t^2 \right\} = \frac{\sqrt{\pi}}{2} e^{+i\frac{\pi}{4}} . \end{cases}$$

Giving the final expression for the ripple contribution to the longitudinal invariant:

$$J_2 = \frac{mqR_0 v \delta(r, \theta_B)}{\sqrt{\pi \varepsilon N_c q |\sin \theta_B|}} \cos(N_c \varphi_0) \cos\left(N_c q \theta_B - \frac{\pi}{4}\right) . \quad (.69)$$

Combining Eq.(.57) and Eq.(.69), as  $\frac{\partial J_2}{\partial \varphi_0} = 0$ , the radial velocity associated to the particle is finite due to ripple and reads

5. Influence of the safety factor on the radial electric field – C. Derivation of Chirikov overlap parameters and diffusion coefficients related to stochastic transport

$$\frac{dr}{dt} = \Omega_B \left( \frac{v}{\Omega_c} \right) \delta(r, \theta_B) \left( \frac{q}{\varepsilon} \right)^{\frac{3}{2}} \underbrace{\sqrt{\frac{N_c}{\pi |\sin \theta_B|}} \cos \left( N_c q \theta_B - \frac{\pi}{4} \right) \sin(N_c \varphi_0)}_{\mathcal{C}} \quad (.70)$$

with the cyclotron frequency  $\Omega_c = \frac{eB_0}{m}$ .

The radial jump  $\Delta r$  experienced by the particle during a banana transit is obtained when averaging the radial velocity during a bounce period  $2\pi/\Omega_B$ .

One must take into account the temporal dependence of  $\varphi_0$ . The angle/action equation gives  $\frac{d\varphi_0}{dt} = \Omega_B \frac{q}{eB_0 r} \frac{\partial J_2}{\partial r}$  with the total  $J_2$ . The part associated to  $\bar{J}_2$  is associated to the motion in an axisymmetric device, i.e. the precession motion  $\bar{\varphi}_0 = \varphi_{00} + \Omega_D t$  with  $\varphi_{00}$  the initial toroidal angle and  $\Omega_D$  the precession frequency. The part associated with  $\tilde{J}_2$  is associated with the ripple perturbation and is here considered subdominant compared to the precession motion. The radial jump then reads

$$\Delta r = \mathcal{C} \Omega_B \left[ \frac{-\cos(N_c \varphi_{00} + 2\pi N_c \frac{\Omega_D}{\Omega_B}) + \cos(N_c \varphi_{00})}{N_c \Omega_D} \right]. \quad (.71)$$

Assuming  $N_c \Omega_D / \Omega_B \ll 1$ , and using once again a Taylor expansion for the cosine, and using the ion Larmor radius expression  $\rho_i = v / \Omega_c$ , the final expression for the radial jump is

$$\Delta r = 2 \sqrt{\frac{N_c \pi}{|\sin \theta_B|}} \left( \frac{q}{\varepsilon} \right)^{\frac{3}{2}} \rho_i \delta(r, \theta_B) \cos \left( N_c q \theta_B - \frac{\pi}{4} \right) \sin(N_c \varphi_{00}). \quad (.72)$$

## C. Derivation of Chirikov overlap parameters and diffusion coefficients related to stochastic transport

In this appendix is the derivation of the Chirikov overlap parameters and diffusion coefficients of the weak and strong perturbation regime defined in Sec.2.5.3.

As a reminder, the form of the normalized Hamiltonian obtained in Sec.2.5.2 is the following

$$\mathcal{H}_{\omega, n_B} = \frac{\omega_{n_B}^2}{2} + \mathcal{C}_{n_B} \frac{\mu B_0 \delta}{2} J_{n_B}(N_c q \theta_B(\mathbf{J}_R) + \tau_{n_B} \omega_{n_B}) \cos(\xi_{n_B}). \quad (.73)$$

From this point, it is necessary to simplify the problem. It is reasonable to assume that banana-trapped orbits satisfy the condition  $N_c q \theta_B \gg n_B^2$ , which allows the use of the asymptotic form of the Bessel function

5. Influence of the safety factor on the radial electric field – C. Derivation of Chirikov overlap parameters and diffusion coefficients related to stochastic transport

$$\mathbf{J}(N_c q \theta_B(\mathbf{J}_R) + \tau_{n_B} \omega_{n_B}) \approx \sqrt{\frac{2}{\pi(N_c q \theta_B(\mathbf{J}_R) + \tau_{n_B} \omega_{n_B})}} \cos\left(N_c q \theta_B(\mathbf{J}_R) - n_B \frac{\pi}{2} - \frac{\pi}{4} + \tau_{n_B} \omega_{n_B}\right). \quad (.74)$$

In Fig.32, this limit is assessed with reasonable parameters, that is  $N_c = 18$  and  $q = 3$ , in a range  $\theta_B \in [0, \pi]$ .

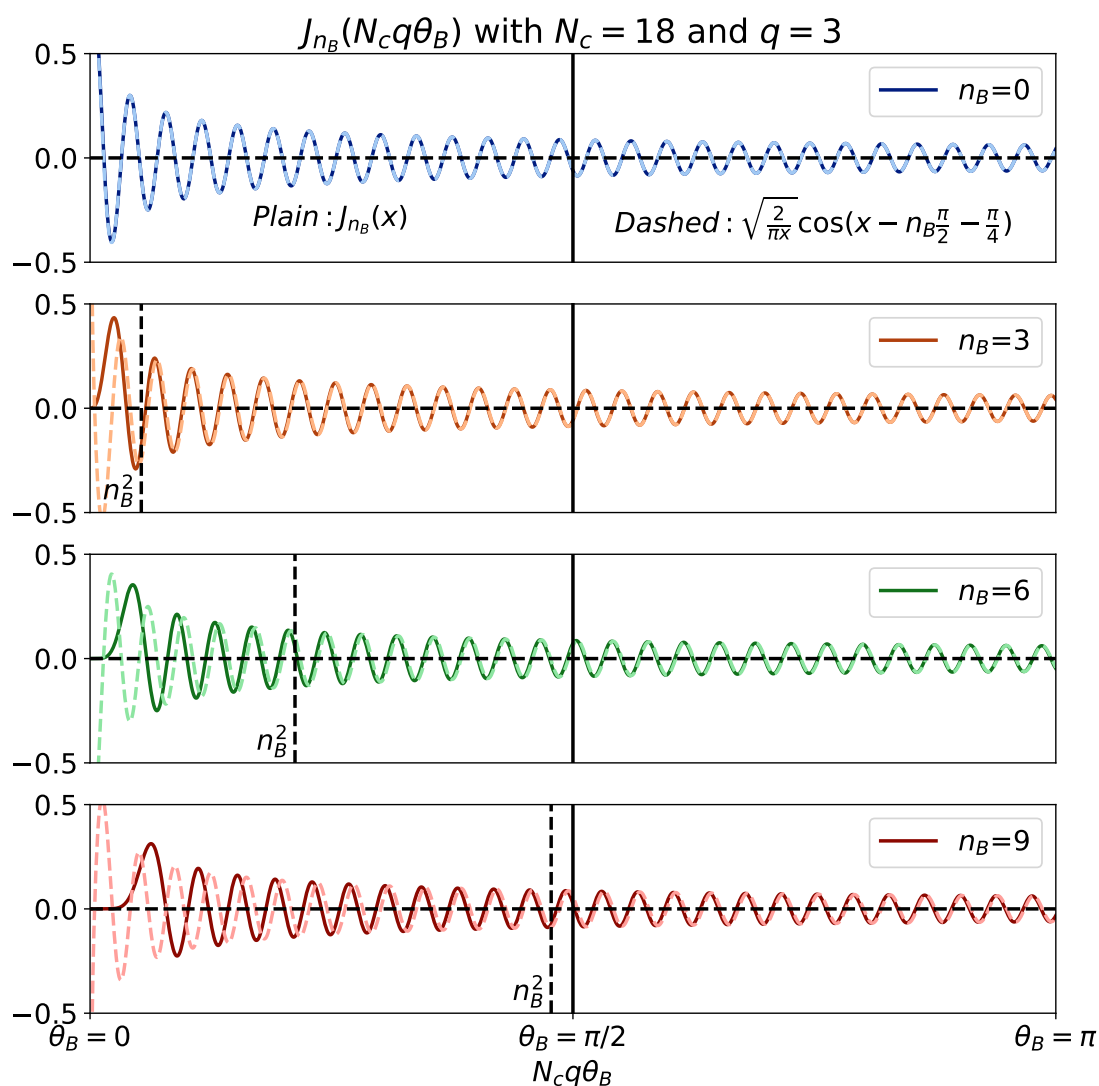


Figure 32. – Comparison between the Bessel function of the first kind (plain) and an approximation (dashed) for different order  $n_B$ , for the argument range  $N_c q [0, \pi]$  with  $q = 3$  and  $N_c = 18$ .

It appears that this approximation is well fulfilled, at least for low  $n_B$  which are the most relevant for transport. The last form of the Hamiltonian then reads

5. Influence of the safety factor on the radial electric field – C. Derivation of Chirikov overlap parameters and diffusion coefficients related to stochastic transport

$$\mathcal{H}_{\omega, n_B} = \frac{\omega_{n_B}^2}{2} + (\delta\omega'_{n_B})^2 \cos(\varphi_{n_B} + \tau_{n_B}\omega_{n_B}) \cos(\xi_{n_B}) \quad (.75)$$

where  $\varphi_{n_B} = N_c q \theta_B(\mathbf{J}_R) - n_B \frac{\pi}{2} - \frac{\pi}{4}$  and

$$\delta\omega'_{n_B} = \sqrt{C_{n_B} \frac{\mu B_0 \delta}{2} \sqrt{\frac{2}{\pi N_c q \theta_B}}} \quad (.76)$$

As the variation of  $\delta\omega'_{n_B}$  with  $\omega_{n_B}$  is weak compared with  $\cos(\varphi_{n_B} + \tau_{n_B}\omega_{n_B})$ , the Hamilton equations of motion read

$$\frac{d\xi_{n_B}}{dt} = \frac{\partial \mathcal{H}_{\omega, n_B}}{\partial \omega_{n_B}} = \omega_{n_B} - (\delta\omega'_{n_B})^2 \tau_{n_B} \sin(\varphi_{n_B} + \tau_{n_B}\omega_{n_B}) \cos(\xi_{n_B}) \quad (.77)$$

$$\frac{d\omega_{n_B}}{dt} = -\frac{\partial \mathcal{H}_{\omega, n_B}}{\partial \xi_{n_B}} = (\delta\omega'_{n_B})^2 \cos(\varphi_{n_B} + \tau_{n_B}\omega_{n_B}) \sin(\xi_{n_B}) \quad (.78)$$

The frequency  $(\delta\omega'_{n_B})^2 \tau_{n_B}$  then characterizes the new structures in the phase-space that appear when the Hamiltonian is deformed by the action. The two regimes of transport can be identified. When  $\delta\omega'_{n_B} \tau_{n_B} \leq S_{\text{lim}}$ , introducing a number  $S_{\text{lim}}$  to be determined, the iso-contours of  $\mathcal{H}_{\omega, n_B}$  are characterized by a single separatrix and the typical cat-eye shape. This regime is labeled *weak perturbation regime*. In the other case  $\delta\omega'_{n_B} \tau_{n_B} > S_{\text{lim}}$ , iso-contours of  $\mathcal{H}_{\omega, n_B}$  are characterized by multiple separatrices and complex structures. This regime is labelled *strong perturbation regime*.

The Chirikov criterion can be estimated in both regimes. For this, it will be assumed that the  $n_B$  dependence of  $\tau_{n_B}$  and  $\delta\omega'_{n_B}$  is weak between two consecutive  $n_B$ . In the weak perturbation regime, the island size is simply  $4\delta\omega'_{n_B}$  and the distance between consecutive perturbations is  $\Omega_B$  so the associated Chirikov parameter is

$$S_{\text{weak}} = \frac{4\delta\omega'_{n_B}}{\Omega_B} \quad (.79)$$

In the strong perturbation regime, the size of the global is structure delimited by the two outermost separatrices and reads  $2\tau_{n_B}(\delta\omega'_{n_B})^2$ . The associated Chirikov parameter is

$$S_{\text{strong}} = 2\tau_{n_B} \frac{(\delta\omega'_{n_B})^2}{\Omega_B} \quad (.80)$$

The value  $S_{\text{lim}} = \delta\omega'_{n_B} \tau_{n_B, \text{lim}}$  that defines the transition between the weak to strong perturbation regime is defined by the condition  $S_{\text{weak}} = S_{\text{strong}}$ . It is then simply  $S_{\text{lim}} = 2$ . The link between the two Chirikov parameters  $S_{\text{weak}} = \frac{S_{\text{lim}}}{\tau_{n_B} \omega'_{n_B}} S_{\text{strong}}$  ensures that  $S_{\text{weak}} < S_{\text{strong}}$  by construction.

One would want to express these criteria as a function of meaningful quantities: the ripple amplitude or the particle velocity for example. Rigorously, it requires to know

5. Influence of the safety factor on the radial electric field – C. Derivation of Chirikov overlap parameters and diffusion coefficients related to stochastic transport

the relation between angle-action coordinates and the position/velocity coordinates. This is not feasible in most cases, including this one. Instead, many more or less reasonable assumptions are made along the way.

Let us start with the weak perturbation regime Chirikov criterion Eq.(79). The main difficulty lies in obtaining an expression of  $C_{n_B}$  that appears in the product  $\delta\omega_{n_B}$ . Developing Eq(2.47) yields

$$C_{n_B} = N_c^2 \frac{\partial \Omega_D}{\partial P_\varphi} \Big|_{\mathbf{J}_R} + n_B^2 \frac{\partial \Omega_B}{\partial J_B} \Big|_{\mathbf{J}_R} + 2n_B N_c \frac{\partial^2 \mathcal{H}_{I,n_B}}{\partial J_B \partial P_\varphi} \Big|_{\mathbf{J}_R} . \quad (.81)$$

Here it is difficult to have an intuition on the scaling between these terms. In the absence of better approximation, it is considered that they all share the same scaling such that we keep the only easily tractable term  $C_{n_B} \sim N_c^2 \frac{\partial \Omega_D}{\partial P_\varphi}$ . In circular geometry,  $\frac{\partial P_\varphi}{\partial r} = -e \frac{B_0 r}{q}$ . Also, we consider that the precession frequency is expressed  $\Omega_D = \frac{q}{r R_0} \Omega_c^{-1} v_\perp^2$  where  $\Omega_c$  is the cyclotron frequency. With these elements, it is possible to find an expression for  $C_{n_B}$  that reads<sup>14</sup>

$$C_{n_B} \approx -(N_c q)^2 s \frac{v_\perp^2}{m \Omega_c^2 R_0 r^3} \quad (.82)$$

where  $s = \frac{r}{q} \frac{dq}{dr}$  is the magnetic shear. Consequently, there is no dependence on  $n_B$  anymore. The interpretation of the resulting Chirikov criterion should then be understood as a unique threshold for stochasticity, accounting for all perturbations induced by ripple. The banana bounce frequency is approximated by  $\Omega_B \approx \sqrt{\varepsilon} \frac{v_\perp}{q R_0}$ , so that the weak perturbation regime Chirikov criterion then reads

$$S_{\text{weak}} = 2 \left( \frac{2}{\pi \theta_B} \right)^{1/4} s^{1/2} \frac{q \rho_c}{R_0} \frac{\delta^{1/2}}{\varepsilon^2} u^{1/2} \quad (.83)$$

with  $u = v_\perp^2 / V_{\text{th}}^2$  ( $V_{\text{th}}$  is the ion thermal velocity). Here kept in the expression,  $\theta_B$  can be set to  $\pi/2$  when necessary. As already mentioned,  $S_{\text{weak}}$  is the lower limit for chaos to arise. It is then possible to estimate the critical normalized energy  $u_c$  for which the trajectories become stochastic (this is the upper limit of the energy integral in Eq(2.34) calculated within the neoclassical theory). It reads

$$u_c = \frac{\pi}{8} \frac{1}{s} \left( \frac{R_0}{q \rho_c} \right)^2 \frac{\varepsilon^4}{\delta} . \quad (.84)$$

This threshold is commonly associated with energetic particles, as the ratio  $\frac{\varepsilon^4}{\delta}$  is really high in most of tokamaks for typical ripple amplitudes. This is why "ripple losses" of particles are usually attributed to fast particles.

Let us now express the strong perturbation regime Chirikov criterion. The main difficulty lies in obtaining an expression of  $C'_{n_B}$  that appears in the product  $\tau_{n_B} (\delta\omega'_{n_B})^2$

14. Note that in the radial derivative of  $\Omega_D$  we considered the term proportional to  $q/r^2$  negligible compared with the one proportional to  $q'/r$

5. Influence of the safety factor on the radial electric field – C. Derivation of Chirikov overlap parameters and diffusion coefficients related to stochastic transport

Here we simply take the expression proposed in [68]

$$C'_{n_B} \approx \frac{N_c q}{m \Omega_c r^2} s \theta_B . \quad (.85)$$

The final expression yields

$$S_{\text{strong}} \approx \frac{1}{2} \sqrt{\frac{2\theta_B}{\pi}} s (N_c q)^{3/2} \frac{\delta}{\epsilon^{5/2}} \frac{q \rho_c}{R_0} u^{1/2} . \quad (.86)$$

We can now estimate the diffusion coefficients associated with the weak regime which is the first to emerge when  $\delta$  increases. In the weak perturbation transport regime, the quasi-linear diffusion coefficient  $D_{\text{QL}}$  holds. The diffusion matrix reads

$$D_{ij} = \pi \sum_{n_B} n_i n_j |h_{n_B}|^2 \delta(n_B \Omega_B + N_c \Omega_D) \quad (.87)$$

where  $\delta$  is the Dirac delta function. As the objective is ultimately to get the radial diffusion, we here select the element linked to the action  $P_\varphi$ . In practice, the  $n_i$  and  $n_j$  coefficient are then replaced by  $N_c$ . The quasi-linear diffusion of interest then reads

$$D_{\text{QL}} = N_c^2 \pi \sum_{n_B} |h_{n_B}|^2 \delta(n_B \Omega_B + N_c \Omega_D) . \quad (.88)$$

Note that this coefficient does not have the dimension of  $(m^2.s^{-1})$  yet, as it is expressed in unity of  $(\partial P_\varphi / \partial r)^2$ .

Using the property  $\delta(ax) = |a|^{-1} \delta(x)$  and replacing the sum on  $n_B$  with an integral, it appears that

$$D_{\text{QL}} = N_c^2 \pi \int dn_B |h(n_B)|^2 \frac{1}{\Omega_B} \delta(n_B + n^*) \quad (.89)$$

where  $n^* = N_c \Omega_D / \Omega_B$ .

Using the property  $\int f(x) \delta(x - x_0) = f(x_0)$ , it is straightforward to show that  $D_{\text{QL}} = N_c^2 \pi |h_{-n^*}|^2 / \Omega_B$ . The Hamiltonian modulus is given by Eq(2.43). The Bessel function modulus can be approximated to its asymptotic form for high arguments:  $|J_{-n^*}(N_c q \theta_B)| = \sqrt{\frac{2}{\pi N_c q \theta_B}}$ .

It leads to the following diffusion coefficient:

$$D_{\text{QL}} = N_c^2 \frac{(\mu B_0 \delta)^2}{2 N_c q \theta_B \Omega_B} . \quad (.90)$$

Dividing by  $(\partial P_\varphi / \partial r)^2$  gives the particle diffusion coefficient

$$D_{\text{QL}} = \frac{1}{8\theta_B} N_c q u^{3/2} D_P \frac{\delta^2}{\epsilon^{5/2}} \quad (.91)$$

where we remind that  $D_P = \frac{q R_0}{V_{\text{th}}} \left( \frac{T}{e B_0 R_0} \right)^2$ .

## D. Explicit expression of the transport matrix coefficients

This section gives the details of the terms that appear in the transport matrix in Sec.2.6. In the general case the ripple perturbation amplitude  $\delta$  depends on  $(r, \theta)$ . It is useful to separate this amplitude in a poloidal average  $\bar{\delta}(r) = \int \frac{d\theta}{2\pi} \delta(r, \theta)$  and a poloidal modulation  $\tilde{\delta}(r, \theta) = \delta(r, \theta) / \bar{\delta}(r)$ .

The transport matrix is symmetrical. Its 6 independent elements are given by the following expressions:

$$d_n = \int_0^{+\infty} du \left(u - \frac{3}{2}\right)^n \mathcal{K}(u) \quad (.92)$$

$$\tilde{d}_n = \int_0^{+\infty} du \left(u - \frac{3}{2}\right)^n \tilde{\mathcal{K}}(u) \quad (.93)$$

$$\hat{d}_n = \int_0^{+\infty} du \left(u - \frac{3}{2}\right)^n \hat{\mathcal{K}}(u) \quad (.94)$$

where

$$\mathcal{K}(u) = \sqrt{\frac{\pi}{2}} e^{-u} u^2 K_{\text{tor},\text{I}}(r, u) \quad (.95)$$

$$\begin{aligned} \tilde{\mathcal{K}}(u) &= \frac{32}{9} \left(\frac{2}{\pi}\right)^{3/2} \left(\frac{\bar{\delta}}{\varepsilon}\right)^{3/2} \frac{G_1}{v^*} e^{-u} u^{5/2} \frac{1}{\bar{v}(u)} \\ &+ 2 \left(\frac{2}{\pi}\right)^{3/2} \frac{1}{N_c q} \left(\frac{\bar{\delta}}{\varepsilon}\right)^2 \frac{1}{v^*} [1 - H(u - u_c)] e^{-u} u^{5/2} \frac{1}{\bar{v}(u)} K_{\text{rip},\text{II}}(r, u) \\ &+ \sqrt{\frac{\pi}{2}} N_c q \left(\frac{\bar{\delta}}{\varepsilon}\right)^2 H(u - u_c) e^{-u} u^2 K_{\text{st}}(r, u) \end{aligned} \quad (.96)$$

$$\hat{\mathcal{K}}(u) = \sqrt{\frac{\pi}{2}} (N_c q) \left(\frac{\bar{\delta}}{\varepsilon}\right)^2 e^{-u} u^2 K_{\text{rip},\text{I}}(r, u) \quad (.97)$$

where  $H$  is the Heaviside function.

## E. Development of a simple model for the neoclassical/turbulent competition

A starting point to study the plasma rotation is the toroidal angular momentum conservation:

5. Influence of the safety factor on the radial electric field – E. Development of a simple model for the neoclassical/turbulent competition

$$\underbrace{m \frac{\partial \langle n R V_T \rangle}{\partial t}}_{\text{Temporal evolution}} = - \underbrace{\langle \nabla \cdot \Pi_\varphi \rangle}_{\text{Reynolds stress}} - \underbrace{\langle T_\varphi \rangle}_{\text{Polarisation}} + \underbrace{\langle \mathcal{J}_D \rangle + \langle \mathcal{J}_E \rangle}_{\text{Radial currents}} + \underbrace{\langle T_M \rangle}_{\text{Magnetic braking torque}} + \underbrace{e\psi(\partial_t n + \nabla \cdot \Gamma)}_{\text{l.h.s of vorticity conservation}} . \quad (.98)$$

Here there is a actually a new term compared with Eq(3.24), the l.h.s. of the vorticity conservation, that was set to zero in Sec.3.3.3 as it was negligible in the simulations treated in that section <sup>15</sup>. The goal is to find the dominant terms in order to simplify the problem. Before developing any physical argument, one can look at Fig.33 obtained with a GYSELA simulation with ripple detailed further, that shows the radial profile of each r.h.s term, averaged temporally and radially, of this equation. The first observation is that the radial current and the l.h.s of the vorticity conservation have similar amplitude and are of opposite signs. These terms then tend to compensate, as expected given their similar structure. Another observation is that the polarization term seems subdominant, which was then confirmed in each of our simulations. However, this polarisation term can play a strong role as shown in [110].

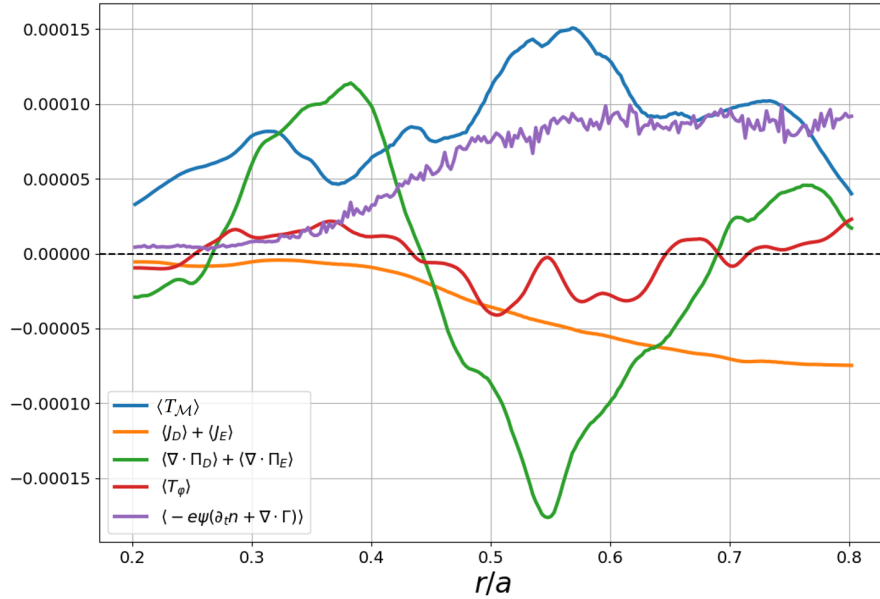


Figure 33. – Radial profile of the r.h.s of the toroidal angular momentum conservation Eq.98. These quantities are temporally averaged between  $100000 < t\omega_{c0} < 150000$  and radially slide-averaged with a  $50\rho_i$  window.

The dominant players for the toroidal flow drive are then the magnetic braking and the Reynolds stress divergence. The Reynolds stress can be separated into a compo-

15. The reason is that the time step in the simulations in Sec.3.3.3 was way shorter, as they were designed to test the angular momentum conservation. Here, the simulations are more numerically costly, such that we could not take the same time step.



5. Influence of the safety factor on the radial electric field – E. Development of a simple model for the neoclassical/turbulent competition

ment due to the magnetic drift  $\langle v_{D_r} v_\varphi \rangle$  and another from the electric drift  $\langle v_{E_r} v_\varphi \rangle$ . Fig.34 displays the radial profile of the total Reynolds stress and its component from the electric drift, for each ripple perturbation used in the presented GYSELA simulations. It appears that the transport of momentum by the magnetic drift is indeed subdominant, in particular when magnetic ripple is present. The approximation  $\langle \Pi \rangle \approx \langle v_{E_r} v_\varphi \rangle$  is then made.

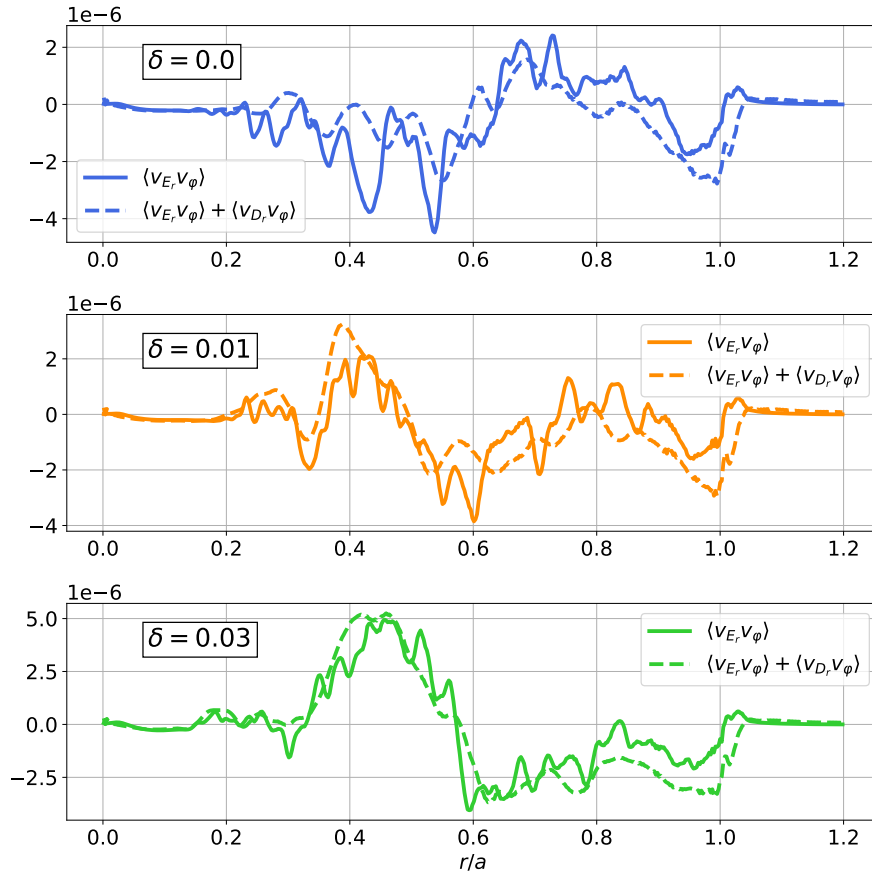


Figure 34. – Radial profile of the total toroidal Reynolds stress (dashed) and the electric drift component of the Reynolds stress (plain), both averaged in time between  $100\,000 < t < 150\,000$  cyclotron periods, for different ripple amplitudes  $\delta$ .

In the end, a simple reduced model keeping only the magnetic braking and the electric Reynolds stress as flow drive is obtained.

## F. Stability of the equilibriums for the model of energy transfer

In this appendix, the stability of the fixed points found in Sec.5.4.3 on the normalized turbulent intensity  $\mathcal{I}$ , normalized zonal flow energy  $\mathcal{E}_0$  and normalized GAMs energy  $\mathcal{E}_G$  are assessed. To this aim, a perturbative treatment is done around the fixed points such that

$$\mathcal{I} = \bar{\mathcal{I}} + \tilde{\mathcal{I}}e^{\lambda\tau}, \quad (.99)$$

$$\mathcal{E}_0 = \bar{\mathcal{E}}_0 + \tilde{\mathcal{E}}_0e^{\lambda\tau}, \quad (.100)$$

$$\mathcal{E}_G = \bar{\mathcal{E}}_G + \tilde{\mathcal{E}}_Ge^{\lambda\tau}. \quad (.101)$$

Neglecting the second-order terms proportional to  $e^{2\lambda\tau}$ , the perturbed system reads

$$\underbrace{\begin{pmatrix} \lambda + \bar{\mathcal{I}} & C_0\bar{\mathcal{I}} & C_G\bar{\mathcal{I}} \\ -\bar{\mathcal{E}}_0 & \lambda a_0 - (\bar{\mathcal{I}} - \mathcal{I}_0 - 2\bar{\mathcal{E}}_0) & 0 \\ -\bar{\mathcal{E}}_G & 0 & \lambda a_G - (\bar{\mathcal{I}} - \mathcal{I}_G - 2\bar{\mathcal{E}}_0) \end{pmatrix}}_A \cdot \begin{pmatrix} \tilde{\mathcal{I}} \\ \tilde{\mathcal{E}}_0 \\ \tilde{\mathcal{E}}_G \end{pmatrix} = \begin{pmatrix} 0 \\ 0 \\ 0 \end{pmatrix}. \quad (.102)$$

The eigenvalues of this system are obtained by setting the determinant of the matrix  $A$  to zero. The equilibrium is stable if all these eigenvalues are negative. Let us find the condition for each equilibrium to be stable.

### F.1. Equilibrium "No flows"

Using the properties of this equilibrium, i.e.  $\bar{\mathcal{E}}_0 = \bar{\mathcal{E}}_G = 0$ , it is straightforward to show that

$$\det(A) = (\lambda + \bar{\mathcal{I}}) \left[ \left( \lambda a_0 - (\bar{\mathcal{I}} - \mathcal{I}_0) \right) \left( \lambda a_G - (\bar{\mathcal{I}} - \mathcal{I}_G) \right) \right] \quad (.103)$$

such that the set  $(\lambda_1, \lambda_2, \lambda_3)$  of eigenvalues read

$$\lambda_1 = -\bar{\mathcal{I}} \quad ; \quad \lambda_2 = \frac{\bar{\mathcal{I}} - \mathcal{I}_0}{a_0} \quad ; \quad \lambda_3 = \frac{\bar{\mathcal{I}} - \mathcal{I}_G}{a_G}. \quad (.104)$$

The turbulent intensity is always positive, so this solution is stable when  $\bar{\mathcal{I}} < \mathcal{I}_0$  and  $\bar{\mathcal{I}} < \mathcal{I}_G$ .

### F.2. Equilibrium "Zonal flows only"

For this equilibrium,  $\bar{\mathcal{E}}_G = 0$  and  $\bar{\mathcal{E}}_0 > 0$  which imposes that  $\bar{\mathcal{I}} - \mathcal{I}_0 - \bar{\mathcal{E}}_0 = 0$  at the fixed point. The matrix  $A$  determinant then reads

5. Influence of the safety factor on the radial electric field – F. Stability of the equilibriums for the model of energy transfer

$$\det(A) = \underbrace{(a_G \lambda - (\bar{\mathcal{I}} - \mathcal{I}_G))}_{\textcircled{1}} \underbrace{\left[ C_0 \bar{\mathcal{I}} \bar{\mathcal{E}}_0 + (\lambda + \bar{\mathcal{I}})(a_0 \lambda + \bar{\mathcal{E}}_0) \right]}_{\textcircled{2}} . \quad (.105)$$

First eigenvalue  $\lambda_1$  is given by  $\textcircled{1}$  and the two other by the second order polynomial  $\textcircled{2}$ . The determinant  $\Delta$  of this polynomial reads

$$\Delta = (\bar{\mathcal{E}}_0 + \bar{\mathcal{I}} a_0)^2 - 4 \bar{\mathcal{E}}_0 \bar{\mathcal{I}} (C_0 + 1) . \quad (.106)$$

If  $\Delta > 0$ , the other eigenvalues  $(\lambda_2, \lambda_3)$  reads

$$\lambda_{2,3} = \frac{-\left(\bar{\mathcal{E}}_0 + \bar{\mathcal{I}} a_0\right) \pm \sqrt{\Delta}}{2 a_0} \quad (.107)$$

both of which are always negative as  $\sqrt{\left(\bar{\mathcal{E}}_0 + \bar{\mathcal{I}} a_0\right)^2 - 4 \bar{\mathcal{E}}_0 \bar{\mathcal{I}} (C_0 + 1)} < \left(\bar{\mathcal{E}}_0 + \bar{\mathcal{I}} a_0\right)$ .

If  $\Delta < 0$  then  $(\lambda_2, \lambda_3)$  are complex and their real parts are always negative. The three eigenvalues are such that

$$\lambda_1 = \frac{\bar{\mathcal{I}} - \mathcal{I}_G}{a_G} ; \quad \text{Re}(\lambda_2) < 0 ; \quad \text{Re}(\lambda_3) < 0 . \quad (.108)$$

### F.3. Equilibrium "GAMs only"

For this equilibrium,  $\bar{\mathcal{E}}_0 = 0$  and  $\bar{\mathcal{E}}_G > 0$  which imposes that  $\bar{\mathcal{I}} - \mathcal{I}_G - \bar{\mathcal{E}}_0 = G$  at the fixed point. By analogy with the previous case, the eigenvalues are

$$\lambda_1 = \frac{\bar{\mathcal{I}} - \mathcal{I}_0}{a_0} ; \quad \text{Re}(\lambda_2) < 0 ; \quad \text{Re}(\lambda_3) < 0 . \quad (.109)$$

### F.4. Equilibrium "Mixed ZF/GAMs"

For this equilibrium,  $\bar{\mathcal{E}}_0 > 0$  and  $\bar{\mathcal{E}}_G > 0$  which impose that  $\bar{\mathcal{I}} - \mathcal{I}_0 - \bar{\mathcal{E}}_0 = 0$  and  $\bar{\mathcal{I}} - \mathcal{I}_G - \bar{\mathcal{E}}_0 = 0$  at the fixed point. The determinant of  $A$  is then a 3rd order polynomial  $\mathcal{P}(\lambda) = \lambda^3 + s\lambda^2 + q\lambda + p$  with

$$s = \left( \bar{\mathcal{I}} + \frac{\bar{\mathcal{E}}_0}{a_0} + \frac{\bar{\mathcal{E}}_G}{a_G} \right) , \quad (.110)$$

$$q = \left( \frac{\bar{\mathcal{I}} \bar{\mathcal{E}}_0}{a_0} (1 + C_0) + \frac{\bar{\mathcal{I}} \bar{\mathcal{E}}_G}{a_G} (1 + C_G) + \frac{\bar{\mathcal{E}}_0 \bar{\mathcal{E}}_G}{a_0 a_G} \right) , \quad (.111)$$

$$p = \frac{\bar{\mathcal{I}} \bar{\mathcal{E}}_0 \bar{\mathcal{E}}_G}{a_0 a_G} (1 + C_0 + C_G) . \quad (.112)$$

5. Influence of the safety factor on the radial electric field – F. Stability of the equilibriums for the model of energy transfer

Each of these scalars is strictly positive. This polynomial takes the form  $\mathcal{P}(\lambda) = (\lambda - \lambda_1)(\lambda - \lambda_2)(\lambda - \lambda_3)$  so the following constraints can be identified:

$$\lambda_1 + \lambda_2 + \lambda_3 = -s < 0 ; \quad (.113)$$

$$\lambda_1\lambda_2 + \lambda_2\lambda_3 + \lambda_1\lambda_3 = q > 0 ; \quad (.114)$$

$$\lambda_1\lambda_2\lambda_3 = -p < 0 . \quad (.115)$$

The coefficients  $s$ ,  $q$  and  $p$  are reals. The inflexion point of this polynomial are the roots of its derivative  $d\mathcal{P}/d\lambda = 3\lambda^2 + 2s\lambda + q$ . The reduced discriminant then reads  $\Delta' = s^2 - 3q$ . If  $\Delta' > 0$ , then the roots of  $d\mathcal{P}/d\lambda$  are real and read

$$\lambda_{\pm} = -s \pm \sqrt{\Delta'} \quad (.116)$$

which are always negative because  $q > 0$  and  $s > 0$ . Fig.35 give the general form of  $d\mathcal{P}/d\lambda$  as a function of  $\lambda$ .

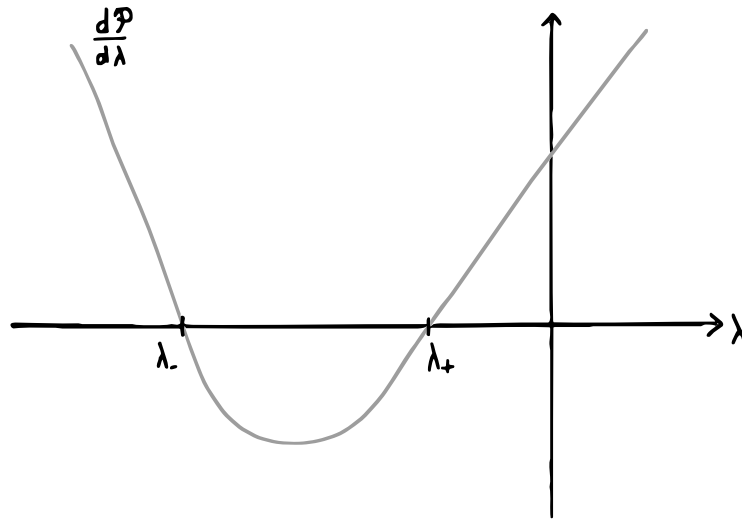


Figure 35. – Form of  $d\mathcal{P}/d\lambda$ .

The constraint  $\lambda_1\lambda_2\lambda_3 < 0$  in the case where each eigenvalue is real gives two different cases. First, all eigenvalues are negative and so the equilibrium is stable. Second, one is negative and the two others are positive. However this last case is not allowed, as  $\lambda_+ < 0$  so  $\lambda_1$  and  $\lambda_2$  have to be negative. The constraint Eq(.115) then guarantees that  $\lambda_3$  is also negative. This situation is drawn in Fig.36a.

Still in the case where  $\Delta' > 0$ , it could occur that one root  $\lambda_3$  is real and the two other ( $\lambda_1, \lambda_2$ ) are complex conjugates. This situation is represented in Fig.36b.

5. Influence of the safety factor on the radial electric field – F. Stability of the equilibriums for the model of energy transfer

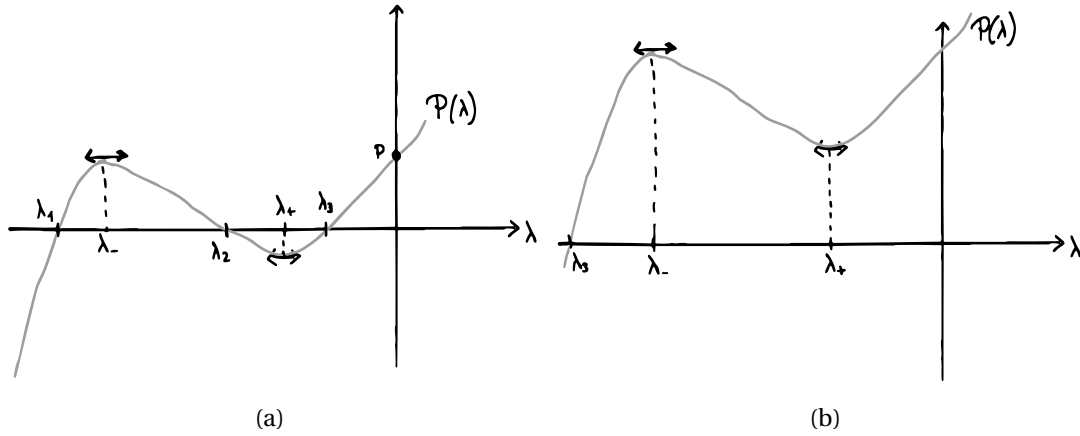


Figure 36. – (a) General form of  $\mathcal{P}(\lambda)$  when all eigenvalues are reals. (b) General form of  $\mathcal{P}(\lambda)$  when  $\Delta' < 0$  or when  $\Delta' > 0$  and two eigenvalues are complex.

Regarding the sign of the eigenvalues, this case is equivalent to the  $\Delta' < 0$  case. Writing  $\lambda_1 = \lambda_r + i\lambda_i$  and  $\lambda_2 = \lambda_r - i\lambda_i$ , the constraint Eq.(115) reads

$$\lambda_3(\lambda_r^2 + \lambda_i^2) < 0 \quad (.117)$$

which directly yields  $\lambda_3 < 0$ . A difficulty arises to obtain the sign of  $\lambda_r$ , which must be negative of the equilibrium to be stable. It is straightforward to show that  $\lambda_r = \frac{q\lambda_3 + p}{2\lambda^2}$ . At the transition from the "ZFs only" or "GAMs only" equilibrium to the "Mixed ZFs/GAMs" equilibrium, either  $\bar{\mathcal{E}}_0 = 0$  or  $\bar{\mathcal{E}}_G = 0$ . Consequently, at the transition,  $p = 0$  and so  $\lambda_r < 0$  and the equilibrium is stable. For non-vanishing values of  $p$ , the equilibrium stays stable as long as  $a_0 \geq 1$  and  $a_G \geq 1$ , which is considered in the model for consistency.

# Bibliography

- [1] H.-O Rama, D. Roberts, M. Tignor, et al. *Climate Change 2022: Impacts, Adaptation and Vulnerability Working Group II Contribution to the Sixth Assessment Report of the Intergovernmental Panel on Climate Change*. Aug. 3, 2022. DOI: [10.1017/9781009325844](https://doi.org/10.1017/9781009325844) (cit. on p. 21).
- [2] I. Hore-Lacy, ed. *Uranium for Nuclear Power: Resources, Mining and Transformation to Fuel*. Woodhead Publishing Series in Energy number 93. Waltham, MA: Elsevier, 2016. 468 pp. ISBN: 978-0-08-100307-7 (cit. on p. 25).
- [3] R.J. Pearson, A.B. Antoniazzi, and W.J. Nuttall. “Tritium Supply and Use: A Key Issue for the Development of Nuclear Fusion Energy”. In: *Fusion Engineering and Design*. Special Issue: Proceedings of the 13th International Symposium on Fusion Nuclear Technology (ISFNT-13) 136 (Nov. 1, 2018), pp. 1140–1148. ISSN: 0920-3796. DOI: [10.1016/j.fusengdes.2018.04.090](https://doi.org/10.1016/j.fusengdes.2018.04.090) (cit. on p. 25).
- [4] J.D. Lawson. “Some Criteria for a Power Producing Thermonuclear Reactor”. In: *Proceedings of the Physical Society. Section B* 70.1 (Jan. 1957), pp. 6–10. ISSN: 0370-1301. DOI: [10.1088/0370-1301/70/1/303](https://doi.org/10.1088/0370-1301/70/1/303) (cit. on p. 27).
- [5] A. Casner, T. Caillaud, S. Darbon, et al. “LMJ/PETAL Laser Facility: Overview and Opportunities for Laboratory Astrophysics”. In: *High Energy Density Physics*. 10th International Conference on High Energy Density Laboratory Astrophysics 17 (Dec. 1, 2015), pp. 2–11. ISSN: 1574-1818. DOI: [10.1016/j.hedp.2014.11.009](https://doi.org/10.1016/j.hedp.2014.11.009) (cit. on p. 27).
- [6] A.B. Zylstra, O.A. Hurricane, D.A. Callahan, et al. “Burning Plasma Achieved in Inertial Fusion”. In: *Nature* 601.7894 (7894 Jan. 2022), pp. 542–548. ISSN: 1476-4687. DOI: [10.1038/s41586-021-04281-w](https://doi.org/10.1038/s41586-021-04281-w) (cit. on p. 27).
- [7] E. Gibney. “Nuclear-Fusion Reactor Smashes Energy Record”. In: *Nature* 602.7897 (7897 Feb. 9, 2022), pp. 371–371. DOI: [10.1038/d41586-022-00391-1](https://doi.org/10.1038/d41586-022-00391-1) (cit. on p. 27).
- [8] S.E. Wurzel and S.C. Hsu. “Progress toward Fusion Energy Breakeven and Gain as Measured against the Lawson Criterion”. In: *Physics of Plasmas* 29.6 (June 2022), p. 062103. ISSN: 1070-664X. DOI: [10.1063/5.0083990](https://doi.org/10.1063/5.0083990) (cit. on p. 28).
- [9] L.D. Landau and E.M. Lifsic. *The Classical Theory of Fields*. Amsterdam; Heidelberg: Elsevier Butterworth Heinemann, 2007. ISBN: 978-0-7506-2768-9 (cit. on p. 31).
- [10] H. Goldstein. *Classical Mechanics*. Addison-Wesley, 1980 (cit. on p. 31).

- [11] V.I. Arnold. *Mathematical Methods of Classical Mechanics*. New York: Springer-Verlag, 1978. ISBN: 978-1-4757-1693-1. URL: <http://catalog.hathitrust.org/api/volumes/oclc/4037141.html> (visited on 08/11/2022) (cit. on p. 33).
- [12] M. Kruskal. “Asymptotic Theory of Hamiltonian and Other Systems with All Solutions Nearly Periodic”. In: *Journal of Mathematical Physics* 3.4 (July 1962), pp. 806–828. ISSN: 0022-2488. DOI: [10.1063/1.1724285](https://doi.org/10.1063/1.1724285) (cit. on p. 33).
- [13] A.J. Lichtenberg and M.A. Lieberman. *Regular and Stochastic Motion*. New York, NY: Springer New York, 1983. ISBN: 978-1-4757-4257-2. URL: <https://doi.org/10.1007/978-1-4757-4257-2> (visited on 08/01/2022) (cit. on p. 33).
- [14] R.G. Littlejohn. “Variational Principles of Guiding Centre Motion”. In: *Journal of Plasma Physics* 29.1 (Feb. 1983), pp. 111–125. ISSN: 0022-3778, 1469-7807. DOI: [10.1017/S002237780000060X](https://doi.org/10.1017/S002237780000060X) (cit. on p. 34).
- [15] X. Garbet, Y. Idomura, L. Villard, et al. “Gyrokinetic Simulations of Turbulent Transport”. In: *Nuclear Fusion* 50.4 (Mar. 2010), p. 043002. ISSN: 0029-5515. DOI: [10.1088/0029-5515/50/4/043002](https://doi.org/10.1088/0029-5515/50/4/043002) (cit. on pp. 38, 86).
- [16] J. Schirmer, G.D. Conway, H. Zohm, et al. “The Radial Electric Field and Its Associated Shear in the ASDEX Upgrade Tokamak”. In: *Nuclear Fusion* 46.9 (Sept. 2006), S780–S791. ISSN: 0029-5515, 1741-4326. DOI: [10.1088/0029-5515/46/9/S13](https://doi.org/10.1088/0029-5515/46/9/S13) (cit. on p. 41).
- [17] A. Fujisawa. “A Review of Zonal Flow Experiments”. In: *Nuclear Fusion* 49.1 (Dec. 2008), p. 013001. ISSN: 0029-5515. DOI: [10.1088/0029-5515/49/1/013001](https://doi.org/10.1088/0029-5515/49/1/013001) (cit. on p. 41).
- [18] Z. Lin, T.S. Hahm, W.W. Lee, et al. “Turbulent Transport Reduction by Zonal Flows: Massively Parallel Simulations”. In: *Science* 281.5384 (Sept. 18, 1998), pp. 1835–1837. DOI: [10.1126/science.281.5384.1835](https://doi.org/10.1126/science.281.5384.1835) (cit. on pp. 41, 131).
- [19] G. Dif-Pradalier, G. Hornung, X. Garbet, et al. “The  $E \times B$  Staircase of Magnetised Plasmas”. In: *Nuclear Fusion* 57.6 (Apr. 2017), p. 066026. ISSN: 0029-5515. DOI: [10.1088/1741-4326/aa6873](https://doi.org/10.1088/1741-4326/aa6873) (cit. on pp. 41, 131).
- [20] P.H. Diamond, S.-I. Itoh, K. Itoh, et al. “Zonal Flows in Plasma—a Review”. In: *Plasma Physics and Controlled Fusion* 47.5 (Apr. 2005), R35–R161. ISSN: 0741-3335. DOI: [10.1088/0741-3335/47/5/R01](https://doi.org/10.1088/0741-3335/47/5/R01) (cit. on pp. 41, 131).
- [21] P.C. de Vries, G. Waidmann, A.J.H. Donné, et al. “MHD-mode Stabilization by Plasma Rotation in TEXTOR”. In: *Plasma Physics and Controlled Fusion* 38.4 (Apr. 1, 1996), pp. 467–476. ISSN: 0741-3335, 1361-6587. DOI: [10.1088/0741-3335/38/4/002](https://doi.org/10.1088/0741-3335/38/4/002) (cit. on pp. 42, 102).
- [22] M.N. Rosenbluth and F.L. Hinton. “Plasma Rotation Driven by Alpha Particles in a Tokamak Reactor”. In: *Nuclear Fusion* 36.1 (Jan. 1996), pp. 55–67. ISSN: 0029-5515. DOI: [10.1088/0029-5515/36/1/I04](https://doi.org/10.1088/0029-5515/36/1/I04) (cit. on pp. 42, 102).

- [23] N. Oyama, G. Saibene, Y. Kamada, et al. “Effect of Toroidal Field Ripple and Toroidal Rotation on H-mode Performance and ELM Characteristics in JET/JT-60U Similarity Experiments”. In: *Journal of Physics: Conference Series* 123 (July 2008), p. 012015. ISSN: 1742-6596. DOI: [10.1088/1742-6596/123/1/012015](https://doi.org/10.1088/1742-6596/123/1/012015) (cit. on pp. 42, 43).
- [24] H. Urano, N. Oyama, K. Kamiya, et al. “H-Mode Pedestal Structure in the Variation of Toroidal Rotation and Toroidal Field Ripple in JT-60U”. In: *Nuclear Fusion* 47.7 (July 2007), pp. 706–713. ISSN: 0029-5515, 1741-4326. DOI: [10.1088/0029-5515/47/7/022](https://doi.org/10.1088/0029-5515/47/7/022) (cit. on pp. 42, 43, 103).
- [25] C. Fenzi, X. Garbet, E. Trier, et al. “On Plasma Rotation with Toroidal Magnetic Field Ripple and No External Momentum Input”. In: *Nuclear Fusion* 51.10 (Oct. 1, 2011), p. 103038. ISSN: 0029-5515, 1741-4326. DOI: [10.1088/0029-5515/51/10/103038](https://doi.org/10.1088/0029-5515/51/10/103038) (cit. on pp. 42, 43, 103).
- [26] M.F.F. Nave, T. Johnson, L.-G. Eriksson, et al. “Influence of Magnetic Field Ripple on the Intrinsic Rotation of Tokamak Plasmas”. In: *Physical Review Letters* 105.10 (Sept. 3, 2010), p. 105005. ISSN: 0031-9007, 1079-7114. DOI: [10.1103/PhysRevLett.105.105005](https://doi.org/10.1103/PhysRevLett.105.105005) (cit. on pp. 42, 102).
- [27] P.C. de Vries, A. Salmi, V. Parail, et al. “Effect of Toroidal Field Ripple on Plasma Rotation in JET”. In: *Nuclear Fusion* 48.3 (Jan. 2008), p. 035007. ISSN: 0029-5515. DOI: [10.1088/0029-5515/48/3/035007](https://doi.org/10.1088/0029-5515/48/3/035007) (cit. on pp. 42, 43).
- [28] B. Chouli, C. Fenzi, X. Garbet, et al. “Investigations of LHCD Induced Plasma Rotation in Tore Supra”. In: *Plasma Physics and Controlled Fusion* 57.12 (Dec. 1, 2015), p. 125007. ISSN: 0741-3335, 1361-6587. DOI: [10.1088/0741-3335/57/12/125007](https://doi.org/10.1088/0741-3335/57/12/125007) (cit. on pp. 42, 109, 112).
- [29] E. Trier, L.-G. Eriksson, P. Hennequin, et al. “Radial Electric Field Measurement in a Tokamak with Magnetic Field Ripple”. In: *Nuclear Fusion* 48.9 (Sept. 2008), p. 092001. ISSN: 0029-5515, 1741-4326. DOI: [10.1088/0029-5515/48/9/092001](https://doi.org/10.1088/0029-5515/48/9/092001) (cit. on pp. 43, 112).
- [30] X. Garbet, J. Abiteboul, E. Trier, et al. “Entropy Production Rate in Tokamaks with Nonaxisymmetric Magnetic Fields”. In: *Physics of Plasmas* 17.7 (July 2010), p. 072505. ISSN: 1070-664X, 1089-7674. DOI: [10.1063/1.3454365](https://doi.org/10.1063/1.3454365) (cit. on pp. 43, 64, 103, 104, 110).
- [31] G. Saibene et al. *Toroidal Field Ripple Effects on H-modes in JET and Implications for ITER*. 2007 34th EPS Conference on Plasma Physics, Warsaw, Poland (2nd - 6th July), 2007 (cit. on p. 43).
- [32] Y. Andrew, T.M. Biewer, K. Crombe, et al. “H-Mode Access on JET and Implications for ITER”. In: *Plasma Physics and Controlled Fusion* 50.12 (Dec. 1, 2008), p. 124053. ISSN: 0741-3335, 1361-6587. DOI: [10.1088/0741-3335/50/12/124053](https://doi.org/10.1088/0741-3335/50/12/124053) (cit. on p. 43).



- [33] L. Vermare, P. Hennequin, C. Honoré, et al. “Formation of the Radial Electric Field Profile in the WEST Tokamak”. In: *Nuclear Fusion* 62.2 (Dec. 2021), p. 026002. ISSN: 0029-5515. DOI: [10.1088/1741-4326/ac3c85](https://doi.org/10.1088/1741-4326/ac3c85) (cit. on pp. 44, 125).
- [34] P. Hennequin, L. Vermare, Nicolas Fedorczak, et al. “The Effect of SOL Flows on Edge and Core Radial Electric Field and Rotation in Tore Supra”. In: *37th EPS Conference on Plasma Physics 2010, EPS 2010 1* (Jan. 1, 2010), pp. 385–388 (cit. on pp. 44, 125).
- [35] H. Meyer, C. Bunting, P.G. Carolan, et al. “The Structure, Evolution and Role of the Radial Edge Electric Field in H-mode and L-mode on MAST”. In: *Journal of Physics: Conference Series* 123 (July 1, 2008), p. 012005. ISSN: 1742-6596. DOI: [10.1088/1742-6596/123/1/012005](https://doi.org/10.1088/1742-6596/123/1/012005) (cit. on p. 44).
- [36] P. Donnel, X. Garbet, Y. Sarazin, et al. “Turbulent Generation of Poloidal Asymmetries of the Electric Potential in a Tokamak”. In: *Plasma Physics and Controlled Fusion* 61.1 (Nov. 2018), p. 014003. ISSN: 0741-3335. DOI: [10.1088/1361-6587/aae4fe](https://doi.org/10.1088/1361-6587/aae4fe) (cit. on p. 44).
- [37] F. Ryter, S.K. Rathgeber, L. Barrera Orte, et al. “Survey of the H-mode Power Threshold and Transition Physics Studies in ASDEX Upgrade”. In: *Nuclear Fusion* 53.11 (Sept. 2013), p. 113003. ISSN: 0029-5515. DOI: [10.1088/0029-5515/53/11/113003](https://doi.org/10.1088/0029-5515/53/11/113003) (cit. on p. 45).
- [38] Y.R. Martin, T. Takizuka, and the ITPA CDBM H-mode Threshold Data Group. “Power Requirement for Accessing the H-mode in ITER”. In: *Journal of Physics: Conference Series* 123 (July 1, 2008), p. 012033. ISSN: 1742-6596. DOI: [10.1088/1742-6596/123/1/012033](https://doi.org/10.1088/1742-6596/123/1/012033) (cit. on p. 45).
- [39] R.W. Brzozowski, F. Jenko, R. Bilato, et al. “A Geometric Model of Ion Orbit Loss under the Influence of a Radial Electric Field”. In: *Physics of Plasmas* 26.4 (Apr. 2019), p. 042511. ISSN: 1070-664X. DOI: [10.1063/1.5075613](https://doi.org/10.1063/1.5075613) (cit. on p. 49).
- [40] T. Kobayashi, K. Itoh, T. Ido, et al. “Experimental Identification of Electric Field Excitation Mechanisms in a Structural Transition of Tokamak Plasmas”. In: *Scientific Reports* 6.1 (Nov. 2016), p. 30720. ISSN: 2045-2322. DOI: [10.1038/srep30720](https://doi.org/10.1038/srep30720) (cit. on p. 49).
- [41] G. Dif-Pradalier, P. Ghendrih, Y. Sarazin, et al. “Transport Barrier Onset and Edge Turbulence Shortfall in Fusion Plasmas”. In: *Communications Physics* 5.1 (1 Sept. 15, 2022), pp. 1–12. ISSN: 2399-3650. DOI: [10.1038/s42005-022-01004-z](https://doi.org/10.1038/s42005-022-01004-z) (cit. on p. 49).
- [42] P. N. Yushmanov. “Diffusive transport processes caused by ripple in tokamaks”. In: *edited by B. B. Kadomtsev (Consultants Bureau, New York)* (1991) (cit. on pp. 55, 64, 103).
- [43] A.N. Kolmogorov. *On Conservation of Conditionally Periodic Motions for a Small Change in Hamilton’s Function*. 1954 (cit. on p. 56).

- [44] D. Zarzoso, D. Del-Castillo-Negrete, R. Dumont, et al. “Towards the prediction and quantification of energetic particle transport and losses in fusion plasmas: the case of alpha particle transport and losses in a JET size tokamak”. In: *28th IAEA Fusion Energy Conference*. Vienne (virtual event), Austria, May 2021. URL: <https://hal.archives-ouvertes.fr/hal-03200051> (cit. on p. 58).
- [45] M.N. Rosenbluth, R.D. Hazeltine, and F.L. Hinton. “Plasma Transport in Toroidal Confinement Systems”. In: *The Physics of Fluids* 15.1 (Jan. 1972), pp. 116–140. ISSN: 0031-9171. DOI: [10.1063/1.1693728](https://doi.org/10.1063/1.1693728) (cit. on p. 59).
- [46] F.L. Hinton and R.D. Hazeltine. “Theory of Plasma Transport in Toroidal Confinement Systems”. In: *Reviews of Modern Physics* 48.2 (Apr. 1, 1976), pp. 239–308. DOI: [10.1103/RevModPhys.48.239](https://doi.org/10.1103/RevModPhys.48.239) (cit. on pp. 59, 64, 140).
- [47] A. Samain and F. Nguyen. “Onsager Relaxation of Toroidal Plasmas”. In: *Plasma Physics and Controlled Fusion* 39.8 (Aug. 1997), pp. 1197–1243. ISSN: 0741-3335. DOI: [10.1088/0741-3335/39/8/005](https://doi.org/10.1088/0741-3335/39/8/005) (cit. on pp. 59, 60).
- [48] H.E. Mynick. “Transport Optimization in Stellarators”. In: *Physics of Plasmas* 13.5 (May 2006), p. 058102. ISSN: 1070-664X. DOI: [10.1063/1.2177643](https://doi.org/10.1063/1.2177643) (cit. on p. 63).
- [49] A.A. Galeev and R.Z. Sagdeev. “Transport phenomena in a collisionless plasma in a toroidal magnetic system”. In: *Zh. Eksp. Teor. Fiz.* 53 (1967), pp. 348–359 (cit. on p. 64).
- [50] A.A. Galeev, R.Z. Sagdeev, H.P. Furth, et al. “Plasma Diffusion in a Toroidal Stellarator”. In: *Physical Review Letters* 22.11 (Mar. 17, 1969), pp. 511–514. ISSN: 0031-9007. DOI: [10.1103/PhysRevLett.22.511](https://doi.org/10.1103/PhysRevLett.22.511) (cit. on p. 64).
- [51] L.M. Kovrizhnykh. “Transport phenomena in toroidal magnetic systems”. In: *Zh. Eksp. Teor. Fiz.* 56 (1969), pp. 877–891 (cit. on p. 64).
- [52] P. Helander and D. J. Sigmar. “Collisional Transport in Magnetized Plasmas”. In: *Cambridge University Press* (2002) (cit. on p. 64).
- [53] T. E. Stringer. “Effect of the Magnetic Field Ripple on Diffusion in Tokamaks”. In: *Nuclear Fusion* 12.6 (Dec. 1972), pp. 689–694. ISSN: 0029-5515. DOI: [10.1088/0029-5515/12/6/010](https://doi.org/10.1088/0029-5515/12/6/010) (cit. on p. 64).
- [54] J.W. Connor and R.J. Hastie. “Neoclassical Diffusion Arising from Magnetic-Field Ripples in Tokamaks”. In: *Nuclear Fusion* 13.2 (Mar. 1, 1973), pp. 221–225. ISSN: 0029-5515, 1741-4326. DOI: [10.1088/0029-5515/13/2/011](https://doi.org/10.1088/0029-5515/13/2/011) (cit. on pp. 64, 103, 104).
- [55] A.H. Boozer. “Enhanced Transport in Tokamaks Due to Toroidal Ripple”. In: *The Physics of Fluids* 23.11 (Nov. 1980), pp. 2283–2290. ISSN: 0031-9171. DOI: [10.1063/1.862922](https://doi.org/10.1063/1.862922) (cit. on p. 64).

- [56] K.C. Shaing, S.P. Hirshman, and J.D. Callen. “Neoclassical Transport Fluxes in the Plateau Regime in Nonaxisymmetric Toroidal Plasmas”. In: *Physics of Fluids* 29.2 (1986), p. 521. ISSN: 00319171. DOI: [10.1063/1.865439](https://doi.org/10.1063/1.865439) (cit. on pp. 64, 103).
- [57] K.C. Shaing. “Neoclassical Flows and Transport in Nonaxisymmetric Toroidal Plasmas”. In: *Physics of Fluids* 26.11 (1983), p. 3315. ISSN: 00319171. DOI: [10.1063/1.864108](https://doi.org/10.1063/1.864108) (cit. on pp. 64, 103).
- [58] P.N. Yushmanov. “Generalized Ripple-Banana Transport in a Tokamak”. In: *Nuclear Fusion* 23.12 (Dec. 1, 1983), pp. 1599–1612. ISSN: 0029-5515, 1741-4326. DOI: [10.1088/0029-5515/23/12/005](https://doi.org/10.1088/0029-5515/23/12/005) (cit. on pp. 64, 103, 104).
- [59] P.N. Yushmanov. “Thermal Conductivity Due to Ripple-Trapped Ions in a Tokamak”. In: *Nuclear Fusion* 22.3 (Mar. 1, 1982), pp. 315–324. ISSN: 0029-5515, 1741-4326. DOI: [10.1088/0029-5515/22/3/001](https://doi.org/10.1088/0029-5515/22/3/001) (cit. on pp. 64, 103).
- [60] K.C. Shaing and J.D. Callen. “Neoclassical Ripple Transport in Tokamaks”. In: *Nuclear Fusion* 22.8 (Aug. 1982), pp. 1061–1068. ISSN: 0029-5515. DOI: [10.1088/0029-5515/22/8/005](https://doi.org/10.1088/0029-5515/22/8/005) (cit. on p. 64).
- [61] K.C. Shaing, J.A. Rome, and R.H. Fowler. “Transport Associated with the Collisionless Detrapping/Retrapping Orbits in a Nonaxisymmetric Torus”. In: *Physics of Fluids* 27.1 (1984), p. 1. ISSN: 00319171. DOI: [10.1063/1.864512](https://doi.org/10.1063/1.864512) (cit. on pp. 64, 103).
- [62] L.M. Kovrizhnykh. “Neoclassical Theory of Transport Processes in Toroidal Magnetic Confinement Systems, with Emphasis on Non-Axisymmetric Configurations”. In: *Nuclear Fusion* 24.7 (July 1, 1984), pp. 851–936. ISSN: 0029-5515, 1741-4326. DOI: [10.1088/0029-5515/24/7/003](https://doi.org/10.1088/0029-5515/24/7/003) (cit. on pp. 64, 103).
- [63] K.C. Shaing, S.A. Sabbagh, and M.S. Chu. “Neoclassical Toroidal Plasma Viscosity in the Superbanana Regime in Tokamaks”. In: *Plasma Physics and Controlled Fusion* 51.5 (Feb. 2009), p. 055003. ISSN: 0741-3335. DOI: [10.1088/0741-3335/51/5/055003](https://doi.org/10.1088/0741-3335/51/5/055003) (cit. on pp. 64, 99).
- [64] K.C. Shaing, S.A. Sabbagh, and M.S. Chu. “Neoclassical Toroidal Plasma Viscosity in the Low Collisionality Regime for Tokamaks”. In: *Plasma Physics and Controlled Fusion* 51.3 (Dec. 2008), p. 035004. ISSN: 0741-3335. DOI: [10.1088/0741-3335/51/3/035004](https://doi.org/10.1088/0741-3335/51/3/035004) (cit. on p. 64).
- [65] K.C. Shaing, S.A. Sabbagh, and M.S. Chu. “Neoclassical Toroidal Plasma Viscosity in the Superbanana Plateau Regime for Tokamaks”. In: *Plasma Physics and Controlled Fusion* 51.3 (Dec. 2008), p. 035009. ISSN: 0741-3335. DOI: [10.1088/0741-3335/51/3/035009](https://doi.org/10.1088/0741-3335/51/3/035009) (cit. on pp. 64, 99).
- [66] S.P. Hirshman and D.J. Sigmar. “Approximate Fokker–Planck Collision Operator for Transport Theory Applications”. In: *Physics of Fluids* 19.10 (1976), p. 1532. ISSN: 00319171. DOI: [10.1063/1.861356](https://doi.org/10.1063/1.861356) (cit. on p. 65).

- [67] R.J. Goldston, R.B. White, and A.H. Boozer. “Confinement of High-Energy Trapped Particles in Tokamaks”. In: *Physical Review Letters* 47.9 (Aug. 31, 1981), pp. 647–649. ISSN: 0031-9007. DOI: [10.1103/PhysRevLett.47.647](https://doi.org/10.1103/PhysRevLett.47.647) (cit. on pp. 66, 67, 72).
- [68] P. Grua and J.-P. Roubin. “Collisionless Diffusion Regimes of Trapped Particles in a Tokamak Induced by Magnetic Field Ripples”. In: *Nuclear Fusion* 30.8 (Aug. 1, 1990), pp. 1499–1509. ISSN: 0029-5515, 1741-4326. DOI: [10.1088/0029-5515/30/8/009](https://doi.org/10.1088/0029-5515/30/8/009) (cit. on pp. 67, 173).
- [69] C.D. Beidler, Y.I. Kolesnichenko, V.S. Marchenko, et al. “Stochastic Diffusion of Energetic Ions in Optimized Stellarators”. In: *Physics of Plasmas* 8.6 (June 2001), pp. 2731–2738. ISSN: 1070-664X, 1089-7674. DOI: [10.1063/1.1365958](https://doi.org/10.1063/1.1365958) (cit. on p. 67).
- [70] R.D. Hazeltine. “Rotation of a Toroidally Confined, Collisional Plasma”. In: *The Physics of Fluids* 17.5 (May 1974), pp. 961–968. ISSN: 0031-9171. DOI: [10.1063/1.1694838](https://doi.org/10.1063/1.1694838) (cit. on p. 77).
- [71] M. Bécoulet, G. Huysmans, X. Garbet, et al. “Physics of Penetration of Resonant Magnetic Perturbations Used for Type I Edge Localized Modes Suppression in Tokamaks”. In: *Nuclear Fusion* 49.8 (July 2009), p. 085011. ISSN: 0029-5515. DOI: [10.1088/0029-5515/49/8/085011](https://doi.org/10.1088/0029-5515/49/8/085011) (cit. on p. 79).
- [72] K. Kim, J.-K. Park, A.H. Boozer, et al. “Calculation of Neoclassical Toroidal Viscosity with a Particle Simulation in the Tokamak Magnetic Braking Experiments”. In: *Nuclear Fusion* 54.7 (July 1, 2014), p. 073014. ISSN: 0029-5515, 1741-4326. DOI: [10.1088/0029-5515/54/7/073014](https://doi.org/10.1088/0029-5515/54/7/073014) (cit. on pp. 79, 103).
- [73] J.-K. Park, A.H. Boozer, and J.E. Menard. “Nonambipolar Transport by Trapped Particles in Tokamaks”. In: *Physical Review Letters* 102.6 (Feb. 11, 2009), p. 065002. DOI: [10.1103/PhysRevLett.102.065002](https://doi.org/10.1103/PhysRevLett.102.065002) (cit. on pp. 79, 99, 103).
- [74] Y. Sun, Y. Liang, K.C. Shaing, et al. “Modelling of the Neoclassical Toroidal Plasma Viscosity Torque in Tokamaks”. In: *Nuclear Fusion* 51.5 (Apr. 2011), p. 053015. ISSN: 0029-5515. DOI: [10.1088/0029-5515/51/5/053015](https://doi.org/10.1088/0029-5515/51/5/053015) (cit. on p. 79).
- [75] L. Vermare, Ö.D. Gürçan, P. Hennequin, et al. “Wavenumber Spectrum of Micro-Turbulence in Tokamak Plasmas”. In: *Comptes Rendus Physique. Propagation and Plasmas: New Challenges, New Applications* 12.2 (Mar. 1, 2011), pp. 115–122. ISSN: 1631-0705. DOI: [10.1016/j.crhy.2010.11.003](https://doi.org/10.1016/j.crhy.2010.11.003) (cit. on p. 80).
- [76] V. Grandgirard, J. Abiteboul, J. Bigot, et al. “A 5D Gyrokinetic Full- $f$  Global Semi-Lagrangian Code for Flux-Driven Ion Turbulence Simulations”. In: *Computer Physics Communications* 207 (Oct. 2016), pp. 35–68. ISSN: 00104655. DOI: [10.1016/j.cpc.2016.05.007](https://doi.org/10.1016/j.cpc.2016.05.007) (cit. on pp. 81, 89, 103).
- [77] A.J. Brizard and T.S. Hahm. “Foundations of Nonlinear Gyrokinetic Theory”. In: *Reviews of Modern Physics* 79.2 (Apr. 2, 2007), pp. 421–468. DOI: [10.1103/RevModPhys.79.421](https://doi.org/10.1103/RevModPhys.79.421) (cit. on p. 86).

- [78] A.J. Brizard. “A Guiding-Center Fokker–Planck Collision Operator for Nonuniform Magnetic Fields”. In: *Physics of Plasmas* 11.9 (Sept. 2004), pp. 4429–4438. ISSN: 1070-664X. DOI: [10.1063/1.1780532](https://doi.org/10.1063/1.1780532) (cit. on p. 86).
- [79] P. Donnel, X. Garbet, Y. Sarazin, et al. “A Multi-Species Collisional Operator for Full-F Global Gyrokinetics Codes: Numerical Aspects and Verification with the GYSELA Code”. In: *Computer Physics Communications* 234 (Jan. 2019), pp. 1–13. ISSN: 00104655. DOI: [10.1016/j.cpc.2018.08.008](https://doi.org/10.1016/j.cpc.2018.08.008) (cit. on p. 86).
- [80] S. Matsuoka, Y. Idomura, and S. Satake. “Global Kinetic Simulations of Neoclassical Toroidal Viscosity in Low-Collisional Perturbed Tokamak Plasmas”. In: *Physics of Plasmas* 24.10 (Oct. 2017), p. 102522. ISSN: 1070-664X, 1089-7674. DOI: [10.1063/1.5008285](https://doi.org/10.1063/1.5008285) (cit. on pp. 90, 103).
- [81] J. Abiteboul, X. Garbet, V. Grandgirard, et al. “Conservation Equations and Calculation of Mean Flows in Gyrokinetics”. In: *Physics of Plasmas* 18.8 (Aug. 2011), p. 082503. ISSN: 1070-664X, 1089-7674. DOI: [10.1063/1.3620407](https://doi.org/10.1063/1.3620407) (cit. on pp. 92, 103, 134).
- [82] G. Dif-Pradalier, P.H. Diamond, V. Grandgirard, et al. “Neoclassical Physics in Full Distribution Function Gyrokinetics”. In: *Physics of Plasmas* 18.6 (June 2011), p. 062309. ISSN: 1070-664X, 1089-7674. DOI: [10.1063/1.3592652](https://doi.org/10.1063/1.3592652) (cit. on pp. 94, 100, 138).
- [83] E.A. Belli and J. Candy. “Kinetic Calculation of Neoclassical Transport Including Self-Consistent Electron and Impurity Dynamics”. In: *Plasma Physics and Controlled Fusion* 50.9 (July 2008), p. 095010. ISSN: 0741-3335. DOI: [10.1088/0741-3335/50/9/095010](https://doi.org/10.1088/0741-3335/50/9/095010) (cit. on p. 96).
- [84] E.A. Belli and J. Candy. “Full Linearized Fokker–Planck Collisions in Neoclassical Transport Simulations”. In: *Plasma Physics and Controlled Fusion* 54.1 (Dec. 2011), p. 015015. ISSN: 0741-3335. DOI: [10.1088/0741-3335/54/1/015015](https://doi.org/10.1088/0741-3335/54/1/015015) (cit. on p. 96).
- [85] H. Sugama and W. Horton. “Nonlinear Electromagnetic Gyrokinetic Equation for Plasmas with Large Mean Flows”. In: *Physics of Plasmas* 5.7 (July 1998), pp. 2560–2573. ISSN: 1070-664X. DOI: [10.1063/1.872941](https://doi.org/10.1063/1.872941) (cit. on p. 97).
- [86] E.A. Belli and J. Candy. “Neoclassical Transport in Toroidal Plasmas with Nonaxisymmetric Flux Surfaces”. In: *Plasma Physics and Controlled Fusion* 57.5 (Apr. 2015), p. 054012. ISSN: 0741-3335. DOI: [10.1088/0741-3335/57/5/054012](https://doi.org/10.1088/0741-3335/57/5/054012) (cit. on pp. 97, 100).
- [87] Y.B. Kim, P.H. Diamond, H. Biglari, et al. “Theory of Neoclassical Ion Temperature-gradient-driven Turbulence”. In: *Physics of Fluids B: Plasma Physics* 3.2 (Feb. 1991), pp. 384–394. ISSN: 0899-8221. DOI: [10.1063/1.859748](https://doi.org/10.1063/1.859748) (cit. on p. 100).
- [88] R. Varennes, X. Garbet, L. Vermare, et al. “Synergy of Turbulent Momentum Drive and Magnetic Braking”. In: *Physical Review Letters* 128.25 (June 23, 2022), p. 255002. DOI: [10.1103/PhysRevLett.128.255002](https://doi.org/10.1103/PhysRevLett.128.255002) (cit. on p. 102).

- [89] P. Mantica, D. Strintzi, T. Tala, et al. “Experimental Study of the Ion Critical-Gradient Length and Stiffness Level and the Impact of Rotation in the JET Tokamak”. In: *Physical Review Letters* 102.17 (Apr. 29, 2009), p. 175002. ISSN: 0031-9007, 1079-7114. DOI: [10.1103/PhysRevLett.102.175002](https://doi.org/10.1103/PhysRevLett.102.175002) (cit. on p. 102).
- [90] T.S. Hahm and K.H. Burrell. “Flow Shear Induced Fluctuation Suppression in Finite Aspect Ratio Shaped Tokamak Plasma”. In: *Physics of Plasmas* 2.5 (May 1995), pp. 1648–1651. ISSN: 1070-664X, 1089-7674. DOI: [10.1063/1.871313](https://doi.org/10.1063/1.871313) (cit. on p. 102).
- [91] Y. Sakamoto, Y. Kamada, S. Ide, et al. “Characteristics of Internal Transport Barriers in JT-60U Reversed Shear Plasmas”. In: *Nuclear Fusion* 41.7 (July 2001), pp. 865–872. ISSN: 0029-5515. DOI: [10.1088/0029-5515/41/7/307](https://doi.org/10.1088/0029-5515/41/7/307) (cit. on p. 102).
- [92] A.G. Peeters, C. Angioni, A. Bortolon, et al. “Overview of Toroidal Momentum Transport”. In: *Nuclear Fusion* 51.9 (Sept. 1, 2011), p. 094027. ISSN: 0029-5515, 1741-4326. DOI: [10.1088/0029-5515/51/9/094027](https://doi.org/10.1088/0029-5515/51/9/094027) (cit. on pp. 102, 103, 107).
- [93] W. Zhu, S.A. Sabbagh, R.E. Bell, et al. “Observation of Plasma Toroidal-Momentum Dissipation by Neoclassical Toroidal Viscosity”. In: *Physical Review Letters* 96.22 (June 9, 2006), p. 225002. ISSN: 0031-9007, 1079-7114. DOI: [10.1103/PhysRevLett.96.225002](https://doi.org/10.1103/PhysRevLett.96.225002) (cit. on p. 103).
- [94] Y. Sun, Y. Liang, H.R. Koslowski, et al. “Toroidal Rotation Braking with  $n = 1$  Magnetic Perturbation Field on JET”. In: *Plasma Physics and Controlled Fusion* 52.10 (Oct. 1, 2010), p. 105007. ISSN: 0741-3335, 1361-6587. DOI: [10.1088/0741-3335/52/10/105007](https://doi.org/10.1088/0741-3335/52/10/105007) (cit. on p. 103).
- [95] A.J. Cole, J.D. Callen, W.M. Solomon, et al. “Peak Neoclassical Toroidal Viscosity at Low Toroidal Rotation in the DIII-D Tokamak”. In: *Physics of Plasmas* 18.5 (May 2011), p. 055711. ISSN: 1070-664X, 1089-7674. DOI: [10.1063/1.3590933](https://doi.org/10.1063/1.3590933) (cit. on p. 103).
- [96] P.N. Yushmanov, J.R. Cary, and S.G. Shasharina. “Transport in Non-Axisymmetric Tori with up-down Asymmetry”. In: *Nuclear Fusion* 33.9 (Sept. 1993), pp. 1293–1303. ISSN: 0029-5515. DOI: [10.1088/0029-5515/33/9/I04](https://doi.org/10.1088/0029-5515/33/9/I04) (cit. on p. 103).
- [97] V.S. Tsypin, A.B. Mikhailovskii, R.M.O. Galvão, et al. “Plasma Rotation in Toroidal Devices with Circular Cross-Sections”. In: *Physics of Plasmas* 5.9 (Sept. 1998), pp. 3358–3365. ISSN: 1070-664X, 1089-7674. DOI: [10.1063/1.873049](https://doi.org/10.1063/1.873049) (cit. on p. 103).
- [98] K.C. Shaing. “Theory of High-Mode Phenomena for Stellarators”. In: *Physical Review Letters* 76.23 (June 3, 1996), pp. 4364–4367. ISSN: 0031-9007, 1079-7114. DOI: [10.1103/PhysRevLett.76.4364](https://doi.org/10.1103/PhysRevLett.76.4364) (cit. on p. 103).
- [99] T. E. Stringer. “Generalized Equations for Plasma of Arbitrary Collision Frequency in Weakly Inhomogeneous Magnetic Field”. In: *Physics of Fluids* 14.10 (1971), p. 2177. ISSN: 00319171. DOI: [10.1063/1.1693309](https://doi.org/10.1063/1.1693309) (cit. on p. 103).

- [100] S. Satake, Y. Idomura, H. Sugama, et al. “Benchmark Test of Drift-Kinetic and Gyrokinetic Codes through Neoclassical Transport Simulations”. In: *Computer Physics Communications* 181.6 (June 2010), pp. 1069–1076. ISSN: 00104655. DOI: [10.1016/j.cpc.2010.02.014](https://doi.org/10.1016/j.cpc.2010.02.014) (cit. on p. 103).
- [101] S. Satake, J.-K. Park, H. Sugama, et al. “Neoclassical Toroidal Viscosity Calculations in Tokamaks Using a delta-f Monte Carlo Simulation and Their Verifications”. In: *Physical Review Letters* 107.5 (July 25, 2011), p. 055001. ISSN: 0031-9007, 1079-7114. DOI: [10.1103/PhysRevLett.107.055001](https://doi.org/10.1103/PhysRevLett.107.055001) (cit. on p. 103).
- [102] N.C. Logan, J.-K. Park, K. Kim, et al. “Neoclassical Toroidal Viscosity in Perturbed Equilibria with General Tokamak Geometry”. In: *Physics of Plasmas* 20.12 (Dec. 2013), p. 122507. ISSN: 1070-664X, 1089-7674. DOI: [10.1063/1.4849395](https://doi.org/10.1063/1.4849395) (cit. on p. 103).
- [103] P. H. Diamond et al. “in *Proceedings of the 15th International Conference on Plasmas Physics and Controlled Nuclear Fusion*”. In: *Seville, 1994 (IAEA, Vienna)* () (cit. on p. 103).
- [104] Y. Camenen, A.G. Peeters, C. Angioni, et al. “Transport of Parallel Momentum Induced by Current-Symmetry Breaking in Toroidal Plasmas”. In: *Physical Review Letters* 102.12 (Mar. 25, 2009), p. 125001. ISSN: 0031-9007, 1079-7114. DOI: [10.1103/PhysRevLett.102.125001](https://doi.org/10.1103/PhysRevLett.102.125001) (cit. on p. 103).
- [105] Ö.D. Gürcan, P.H. Diamond, and T.S. Hahm. “Turbulent Equipartition and Homogenization of Plasma Angular Momentum”. In: *Physical Review Letters* 100.13 (Apr. 3, 2008), p. 135001. ISSN: 0031-9007, 1079-7114. DOI: [10.1103/PhysRevLett.100.135001](https://doi.org/10.1103/PhysRevLett.100.135001) (cit. on pp. 103, 104, 113, 120).
- [106] K. Ida and J.E. Rice. “Rotation and Momentum Transport in Tokamaks and Helical Systems”. In: *Nuclear Fusion* 54.4 (Apr. 1, 2014), p. 045001. ISSN: 0029-5515, 1741-4326. DOI: [10.1088/0029-5515/54/4/045001](https://doi.org/10.1088/0029-5515/54/4/045001) (cit. on p. 103).
- [107] Y. Idomura. “Full-  $f$  Gyrokinetic Simulation over a Confinement Time”. In: *Physics of Plasmas* 21.2 (Feb. 2014), p. 022517. ISSN: 1070-664X, 1089-7674. DOI: [10.1063/1.4867180](https://doi.org/10.1063/1.4867180) (cit. on p. 103).
- [108] Y. Idomura. “Toroidal Angular Momentum Balance during Rotation Changes Induced by Electron Heating Modulation in Tokamak Plasmas”. In: *Physics of Plasmas* 24.8 (Aug. 2017), p. 080701. ISSN: 1070-664X, 1089-7674. DOI: [10.1063/1.4996017](https://doi.org/10.1063/1.4996017) (cit. on p. 103).
- [109] R.E. Waltz, G.M. Staebler, and W.M. Solomon. “Gyrokinetic Simulation of Momentum Transport with Residual Stress from Diamagnetic Level Velocity Shears”. In: *Physics of Plasmas* 18.4 (Apr. 2011), p. 042504. ISSN: 1070-664X, 1089-7674. DOI: [10.1063/1.3579481](https://doi.org/10.1063/1.3579481) (cit. on p. 103).
- [110] C.J. McDevitt, P.H. Diamond, Ö.D. Gürcan, et al. “Toroidal Rotation Driven by the Polarization Drift”. In: *Physical Review Letters* 103.20 (Nov. 13, 2009), p. 205003. DOI: [10.1103/PhysRevLett.103.205003](https://doi.org/10.1103/PhysRevLett.103.205003) (cit. on pp. 103, 175).

- [111] T.S. Hahm, P.H. Diamond, O.D. Gurcan, et al. “Nonlinear Gyrokinetic Theory of Toroidal Momentum Pinch”. In: *Physics of Plasmas* 14.7 (July 2007), p. 072302. ISSN: 1070-664X, 1089-7674. DOI: [10.1063/1.2743642](https://doi.org/10.1063/1.2743642) (cit. on pp. 103, 104, 113).
- [112] A.G. Peeters, C. Angioni, and D. Strintzi. “Toroidal Momentum Pinch Velocity Due to the Coriolis Drift Effect on Small Scale Instabilities in a Toroidal Plasma”. In: *Physical Review Letters* 98.26 (June 28, 2007), p. 265003. ISSN: 0031-9007, 1079-7114. DOI: [10.1103/PhysRevLett.98.265003](https://doi.org/10.1103/PhysRevLett.98.265003) (cit. on pp. 103, 104).
- [113] Ö.D. Gürcan, P.H. Diamond, T.S. Hahm, et al. “Intrinsic Rotation and Electric Field Shear”. In: *Physics of Plasmas* 14.4 (Apr. 2007), p. 042306. ISSN: 1070-664X, 1089-7674. DOI: [10.1063/1.2717891](https://doi.org/10.1063/1.2717891) (cit. on pp. 103, 118).
- [114] W.M. Solomon, K.H. Burrell, A.M. Garofalo, et al. “Advances in Understanding the Generation and Evolution of the Toroidal Rotation Profile on DIII-D”. In: *Nuclear Fusion* 49.8 (Aug. 2009), p. 085005. ISSN: 0029-5515, 1741-4326. DOI: [10.1088/0029-5515/49/8/085005](https://doi.org/10.1088/0029-5515/49/8/085005) (cit. on p. 103).
- [115] F.J. Casson, A.G. Peeters, Y. Camenen, et al. “Anomalous Parallel Momentum Transport Due to E×B Flow Shear in a Tokamak Plasma”. In: *Physics of Plasmas* 16.9 (Sept. 2009), p. 092303. ISSN: 1070-664X, 1089-7674. DOI: [10.1063/1.3227650](https://doi.org/10.1063/1.3227650) (cit. on pp. 103, 113).
- [116] M. Barnes, F.I. Parra, J.P. Lee, et al. “Intrinsic Rotation Driven by Non-Maxwellian Equilibria in Tokamak Plasmas”. In: *Physical Review Letters* 111.5 (Aug. 1, 2013), p. 055005. ISSN: 0031-9007, 1079-7114. DOI: [10.1103/PhysRevLett.111.055005](https://doi.org/10.1103/PhysRevLett.111.055005) (cit. on p. 103).
- [117] C.-C. Chen, P.H. Diamond, R. Singh, et al. “Potential Vorticity Transport in Weakly and Strongly Magnetized Plasmas”. In: *Physics of Plasmas* 28.4 (Apr. 2021), p. 042301. ISSN: 1070-664X, 1089-7674. DOI: [10.1063/5.0041072](https://doi.org/10.1063/5.0041072) (cit. on p. 103).
- [118] P.W. Terry. “Suppression of Turbulence and Transport by Sheared Flow”. In: *Reviews of Modern Physics* 72.1 (Jan. 1, 2000), pp. 109–165. ISSN: 0034-6861, 1539-0756. DOI: [10.1103/RevModPhys.72.109](https://doi.org/10.1103/RevModPhys.72.109) (cit. on p. 103).
- [119] L. Vermare, P. Hennequin, Ö.D. Gürcan, et al. “Impact of Collisionality on Fluctuation Characteristics of Micro-Turbulence”. In: *Physics of Plasmas* 18.1 (Jan. 2011), p. 012306. ISSN: 1070-664X, 1089-7674. DOI: [10.1063/1.3536648](https://doi.org/10.1063/1.3536648) (cit. on pp. 106, 124).
- [120] P.H. Diamond, C.J. McDevitt, Ö.D. Gürcan, et al. “Physics of Non-Diffusive Turbulent Transport of Momentum and the Origins of Spontaneous Rotation in Tokamaks”. In: *Nuclear Fusion* 49.4 (Apr. 2009), p. 045002. ISSN: 0029-5515, 1741-4326. DOI: [10.1088/0029-5515/49/4/045002](https://doi.org/10.1088/0029-5515/49/4/045002) (cit. on p. 109).
- [121] X. Garbet, Y. Sarazin, P. Ghendrih, et al. “Turbulence Simulations of Transport Barriers with Toroidal Velocity”. In: *Physics of Plasmas* 9.9 (Sept. 2002), pp. 3893–3905. ISSN: 1070-664X, 1089-7674. DOI: [10.1063/1.1499494](https://doi.org/10.1063/1.1499494) (cit. on p. 113).



- [122] W.X. Wang, T.S. Hahm, S. Ethier, et al. “Gyrokinetic Studies on Turbulence-Driven and Neoclassical Nondiffusive Toroidal-Momentum Transport and the Effect of Residual Fluctuations in Strong  $E \times B$  Shear”. In: *Physical Review Letters* 102.3 (Jan. 23, 2009), p. 035005. ISSN: 0031-9007, 1079-7114. DOI: [10.1103/PhysRevLett.102.035005](https://doi.org/10.1103/PhysRevLett.102.035005) (cit. on p. 120).
- [123] J.-K. Park, S.M. Yang, N.C. Logan, et al. “Quasisymmetric Optimization of Nonaxisymmetry in Tokamaks”. In: *Physical Review Letters* 126.12 (Mar. 26, 2021), p. 125001. ISSN: 0031-9007, 1079-7114. DOI: [10.1103/PhysRevLett.126.125001](https://doi.org/10.1103/PhysRevLett.126.125001) (cit. on p. 121).
- [124] P. Hennequin, C. Honoré, A. Truc, et al. “Doppler Backscattering System for Measuring Fluctuations and Their Perpendicular Velocity on Tore Supra”. In: *Review of Scientific Instruments* 75.10 (Oct. 2004), pp. 3881–3883. ISSN: 0034-6748. DOI: [10.1063/1.1787920](https://doi.org/10.1063/1.1787920) (cit. on p. 123).
- [125] P. Hennequin, C. Honoré, A. Truc, et al. “Fluctuation Spectra and Velocity Profile from Doppler Backscattering on Tore Supra”. In: *Nuclear Fusion* 46.9 (Aug. 2006), S771–S779. ISSN: 0029-5515. DOI: [10.1088/0029-5515/46/9/S12](https://doi.org/10.1088/0029-5515/46/9/S12) (cit. on p. 123).
- [126] C. Honoré, P. Hennequin, A. Truc, et al. “Quasi-Optical Gaussian Beam Tracing to Evaluate Doppler Backscattering Conditions”. In: *Nuclear Fusion* 46.9 (Aug. 2006), S809–S815. ISSN: 0029-5515. DOI: [10.1088/0029-5515/46/9/S16](https://doi.org/10.1088/0029-5515/46/9/S16) (cit. on p. 124).
- [127] R.E. Waltz, G.M. Staebler, W. Dorland, et al. “A Gyro-Landau-fluid Transport Model”. In: *Physics of Plasmas* 4.7 (July 1997), pp. 2482–2496. ISSN: 1070-664X. DOI: [10.1063/1.872228](https://doi.org/10.1063/1.872228) (cit. on pp. 128, 132, 133, 148).
- [128] C.C. Petty, J.E. Kinsey, and T.C. Luce. “Safety Factor Scaling of Energy Transport in L-mode Plasmas on the DIII-D Tokamak”. In: *Physics of Plasmas* 11.3 (Mar. 2004), pp. 1011–1018. ISSN: 1070-664X. DOI: [10.1063/1.1645791](https://doi.org/10.1063/1.1645791) (cit. on pp. 128, 132).
- [129] G. Dif-Pradalier, G. Hornung, P. Ghendrih, et al. “Finding the Elusive  $E \times B$  Staircase in Magnetized Plasmas”. In: *Physical Review Letters* 114.8 (Feb. 27, 2015), p. 085004. DOI: [10.1103/PhysRevLett.114.085004](https://doi.org/10.1103/PhysRevLett.114.085004) (cit. on p. 131).
- [130] T. Dannert and F. Jenko. “Gyrokinetic Simulation of Collisionless Trapped-Electron Mode Turbulence”. In: *Physics of Plasmas* 12.7 (July 2005), p. 072309. ISSN: 1070-664X, 1089-7674. DOI: [10.1063/1.1947447](https://doi.org/10.1063/1.1947447) (cit. on p. 132).
- [131] M. Ottaviani, W. Horton, and M. Erba. “The Long Wavelength Behaviour of Ion-Temperature-Gradient-Driven Turbulence and the Radial Dependence of the Turbulent Ion Conductivity”. In: *Plasma Physics and Controlled Fusion* 39.9 (Sept. 1997), pp. 1461–1477. ISSN: 0741-3335. DOI: [10.1088/0741-3335/39/9/012](https://doi.org/10.1088/0741-3335/39/9/012) (cit. on p. 133).

- [132] G.D. Conway, A.I. Smolyakov, and T. Ido. “Geodesic Acoustic Modes in Magnetic Confinement Devices”. In: *Nuclear Fusion* 62.1 (Dec. 2021), p. 013001. ISSN: 0029-5515. DOI: [10.1088/1741-4326/ac0dd1](https://doi.org/10.1088/1741-4326/ac0dd1) (cit. on pp. 141, 148).
- [133] P. Angelino, A. Bottino, R. Hatzky, et al. “Effects of Plasma Current on Nonlinear Interactions of ITG Turbulence, Zonal Flows and Geodesic Acoustic Modes”. In: *Plasma Physics and Controlled Fusion* 48.5 (Mar. 2006), pp. 557–571. ISSN: 0741-3335. DOI: [10.1088/0741-3335/48/5/005](https://doi.org/10.1088/0741-3335/48/5/005) (cit. on p. 141).
- [134] N. Miyato, Y. Kishimoto, and J. Li. “Global Structure of Zonal Flow and Electromagnetic Ion Temperature Gradient Driven Turbulence in Tokamak Plasmas”. In: *Physics of Plasmas* 11.12 (Dec. 2004), pp. 5557–5564. ISSN: 1070-664X. DOI: [10.1063/1.1811088](https://doi.org/10.1063/1.1811088) (cit. on p. 141).
- [135] V.B. Lebedev, P.N. Yushmanov, P.H. Diamond, et al. “Plateau Regime Dynamics of the Relaxation of Poloidal Rotation in Tokamak Plasmas”. In: *Physics of Plasmas* 3.8 (Aug. 1996), pp. 3023–3031. ISSN: 1070-664X. DOI: [10.1063/1.871638](https://doi.org/10.1063/1.871638) (cit. on p. 142).
- [136] N. Winsor, J.L. Johnson, and J.M. Dawson. “Geodesic Acoustic Waves in Hydro-magnetic Systems”. In: *The Physics of Fluids* 11.11 (Nov. 1968), pp. 2448–2450. ISSN: 0031-9171. DOI: [10.1063/1.1691835](https://doi.org/10.1063/1.1691835) (cit. on p. 142).
- [137] K. Miki and P.H. Diamond. “Novel States of Pre-Transition Edge Turbulence Emerging from Shearing Mode Competition”. In: *Nuclear Fusion* 51.10 (Aug. 2011), p. 103003. ISSN: 0029-5515. DOI: [10.1088/0029-5515/51/10/103003](https://doi.org/10.1088/0029-5515/51/10/103003) (cit. on pp. 144–146).
- [138] F.L. Hinton and M.N. Rosenbluth. “Dynamics of Axisymmetric and Poloidal Flows in Tokamaks”. In: *Plasma Physics and Controlled Fusion* 41 (3A Jan. 1999), A653–A662. ISSN: 0741-3335. DOI: [10.1088/0741-3335/41/3A/059](https://doi.org/10.1088/0741-3335/41/3A/059) (cit. on p. 148).
- [139] Z. Gao, K. Itoh, H. Sanuki, et al. “Eigenmode Analysis of Geodesic Acoustic Modes”. In: *Physics of Plasmas* 15.7 (July 2008), p. 072511. ISSN: 1070-664X. DOI: [10.1063/1.2956993](https://doi.org/10.1063/1.2956993) (cit. on p. 148).
- [140] Y. Sarazin, G. Dif-Pradalier, X. Garbet, et al. “Key Impact of Phase Dynamics and Diamagnetic Drive on Reynolds Stress in Magnetic Fusion Plasmas”. In: *Plasma Physics and Controlled Fusion* 63.6 (May 2021), p. 064007. ISSN: 0741-3335. DOI: [10.1088/1361-6587/abf673](https://doi.org/10.1088/1361-6587/abf673) (cit. on p. 152).
- [141] T.A. Gianakon, S.E. Kruger, and C.C. Hegna. “Heuristic Closures for Numerical Simulations of Neoclassical Tearing Modes”. In: *Physics of Plasmas* 9.2 (Feb. 2002), pp. 536–547. ISSN: 1070-664X. DOI: [10.1063/1.1424924](https://doi.org/10.1063/1.1424924) (cit. on p. 153).
- [142] F. Palermo, X. Garbet, and A. Ghizzo. “Bicoherence Analysis of Streamer Dynamics Induced by Trapped Ion Modes”. In: *The European Physical Journal D : Atomic, molecular, optical and plasma physics* 69.1 (Jan. 2015), pp. 8–8. DOI: [10.1140/epjd/e2014-50240-2](https://doi.org/10.1140/epjd/e2014-50240-2) (cit. on p. 156).

- [143] Y.C. Kim and E.J. Powers. “Digital Bispectral Analysis and Its Applications to Nonlinear Wave Interactions”. In: *IEEE Transactions on Plasma Science* 7.2 (June 1979), pp. 120–131. ISSN: 1939-9375. DOI: [10.1109/TPS.1979.4317207](https://doi.org/10.1109/TPS.1979.4317207) (cit. on p. 156).
- [144] P.H. Diamond, M.N. Rosenbluth, E. Sanchez, et al. “In Search of the Elusive Zonal Flow Using Cross-Bicoherence Analysis”. In: *Physical Review Letters* 84.21 (May 22, 2000), pp. 4842–4845. DOI: [10.1103/PhysRevLett.84.4842](https://doi.org/10.1103/PhysRevLett.84.4842) (cit. on p. 156).
- [145] H. Han, S.J. Park, C. Sung, et al. “A Sustained High-Temperature Fusion Plasma Regime Facilitated by Fast Ions”. In: *Nature* 609.7926 (7926 Sept. 2022), pp. 269–275. ISSN: 1476-4687. DOI: [10.1038/s41586-022-05008-1](https://doi.org/10.1038/s41586-022-05008-1) (cit. on p. 160).